

Geotechnical and environmental performance of retaining structures in unsaturated soils

Présentée le 20 juillet 2020

à la Faculté de l'environnement naturel, architectural et construit
Laboratoire de mécanique des sols - Chaire gaz naturel Petrosvibri
Programme doctoral en mécanique

pour l'obtention du grade de Docteur ès Sciences

par

Gianluca SPERANZA

Acceptée sur proposition du jury

Dr M. Farhat, président du jury
Prof. L. Laloui, Dr A. Ferrari, directeurs de thèse
Prof. A. Tarantino, rapporteur
Prof. D. Toll, rapporteur
Prof. C. Fivet, rapporteur

To my lovely family

Acknowledgments

I am thankful to my supervisors, Prof. Laloui and Dr. Alessio Ferrari. I thank both of them for allowing me to develop myself in such a stimulating environment. Prof. Laloui is the supervisor that every PhD candidate would like to have. I have really appreciated his suggestions, feedback, and incentives for all the activities within my PhD. He always challenged me in giving always something more. I'm also grateful to Dr. Alessio Ferrari who has contributed significantly to my professional and scientific growth. I would like to thank him for his dedication to supervising my thesis work and for having transmitted me his culture of the detail.

I wish to thank Dr. M. Farhat for having chaired the examination jury, Prof. A. Tarantino, Prof. D. Toll, and Prof. C. Fivet for the valuable comments on my dissertation and for having taken part of the jury committee.

I wish to acknowledge the support of the European Commission via the Marie Skłodowska-Curie Innovative Training Networks (ITN-ETN) who has sponsored this research project and the Industrial partners Nobatek/ Inef4. I want to thank in particular Pyrène and Maxime for their support.

I'm also thankful to all the laboratory technicians who have worked in the laboratory during these years and who have helped me a lot with the experimental activities. In particular, a special thank is for Patrick Dubey, Luc Morier-Genoud, and Nikolov Kosta.

I forgot to mention above that one of the best attitudes that characterize both Prof. Laloui and Dr. Ferrari is the capability in selecting good employees for the Laboratory for Soil Mechanics. I'm not referring to their scientific skills but mainly to their human attitude! During the last three and a half years I met dozens of different people. I have learned a lot from each of them. They were always available in sharing both working time and free time. Thank you to Jacopo, my Terre-brother, my officemate, my roommate in hotels during external events, and, above all, a new honest friend. A lovely thanks to Angelica, my psychotherapist-colleague, always available in sharing joys and pains. Thank you to my PhD-older brother and sister Alberto and Eleonora; they have transferred me the right experience to avoid the "ssss.." effect! A special thanks to my English teacher-colleague Barnaby, to my ski-teacher-

colleague Elena and to the most skilled skier “Ingeniero de terreno”, also known as Jose. A special thanks to Aldo, a “font of knowledge”, always available to provides help, feedback, and ideas for both research and cuisine. I’m really grateful to Cristiano, Etienne, Ariadni, Ray, Benoît, Margaux (French teacher also), Maren, Lorenzo, Wioletta, Sarah, Stefano, Jinwoo (and his “noodles” theory), Tae, Kim, Dimitrios (also officemate), Eleni, Kwangwoo, Alexandra, Alessandro, Valentina, for all the valuable feedback I got during the group meetings.

I would like to thank a lot Patrycja because she showed me that the intensity of the happiness in reaching each goal is proportional to the amount of energy that you put in it.

I want to thank also the LEMR group and in particularly Chiara, Felipe, Mateo, and Corentin.

A special acknowledge to all the TERRE network and in particular to the ESRs, for all the research discussion we had and all the wonderful evening past together around Europe (Roberta, Riccardo, Alessandro, Raniero, Javier, Elodie, Abhijith, Sofia, Alessia, Lorenzo, Emmanuel, Pavlina, and Sravan).

I am also grateful to “Les lausannois”, the cuisine whatsapp group (Chiara, Jacopo, Gianluca “Méssié”, Eleonora, Cristina e Nicolas “Leclerc”).

I cannot forget all my flatmates. Firstly Peggy, a really nice person, always available in helping whoever needs. She taught me French and to eat red cabbage. We have shared the flat with a lot of nice people during the last three years: Francesco, Valentina, Matteo, Chase, and Romans.

I am awfully grateful to my family: my mother, my father, and my brother for having encouraged all my ambitions. A special thanks to my girlfriend Marinella, who has always supported me every day, with incredible love.

And finally, I want to thank that part of me that has managed to sacrifice my dearest loves, to live away from my family, and to insist on overcoming all the dark moments that have occurred. I want to thank that part of me that has always believed in it!

Table of contents

Table of contents.....	iii
Abstract.....	vii
Keywords.....	viii
Riassunto	ix
Parole chiave.....	x
List of Figures.....	xi
List of Tables	xviii
List of Symbols	xix
Chapter 1	1
1. Introduction.....	3
1.1 The general context of the thesis.....	3
1.2 Thesis objective and contribution	3
1.3 Outline of the thesis	5
Chapter 2	9
2. Life cycle assessment model of retaining structures in unsaturated soils	11
2.1 Foreword.....	11
2.2 Introduction	12
2.3 Background.....	13
2.3.1 Retaining structures in unsaturated soils	13
2.3.2 Life cycle assessment of retaining structures.....	16
2.4 Selected methods	19
2.4.1 Theoretical framework adopted for estimating lateral earth pressure in unsaturated soils.....	20
2.4.2 An LCA model for a retaining structure.....	25
2.4.3 The analyzed case	28

2.5	Results and Discussion	31
2.6	Conclusions.....	39
Chapter 3	43
3.	Active earth pressure of unsaturated soils under transient flow.....	45
3.1	Foreword.....	45
3.2	Analytical solution of transient seepage in unsaturated soils	46
3.2.1	Steady-state solution	49
3.2.2	Transient solution.....	50
3.2.3	Infiltration model.....	52
3.3	Uncoupled hydro-mechanical analyses.....	53
3.4	Illustrative example and parametric study on three soil types.....	55
3.5	Conclusions.....	63
Chapter 4	65
4.	Experimental investigation on the hydro-mechanical properties of a sandy and a silty soil: implications on the lateral earth pressure	67
4.1	Foreword.....	67
4.2	Itterbeck sand.....	68
4.2.1	Physical properties.....	68
4.2.2	Direct shear tests from very low to high vertical stress.....	70
4.2.3	Water retention behaviour	75
4.3	The employed High Capacity Tensiometers.....	79
4.3.1	Manufacturing	81
4.3.2	Saturation and cavitation of the tensiometers	83
4.3.3	Calibration and preconditioning prior suction measurements.....	86
4.4	Sion Silt.....	89

4.5	Conclusions: implication of the assumed water retention model on the lateral earth pressure.....	95
Chapter 5		97
5.	Physical modelling of retaining structures interacting with unsaturated soils.....	99
5.1	Foreword.....	99
5.2	The physical model	100
5.3	Design, building, and calibration of the experimental devices.....	101
5.3.1	The water-filled hydraulic cylinder.....	101
5.3.2	Linear guideways.....	104
5.3.3	The High Capacity Tensiometers.....	105
5.3.4	The instrumentations for the PIV.....	106
5.3.5	The instruments for controlling groundwater level and to simulate rainfall events.....	107
5.4	Experimental phases and tested soil	108
5.5	Results and analysis.....	112
5.5.1	Effects of partial saturation on the failure mechanism at the active state	112
5.5.2	Effect of partial saturation on the lateral earth thrust at the at-rest state	122
5.6	Conclusions.....	131
Chapter 6		133
6.	Long-term performance and life cycle assessment of energy piles in three different climatic conditions	135
6.1	Foreword.....	135
6.2	Introduction	135
6.3	Material and methods	137

6.3.1 3D Finite Element Modelling of an Energy Pile Group.....	138
6.3.2 Life Cycle Assessment.....	146
6.4 Results and Discussion	150
6.4.1 Energy Demand and Supply	151
6.4.2 Temperature Fluctuations along Energy Piles and in the Surrounding Soil.....	153
6.4.3 Life Cycle Impact Assessment.....	154
6.5 Conclusions.....	159
Chapter 7	161
7. Conclusions.....	163
7.1 Thesis contribution.....	164
7.2 Prospective and future research	168
Chapter 8	171
8. References.....	173
Appendix.....	189
Appendix A – Details of the box design.....	191
Appendix B – Midpoint indicators’ scores.....	193
Curriculum Vitae.....	197

Abstract

Presently, environmental issues are considered as critical aspects concerning the market competitiveness in the building and construction sector. However, the construction sector is regarded as one of the main areas contributing to CO₂ emissions and resource consumption worldwide. In recent years, industry and academia have been investing significantly in order to produce innovative low-carbon technologies. Other than the significant effort that has been invested in the energy and environmental efficiency of buildings, few research studies concerning geotechnical structure and infrastructure are available in the literature. These previously lacking research activities have been conducted in the framework of the European project TERRE (Training Engineers and Researchers to Rethink geotechnical Engineering for a low carbon future), which was devoted to expanding this innovation to the geo-infrastructure industry. Specifically, the performance of retaining structures in unsaturated soils is investigated in the attempt to optimize their design procedures. Moreover, the thesis deals with the quantification of the environmental impacts of geostructures by comparing conventional and low-carbon geotechnical design solutions.

Geotechnical analyses and design procedures for retaining structures mainly consider the retained soils as dry or saturated. The partially saturated condition implies the presence of negative pore-water pressures (suction) that contribute to increasing both the strength and the stiffness of the retained geomaterial. Suction can be considered as a natural 'low-carbon' soil reinforcement that can be deployed to reduce the overdesign of both temporary and permanent retaining structures. However, the advantages provided by the condition of partial saturation can evolve with time due to the influence of environmental actions. In this regard, analytical and experimental analyses have been performed to investigate the interaction between unsaturated soils and retaining structures. Simplified geomechanical analytical solutions are implemented in geotechnical design procedures and compared with experimental results. The latter have been conducted by adopting a 1g-physical model designed and built for this purpose. The apparatus is found to be capable of investigating several soil conditions. In particular, the horizontal component of the lateral earth thrust has been experimentally measured in both the at-rest and active states. The effects of the partial saturation (e.g., increase or decrease of the lateral earth thrust, failure mechanism in the active state) have been observed by considering suction profile evolution. The analytical

models have been found to be in generally good agreement with the performed tests. However, the water retention curve of the involved soils is found to play a key role in the computation of the lateral earth thrust.

Moreover, in collaboration with the industrial partner Nobatek/Inef4, the life cycle assessment (LCA) methodology has been employed to demonstrate the potential benefits provided by the considered eco-friendly geotechnical solutions. Two types of geostructures are considered: a retaining wall designed according to the mechanics of unsaturated soils and a thermo-activated group of piles to satisfy the heating and cooling demand of an office building. By highlighting their potentials and critical issues, the performed analyses have shown a possible significant reduction of the environmental impacts associated with the adoption of these low-carbon solutions.

Keywords

Earth thrust; suction; physical modeling; Life Cycle Assessment (LCA).

Riassunto

Oggigiorno le tematiche ambientali sono considerate fattori chiave per quanto riguarda la competitività sul mercato del settore dell'edilizia e delle costruzioni. D'altra parte, quest'ultimo è considerato uno delle principali aree che più contribuiscono alle emissioni di CO₂ ed al consumo di risorse a livello mondiale. Negli ultimi anni, l'industria e la ricerca hanno investito in modo significativo in tecnologie innovative a basse emissioni di CO₂. Nonostante considerevoli sforzi siano stati investiti nell'efficientamento energetico ed ambientale degli edifici, in letteratura sono disponibili meno studi riguardanti le strutture e le infrastrutture geotecniche. Le attività di ricerca presentate in questa tesi sono state condotte nell'ambito del progetto europeo TERRE (Training Engineers and Researchers to Rethink geotechnical Engineering for a low carbon future) principalmente dedicato ad estendere i principi di innovazione sostenibile al settore delle opere geotecniche. Nello specifico, il lavoro di tesi è incentrato sul comportamento delle opere di sostegno in terreni parzialmente saturi nel tentativo di ottimizzare la loro metodologia di progettazione. Inoltre, la tesi si occupa di quantificare l'impatto ambientale delle strutture geotecniche confrontando soluzioni convenzionali e quelle a basse emissioni di CO₂.

Analisi e procedure di progettazione geotecnica per le strutture di sostegno considerano convenzionalmente i terreni ritenuti asciutti o totalmente saturi. Le condizioni di parziale saturazione implicano la presenza di pressioni negative (suzione) che contribuiscono ad aumentare sia la resistenza che la rigidezza dei terreni. La suzione può essere considerata come un rinforzo naturale del terreno "a bassa emissione di CO₂" che può essere utilizzato per ovviare al sovradimensionamento delle opere di sostegno sia temporanee che permanenti. Tuttavia, i vantaggi forniti dalla condizione di parziale saturazione possono evolvere nel tempo a causa degli effetti indotti delle azioni ambientali. A questo proposito, sono state effettuate analisi analitiche e sperimentali per indagare l'interazione tra i terreni non saturi e le strutture di contenimento. Soluzioni analitiche semplificate sono state implementate nella procedura di progettazione geotecnica e confrontate con i risultati sperimentali. Questi ultimi sono stati condotti mediante l'utilizzo di un modello fisico appositamente progettato e costruito. L'apparato si è rivelato in grado di indagare diverse condizioni del terreno ritenuto. In particolare, la componente orizzontale della spinta laterale è stata misurata sperimentalmente sia in stato di riposo che attivo. Gli effetti della parziale saturazione (l'aumento o la diminuzione della spinta laterale ed il meccanismo di rottura allo stato attivo)

sono stati osservati considerando l'evoluzione delle pressioni negative dell'acqua. I modelli analitici sono risultati essere in generale accordo con le evidenze sperimentali riscontrate. Tuttavia, la curva di ritenzione idrica dei terreni coinvolti è risultata avere un ruolo chiave nel calcolo della spinta laterale delle terre.

Inoltre, in collaborazione con il partner industriale Nobatek/Inef4, è stata utilizzata la metodologia “analisi del ciclo di vita (ACV)” per dimostrare i potenziali benefici forniti dalle adottate soluzioni eco-compatibili. In particolare, sono state considerate due tipologie di geostrutture: un muro di contenimento progettato secondo la meccanica dei terreni parzialmente saturi e un gruppo di pali attivati termicamente per soddisfare la domanda di riscaldamento e raffreddamento di un edificio per uffici. Entrambe le analisi effettuate, mettendone alla luce potenzialità e criticità, hanno evidenziato una possibile significativa riduzione degli impatti ambientali grazie all'adozione di soluzioni a basse emissioni di CO₂.

Parole chiave

Spinta delle terre; suzione; modellazione fisica; analisi del ciclo di vita (ACV).

List of Figures

Figure 2.1. Evolution of pore water-pressure (u_w), degree of saturation (S_r), and continuity of water/air phase versus depth above the groundwater table.....	14
Figure 2.2. Stages of a Life Cycle Assessment.	17
Figure 2.3. Methodology adopted for the coupled environmental–geotechnical analysis.	20
Figure 2.4. Pore water pressure and lateral earth pressure distribution at imposed infiltration/exfiltration rate. drying and wetting periods..	23
Figure 2.5. Pore water pressure, total vertical stress, effective vertical stress, effective horizontal stress and total horizontal stress profiles at the very early stages of the rainfall event.....	25
Figure 2.6. Description of the life cycle system proposed for a retaining wall.	26
Figure 2.7. Schematic representation of the analyzed case study. ..	29
Figure 2.8. a) Experimental and adopted model of the water retention behavior of the three soils; evolution of hydraulic conductivities with matric suction for b) silt, c) clayey-silty sand, and d) sand.	30
Figure 2.9. Evolution of the degree of saturation (a_1 , a_2 , a_3), the lateral stress induced by matric suction (b_1 , b_2 , b_3), and the lateral earth pressure with depth (c_1 , c_2 , c_3) at different infiltration rates.....	32
Figure 2.10. Comparison of the lateral earth pressure distributions for the UDA (scenario 1 and 2) and the CDA for the silt and the clayey-silty sand.	33
Figure 2.11. Life Cycle Impact Assessment midpoint results and related uncertainty of the CDA and UDA (silt).....	35
Figure 2.12. Life Cycle Impact Assessment midpoint results and related uncertainty of the CDA and UDA (clayey-silty sand).....	36

Figure 2.13. Life Cycle Impact Assessment midpoint results and related uncertainty of the CDA and UDA (sand).	37
Figure 2.14. Life Cycle Impact Assessment endpoint results and related uncertainty for (a) silt, (b) clayey-silty sand, and (c) sand.....	38
Figure 2.15. Endpoint scores of each stage in the life cycle of a retaining cantilevered wall. (classic design approach with silt).	40
Figure 3.1. Schematic representation of one-dimensional infiltration model: geometry and assumed initial condition.....	48
Figure 3.2. Comparisons between potential infiltration and various rainfall intensities.	52
Figure 3.3. Effective rainfall capacity and ponding time.....	53
Figure 3.4 Geometry of the investigated problem at the initial condition and during the rainfall event.	55
Figure 3.5 Water retention curve in terms of volumetric water content for a) silt, b) clayey-silty sand, and c) sand.....	56
Figure 3.6 Evolution of the matric suction, effective stress parameter, and lateral earth pressure profiles with the time.....	59
Figure 3.7 a)Extreme value analysis for five-days data: b) histogram of extrema, fitting with the GEV density distribution; c) evolution of the return level with the return period, the upper and lower lines represent the 95% confidence intervals (MeteoSwiss, 2016).	61
Figure 3.8 Evolution of the matric suction, effective stress parameter, and lateral earth pressure profiles during the 5 days of rain. Infiltration rate equal to 1.36 mm/h for all the considered soils.....	62
Figure 4.1 Itterbek sand under a microscope (Terzis, 2017).....	69
Figure 4.2 Grain size distribution.	70
Figure 4.3 Evolution of soil bulk density with the void ratio at different degree of saturation.	71

Figure 4.4 Schematic representation of the employed direct shear test device for low vertical stress.....	72
Figure 4.5 a) Results of the direct shear tests performed in the range of vertical stress expected in the physical model; b) Peak failure envelope at low effective stress; c) Results of the direct shear tests performed in the range 10-50 kPa; d) Failure envelopes in the range 10-50 kPa.....	73
Figure 4.6 a) Results of the direct shear tests performed in the range 50-250 kPa; b) Peak failure envelope in the range 50-250 kPa; c) Results of the direct shear tests performed in the range 100-250 kPa; d) Failure envelopes in the range 100-500 kPa.....	74
Figure 4.7 a) Peak and constant volume failure envelope of the all performed tests; b) evolution of the peak and the CV shear strength angle within selected ranges of vertical effective stress.....	75
Figure 4.8 a)Schematic representation of the performed test; b) overall picture of the employed device; c) specimens on the ceramic disc; d) and e) zoom on the burette and the measuring cylinder.....	76
Figure 4.9 Water rentention curve: experimental and modelling results.	78
Figure 4.10 Schematic layout of the Trento tensiometer (modified after Tarantino and Mongiovi, 2002).....	81
Figure 4.11. a)Tensiometer's body; b) detail of the diaphragm; c) saturation chamber; d) porous ceramic AEV = 1.5 MPa; e) Size-reduction of the porous ceramic; f) Tensiometers' body after stress relieving heat treatment; g) Manufactured tensiometer.	83
Figure 4.12. The device employed for the first saturation of the tensiometers.....	84
Figure 4.13. Voltage evolution recorded by the data acquisition system during the first saturation of a tensiometer.....	85
Figure 4.14. Voltage evolution recorded by the data acquisition system during cavitation.....	86

Figure 4.15. a) Calibration curve in the range 0 – 2000 kPa; b) check of the calibration in range 0 – 2000 kPa; c) calibration curve in the range 0 – 100 kPa; d) check of the calibration in range 0 – 100 kPa.	87
Figure 4.16. View of the experiment setup.	90
Figure 4.17. Matric suction evolution with time, drying test 1.	91
Figure 4.18. Matric suction evolution with time, wetting test 1.	92
Figure 4.19. Shrinkage and swelling during drying and wetting paths, zoom on the specimen border.	93
Figure 4.20. a) Water retention curves; b) evolution between void ratio and matric suction with water content.	94
Figure 4.21. Evolution of shear strength with suction at different normal stress: comparison between the adopted water retention curve (main drying or main wetting curve) for the silt (left) and the sand (right).	96
Figure 5.1. a) 3D schematic conception of the physical model; b) hydraulic water filled cylinder detail; c) overview of the experimental set-up; d) detail of a linear guideway; e) detail of a tensiometer's support.	101
Figure 5.2. Design graphs for the choice of the hydraulic cylinder's diameter.	102
Figure 5.3. a) Evolution of the measured force and the measured pressure applied to the water-filled hydraulic cylinder during the calibration phase (scenario 1); b) calibration curve during loading and unloading steps at constant volume (scenario 1); c) calibration curve during loading at constant volume and unloading with variation of volume (scenario 2); d) variation of volume during loading and unloading (scenario 2).	104
Figure 5.4. Details of the designed linear guides and assembling in the physical model.	105
Figure 5.5 Calibration curve tensiometer 1.	106
Figure 5.6 Calibration curve of the rainfall simulator.	108
Figure 5.7 Schematic representation of the performed tests.	109

Figure 5.8. Water retention behaviour. Experimental data and employed fitting models.	111
Figure 5.9. a) Evolution of the measured horizontal displacement during the backfilling phase (Test1.1a); b) comparison between experimental data and Jacky's theoretical model (Test1.1a).	114
Figure 5.10 a) Results of Test 1 and Test 2 in terms of force evolution with the horizontal displacement; b) zoom on the first millimeter of the tests.	115
Figure 5.11 Measured pore water pressure with the tensiometers.	116
Figure 5.12. Results of the PIV analysis Test 1.1a.	117
Figure 5.13. Results of the PIV analysis Test 1.2.	118
Figure 5.14 a) Failure surface view from the top (Test 1.1a); b) Failure surface lateral view (Test 1.1a); c) Failure surface lateral view (Test 1.2).	119
Figure 5.15 a) Matric suction profile in the unsaturated portion of the retained soil; b) Degree of saturation profile; c) unit weight profile; d) lateral earth pressure distribution according to extended Rankine's theory.	121
Figure 5.16 Comparison between experimental results and theoretical formulation.	122
Figure 5.17. a) Measured horizontal component of the lateral earth thrust; b) measured horizontal component of the lateral earth thrust, zoomed-in at the time of the GWT lowering c) measured horizontal component of the lateral earth thrust, zoomed-in at the time of the rainfall event simulation; d) measured matric suction at the time of the GWT lowering; e) measured matric suction at the time of the rainfall event simulation.	123
Figure 5.18. Representation of the drying and wetting paths on the SWRC at 10 cm, 20 cm, 30 cm, 40 cm and 50 cm of depth.	126
Figure 5.19. Evolution with the depth of the pore water pressure, the degree of saturation, the total vertical stress, and the lateral earth pressure	

coefficients computed for the Test 2.1 2.2 and 2.3 according to the analytical model.....	128
Figure 5.20. Evolution with the time of the lateral earth pressure coefficient computed at different depths.	129
Figure 5.21. The horizontal component of the lateral earth thrust, a comparison between the analytical model and the experimental values.	130
Figure 6.1. Heating/cooling demand histogram; minimum and maximum mean daily temperatures at Seville, Rome, and Berlin.....	138
Figure 6.2. a) Finite element mesh; b) Energy pile foundation layout; c) Energy pile geometry and pipe positions.....	139
Figure 6.3. Scheme of a GSHP system.....	144
Figure 6.4. COP of GSHP with respect to the source temperature.	145
Figure 6.5. a) Office building with pile foundation furnished by a conventional heating and cooling system; b) Office building equipped with energy piles.....	147
Figure 6.6 Temperature fluctuation of the water circulating in the pipes due to intermittent operation of GSHP during transition from a) Heating to cooling, b) Cooling to heating (Seville).....	151
Figure 6.7. Annual distribution of energy demand and supply; temperature of the heat carrier fluid for a) Seville, b) Rome, and c) Berlin cases.....	152
Figure 6.8 Pile and soil temperature during geothermal operations in a) Seville, b) Rome, and c) Berlin.	155
Figure 6.9. Contribution to the total environmental impact in terms of climate change from the different LC stages (average of the three reference cities).	156
Figure 6.10. Indicators of the environmental performance of the conventional system and the energy piles for the three reference cities.	157

Figure 6.11 Evolution of the environmental indicators of the conventional system and the energy piles during the reference year for the three reference cities.	158
Figure A.1. Details of box the design.....	191
Figure A.2. Midpoint indicators of the conventional system and the energy piles for Seville.....	193
Figure A.3. Midpoint indicators of the conventional system and the energy piles for Rome	194
Figure A.4. Midpoint indicators of the conventional system and the energy piles for Berlin	195

List of Tables

Table 2.1. Adopted physical-hydro-mechanical parameters of soils. γ_{dry} : dry unit weight, γ_{sat} : saturated unit weight, ϕ' : shear strength angle, c' : intercept cohesion, k_s : saturated hydraulic conductivity, α , n , and m : parameters of the van Genuchten model.	30
Table 2.2. The horizontal component of the retained earth's thrust for each of the three reference soils and the consequent amount of material required depending on the retaining wall's design type.	34
Table 3.1. Soils' properties.....	57
Table 4.1. Ittembeck sand's physical properties.	70
Table 4.2. Calibration parameters of van Genuchten model.	79
Table 4.3. Suction measurement instruments Murray and Sivakumar (2010) modified.....	80
Table 4.4. Unloading by steps (on the left) drying cycles (on the right) example for a HCT.....	88
Table 4.5. Calibration parameters of Van Gehuchten's model.....	94
Table 5.1. Results of the sensitivity mesh analysis.....	107
Table 5.2. Parameters of the adopted fitting curves modelling the water retention behaviour.....	112
Table 6.1 Material properties for the soil and pile domains.....	143
Table 6.2 Properties assigned for the pipe	143
Table 6.3 LCI of the conventional systems for the three reference cities (SV: Seville; RM: Rome; BE: Berlin).....	148
Table 6.4 LCI of energy piles for the three reference cities (SV: Seville; RM: Rome; BE: Berlin).	149

List of Symbols

Symbol	Name	Unit
Roman Symbols		
A_p	Cross sectional area of pipe	m^2
c	Specific heat capacity	$J/(kg \cdot K)$
C	Moisture capacity	$1/m$
C_c	Coefficient of curvature	-
c_f	Specific heat capacity of the fluid	$J/(kg \cdot K)$
c'	Effective cohesion	Pa
COP	Coefficient of performance of the heat pump	-
$COP_{C,c}$	Carnot coefficient of performance for cooling	-
$COP_{C,h}$	Carnot coefficient of performance for heating	-
C_u	Coefficient of uniformity	-
d	Absolute displacement	mm
D	Diameter	mm
D	Diffusivity (chapter 3)	m^2/s
div	Divergence operator	-
d_h	Hydraulic diameter of the pipe	m
D_{10}	Dimensions of the grains corresponding to 10%, the passing to the sieve	mm
D_{30}	Dimensions of the grains corresponding to 30% of the passing to the sieve	mm

D_{60}	Dimensions of the grains corresponding to 60% of the passing to the sieve	mm
e	Void ratio	
e_{\max}	Maximum void ratio	-
e_{\min}	Minimum void ratio	-
e_0	Initial void ratio	-
F	Force	N
f_D	Darcy friction factor	-
g	Gravity acceleration	m/s^2
h	Total head	m
H	Total height of the considered domain	m
h_{eff}	Effective heat transfer coefficient of the pipe	$W/(m^2 \cdot K)$
h_{int}	Convective heat transfer coefficient inside the pipe	$W/(m^2 \cdot K)$
h_m	Matric suction head	
i	Infiltration rate	m/s
i_c	Horton's model parameter, infiltration rate at steady state.	m/s
i_0	Infiltration rate for steady state analysis	m/s
\bar{t}_0	Horton's model parameter, infiltration rate at time zero.	m/s
i_1	Initial infiltration rate for transient analysis	m/s
k	Hydraulic conductivity	m/s
k_c	Horton's model parameter, decay rapidity of potential infiltration rate	s

k_s	Saturated hydraulic conductivity	m/s
k_x	X component of hydraulic conductivity tensor	m/s
K_y	Y component of hydraulic conductivity tensor	m/s
K_z	Z component of hydraulic conductivity tensor	m/s
K_0	At rest lateral earth pressure coefficient	-
K^*_0	At rest lateral earth pressure coefficient defined in total stress	-
L	Total length of the considered domain	m
\mathbf{L}	Laplacian operator	-
n	Porosity or Van Genuchten fitting parameter	-
m	Van Genuchten fitting parameter	-
m_α	Slopes of ACMEG SWRC model	1/Pa
Nu	Nusselt number	-
Nu_{turb}	Nusselt number under turbulent flow conditions	-
P_0	Horizontal component of lateral earth thrust at rest	N
Pr	Prandtl number	-
q'_w	Heat transfer through the unit length of the pipe wall	W/m
Q_{aux}	Energy supplied by the auxiliary system	W
Q_{prim}	Energy supplied by the energy piles	W
Q_{sec}	Energy supplied to the building	W
R	Universal gas constant	J/(mol·K)
Re	Reynolds number	-

RH	Relative umidity	-
r	Rain intensity	m/s
r_d	Design rain intensity	m/s
r_{in}	Inner diameter of the pipe	m
r_{out}	Outer diameter of the pipe	m
s	Suction	Pa
S	Effective degree of saturation	-
s^L	Laplace-transform complex variable	-
S_r	Degree of saturation	-
$S_{r,res}$	Residual degree of saturation	-
T	Temperature	K
T_f	Temperature of the fluid	K
T_{out}	Outer temperature of the pipe	K
t	Time	s
t_p	Ponding time	s
u_a	Air pressure	Pa
u	Horizontal component of the displacement	mm
$u_{f,i}$	Fluid velocity vector	m/s
u_w	Water pressure	Pa
u	Vertical component of the displacement	mm
v_x	X component of fluid velocity vector	m/s
v_y	Y component of fluid velocity vector	m/s

v_z	Z component of fluid velocity vector	m/s
$v_{w0} =$	Specific volume of water	kg/m ³
Y		
z	Depth	m
z_c	Depth of cracks	m

Greek Symbols

α	Van Genuchten fitting parameter	1/Pa
β	Gardner's model fitting parameter	1/m
$\beta_{1,d}$	Slope 1 of the failure surface dry condition	-
$\beta_{2,d}$	Slope 2 of the failure surface dry condition	-
δ_H	Horizontal displacement	mm
δ_{ij}	Kronecker's delta	-
$\delta_{1,u}$	Slope 1 of the failure surface unsaturated condition	-
$\delta_{2,u}$	Slope 2 of the failure surface unsaturated condition	-
γ	Soil unit weight	N/m ³
γ_d	Dry unit weight	N/m ³
γ_{sat}	Saturated unit weight	N/m ³
γ_w	Unit weight of water	N/m ³
γ'	Buoyant (submerged) unit weight	N/m ³
ϕ	Matrix flux potential at steady state	m ² /s
Φ	Matrix flux potential	m ² /s
Φ_0	Initial matrix flux potential	m ² /s

$\tilde{\Phi}$	Laplace transformation of the matrix flux potential	m^2/s
ϕ'	Shear strength angle	-
ϕ'_{cv}	Constant Volume Shear strength angle	-
ϕ'_p	Peak shear strength angle	-
λ	Thermal conductivity	$\text{W}/(\text{m}\cdot\text{K})$
λ_f	Thermal conductivity of the fluid	$\text{W}/(\text{m}\cdot\text{K})$
λ_p	Thermal conductivity of the pipe	$\text{W}/(\text{m}\cdot\text{K})$
η_{hp}	Efficiency factor of the heat pump	-
θ	Volumetric water content	-
θ_r	Residual volumetric water content	-
θ_s	Saturated volumetric water content	-
ρ	Density	kg/m^3
ρ_f	Density of the fluid	kg/m^3
ρ_s	Mass density of solid grains	kg/m^3
ρ_w	Water density	kg/m^3
σ_h	Total horizontal stress	Pa
σ'_{ij}	Component ij of the effective stress tensor	Pa
σ_n	Total normal stress	Pa
$\sigma_{\text{net},ij}$	Component ij of the net stress tensor	Pa
σ_v	Total vertical stress	Pa
τ	Shear stress	Pa
τ_f	Shear strength at failure	Pa

ψ_t	Total suction	Pa
χ	Effective stress parameter	-
ω_v	Molecular mass of water	Kg/kmol

Chapter 1

Introduction

1. Introduction

1.1 The general context of the thesis

Energy and environmental issues are considered key factors nowadays not only in the context of sustainable development but also in market competition. According to the Paris agreement on climate change, one of the long-term objectives to be reached by 2050 is the reduction of greenhouse gas emissions by 80-95%. Together, buildings and construction account for 39% of global carbon emissions (T. Abergel et al. 2018). Operational emissions, including heating, cooling, and lighting, account for 28%, and, as a consequence, the residual 11% of the carbon footprint is related to materials and construction processes. Doubtless, the construction sector can be considered one of the main areas responsible for all carbon emissions.

This research is carried out in the framework of the TERRE European Project (Training Engineers and Researchers to Rethink geotechnical Engineering for a low carbon future) funded by the European Commission. The project deals with technological innovation aimed at contributing to carbon emission reduction, exploring novel design concepts for low-carbon geotechnical infrastructure. Industry and research in the construction sector have been investing significantly in recent years to produce innovative low-carbon technologies. The project's intent is to expand this innovation to the geo-infrastructure industry. The Ph.D. candidate is involved in this inter-sectoral and intra-European project via a "joint-enrolment" between the Laboratory of Soil Mechanics of the Swiss Federal Institute of Lausanne (EPFL) and the industrial partner Nobatek/Inef4.

1.2 Thesis objective and contribution

The thesis deals with two main objectives: the first relates to the geomechanical performance of geostructures in unsaturated soils, with particular regard to retaining structures, and the second deals with the estimation of the environmental impacts of geostructures by comparing conventional and low-carbon geotechnical design solutions.

The first objective addresses the substantial intersection between low-carbon geotechnical engineering and unsaturated soil mechanics. Partially saturated soils can usually be found

in the upper portion of the soil profile above the phreatic surface. This zone, also called the vadose zone, is characterized by negative pore-water pressure (suction) and, generally, a degree of saturation lower than unity. On the other hand, the portion of soil below the groundwater level is usually affected by full saturation and positive pore water pressure. Rarely, the hydrological features of the specific site can result in the groundwater level being located at the ground surface.

Therefore, geotechnical structures often interact with the portion of the soil profile above the water level. Unlike dry or totally saturated soils, partially saturated soils can be characterized by higher strength and stiffness due to the positive contribution provided by negative pore water pressure. On the other hand, the soils in the vadose zone are subjected to climatic actions that can affect the pore water pressure distribution (infiltrations or evapotranspiration) affecting the mechanical response as a result. Even if the hydro-mechanical behavior of unsaturated soils has been extensively investigated in the literature, in engineering design practice geotechnical analyses are still performed considering the soils either as dry or fully saturated. These assumptions can lead to either overly conservative or unsafe design solutions. Remarking that safety must be considered as a priority, the contribution provided by negative pore-water pressure can be considered as a natural ‘low-carbon’ soil reinforcement that can be deployed to reduce the overdesign of geostructures. The adoption of unsaturated soil mechanics in the engineering practice not only allows for the consideration of climatic effects on geostructures (hardly possible through conventional geotechnical methods) but can also contribute to meeting the increasing financial and environmental pressures to reduce overdesign (Tarantino and Di Donna, 2019). The main challenge of the unsaturated design approach is that negative pore-water pressure can be potentially lost due to environmental actions.

Consequently, the accurate prediction of the water flow regime is revealed as critical. Specifically, in this thesis, the carbon-efficient design of retaining structures is investigated, exploiting the possibility of using the mechanics of unsaturated soils. Analytical models capable of performing uncoupled one-dimensional hydro-mechanical analyses have been implemented to study the effects induced by suction evolution during wetting periods (rainwater infiltrations). Steady-state analyses are presented to show the role played by the infiltration rate and the hydraulic parameters of the unsaturated retained soils. Transient analyses are

performed to understand how long it is possible to rely on the suction contribution to the stability of the soil-structure system during the rainfall event.

Furthermore, as will be discussed later in the dissertation, one of the most relevant points is represented by the identification of the hydraulic properties of the retained soils (e.g., retention properties), not only in terms of correctness in the experimental determination but also in terms of timeliness and ease of obtainment. Indeed, together with the number of soil parameters needed to provide rigorous geomechanical modeling of unsaturated soils, the time required to obtain them represents a key issue to fill the gap between the scientific community and engineering practice. Moreover, the results of an experimental campaign are presented. The tests performed at the Laboratory for Soil Mechanics at EPFL provide a validation of the simplified analytical analyses or, at the very least, provide an understanding as to how far these models are from the experimental evidence by highlighting their capabilities and weaknesses. In this regard, a new experimental apparatus (1g-physical model) has been designed and built.

The second objective (in collaboration with the industrial partner Nobatek/Inef4) deals with the development of methods for carbon footprint assessment where resource consumption and environmental effects are considered. The approach is based on the application of known carbon footprint assessment techniques (i.e., life-cycle assessment) for geotechnical construction. The procedures for the estimation of the environmental impacts of geotechnical technologies are investigated by integrating geostructures characteristics. In particular, two types of geostructures are considered: a retaining wall and a deep foundation. In the former, a life cycle assessment model is built for a retaining wall designed according to both conventional and unsaturated design approaches. In the latter, a life cycle assessment model is implemented to evaluate the environmental performance of a thermo-activated group of piles to satisfy the heating and cooling demand of an office building in contrasting geographical locations in Europe. Both analyses intend to compare conventional with low-carbon solutions.

1.3 Outline of the thesis

The content of the thesis is presented in the following order:

Chapter 2 preliminary presents a literature review recalling some fundamentals about the interaction between retaining structures and unsaturated soils. The environmental performance of retaining structures is then critically reviewed. The design of a cantilever retaining structure interacting with unsaturated soils is described, considering the infiltration rate in steady-state conditions for three different types of retained soils. Next, an LCA model for a cantilever retaining wall, from the extraction of raw materials to the disposal scenario, is proposed; the impacts of each of the life cycle stages are identified. The combination of life cycle thinking and multicriteria analysis provides a comprehensive picture of the geostructure's environmental impact and allows for the identification of burden shifting from one product life-cycle stage to another or from one impact category to another.

Chapter 3 presents a one-dimensional analytical closed-form formulation in the framework of uncoupled transient hydro-mechanical analyses. The procedure has been implemented by considering three different geomaterials as retained soils. The geomaterials were suitably chosen to highlight the role played by their hydro-mechanical properties and their effects on both the computation of the lateral earth pressure and its evolution with time. Assumptions and limitations of the implemented models are also highlighted and discussed.

Chapter 4 presents an experimental investigation of the water retention properties of two soils: a coarse-grained geomaterial (sand) and a fine-grained soil (silt). Two experimental techniques are used for the characterization of their retention behavior in terms of both drying and wetting paths. The hanging water column method is used to investigate the sand, which is the tested soil in the physical model. The silt's retention properties are obtained through the combined use of high capacity tensiometers and a dew-point hygrometer. The tensiometers which are used in the physical model have been manufactured with the help of the secondments of the TERRE project and the expertise of the University of Strathclyde. Manufacturing, saturation, and calibration procedures are also detailed. For both of the geomaterials, drying and wetting paths are investigated, highlighting the implications of the water retention model choice on the computation of the lateral earth pressure distribution.

Chapter 5 presents a new physical model capable of investigating the interaction between retaining walls and unsaturated soil. In this chapter, first, the experimental apparatus is

presented, then experimental results are provided. In particular, the main aim of the reported performed tests is to study the effects of the partially saturated condition on the failure mechanisms at the active state and the influence of matric suction changes on the lateral earth thrust at rest. The experimental results are interpreted by making a comparison with the analytical models available in literature to validate these theoretical approaches or understand the grade of accuracy to be expected.

Chapter 6 A life cycle assessment model is implemented to compare the environmental performance of energy piles and a group of conventional piles. The results of a finite element model, which takes the heating and cooling demands of a reference building, as well as the intermittent operations of a ground source heat pump, into consideration are used to examine the long-term performance of energy piles and are used as input parameters for the life cycle assessment analysis. The environmental enhancement provided by the adoption of a ground source heat pump system is quantified with respect to a conventional heating and cooling system.

Chapter 7 provides general conclusions and summarizes the principal achievements of the thesis. Furthermore, perspectives for further research are highlighted.

Chapter 2

Life cycle assessment model of retaining structures in unsaturated soils

2. Life cycle assessment model of retaining structures in unsaturated soils

2.1 Foreword

Retaining structures above groundwater level support soils that are usually in a state of partial saturation and subject to the actions of atmospheric agents. The current design approach takes into account the possible extremes of soil conditions—either totally dry or totally saturated—but it neglects matric suction’s contribution to soil shear strength. The present work aims to describe how the mechanics of unsaturated soils can positively influence the sustainability of retaining structures through a holistic, multidisciplinary, geotechnical, and environmental analysis. The geotechnical analysis allows estimating the lateral earth pressure of a geostructure in both unsaturated and extreme soil conditions (dry or saturated), which will directly influence the geometrical dimensions of the geostructure and consequently the amount of material employed for the geostructure construction. Next, the environmental analysis is performed with the standardized and globally applied Life Cycle Assessment (LCA) tool, in order to quantify the potential environmental impacts of the retaining structure according to both a life cycle and a multi-criteria perspective. First, an LCA model is built for a cantilever retaining wall, incorporating all the life cycle stages from the extraction of raw materials used for the wall construction to the disposal scenario of the wall, according to two design approaches: (a) an unsaturated design approach (UDA), i.e. when unsaturated soils’ principles are considered in the design procedure, and (b) a conventional design approach (CDA), i.e. the soil is considered dry or totally saturated. Three different types of retained soil (i.e. fine-grained soil, volcanic ash, and coarse-grained soil) are considered. Then, the associated environmental impacts on climate change, human health, ecosystems and resources are calculated for the two design approaches, and their comparison allows quantifying the potential reductions in environmental damages resulting from the adoption of unsaturated-soil mechanics. The presented case study shows a high potential reduction in environmental impacts for retaining walls interacting with fine-grained soils (silt), lower potential environmental benefits with volcanic ash (clayey-silty sand), but no environmental gain for interaction with a coarse-grained soil (sand) compared to a conventional design approach considering extreme soil conditions.

2.2 Introduction

About 33% of the Earth's surface is considered arid or semi-arid (Dregne, 1976). Geotechnical works (i.e., foundations, retaining structures, railway and road embankments) built in these areas thus usually interact with unsaturated soils (Siemens, 2017). Civil engineering infrastructure must be designed to be safe throughout its whole lifetime, complying with ultimate limit state (ULS) and serviceability limit state (SLS) criteria. Current design approaches only consider fully saturated or totally dry soil conditions. Nevertheless, it could easily be argued that, on average, geotechnical practitioners deal more with unsaturated soils than with saturated soils (Houston, 2019).

Research efforts have aimed to analyze the mechanical and hydraulic behavior of unsaturated soils. It is well known that the presence of matric suction may increase the stiffness and shear strength of the involved geomaterials (e.g., Ho and Fredlund, 1982; Escario and Saez, 1986; Gan et al., 1988; Han and Vanapalli, 2016; Rosone et al., 2016). This phenomenon holds until the negative pore pressure in the soil ceases (for example due to rainfall infiltration).

A quantitative assessment of matric suction's impact on the design of geotechnical works is challenging, mainly due to the complex interactions between civil engineering infrastructure and soils which are not fully saturated. Siemens (2017) showed some application-driven examples by illustrating unsaturated soils' principles in order to bridge the gap between research and practice. Within this framework, we refer to *unsaturated design approach* (UDA) when unsaturated soils' principles are considered in the design procedure, and to *conventional design approach* (CDA) if soil is considered dry or totally saturated.

The aim of this research is to investigate how the UDA, by taking into account the potential benefits of matric suction, can influence the environmental performance of earth retaining walls. Basu *et al.* (2014) provided a framework for the sustainability of geotechnical engineering, highlighting that studies about geotechnology sustainability should follow a holistic approach. Life Cycle Assessment (LCA) is an internationally standardized and globally applied product-oriented tool used to assess the potential environmental impacts of a product/service through its life cycle, i.e. from raw material extraction to its end of life. LCA is a multicriteria approach covering a broad range of environmental issues (e.g. climate change,

resource depletion, or toxicity), and the impacts are calculated for a functional unit which reflects the function(s) provided by the system. The combination of life cycle thinking and multicriteria analysis allows to have a complete picture of the potential impacts of the system and prevents burden shifting from a product life-cycle stage to another, or from one impact category to another, and allows proposing appropriate solutions to these issues (i.e. eco-design). In the light of these considerations, LCA seems a promising tool to comprehensively assess the environmental performance of earth retaining walls. Nevertheless, correctly implementing an LCA model for geostructures remains a challenge still under investigation by the research community (Kendall, Raymond, Tipton, & DeJong, 2017).

The present work begins by recalling some of the fundamentals about the interactions between retaining structures and unsaturated soils, including theoretical, numerical, and experimental aspects. Next, it introduces the LCA methodology, and then critically reviews its application with regards to retaining structures. Afterwards, in order to quantify the effects of the UDA on the environmental impacts of constructing a retaining wall, we present the theoretical framework for estimating lateral earth pressure in unsaturated soils and, consequently, we propose an LCA model for retaining structures. Next, an illustrative case study is presented to illustrate the feasibility of the proposed approach. The environmental performances of the retaining wall designed according to both CDA and UDA are compared by considering fine-grained soils, volcanic ash, and coarse-grained material as retained soils. Moreover, an uncertainty analysis for the environmental aspects of the analyzed case study is also carried out.

2.3 Background

2.3.1 Retaining structures in unsaturated soils

Unsaturated soils are composed by a solid phase (solid skeleton) and two immiscible fluid phases (water and air). Figure 2.1 shows the typically conceptualized distribution of pore water-pressure above the groundwater table (GWT); its distribution is mainly linked to the continuity of both the water and air phases (Wroth and Houlsby, 1985), and possible fluctuations in suction profiles are the consequences of environmental actions like infiltration or evaporation/evapotranspiration.

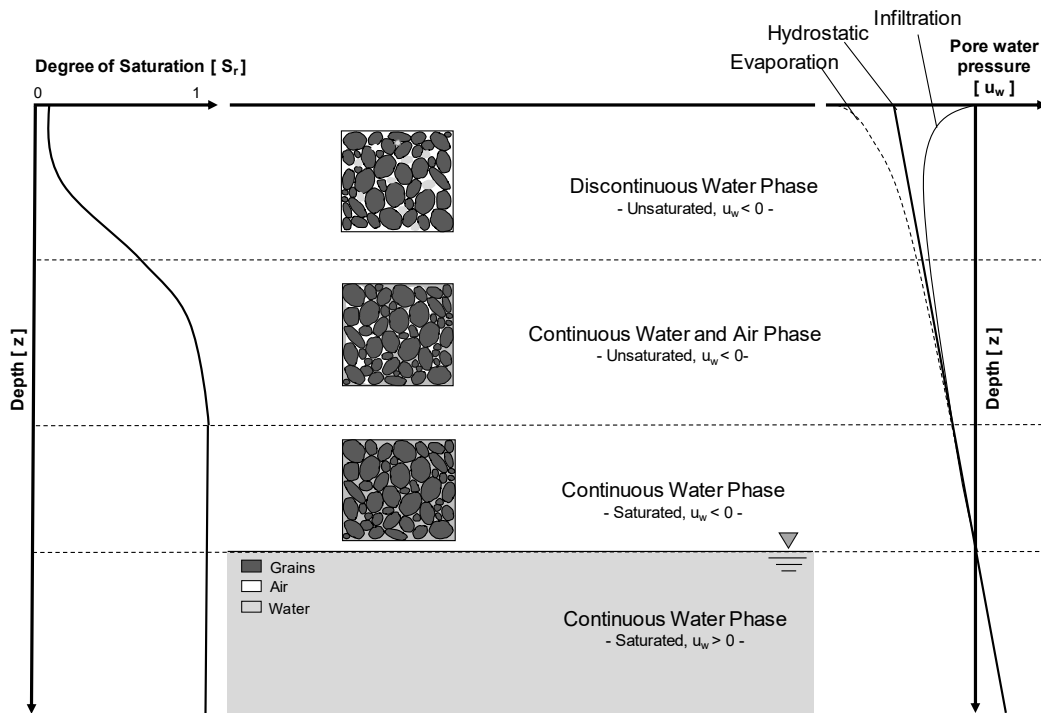


Figure 2.1. Evolution of pore water-pressure (u_w), degree of saturation (S_r), and continuity of water/air phase versus depth above the groundwater table.

Although retaining structures often interact with unsaturated geomaterials, they are designed using approaches that consider the soil to be either totally dry or totally saturated. This is despite the fact that the impact of environmental fluctuations on retaining structures was first documented nearly 100 years ago. Following a year of in situ measurements on a retaining wall, McNary (1925) concluded that lateral earth pressure could vary from the average value by $\pm 30\%$. Terzaghi et al. (1996) highlighted how backfill's properties could be affected and changed from season to season, causing an increase or decrease in the lateral earth pressure associated with states of partial saturation or partial desiccation. Pufahl et al. (1983) and Fredlund and Rahardjo (1993) extended Rankine's lateral earth pressure theory for both active and passive cases. Moreover, they considered the possible formation of cracks due to high suction values induced by long periods of drying.

Zhang et al. (2010) presented a unified solution for unsaturated-soil shear strength and active earth pressure. They consequently proposed an application on the evaluation of the critical embedment depth of a rigid retaining wall against overturning in unsaturated soils. Their results were compared with a lower bound solution provided by Amabile et al. (2012). Tavakkoli and Vanapalli (2011) provided some background on how the lateral

earth pressure could be estimated using the mechanics of unsaturated soils via both the effective and total stress approaches. Liang et al. (2012) proposed the unified solution of Coulomb's active earth pressure for unsaturated soils. Vanapalli and Oh (2012) investigated the stability of unsupported vertical trenches in unsaturated soils by analyzing a fully-instrumented vertical trench in the field. Stanier and Tarantino (2013) proposed an approach to predict the stability of vertical cuts in cohesionless soils above the water table. Most studies adopted a linear relationship between matric suction and depth. However, Fredlund and Rahardjo (1993) introduced a scale factor in an attempt to simulate the fluctuation of matric suction profiles. With regard to the theoretical approach proposed by Lu and Likos (2004), on the evolution of the matric suction profile due to infiltration and evaporation, Vahedifard et al. (2015) proposed a parametrical analysis of active earth pressure for unsaturated retaining structures, varying such parameters as shear strength angle, interface friction angle, soil type, and air entry pressure. Vahedifard et al. (2016) investigated the behavior of geosynthetic, reinforced soil structures in unsaturated soils with different infiltration rates. Using numerical modelling, Vahedifard et al. (2017) later presented the behavior of a mechanically stabilized earth wall after extreme precipitation events. Scotto di Santolo et al. (2017) presented a case study on a gravity retaining-wall, by performing a coupled hydro-mechanical analysis that took into account seepage and in situ measurements of matric suction.

Only a small number of experiments strictly related to the interactions between unsaturated soils and earth retaining structures are to be found in the literature. Gu et al. (2010) set up a centrifugal model to study the at-rest earth-pressure of expansive soil against a retaining wall. The authors assumed the soil to be elastic and proposed two at-rest earth-pressure coefficients, one related to the net overburden pressure and the other related to matric suction. Vo and Russel (2016) modelled the interaction between unsaturated soils and retaining structures by focusing on the passive case of lateral earth pressure, using a 1g small-scale model. They interpreted their results by assuming the soil to be a rigid, perfectly plastic continuum through the extension of slip line theory and by considering the mechanics of unsaturated soils. Accordingly, the comparison of their experimental results and the theoretical framework was unsatisfactory to them due to the framework's assumptions.

Analyzing the research reported above shows that different approaches can be used to investigate the interactions between unsaturated soils and retaining structures. With the aim of including the properties of unsaturated soils into design procedures, it is important to highlight the key role played by the assumption of matric-suction distribution and its variation in relation to infiltrations. Because of that variation in matric-suction distribution, seepage analyses are to be recommended, paying due attention to the chosen infiltration rates. In this regard, it is possible to identify a theoretical framework, among the approaches recalled above, to compute the lateral earth pressure of unsaturated soils during rainfall events. In section 2, we describe the procedure adopted for investigating interactions between unsaturated soils and retaining structures, and then this approach is applied to a case study.

2.3.2 Life cycle assessment of retaining structures

It is estimated that civil engineering projects account for about 40% of global energy consumption, and these also have major influence on mineral extraction for the production of construction materials (Dixit, et al., 2010). In order to assess the environmental impacts associated not only with the use stage of the geostructure but also its construction and its end of life stages, an environmental assessment based on life cycle thinking should be adopted. In this context, we chose the Life Cycle Assessment methodology to evaluate the environmental performance of geostructures. In contrast to other environmental assessment methodologies, LCA provides a more complete estimate of impacts on the environment, going further than mere gas emissions and resource depletion.

LCA is a means of systematically and quantitatively evaluating the environmental impacts of a product or service system through all the stages of its life. The method initially consisted of four distinct stages (ISO, 2006), which were soon increased to five (EC-JRC, 2010): (i) goal definition, (ii) scope definition, (iii) life cycle inventory, (iv) life cycle impact assessment, and (v) interpretation (Figure 2.2).

During goal definition, the intended applications and reasons for carrying out the study should be identified. Moreover, any assumptions, comparative studies, impact coverage, and the limitations due to the method should be presented too.

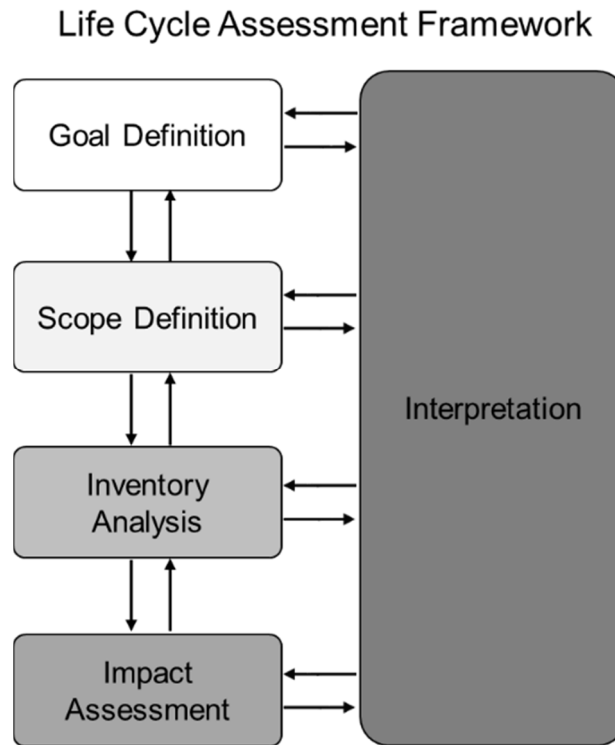


Figure 2.2. *Stages of a Life Cycle Assessment.*

Scope definition must define three relevant concepts:

- the system boundaries (a whole life cycle should embed all the flows from raw material extraction, through to materials processing, production, distribution and use stages, to waste management, e.g., disposal or recycling);
- the functional unit (representing the service offered by the system or a measure of the system's function during its lifetime);
- the reference flow (a quantitative reference unit allowing for the satisfaction of the functional unit).

The Life Cycle Inventory (LCI) identifies and quantifies all the flows between the system being studied and the environment, i.e., all resource consumption (raw materials, energy, water, and land) and all substance emissions into the environment.

The whole life cycle of each material considered in the model should be taken into account. For example, if we use the LCA model for a retaining wall, then the concrete is considered

within the model and its own life cycle from the extraction of raw materials up to the disposal is automatically included.

The Life Cycle Impact Assessment (LCIA) classifies the flows listed in the LCI according to their potential effects on the environment. The inventoried flows are multiplied by a characterization factor, which quantifies the extent to which they contribute to a given environmental impact category.

The interpretation stage occurs after each of the other LCA stages so that there is a critical analysis of each stage's results. Moreover, at the end of the overall process, the interpretation stage helps to identify conclusions and recommendations.

Even though the number of studies using LCA in other civil engineering sectors has grown significantly in recent years, there are few LCAs of geostructures to be found in the literature. With a focus on retaining structures, Chau et al. (2008) and Inui et al. (2011) estimated the embodied energy and gas emissions of two types of diaphragms, performing a parametric analysis of four wall technology types (cantilever steel tubular-pile walls, cantilever secant concrete-pile walls, steel sheet-pile walls with tension piles, mini-pile walls with tension piles). Rafalko et al. (2010) implemented an LCA model for a mechanically stabilized earth wall and a gravity wall. Soga et al. (2011) presented a literature review about the embodied energy of soil-retaining geosystems. Lee and Basu (2015) and Giri and Reddy (2015) implemented an LCA model for a mechanically stabilized earth wall (geo-grid and steel) and proposed a multi-criteria analysis for the complete assessment of its sustainability. Damians et al. (2016) presented an LCA model for retaining structures and performed a sensitivity analysis on three types of retaining wall (a mechanically stabilized earth wall, a gravity wall, and a cantilevered wall), providing detailed information about the environmental indicators and impact categories chosen. Regrettably, they did not perform uncertainty analyses and their systems did not consider the wall's end of life (EOL). Nevertheless, most published studies assessed only a limited set of environmental indicators, providing a partial picture of all the potential environmental damages of the studied systems. Moreover, most of the proposed models do not consider EOL and few studies carry out sensitivity and uncertainty analyses. It follows that different analyses of similar problems lead to non-similar results. Kendall et al. (2017) believed that the discrepancies between results were due

to a lack of standard methodologies for conducting LCAs for geostucture-type systems. Given the shortcomings described, I propose an LCA model for retaining structures which (i) includes the wall's end of life (EOL) in the system boundaries, (ii) considers soil conditions for the design of the system, directly influencing the Life Cycle Inventory of the system, (iii) covers all environmental aspects (climate change, and damages to human health, ecosystems and resources) and (iv) includes an uncertainty analysis.

2.4 Selected methods

Retaining walls are designed to satisfy prescribed requirements, generally in terms of overturning, sliding, and bearing capacity, as well as their overall stability. Eurocode 7 (2004) states that when considering structures retaining earth of medium or low permeability (silts and clays), water pressures should be assumed to be acting behind the wall. The water table level should be set as the top of the retained geomaterial unless a reliable drainage system is installed, or infiltration is prevented. Bond and Harris (2008) considered this approach too conservative. This problem is a direct consequence of considering the retaining soil to be fully saturated or totally dry. The present work uses an approach based on the adoption of unsaturated soil mechanics via the estimation of lateral earth pressures by way of a consideration of infiltration rates.

An illustrative case is used to show the quantitative differences between the CDA and the UDA. A reduction in lateral earth pressure allows for a reduction in the geometrical dimensions of the wall, with a related decrease in the amount of material employed. Environmental performance is quantified by using an LCA for both design approaches (CDA, UDA).

Figure 2.3 shows the methods adopted in the present work for the joint environmental-geotechnical analysis.

Geotechnical and structural designs are prepared following the requirements of Eurocodes 7 and 2, and environmental performance is quantified using the international standards recalled above. Uncertainty analysis of the environmental results has been performed in order to achieve the range of variation of the estimated results. A Monte Carlo technique was chosen as the statistical method. Sensitivity analyses were carried out on three soil

types to highlight how their different physical and mechanical features should affect the design of geotechnical structures and can have an impact on their environmental performance.

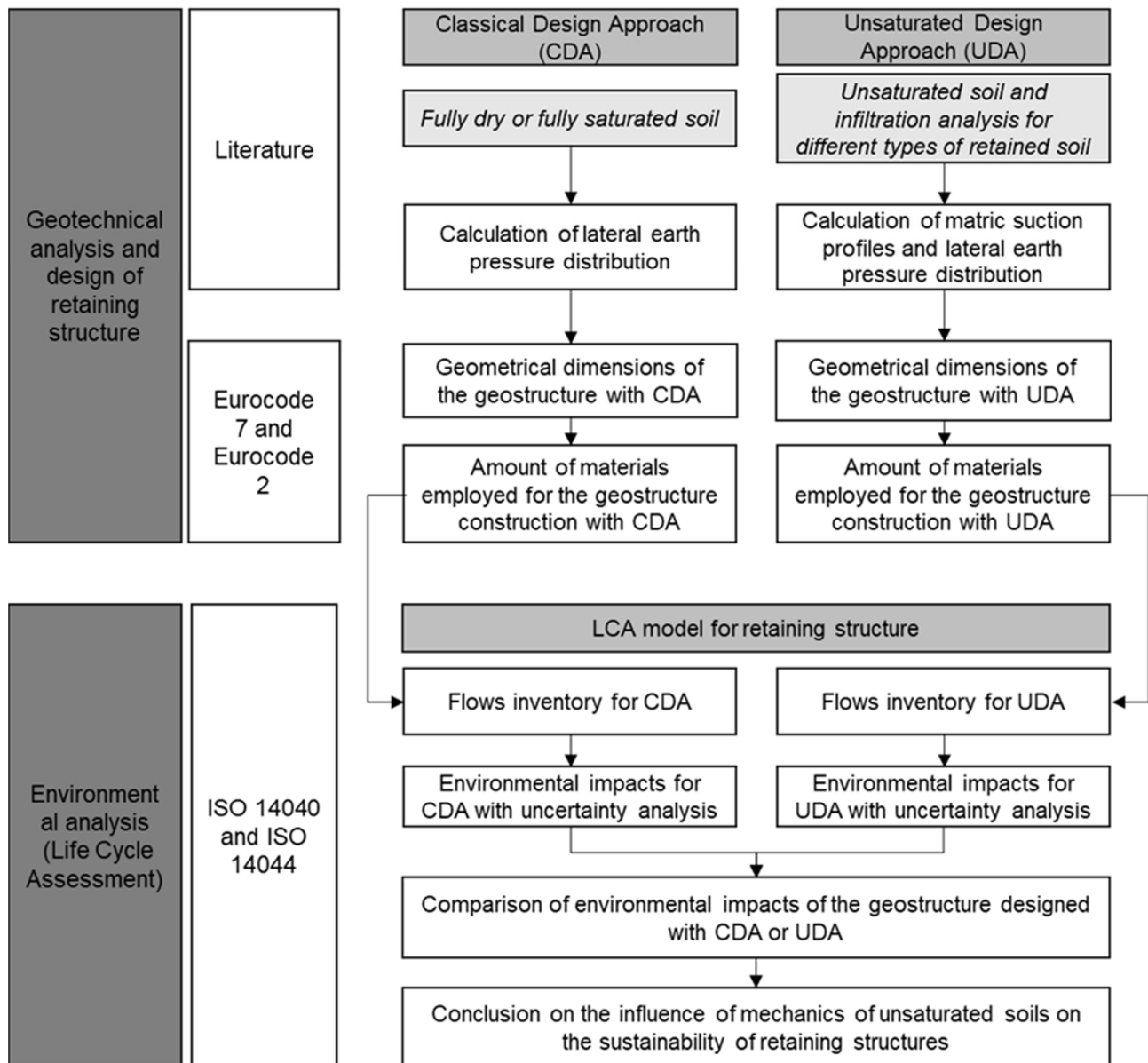


Figure 2.3. Methodology adopted for the coupled environmental–geotechnical analysis.

2.4.1 Theoretical framework adopted for estimating lateral earth pressure in unsaturated soils

As introduced, several formulations exist for the computation of the lateral pressure of unsaturated soils. In this section, the adopted theoretical framework is reported according to the available best practice for the computation of the lateral thrust during rainfall events. Granular soils are considered in the present formulation. The mechanical behavior of these soils can be modelled using Bishop's (1959) definition of effective stress (e.g. Tarantino and

El Mountassir, 2013). Water retention behavior is coupled with mechanical behavior through the following equations:

$$\sigma'_{ij} = \sigma_{net,ij} + \chi s \delta_{ij} \quad (2.1)$$

$$s = u_a - u_w \quad (2.2)$$

where σ'_{ij} is the effective stress tensor, $\sigma_{net,ij}$ is the net stress tensor, χ is the effective stress parameter, u_a the air pressure, u_w the water pressure, $u_a - u_w$ the matric suction and δ_{ij} is Kronecker's delta.

Matric suction's influence on lateral earth pressures can be better investigated by its effect on shear strength. Substituting Bishop's (1959) definition of effective stress into the Mohr-Coulomb failure criteria, it is possible to achieve:

$$\tau_f = c' + [(\sigma_n - u_a) + \chi(u_a - u_w)] \tan \varphi' \quad (2.3)$$

Where τ_f is the available shear strength, c' and φ' are the intercept cohesion and the shear strength angle, respectively, σ_n is the total normal stress. According to Vanapalli et al., 1996, the effective stress parameter can be imposed equal to the effective degree of saturation (S).

$$\chi = S = \frac{S_r - S_{r,res}}{1 - S_{r,res}} \quad (2.4)$$

Authors such as Brooks and Corey (1964) and van Genuchten (1980) have proposed analytical expressions to model the water retention behavior in order to fit experimental results. Among other authors, Airò *et al.* (2010) and Salager *et al.* (2013) remarked that modelling water-retention phenomena is affected by the ongoing deformations of soil. Due to the nature of the considered soils, we decided to adopt a van Genuchten model, without taking into account the possible influences of deformation:

$$S = \chi = \left(\frac{1}{1 + [\alpha(u_a - u_w)]^n} \right)^m \quad (2.5)$$

α , n , and m are calibration parameters of the model that describes the water retention behavior of the retained soil.

Substituting equation (5) in equation (3) gives:

$$\tau_f = c' + \left[(\sigma_n - u_a) + \left(\frac{1}{1 + [\alpha(u_a - u_w)]^n} \right)^m (u_a - u_w) \right] \tan \phi' \quad (2.6)$$

Starting from equation (6) it is possible to compute the net horizontal stress ($\sigma_h - u_a$) according to the extended Rankine's theory which considers the mechanics of unsaturated soils:

$$\sigma_h - u_a = (\sigma_v - u_a)K_A - 2\sqrt{K_A}c' - \left(\frac{1}{1 + [\alpha(u_a - u_w)]^n} \right)^m (u_a - u_w)(1 - K_A) \quad (2.7)$$

where, σ_v is the total vertical stress, and K_A is Rankine's conventional active earth pressure coefficient:

$$K_A = \tan^2 \left(\frac{\pi}{4} - \frac{\phi'}{2} \right), \quad (2.8)$$

A similar derivation can be used for the passive state. Equation (2.7) highlights the dependency of the lateral earth pressure on suction. The computation of the lateral thrust will be then related to the suction distribution with depth resulting from the different settings (e.g. infiltration, hydrostatic condition, ...).

Lu and Likos (2004) presented an analytical expression for the 1D distribution of matric suction associated with a steady-state infiltration. The solution assumes the continuity of the water phase in the media and is based on the coupling of the Darcy's law for unidimensional unsaturated flow with the Gardner's model (1958) describing the evolution of hydraulic conductivity with matric suction:

$$i = -k \left[\frac{d \left(z + \frac{u_a - u_w}{\rho_w g} \right)}{dz} \right] = -k \left[\frac{1}{\gamma_w} \frac{d(u_a - u_w)}{dz} + 1 \right] \quad (2.9)$$

$$k = k_s e^{[-\alpha(u_a - u_w)]}$$

where γ_w is the unit weight of water, z is the depth, g is the gravitational acceleration, k is the hydraulic conductivity, k_s is the saturated hydraulic conductivity, and i is the infiltration flux, assumed as negative for a water inlet in the retained soil. Positive values of i are associated with exfiltration rates.

By integrating equation (2.9), and imposing that suction is zero at the groundwater table depth (Y), it is possible to get:

$$(u_a - u_w) = -\frac{1}{\alpha} \ln \left[\left(1 + \frac{i}{k_s} \right) e^{-\gamma_w \alpha (Y-z)} - \frac{i}{k_s} \right], \quad (2.10)$$

Equation (2.10) allows to compute the possible matric suction profiles depending on both the infiltration/exfiltration rate (Figure 2.4a). When i is imposed equal to zero, the hydrostatic distribution of the pore water pressure is recovered. By substituting equation (2.10) in (2.7) it is possible to obtain the lateral earth pressure distributions at given infiltration/exfiltration rates (Figure 2.4b). The conditions of steady-state infiltration during rainfall events are considered in the present work as scenario 1.

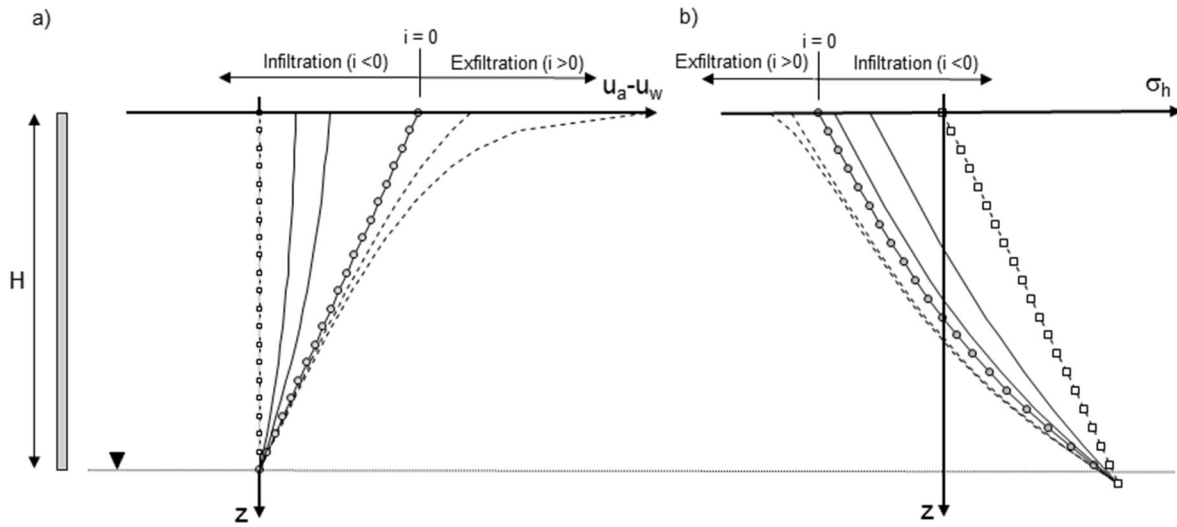


Figure 2.4. Pore water pressure and lateral earth pressure distribution at imposed infiltration/exfiltration rate. drying and wetting periods.

As seen in Figure 2.4a, during dry periods pore water pressure can reach highly negative values. Matric suction may result in tensile stress in the soil, and, on the other hand, it can increase its tensile strength. When the tensile stress reaches the tensile strength of the soil, cracks will open. When rainfall events happen in these conditions, the cracks will be quickly filled by water. The role of existing cracks of known depth (Z_c) on the computation of lateral pressure has been discussed by Pufahl et al. (1983). In this work, by taking into account that cracks may be filled with water, the mass of soil within the depth Z_c is assumed cautiously saturated with pore water pressure in a hydrostatic distribution with zero pressure at the top. Figure 2.5 sketches the distribution of the pore water pressure, the total vertical stress, the effective vertical stress, the effective horizontal stress and the total horizontal stress. In particular, the latter can be computed as follows:

For $z < Z_c$

$$\sigma_h = \gamma' z K_A - 2\sqrt{K_A} c' + \gamma_w z \quad (2.11)$$

For $z > Z_c$

$$\sigma_h = u_a + (\sigma_v - u_a) K_A - 2\sqrt{K_A} c' - \left(\frac{1}{1 + [\alpha(u_a - u_w)_d]^n} \right)^m (u_a - u_w)_d (1 - K_A) + \gamma_{sat} Z_c K_A \quad (2.12)$$

where, γ' is the buoyant saturated unit weight, γ_{sat} the saturated unit weight, and $(u_a - u_w)_d$ is the matric suction profile below the depth of the crack (Figure 2.4). The latter can be calculated by imposing the exfiltration rate which simulates the dry period. Conservatively, a linear distribution of the matric suction in equilibrium with the water table will be assumed ($i = 0$), as shown in Figure 2.5. Indeed, the higher the matric suction values in the retained soil, the deeper the tension zone will be, with a consequent reduction of the active pressure. This is the assumed pore water pressure distribution for scenario 2, which would correspond to the start of water infiltration from the filled cracks into the underneath soil.

Over time, below the cracks, seepages will reduce the matric suction and modify the lateral earth pressure progressively. By assuming that the position of the GWT is fixed (e.g. as a result of the hydraulic settings of the considered site), with the progress of the infiltration, the cracks will close, and a steady-state condition will be obtained. This condition is modelled by the analytical solution of the first scenario (equation 2.7).

The lateral thrust adopted for the UDA is the maximum between the two described scenarios. The water retention properties of the soil affect the lateral earth pressure distribution and, consequently, the choice of the most precautionary scenario.

On the other hand, for the CDA, if the GWT is imposed at the top of the retained soil, the lateral earth pressure distribution can be determined by:

$$\sigma_h = \gamma' z K_A - 2\sqrt{K_A} c' + \gamma_w z \quad (2.13)$$

If the GWT is located at the base of the foundation and the soil is considered totally dry, the lateral earth pressure distribution can be computed as:

$$\sigma_h = \gamma_d z K_A - 2\sqrt{K_A} c' \quad (2.14)$$

Where γ_d is the dry unit weight.

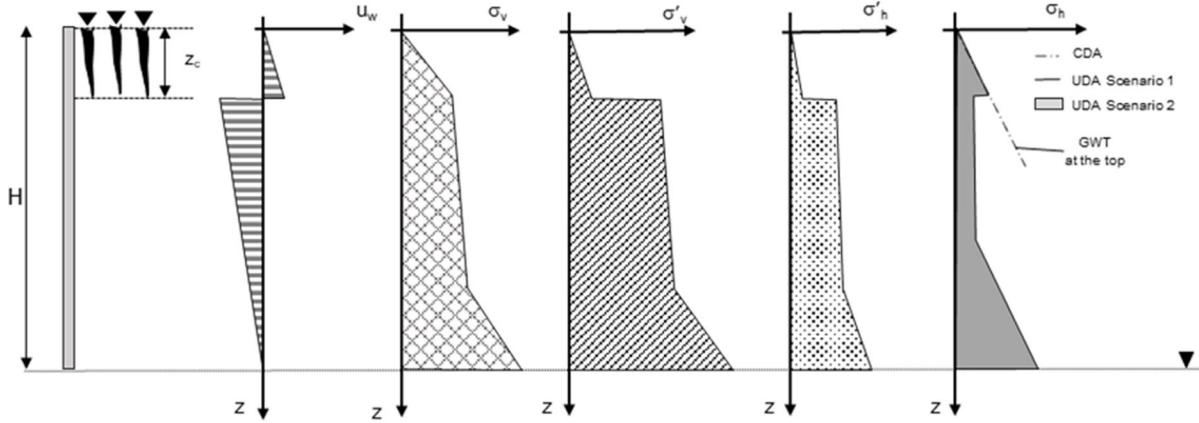


Figure 2.5. Pore water pressure, total vertical stress, effective vertical stress, effective horizontal stress and total horizontal stress profiles at the very early stages of the rainfall event.

2.4.2 An LCA model for a retaining structure

Generally, different goals and scopes can be identified when an LCA model is implemented for retaining structures. This work aims to quantify the overall environmental impact of all the life cycle stages of a cantilever retaining wall and to investigate how the UDA can influence the geostructure's environmental performance, taking into account the potential benefits of matric suction.

The geostructure's primary function is to retain soils and the functional unit adopted is to retain soil per 1 meter of the geostructure's width during its lifetime. Plane strain conditions are usually considered in the design of retaining walls. As a consequence, the selected reference flow (the flow allowing for the satisfaction of the functional unit) is 1-meter width of the designed cantilever wall.

Figure 2.6 shows the life cycle system chosen for the retaining wall. It includes raw material extraction for producing construction materials, transportation from the production site to the field, the construction phase itself, and EOL (the disposal scenario). The use phase is not considered in the system because it is assumed that there are no related impacts.

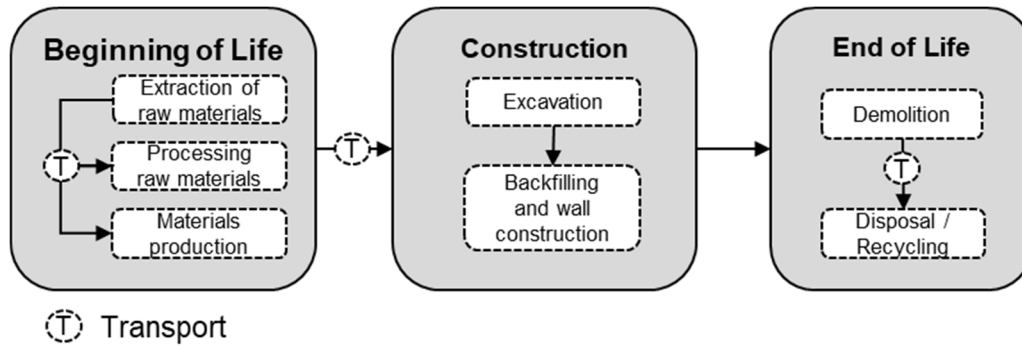


Figure 2.6. Description of the life cycle system proposed for a retaining wall.

For all these life cycle stages, the flows between the system and the environment had to be identified and quantified. To achieve this, we inventoried all the geostructure construction materials employed based on both CDA and UDA, as well as transport, construction and end-of-life hypotheses. The transportation distances to the construction site and to the waste treatment site were assumed to be 50 km for each material as well as for the construction engines. The disposal scenario was modelled as either landfill and/or incineration and/or recycling for each material, based on available statistical data. The recycling (RR), incineration (IR) and landfilling (LR) rates for the different materials were fixed as follows: for concrete IR=0%, LR=80% RR=20% (DSE, 2007), for reinforcing steel IR=0%, LR=2% RR=98% (Eurofer, 2012), for wood IR=100%, LR=0% RR=0%.

Given that the complete life cycle of each material (e.g. concrete) and each process (e.g. transport, or waste treatment) considered in the model should be taken into account, and due to the amount of data needed in order to be able to perform an LCA study of a full supply chain, LCA practitioners generally rely on existing LCI databases to have inventory data for the complete supply chains. For our case study, we used the ecoinvent v3.1 database (Wernet, G. et al., 2016), which is currently the most widely used LCI database, to obtain datasets covering all relevant environmental flows, such as resource extractions, land use and emissions, as well as all material and energy inputs and products for our system background.

Then, the flows listed in the LCI had to be classified according to their potential effect(s) on the environment. Various impact assessment models exist to characterize the inventory flows and assess their potential environmental impacts for more than a dozen impact categories and are generally grouped into LCIA methods. EC-JRC, (2010) analyzed its existing environmental impact assessment methodologies for use in LCA. We selected the Impact

2002+ (Jolliet, et al., 2003) LCIA method for the present study. This method characterizes inventory flows and assesses their potential impacts by using 15 midpoint indicators and 4 endpoint indicators. These two types of indicators are chosen at two different levels of the environmental impact pathways: midpoint indicators (also called impact categories) reveal a change in the environment caused by a human intervention, whereas endpoint indicators (also called damages) further examine cause–effect chains and assess damage to (in most cases) three areas of protection, i.e., human health, ecosystem quality, and resources. This impact assessment methodology was chosen because it provides an intermediate solution between midpoint-oriented and damage-oriented approaches. The latter allow for an easier interpretation of the results by non-experts in LCA.

The types of damage assessed by Impact 2002+ are:

- *Climate Change*, measured in kg of CO₂ in air equivalents, derived from the single impact category of global warming;
- *Resources*, measured in MJ, derived from Non-renewable energy and Mineral extraction impact categories;
- *Ecosystem Quality*, measured in PDF per m²/y (Potentially Disappeared Fraction), derived from the impact categories of Aquatic ecotoxicity, Terrestrial ecotoxicity, Terrestrial acidification/nitrification, Aquatic acidification, Water eutrophication, and Land occupation;
- *Human Health*, measured in disability-adjusted life years (DALYs) and derived from the impact categories of Human toxicity (later subdivided into Carcinogens and Non-carcinogens), Respiratory inorganics, Ionizing radiation, Ozone layer depletion, and Respiratory organics.

In addition, LCA practitioners also generally rely on operational LCA software to manage the interface between LCI databases and LCIA methods. In our case, the system was modelled using the SimaPro 8 LCA software (PRé Consultants B.V., 2010).

A parameter uncertainty analysis of the environmental results has been performed in order to achieve the range of variation of the estimated results. A Monte Carlo technique was chosen as the statistical method. A scenario analysis was carried out on three soil types to

highlight how their different physical and hydro-mechanical features can affect the design of geostuctures and have an impact on their environmental performance.

To carry out the uncertainty analysis, normal distribution was chosen for the amount of materials coming from the geotechnical design (i.e. foreground data) whose design values were considered as average values. Regarding the background data, the LCI data (available in the LCI database), meanwhile, presents a percentage of imprecision assimilated to the 95% confidence interval for the data assuming a log-normal distribution.

2.4.3 The analyzed case

The retaining wall selected for the analyzed case is a 3 m-high, cantilever, reinforced-concrete gravity wall; its schematic representation is sketched in Figure 2.7. The depth of the crack (Z_c) is imposed equal to 0.75 m for fine soils.

The GWT is set at the foundation level, and this level is assumed to be fixed and governed by the hydraulic boundary conditions specific to the site (e.g., the aquifer is in a subsoil layer presenting greater hydraulic conductivity than the soil retained above it). Moreover, to err on the side of caution, the presence of a drainage system that could help to maintain partial saturation conditions in the retained geomaterials is not considered. These assumptions allow us to analyze the problem using a one-dimensional infiltration rates (subsection 3.1). If, on the other hand, we were to incorporate the presence of a drainage system, the soil-structure system's hydraulic behavior would change, and the problem would have to be investigated using a two-dimensional model. This would result in a loss of the closed form solution.

Three types of soil are examined: soil 1 is a silt with a grain-size distribution of 72% silt, 8% clay, and 20% sand; soil 2 is a clayey-silty sand characterized by 48% sand and a silt-size fraction of 50%; and soil 3 is a coarse-grained soil (cohesionless sand). Table 2.1 summarizes the physical hydro-mechanical parameters of the geomaterials. Regarding the silt parameters, data were collected from the experimental investigations made by Geiser (1999), Péron, (2008), Geiser *et al.* (2000), and Salager (2007); for the clayey-silty sand, data were found in Ferrari *et al.* (2013), Laloui *et al.* (2015), and Eichenberger *et al.* (2013)

while for the sand, experiments were performed in the laboratory to obtain the water retention curve and the shear strength angle by performing the hanging water column method (Haines, 1930) and conventional direct shear tests.

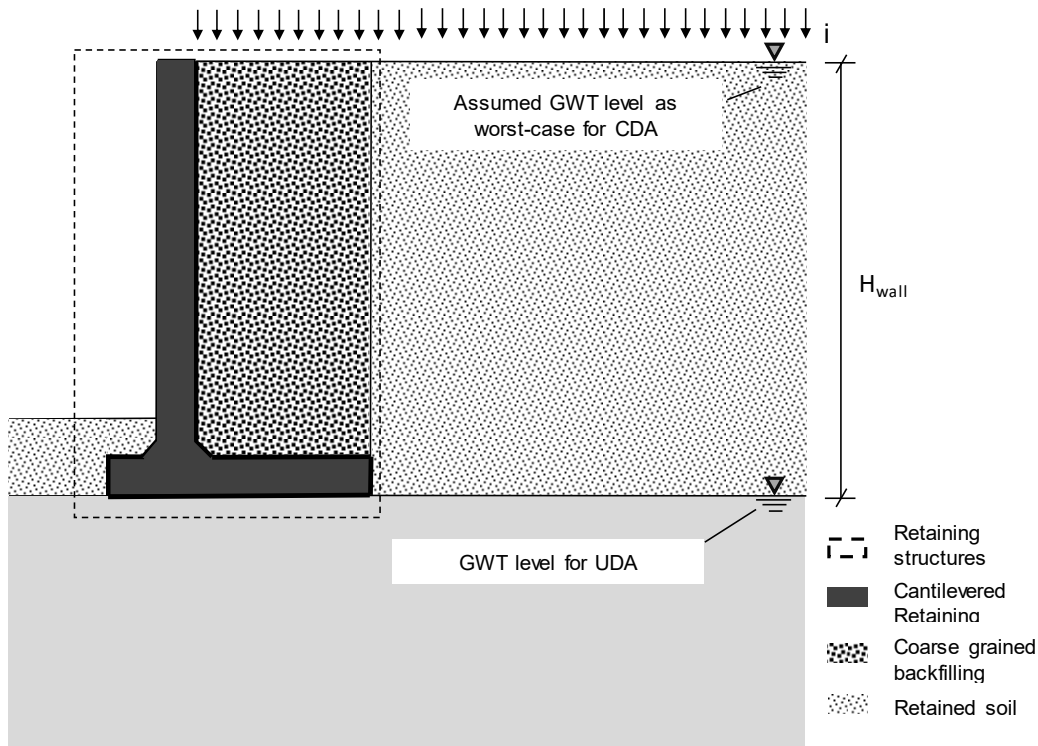


Figure 2.7. Schematic representation of the analyzed case study.

The van Genuchten soil water retention curves (SWRCs) for these three soils are depicted in Figure 2.8a, whereas Figure 2.8b, c, and d show the evolution of the hydraulic conductivity function over suction determined from these SWRCs, following Gardner's model according to equation (2.9).

For the computation of the lateral earth pressure, following the CDA, soil above the GWT can be considered either totally dry or totally saturated. To be on the safe side, Eurocode 7 suggests considering the GWT to be at the top of the retained soil for fine soils. Consequently, in the design phase, the total lateral earth pressure will also account for the hydrostatic distribution of the pore water pressure. While, regarding the UDA, in order to identify the worst condition, two scenarios are analyzed according to section 3.1: i) the evolution of the lateral earth pressure with different seepage rates (Scenario 1:); ii) the possibility of having, after long dry periods, cracks filled with water at the top of the retained soil (Scenario 2).

Table 2.1. Adopted physical-hydro-mechanical parameters of soils. γ_{dry} : dry unit weight, γ_{sat} : saturated unit weight, ϕ' : shear strength angle, c' intercept cohesion, k_s : saturated hydraulic conductivity, α , n , and m : parameters of the van Genuchten model.

Soil [-]	γ_{dry} [kN/m ³]	e_0 [-]	ϕ' [-]	c' [kPa]	k_s [m/s]	α [1/kPa]	n [-]	m [-]
Silt	16.70	0.69	32.0°	0	$1.00 \cdot 10^{-7}$	$2.26 \cdot 10^{-2}$	5.34	0.13
Clayey-silty sand	9.90	0.67	35.5°	0	$4.80 \cdot 10^{-6}$	$9.18 \cdot 10^{-2}$	2.19	0.42
Sand	16.50	0.61	35.0°	0	$1.00 \cdot 10^{-4}$	0.23	6.23	0.44

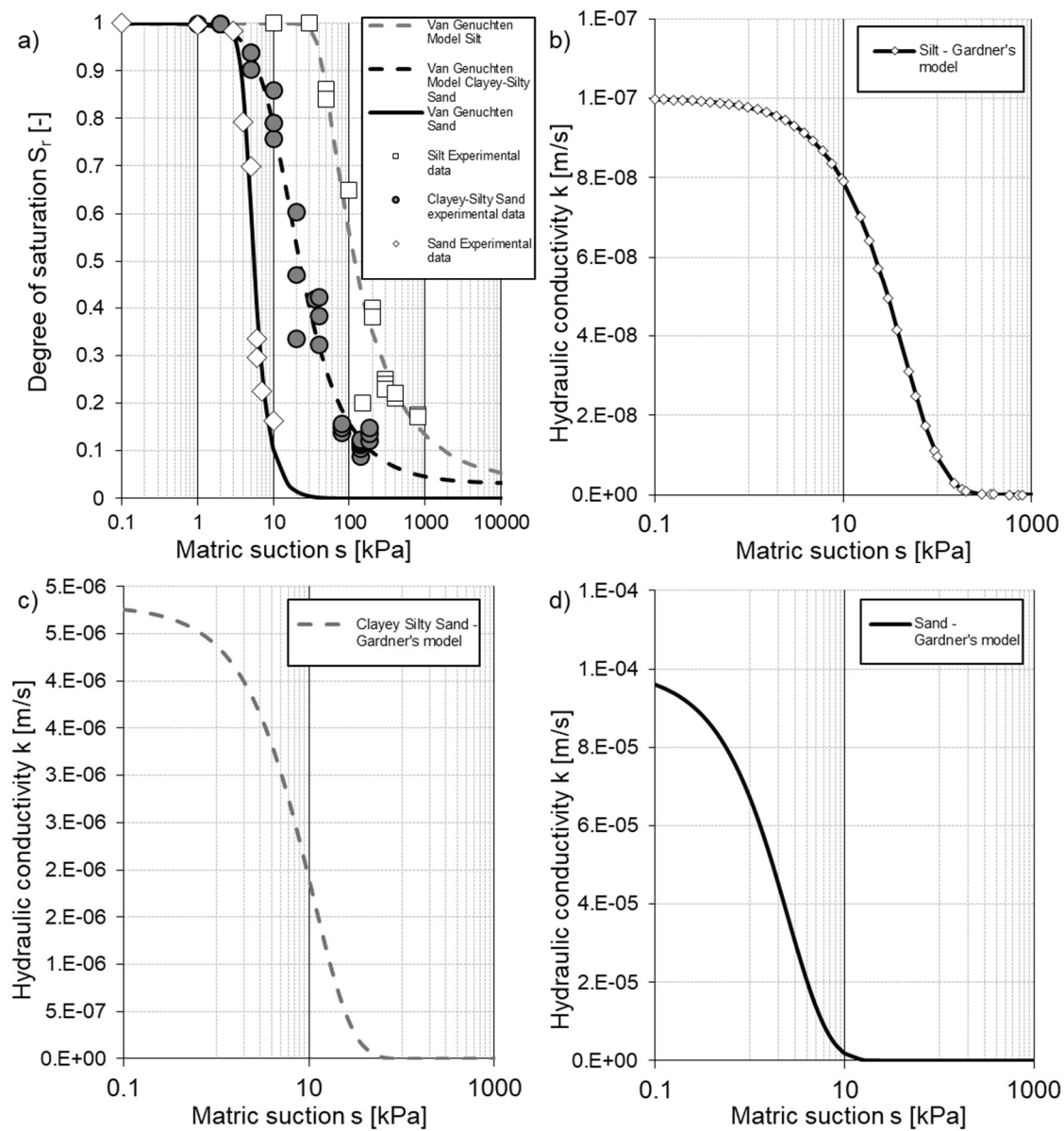


Figure 2.8. a) Experimental and adopted model of the water retention behavior of the three soils; evolution of hydraulic conductivities with matric suction for b) silt, c) clayey-silty sand, and d) sand.

Once the lateral earth pressure distribution has been achieved, the geotechnical design of the retaining wall is performed by satisfying the need for overall stability, equilibrium at translation and overturning, and bearing capacity. Moreover, structural design considers the shear strength and bending strength of all the wall's cross sections relative to the effects of computed actions. The case study's wall design followed Approach 2 of Eurocode 7 to satisfy the geotechnical requirements and Eurocode 2 for the structural elements. The amount of material needed for the stabilization of the retained soil has been chosen as the minimum amount needed for the simultaneous satisfaction of the geotechnical and structural requirements (i.e. choosing the solution corresponding to a set of minimum admissible ratios between design actions and design resistances). Then, the amount of material required for constructing the retaining wall is used as an input for the LCA model.

2.5 Results and Discussion

The theoretical framework for estimating lateral earth pressure in unsaturated soils and the proposed LCA model for retaining structures were applied to the described case study. Regarding scenario 1, Figure 2.9 (a1, a2, a3) shows varying degrees of saturation with depth, under different infiltration fluxes. The key parameter of the analysis is the air-entry values, which can be correlated to the α parameters. The degree of saturation increases with the magnitude of the infiltration flux. The latter leads to an increase of the lateral earth pressure (Figure 2.9 b1, b2, and b3). Therefore, the choice of the infiltration rate should be made according to the intensity of the rainfall events and the infiltration capacity of the retained soils. In steady-state conditions the maximum amount of water that can infiltrate into the soil is equal in magnitude to the saturated hydraulic conductivity. This condition corresponds to the highest earth thrust for this scenario. For this reason, scenario 1 is analyzed assuming $|i| = k_s$.

Moreover, Figure 2.9 b1, b2, and b3 report also the active earth pressure distributions by considering the soils above the GWT dry (equation 14); in general, this condition (indicated as "Dry" in the figures) appears as less conservative for all the considered soils with respect to the scenario 1 of the UDA ($|i| = k_s$). For the sand (Figure 2.9 b3), under different infiltration fluxes, the lateral stress distribution is similar to that expected in dry condition, as a consequence of its limited water retention properties.

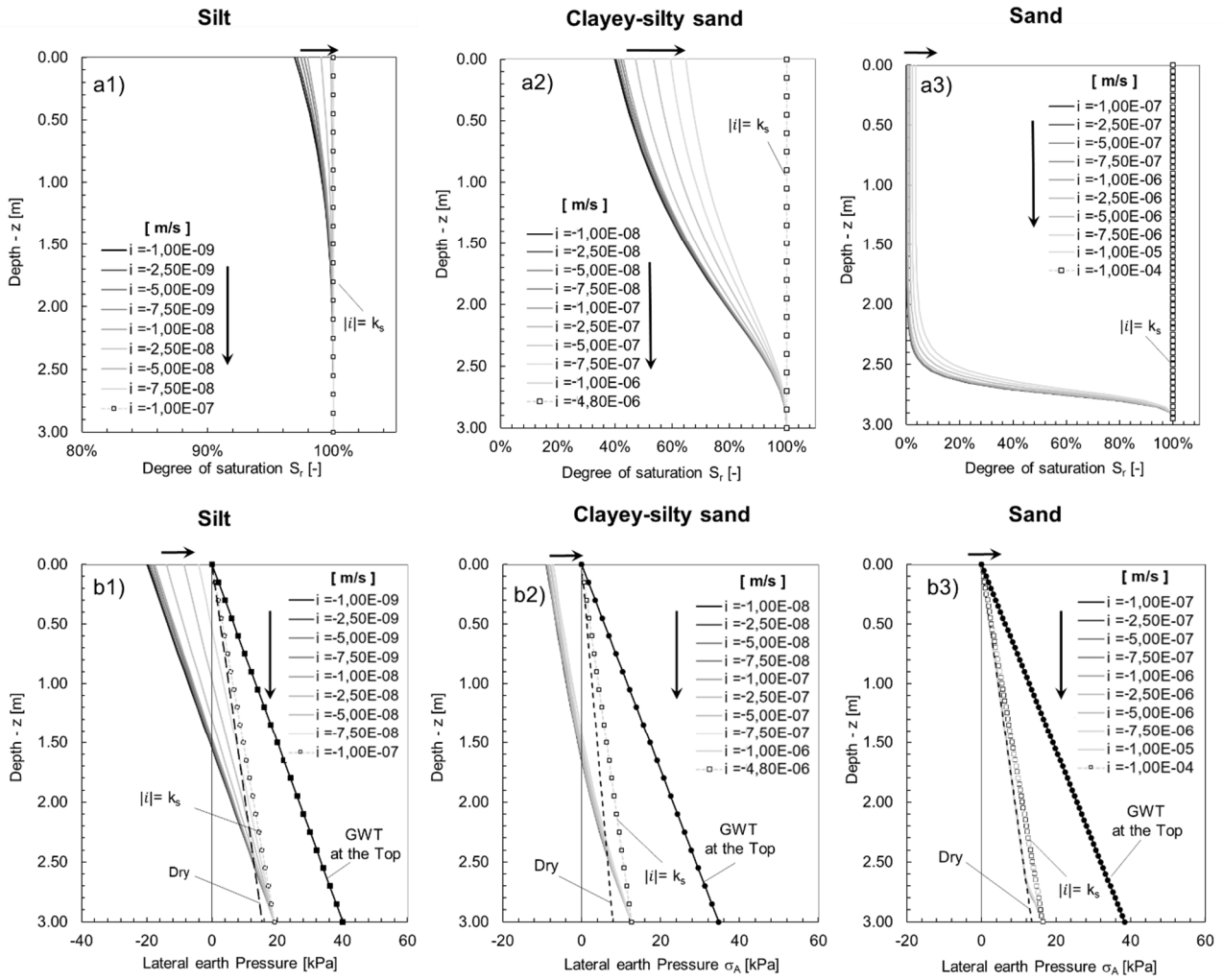


Figure 2.9. Evolution of the degree of saturation (a1, a2, a3), the lateral stress induced by matric suction (b1, b2, b3), and the lateral earth pressure with depth (c1, c2, c3) at different infiltration rates.

Figure 2.10 shows the evolution of the lateral earth pressure for scenario 2. Only the silt and the clayey-silt sand are considered. Moreover, Figure 2.10 states the differences between the CDA and UDA for the considered retained soils. When dealing with fully saturated soils (GWT at the top of the retaining wall), the lateral active earth thrust is significantly higher with respect to that obtained in the UDA, even when the infiltration flux is set equal in magnitude to the saturated hydraulic conductivity of the soil.

Once the lateral earth pressure distributions for both CDA and UDA were identified, they were employed for the design of the retaining wall for all the considered cases. For the UDA, the scenario corresponding to the highest thrust was selected. The consequential amounts of materials are used as input data for the LCA. Table 2.2 summarizes the input data employed for the environmental analyses.

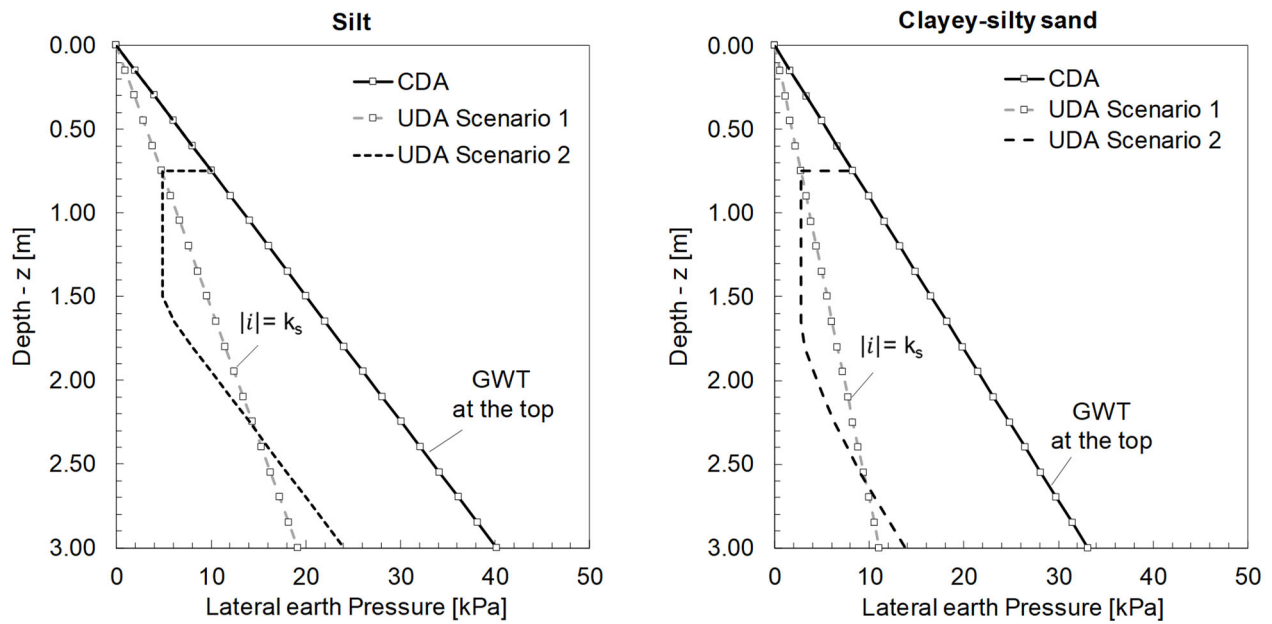


Figure 2.10. Comparison of the lateral earth pressure distributions for the UDA (scenario 1 and 2) and the CDA for the silt and the clayey-silty sand.

Designing a cantilevered wall using the two different design approaches results in different impacts on the environment. Figure 2.11, Figure 2.12 and Figure 2.13 show the midpoint results of the LCIA for both design approaches and respectively for the three retained soil types.

If we select the case of silt, we can see that all of the indicators are clearly lower for the UDA than for the CDA (Figure 2.11). The mean difference in midpoint indicators is 42.5%, with a minimum difference of 20.0% for land occupation (high uncertainty) and a maximum difference of 45.8% for mineral extraction. This is due to high differences in lateral earth pressure between conventional and unsaturated soil conditions for this type of retained soil, influencing the geostucture design, and hence the amount of materials needed for its construction.

The comparison between the CDA and the UDA leads to different results also for the clayey-silty sand (Figure 2.12). There is less difference between UDA and CDA for the clayey-silty sand than for the silt. Indeed, even if the clayey-silty sand's hydraulic conductivity is still comparable with that of the silt, the clayey-silty sand has a lower air-entry value and a very low dry unit weight (9.9 kN/m^3). The latter has also a significant effect on the sizing of the wall foundation to satisfy the related bearing capacity check.

Table 2.2. The horizontal component of the retained earth's thrust for each of the three reference soils and the consequent amount of material required depending on the retaining wall's design type.

	Silt		Clayey-silty sand		Sand	
	CDA	UDA*	CDA	UDA*	CDA	UDA
Horizontal component of the retained earth's thrust [kN]	58.80	29.00	49.00	14.90	26.80	24.80
Input for the LCA						
Concrete [m ³]	3.08	1.68	2.32	2.00	1.72	1.72
Rebars [kg]	173.52	93.15	116.83	104.99	94.63	94.63
Sawn wood [m ³]	0.66	0.62	0.62	0.62	0.62	0.62
Excavation [m ³]	8.85	5.64	9.88	8.06	5.98	5.98
Backfilling [m ³]	7.40	5.00	8.60	7.10	5.30	5.30

* Maximum value between scenario 1 and 2.

Conversely, the two different approaches for the coarse-grained soil lead to very similar environmental impacts (Figure 2.13).

In order to have an overview of the environmental damage produced by the retaining wall, the Impact 2002+ methodology allows us to report all the results in terms of endpoint parameters (Figure 2.14), thus providing a quantitative measure of damage. In this context, for the silt case, the differences between the two design approaches can be quantified as: 428.7 kg of CO_{2,eq} for Climate change, $4.3 \cdot 10^{-4}$ DALY for Human health, 123.9 PDF m²/y for Ecosystem quality, and 4325 MJ for Resources.

On the other hand, the endpoint results for the clayey-silty sand case show slightly lower environmental damages following the UDA: 85.4 kg of CO_{2,eq} for Climate change, $8.0 \cdot 10^{-5}$ DALY for Human health, 24.8 PDF m²/yr for Ecosystem quality, and 852 MJ for Resources. Moreover, the sand case shows (in agreement with the midpoint results) that there are no environmental improvements to be had by using the mechanics of unsaturated soils. That is why, as mentioned before, this comparison has been performed by assuming, as in a CDA, that the sand soil above the GWT is totally dry.

The ranges of variation of the results are reported for both midpoints and endpoints (Figures 2.12–2.14) and were obtained from our uncertainty analysis. There is high uncertainty for Aquatic eutrophication and Land occupation midpoint indicators, whereas there is low uncertainty in the Global warming midpoint indicator, resulting in high uncertainty for the damage to ecosystem quality and low uncertainty for Climate change endpoint indicator.

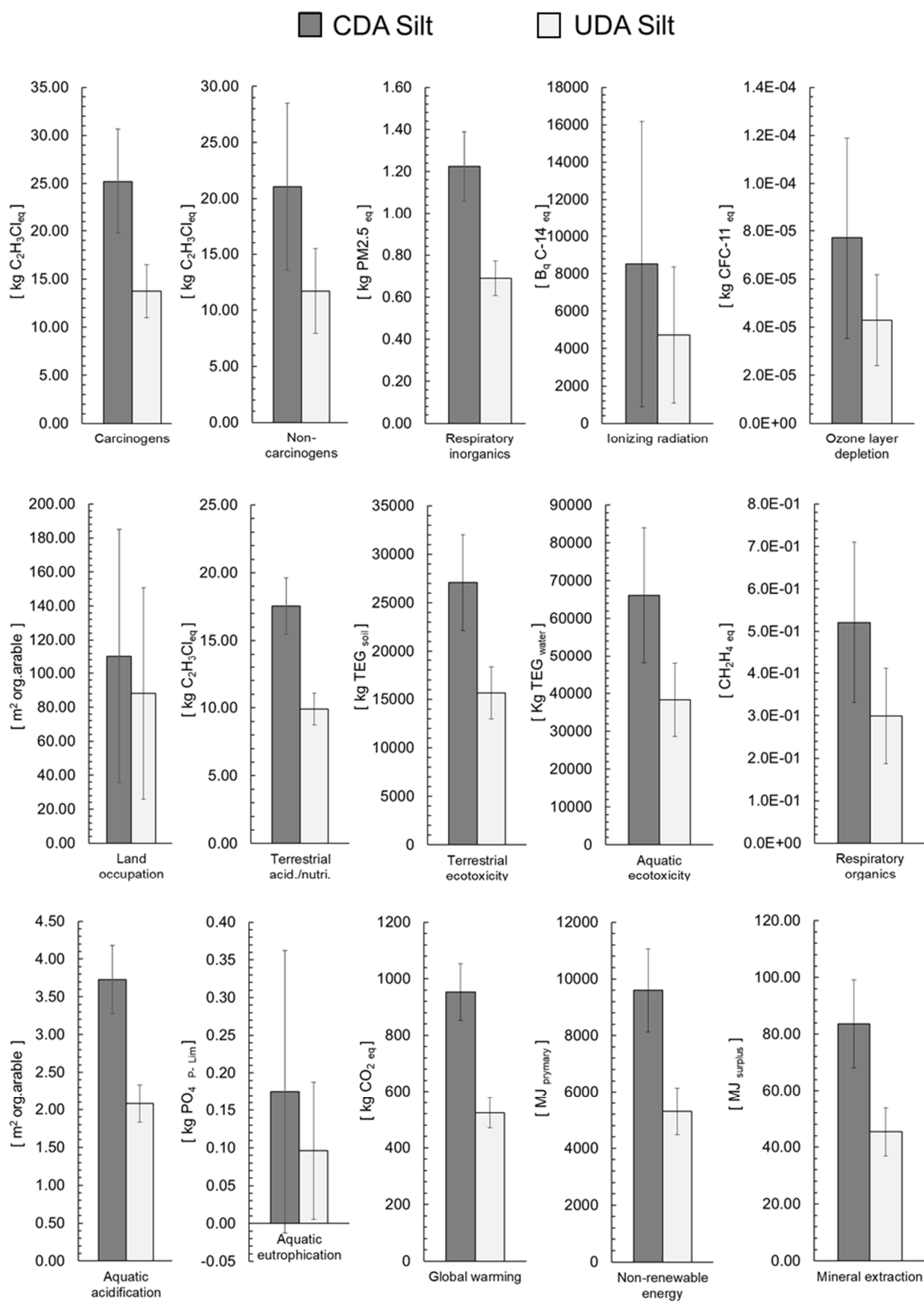


Figure 2.11. Life Cycle Impact Assessment midpoint results and related uncertainty of the CDA and UDA (silt).

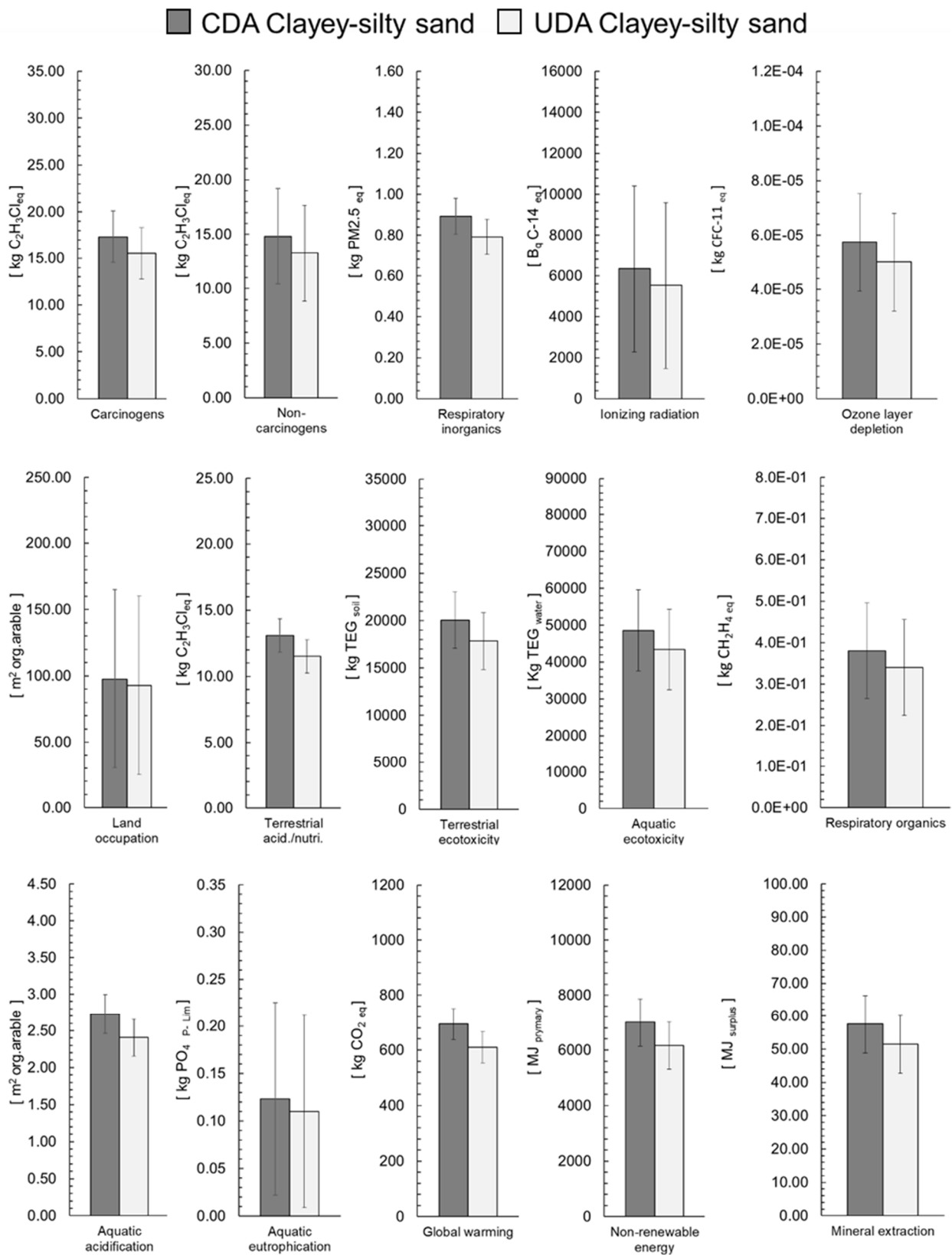


Figure 2.12. Life Cycle Impact Assessment midpoint results and related uncertainty of the CDA and UDA (clayey-silty sand).

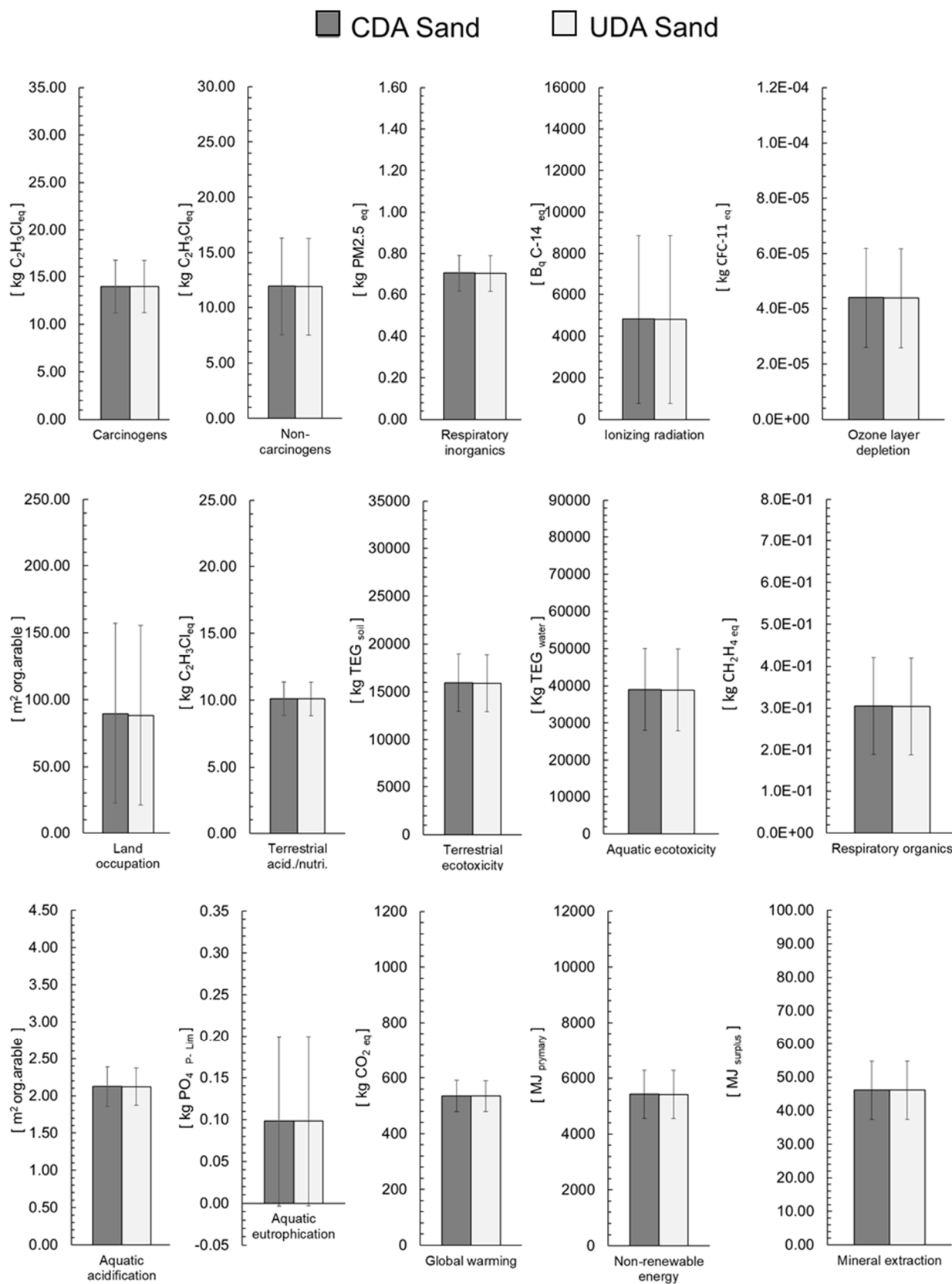


Figure 2.13. Life Cycle Impact Assessment midpoint results and related uncertainty of the CDA and UDA (sand).

Moreover, LCA allows the identification of each stage's contribution to the total environmental impact of constructing the retaining wall. To illustrate this, Figure 2.15 shows the case involving a CDA with silt as the retained soil and each stage's contribution to the end-point score. Construction material production is the main contributor to the four endpoint results, followed by EOL, transportation, and the construction phase itself.

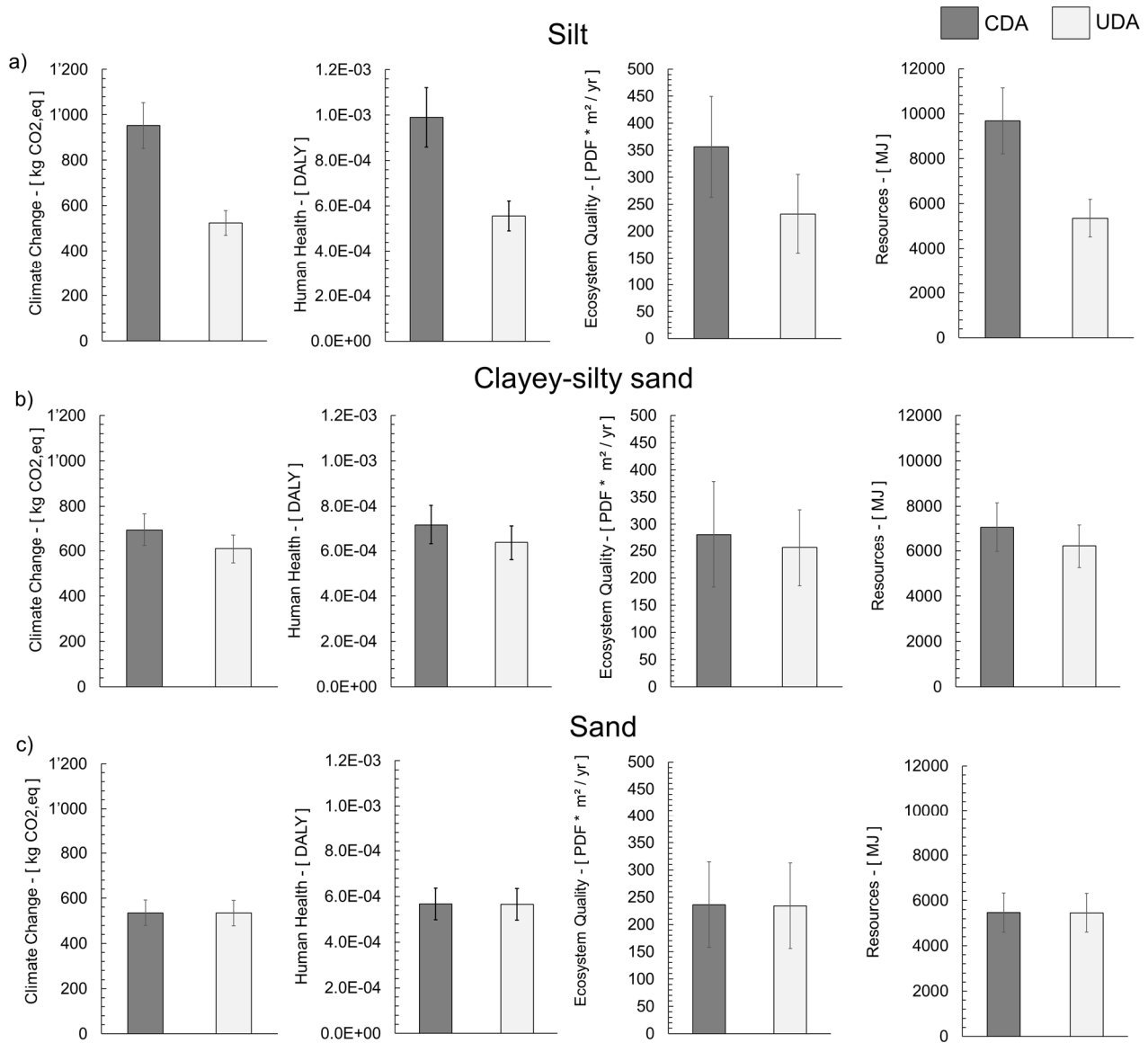


Figure 2.14. Life Cycle Impact Assessment endpoint results and related uncertainty for (a) silt, (b) clayey-silty sand, and (c) sand.

Focusing on material production, concrete production provides the greatest impact (48.39%) on the total score for damage on the Climate change indicator. For the Resources

indicator, concrete and rebars show similar impact results (31.7% and 40.2%, respectively). However, the production of reinforcing steel makes up 54.6% of the Human health indicator's final score—more than concrete (18.1%). The production of sawnwood is the main contributor to the final Ecosystem quality score (34.7%), followed by rebar (27.3%) and concrete (19.1%) production.

The strong impact of concrete and reinforcing steel production on all the environmental indicators highlights the importance of considering the mechanics of unsaturated soils in the design of the geostructure, because the amounts of concrete and reinforcing steel can significantly change depending on the design approach considered. In addition, many of the studies reported in subsection 2.2 adopted a “cradle to operation” model of the retaining wall life cycle, leaving out an EOL scenario. The present work presented a “cradle to grave” approach, considering the wall's demolition and recycling of the materials in the life cycle model, in agreement with the European standard EN 15978, (2011) relating to the sustainability of construction works. Figure 2.15 shows that the EOL has a non-negligible influence on the analysis (20% of the damages to Human Health, 17% of the damages to Resources, 7% of the damages to Ecosystem Quality and 5% of Climate Change impact) and should not be neglected in life cycle modelling.

2.6 Conclusions

Life cycle assessment is a powerful tool that allows a holistic approach to quantifying the impacts of a product, process or service on the environment. Geotechnical design influences the environmental performance of geostructures and, as a consequence, their sustainability.

The present work began by recalling some fundamentals about the interaction between retaining structures and unsaturated soils. It then critically reviewed the environmental performance of retaining structures. The design of a cantilever retaining structure interacting with unsaturated soils was described for three different types of retained soils. Next, we proposed an LCA model for the cantilever retaining wall, from the extraction of raw materials to the disposal scenario; the impacts of each of the life cycle stages were identified.

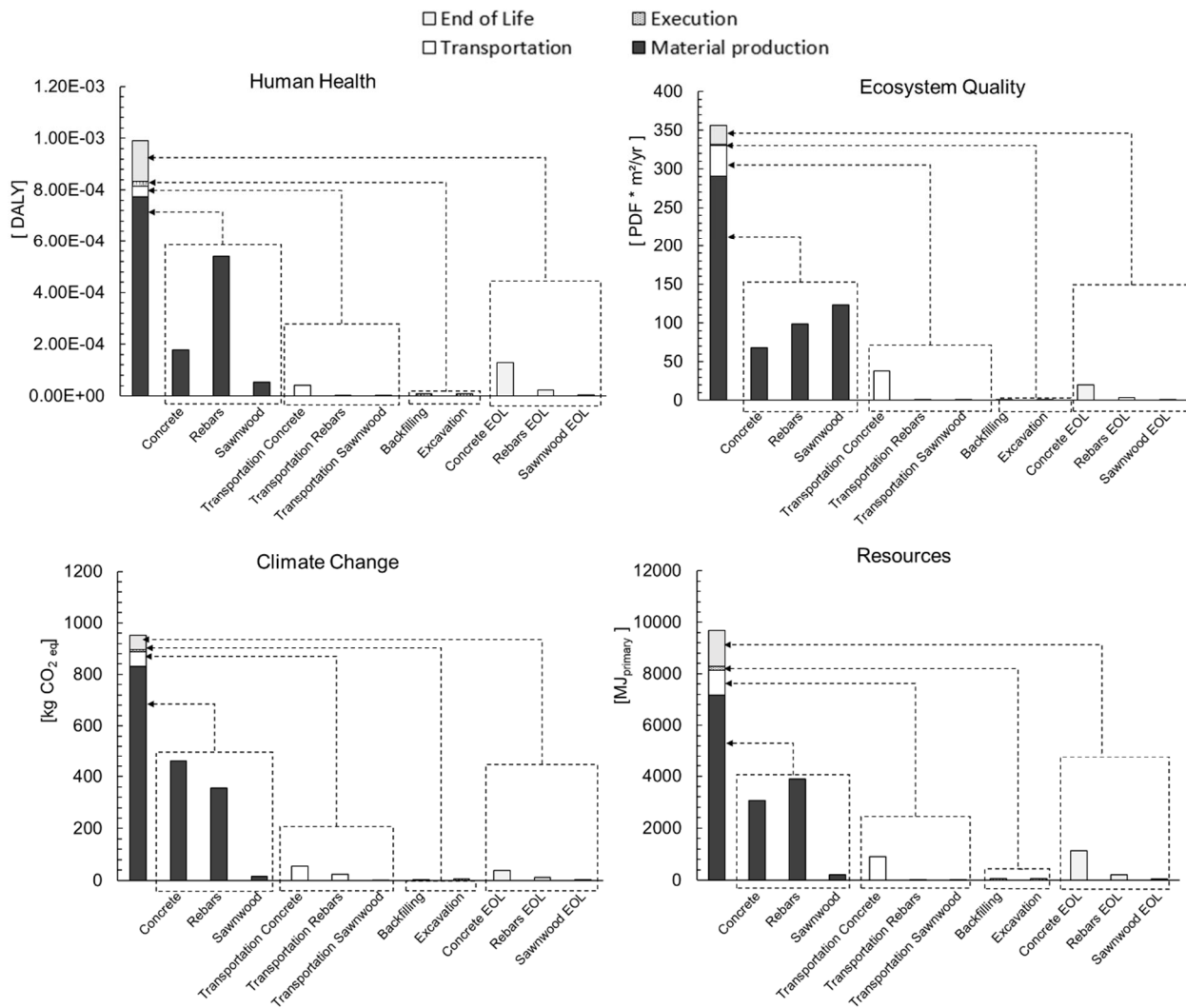


Figure 2.15. Endpoint scores of each stage in the life cycle of a retaining cantilevered wall. (classic design approach with silt).

With respect to the other models found in the literature, the end of life scenario modelled here turned out to be a non-negligible stage in the retaining wall's life cycle, leading to significant negative environmental impacts in the disposal scenario. However, it could lead to a positive impact if appropriate recycling was considered. We provided a clear track of the environmental indicators and impact categories chosen for the LCA. The combination of life cycle thinking and multicriteria analysis provides a comprehensive picture of the geo-structure's environmental impacts and allows to identify burden shifting from one product life-cycle stage to another or from one impact category to another.

Other environmental assessments disregarding the upstream and downstream activities in the supply chain or only focusing on one or two environmental indicators can lead to partial conclusions and wrong decisions regarding the design of geostructures.

Moreover, an uncertainty analysis was performed to evaluate the likelihood of the findings. This should be mandatory for any LCA, considering the significant amount of uncertainties related to the data involved.

Furthermore, in the attempt to optimize the design of geostructures, the authors encourage the use of the UDA in geotechnical practice as suggested recently by Houston (2019) recognizing that a deep knowledge of the hydro-mechanical behavior of unsaturated soils is available nowadays. If we specifically refer to the adoption of unsaturated soil mechanics for the design of retaining structures, performing seepage analyses and assessing the loss of the matric suction is considered the critical point.

However, the literature review and the presented case on interactions between unsaturated soils and the retaining structure show the need to introduce simplified hypotheses such as the continuity of the water phase in soil and estimates of the lateral earth pressure in unsaturated soils into the framework of plastic equilibrium of soils. More investigations are needed to fill the gap between the CDA and the UDA. Nonetheless, the present study's main conclusion is that the environmental performance of retaining structures is affected by the physical-mechanical-hydraulic parameters of soils, and the mechanics of unsaturated soils play an important role in meeting the challenge of constructing sustainable geostructures.

Chapter 3

Active earth pressure of unsaturated soils under transient flow

3. Active earth pressure of unsaturated soils under transient flow

3.1 Foreword

The performance of geostuctures, and specifically of retaining structures, depends on environmental actions. Heavy rainfall events or long wet periods can cause failures due to the progressive increase of the degree of saturation and, hence, to the reduction of the positive contribution provided by the matric suction to the shear strength of the soil. Moreover, the increase in weight of the retained soil affects also the lateral earth pressure distribution. Numerous contributions can be found in the literature regarding the performance of natural slopes and geostuctures due to changes in the water content during rainfall events (Terzaghi et al., 1996, Ng et al., 2003, Collin, 2001, Xu and Zhang, 2010, Yoo, 2013, Camera et al., 2012, Chandrasekaran et al., 2013, Laloui et al., 2016, Rosone et al., 2018). The previous studies have highlighted the importance of evaluating the response of the investigated system to infiltration during adverse meteorological events. Therefore, it is particularly important to investigate the time-dependent response of the considered geostucture during rainwater infiltration. Among the other geotechnical works, the retaining structures are strongly influenced by the time-dependent evolution of the degree of saturation. In this regard, some recent numerical analyses have been performed to study the evolution with time of retaining structure's performance (e.g., Camera et al., 2012, Vahedifard et al., 2017, and Scotto di Santolo et al. 2017). Anyway, the adoption of numerical approaches requires not only an advanced knowledge of soil's hydro-mechanical properties but also advanced tools capable of reproducing numerically their hydro-mechanical transient behaviour during the rainfall events.

In this chapter, the unsaturated soil-retaining structure problem is still investigated analytically in the attempt to provide a less complicated tool capable of catching the progressive evolution of the lateral earth pressure with time. Chapter 2 has shown how the mechanics of the unsaturated soils can be employed in the estimation of the lateral earth pressure and the design of the retaining structures. Among the limitations of the analytical approach described in the previous chapter, the computation of the matric suction and the degree of

saturation only at the steady-state condition stood out. In this chapter, the attention is focused on the computation of the lateral earth pressure under transient flow. This is why there is the need to provide a quantitative assessment of the lateral earth actions during precipitations and, as a consequence, the evolution of the factor of safety with the time.

In the following sections, an uncoupled hydro-mechanical approach is presented where the solution to the one-dimensional Richard's equation (Richards, 1931) is employed for the computation of lateral earth actions. Rankine's theory has been adopted to estimate the time-dependent action of unsaturated soils on the retaining structure at the active state. This theory is associated with the lower bound theorem of limit analysis and therefore provides a conservative solution for the active thrust (within the assumptions of limit analysis, i.e. rigid-perfectly plastic behaviour and associated flow rule). In the spirit of the uncoupled hydro-mechanical approach, first, the hydraulic part of the problem is presented by solving the partial differential equation describing the transient flow in unsaturated soil, then the suction and volumetric water content profiles are employed for the computation of the mechanics through a convenient definition of the effective stress.

A parametric study is presented on three types of retained soils: a silt, a clayey silty sand and a sand. The infiltration time needed to achieve the new steady-state condition has been evaluated for the three investigated soils.

3.2 Analytical solution of transient seepage in unsaturated soils

The downward water flux in unsaturated soils has been studied with several attempts to model it analytically (e.g., Philip, 1969, Warrick et al. 1985, Srivastava and Yeh 1991, Chen et al., 2003, F. Yuan and Lu, 2005). Yuan and Lu (2005) have provided an exhaustive review of the one-dimensional analytical closed-form formulation for transient seepage toward the water table. In this chapter, their mathematical formulation is revised and adapted for the hydraulic part of the hydro-mechanical uncoupled approach presented in the next paragraph.

As introduced above, transient flow in unsaturated soil is commonly described by Richard's equation that can be derived starting from the continuity equation:

$$-\rho_w \left(\frac{\partial v_x}{\partial x} + \frac{\partial v_y}{\partial y} + \frac{\partial v_z}{\partial z} \right) = \frac{\partial(\rho_w \vartheta)}{\partial t} \quad (3.1)$$

Where ρ_w is the water density, ϑ is the volumetric water content, t is the time, and v_x , v_y and v_z are the flow velocities in the three directions x , y , z .

Under the hypothesis of the validity of Darcy's law, the velocities can be related to the hydraulic head ($h = z + h_m$) through the hydraulic conductivity functions:

$$\begin{cases} v_x = -k_x(h_m) \frac{\partial h}{\partial x} \\ v_y = -k_y(h_m) \frac{\partial h}{\partial y} \\ v_z = -k_z(h_m) \frac{\partial h}{\partial z} \end{cases} \quad (3.2)$$

where h_m is the matric suction head:

$$h = z + h_m = z + \frac{(u_a - u_w)}{\rho_w g} \quad (3.3)$$

The velocities can be substituted in the continuity equation achieving the 3-dimensional Richard's equation:

$$\frac{\partial}{\partial x} \left[k_x(h_m) \frac{\partial h}{\partial x} \right] + \frac{\partial}{\partial y} \left[k_y(h_m) \frac{\partial h}{\partial y} \right] + \frac{\partial}{\partial z} \left[k_z(h_m) \left(\frac{\partial h}{\partial z} \right) \right] = \frac{1}{\rho_w} \frac{\partial(\rho_w \vartheta)}{\partial t} \quad (3.4)$$

or in a more compact notation by making the hypothesis of incompressible fluid:

$$\text{div}[k(h_m) \nabla h_t] = C(h_m) \frac{\partial h_m}{\partial t} \quad (3.5)$$

$C(h_m) = \frac{\partial \vartheta}{\partial h_m}$ is called specific moisture capacity and it is achieved by considering the variation of the volumetric water content in time $\left(\frac{\partial \vartheta}{\partial t} = \frac{\partial \vartheta}{\partial h_m} \frac{\partial h_m}{\partial t} \right)$.

For one dimensional flow in unsaturated soils, Richard's equation can be written as:

$$\frac{\partial}{\partial z} \left[k_z(h_m) \left(\frac{\partial h_m}{\partial z} + 1 \right) \right] = C(h_m) \frac{\partial h_m}{\partial t} \quad (3.6)$$

With the following initial and boundary conditions:

$$h_m(z, 0) = h_{m,0}(z) \quad (3.7)$$

$$h_m(0, t) = h_{m,1} \quad (3.8)$$

$$\left[k(h_m) \left(\frac{\partial h_m}{\partial z} + 1 \right) \right]_{z=L} = -i_1(t) \quad (3.9)$$

The geometry of the problem is reported in Figure 3.1. The initial suction head distribution is assumed to be a steady-state distribution.

The Richard's equation is non-linear, and, for mathematical convenience, the exponential model can be chosen to model the water content and the hydraulic conductivity evolution with the matric suction:

$$k_z(h_m) = k_s e^{-\alpha \rho_w g h_m} = k_s e^{\beta h_m} \quad (3.10)$$

$$\vartheta(h_m) = \vartheta_r + (\vartheta_s - \vartheta_r) e^{-\alpha \rho_w g h_m} = \vartheta_r + (\vartheta_s - \vartheta_r) e^{\beta h_m} \quad (3.11)$$

Where k_s is the saturated hydraulic conductivity, ϑ_s and ϑ_r are respectively the saturated and the residual volumetric water content and β is a fitting parameter also correlated to the soil pore-size distribution parameter representing the reduction rate of the hydraulic conductivity and water content function (Gardner, 1958).

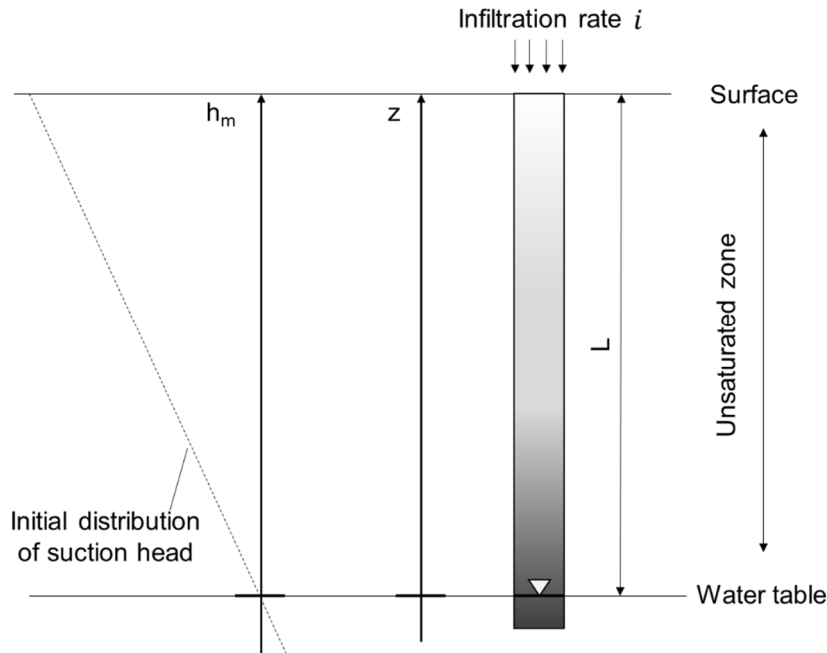


Figure 3.1. Schematic representation of one-dimensional infiltration model: geometry and assumed initial condition.

The adoption of exponential models allows to achieve the derivative of the involved functions easily:

$$C(h_m) = \frac{\partial \theta}{\partial h_m} = \beta(\vartheta_s - \vartheta_r)e^{\beta h_m} \quad (3.12)$$

Richard's equation, being highly nonlinear, needs to be linearized. Using Kirchoff's transformation, it is possible to identify a matrix flux potential Φ as follows:

$$\Phi(z, t) = \int_{-\infty}^{h_m} k(h_m) dh_m = \frac{k(h_m)}{\beta} \quad (3.13)$$

As a consequence, Richard's equation can be linearized as:

$$\frac{\partial^2 \Phi}{\partial z^2} + \beta \frac{\partial \Phi}{\partial z} = \frac{1}{D} \frac{\partial \Phi}{\partial t} \quad (3.14)$$

And the initial and boundary conditions:

$$\Phi(z, 0) = \frac{k_s}{\beta} e^{\beta h_{m,0}(z)} \quad (3.15)$$

$$\Phi(0, t) = \frac{k_s}{\beta} e^{\beta h_{m,1}} \quad (3.16)$$

$$\left[\frac{\partial \Phi}{\partial z} + \beta \Phi \right]_{z=L} = -i_1(t) \quad (3.17)$$

Where $D = \frac{k_s}{\beta(\vartheta_s - \vartheta_r)}$ is the diffusivity.

The initial condition is assumed to be a steady-state solution. For this reason, Richard's equation is firstly solved in steady-state conditions; subsequently, the solution is employed as a condition at $t=0$.

3.2.1 Steady-state solution

In steady-state conditions, the differential equation can be written as:

$$\frac{d^2 \Phi_0}{dz^2} + \beta \frac{d\Phi_0}{dz} = 0 \quad (3.18)$$

And as a consequence, the boundary conditions:

$$\Phi_0(0) = \frac{k_s}{\beta} e^{\beta h_{m,1}} \quad (3.19)$$

$$\left[\frac{d\Phi_0}{dz} + \beta \Phi_0 \right]_{z=L} = -i_0 \quad (3.20)$$

Where i_0 is the seepage rate at time $t = 0$.

Imposing:

$$\Phi_0 = \phi - \frac{q_0 + k_s e^{\beta h_{m,1}}}{1 + \beta L} z + \frac{k_s}{\beta} e^{\beta h_{m,1}} \quad (3.21)$$

the steady-state equation and the imposed boundary conditions can be rewritten as:

$$\frac{d^2\phi}{dz^2} + \beta \frac{d\phi}{dz} = 0 \quad (3.22)$$

$$\phi(0) = 0 \quad (3.23)$$

$$\left[\frac{d\phi}{dz} + \beta \phi \right]_{z=L} = 0 \quad (3.24)$$

Hence, the general solution can be achieved for the steady-state solution:

$$\Phi_0(z) = \frac{k_s e^{\beta(h_{m,1}-z)}}{\beta} + \frac{i_0}{\beta} (e^{-\beta z} - 1) \quad (3.25)$$

3.2.2 Transient solution

Starting from the steady-state solution as initial condition and taking the Laplace transformation, it is possible to write:

$$\frac{d^2\tilde{\Phi}}{dz^2} + \beta \frac{d\tilde{\Phi}}{dz} - \frac{s^L}{D} \tilde{\Phi} + \frac{\Phi_0}{D} = 0 \quad (3.26)$$

And the boundary conditions:

$$\tilde{\Phi}(0) = \frac{\Phi_1(0)}{s^L} = 0 \quad (3.27)$$

$$\left[\frac{d\tilde{\Phi}}{dz} + \beta\tilde{\Phi} \right]_{z=L} = -\tilde{i}_1(s^L) \quad (3.28)$$

Where $\tilde{\Phi} = L(\Phi)$, $\tilde{i}_1 = L(i_1)$ and s^L is the Laplace-transform complex variable.

Solving equation (3.26) to (3.28) and taking the inverse of the Laplace transformation it is possible to achieve the matrix flux potential for transient conditions:

$$\Phi(z, t) = \Phi_0(z) + 8D e^{\frac{\beta(L-z)}{2}} F(\lambda_n) G(t) \quad (3.29)$$

With:

$$F(\lambda_n) = \sum_{n=1}^{\infty} \frac{\left(\lambda_n^2 + \frac{\alpha^2}{4} \right) \sin(\lambda_n L) \sin(\lambda_n z)}{2\beta + \beta^2 L + 4L\lambda_n^2} \quad (3.30)$$

$$G(t) = \int_0^t [i_0 - i_1(\tau)] e^{-D\left(\lambda_n^2 + \frac{\beta^2}{4}\right)(t-\tau)} d\tau \quad (3.31)$$

Where λ_n is the n-th positive root of the equation $\sin(\lambda L) + \left(\frac{2\lambda}{\beta}\right) \cos(\lambda L) = 0$

If the seepage rate q_1 is constant the transient solution can be simplified to:

$$\Phi(z, t) = \Phi_{0,i_1}(z) - 8(i_0 - i_1) e^{\frac{\beta(L-z)}{2}} \sum_{n=1}^{\infty} \frac{\sin(\lambda_n L) \sin(\lambda_n z)}{2\beta + \beta^2 L + 4L\lambda_n^2} e^{-D\left(\lambda_n^2 + \frac{\beta^2}{4}\right)t} \quad (3.32)$$

From where it is possible to explicit the matrix suction head:

$$h_m(z, t) = \frac{1}{\beta} \ln \frac{\beta\Phi(z, t)}{k_s} \quad (3.33)$$

Or the matrix suction:

$$u_a - u_w = \rho_w g h_m(z, t) = \rho_w g \frac{1}{\beta} \ln \frac{\beta\Phi(z, t)}{k_s} \quad (3.34)$$

3.2.3 Infiltration model

Among the different infiltration models available in the literature (e.g., Green-Ampt, 1911, Horton, 1933, Phillip, 1957), the Horton's model has been chosen considering that it has been demonstrated to be an analytical solution of Richard's equation.

It can be expressed as:

$$\frac{di(t)}{dt} = -\frac{i(t) - i_c}{k_c} \quad (3.35)$$

where $\frac{di(t)}{dt}$ is the rate of potential infiltration i_p ; i_c is the value of $i(t)$ for $t \rightarrow \infty$ and is equal to the saturated hydraulic conductivity; k_c is the decay rapidity of $i(t)$;

Integrating the 3.35 we get:

$$i(t) = i_c + (\bar{i}_0 - i_c)e^{-\frac{t}{k_c}} \quad (3.36)$$

where \bar{i}_0 is the value of $i(t)$ at initial condition ($t=0$).

Figure 3.2 shows three possible conditions: i) the rainfall intensity is always higher than the potential infiltration; ii) the rainfall intensity is always lower than the potential infiltration; iii) intermediate condition when initially the rainfall intensity is lower than the potential infiltration and then higher. The latter situation frequently happens in nature, considering that usually, rainfall intensity at the beginning is lower than the infiltration capacity. The rain initially infiltrates totally until the saturation of the first surface layers of the soil happens. At that time, a veil of water begins to form, giving rise to the surface runoff.

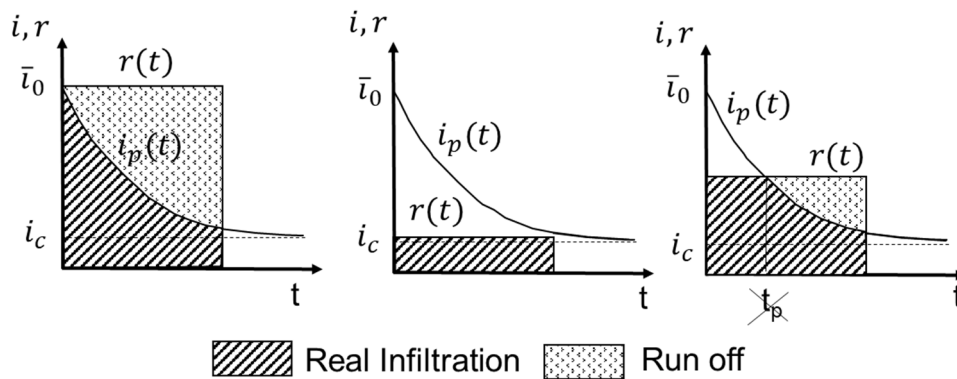


Figure 3.2. Comparisons between potential infiltration and various rainfall intensities.

This condition occurs when the intensity of rain $r_d(t)$ equals the rate of potential infiltration $i(t)$. The interval of time between the beginning of the rain and the reaching of saturation is called saturation time (or ponding time), t_p . The effective infiltration rate from this moment onwards coincides with the potential one ($i(t) = i_p(t)$). If we compare the amount of water infiltrated and the amount of expected infiltrated water (comparing the integrals) we found a discrepancy. For this reason, the potential infiltration curve $i_p(t)$ has to be shifted to satisfy the equality of water volumes. In other words, assuming a given rainfall intensity $r_d(t)$, the $i(t)$ curve (Figure 3.3) will describe the effective infiltration only if $r_d(t) > i(t)$ for each time. If this condition is not respected, the effective infiltration rate $i(t)$ will be higher. $i(t)$ is considered to be equal in shape to $i_p(t)$ but translated of a t_0 time step so that at the time t_p (ponding time), the volume infiltrated since the beginning of the rainfall event is equal to the maximum that can infiltrate, and the rainfall intensity coincides with the effective rainfall capacity $i(t)$.

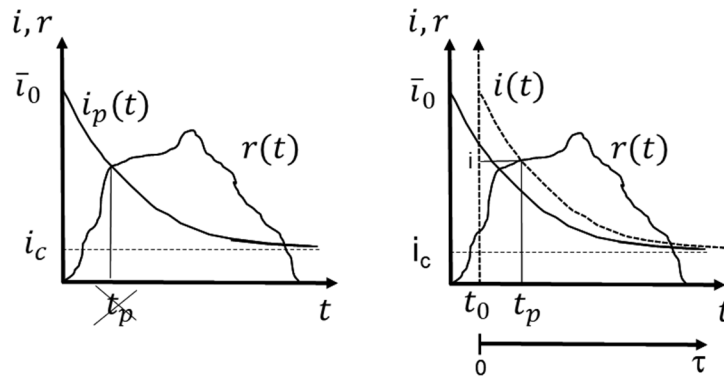


Figure 3.3. Effective rainfall capacity and ponding time.

According to Horton's model, the ponding time can be computed as:

$$t_p = \frac{1}{rk} \left[(i_0 - r) - \left(f_c \log \left(\frac{r - i_c}{i_0 - i_c} \right) \right) \right] \quad (3.37)$$

3.3 Uncoupled hydro-mechanical analyses

Once the distribution of the matric suction head and the volumetric water content is known in the space and in the time, they can be employed for the resolution of the mechanical part of the problem.

As was pointed out previously, the interactional behaviour between retaining structures and unsaturated soils can be investigated by considering the extension of the classical theories (i.e., Rankine's theory).

Selecting an adequate effective stress definition, it is possible to compute the available shear strength at failure (τ_f). Here, the Bishop's definition of effective stress (Bishop, 1959) is selected among the others available in the literature:

$$\sigma'_{ij} = (\sigma_{ij} - u_a \delta_{ij}) + \chi(u_a - u_w) \delta_{ij} \quad (3.38)$$

where σ'_{ij} is the effective stress tensor, σ_{ij} is the total stress tensor, χ is the effective stress parameter, u_a is the air pressure (imposed equal to 0 kPa), u_w is the water pressure, and δ_{ij} the Kronecker's delta. Due to the hypotheses introduced in the hydraulic part of the problem formulation, a compatible imposition of the effective stress parameter must be done. Vanapalli et al., (1996), provided an expression of the effective stress parameters as reported below:

$$\chi = \frac{S_r - S_{r,res}}{1 - S_{r,res}} = \frac{\vartheta - \vartheta_r}{\vartheta_s - \vartheta_r} \quad (3.39)$$

That can be extended to the transient condition:

$$\chi = \frac{\vartheta(z, t) - \vartheta_{res}}{1 - \vartheta_{res}} = \frac{e^{\frac{\beta}{\rho_w g}[(u_a - u_w)(z, t)]} - \vartheta_{res}}{\vartheta_s - \vartheta_{res}} \quad (3.40)$$

The available shear strength can be then computed as

$$\tau_f = c' + [(\sigma_n - u_a) + \chi(u_a - u_w)] \tan \varphi' \quad (3.41)$$

where σ_n is the total normal stress, c' and φ' are respectively the intercept cohesion and the shear strength angle.

Generally, we can consider the schematic representation of a retaining wall reported in Figure 3.4 to focus on the computation of the lateral earth actions in transient conditions. In this generic example, the GWT is placed at the bottom of the retaining structure, and infiltrations are supposed to happen at the upper part of the retained soil that is initially in unsaturated condition.

For the active case, the lateral earth pressure, according to Rankine's theory, can be computed as follows:

$$\sigma_{h,A}(z, t) - u_a = [\sigma_v(z, t) - u_a]K_A - 2c'\sqrt{K_A} - \frac{\frac{\beta}{e\rho_w g}[(u_a - u_w)(z, t)] - \vartheta_{res}}{\vartheta_s - \vartheta_{res}}[(u_a - u_w)(z, t)](1 - K_A) \quad (3.42)$$

where $\sigma_{h,A}$ is the active total lateral earth pressure, σ_v the vertical total stress and K_A the active earth pressure coefficient.

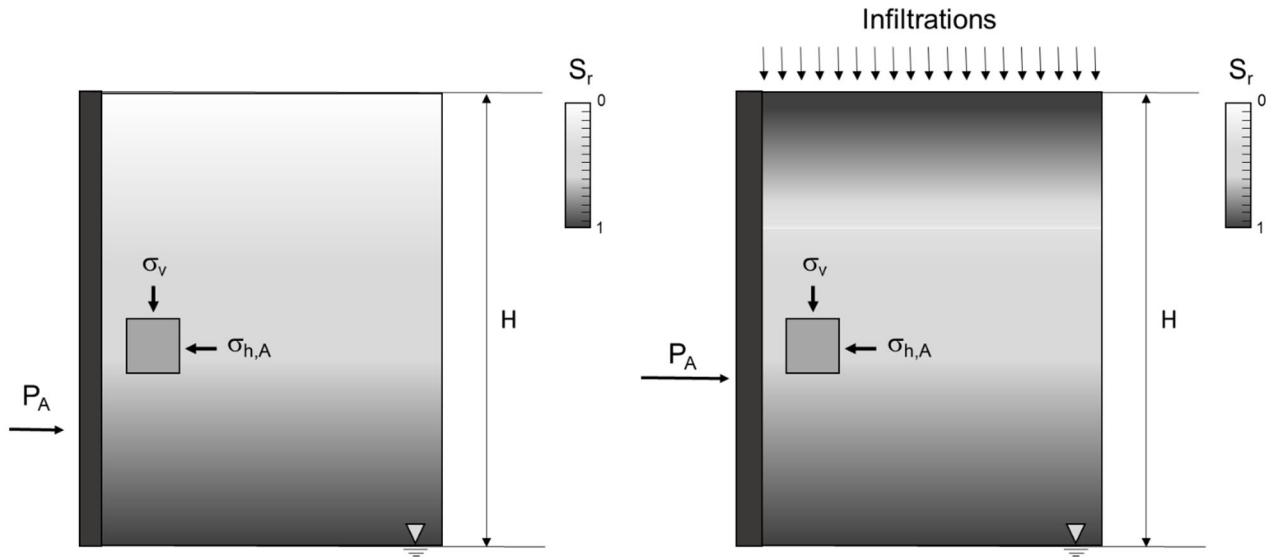


Figure 3.4 Geometry of the investigated problem at the initial condition and during the rainfall event.

The vertical total stress during the infiltrations will depend on the volumetric water content. Consistently with the assumption of weak coupling, the variation of porosity with suction is not considered, and the changing with the time of the total vertical stress can be calculated as:

$$\sigma_v(z, t) = \rho g z = [\rho_d + \vartheta(z, t)\rho_w]gz \quad (3.43)$$

Where ρ is the soil density ρ_d the dry density and g the gravity.

3.4 Illustrative example and parametric study on three soil types

In this section, the presented uncoupled hydro-mechanical approach is applied to an illustrative case study in order to assess the evolution of the later earth pressure distribution at the active state when the retained soil is subjected to the transient flow. The sensitivity of the analysis on three types of retained soils is presented. The considered soils are a silt, a

clayey silty sand and a fine sand as already reported in chapter 2. Here the water retention behaviour is described by the volumetric water content due to the assumptions in the mathematical formulation of the hydraulic analysis. Regarding the silt's parameters, data were collected from the experimental investigations made by Geiser (1999), Péron, (2008), Geiser et al. (2000), and Salager (2007); for the clayey-silty sand, data were found in Ferrari et al. (2013), Laloui et al. (2015), and Eichenberger et al. (2013), while, for the sand, the experimental results reported in Chapter 4 are used. In Figure 3.5, the water retention curve is reported for the three soils by comparing the experimental data and the exponential models.

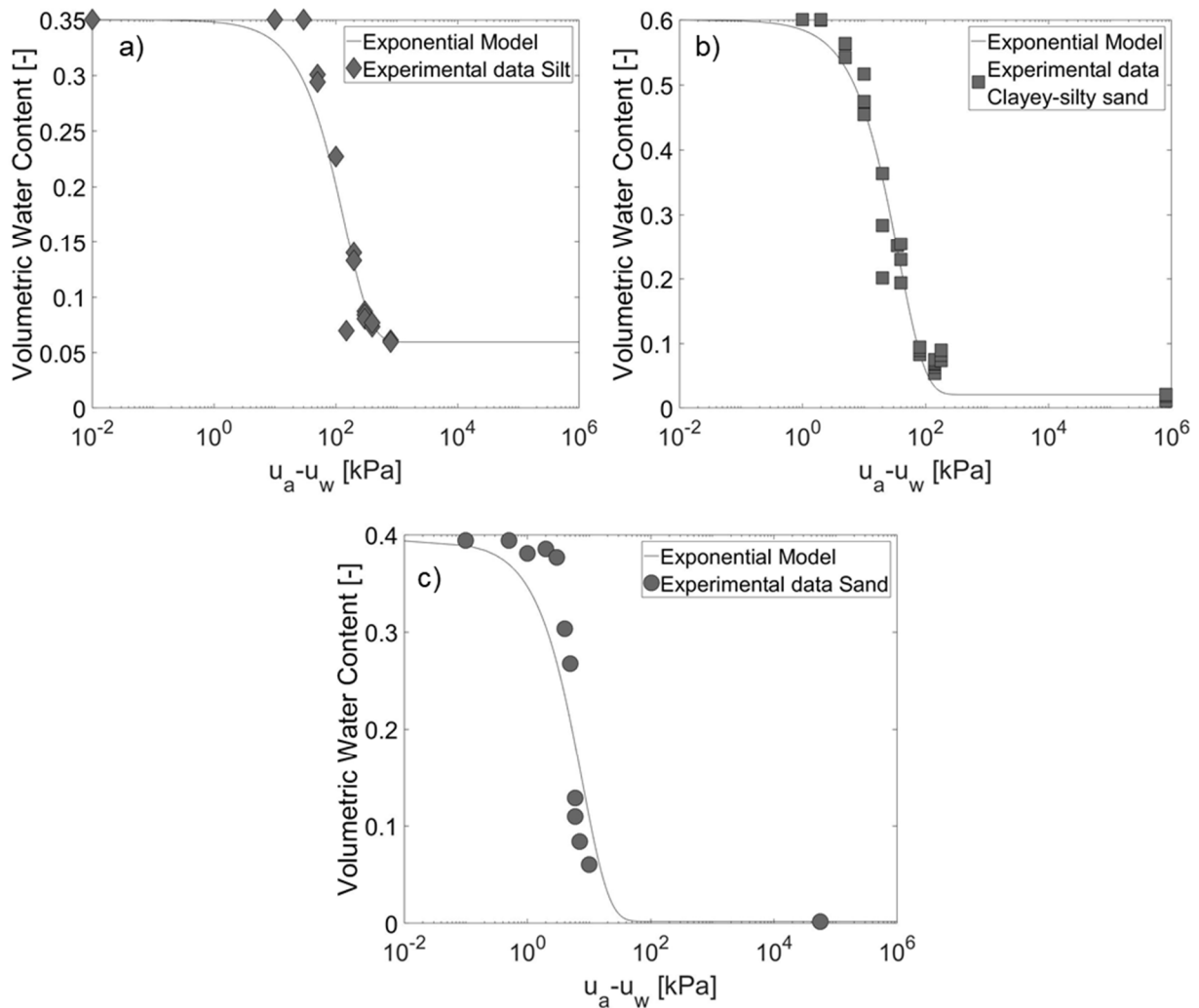


Figure 3.5 Water retention curve in terms of volumetric water content for a) silt, b) clayey-silty sand, and c) sand.

Even if in the literature alternative models exist (Van Genuchten, 1980, Broadbridge and White, 1988, Ross and Parlange 1994, Kim et al., 1996), the exponential model, that can be

used to solve in the transient condition Richard's equation in analytical closed-form formulation, seems to reproduce quite well the experimental results. A slightly worse fitting is present in correspondence of the air entry value for the silt and the sand, while for the clayey-silty sand the model fits almost properly the data. A worse fitting can be recognized for the sand.

The experimental data in terms of volumetric water content were obtained starting from the degree of saturation assuming that the volume remains constant at any suction change. This assumption is consistent with that made for the study of the transient problem (section 3.2.2). However, the assumption can be considered more reliable for the clayey-silty sand and the sand than for the silt soil (see Chapter 4). The exponential model was achieved by applying the least squares method by changing the fitting parameter in the model described by equation (3.10). It has to be remarked that the same parameter β is used for both hydraulic conductivity and water retention functions. A value of β that allows a good fitting of the volumetric water content can produce a significant mismatch for hydraulic conductivity, and vice versa. This statement represents a limitation of the analytical method, but it is the inevitable price to pay for the privilege to handle an analytical solution.

The soil properties in terms of dry unit weight (γ_d), shear strength angle (φ'), effective cohesion (c'), and the parameters of the exponential model employed in the analyses are reported in Table 3.1.

Table 3.1. Soils' properties.

Soil [-]	γ_{dry} [kN/m ³]	φ' [-]	c' [kPa]	k_s [m/s]	β [m]	ϑ_s [-]	ϑ_r [-]
Silt	16.70	32.0°	0	$1.00 \cdot 10^{-7}$	-0.07	0.35	0.06
Clayey-silty sand	9.90	35.5°	0	$4.80 \cdot 10^{-6}$	-0.27	0.60	0.02
Sand	16.50	35.0°	0	$1.00 \cdot 10^{-4}$	-1.3	0.39	0

The height of the wall is assumed of being 3 m, and the seepage rate is imposed equal to the saturated hydraulic conductivity. As discussed in the subsection 3.2.3, the infiltration rate will depend on the rainfall intensity. A seepage rate equal to the saturated hydraulic conductivity leads to a totally disappearing of the matric suction at the steady-state condition which corresponds to an increase of the lateral earth thrust.

A constant infiltration is considered as a boundary condition, and it is imposed firstly equal to the saturated hydraulic conductivity ($i = k_s$) of the considered soil, then realistic values of the seepage rate are considered by analyzing statistically some available rainfall data. This assumption allows for modeling the condition of unsaturated retained soil under a seepage rate, representing extreme precipitations. However, it cannot be considered as the worse scenario for the transient analyses because at the early stages of the rainfall events the amount of water that can infiltrate in the soils can be higher and a time-dependent boundary conditions should be imposed according to the chosen infiltration model (e.g. Horton's model).

According to the previous sections, the uncoupled hydro-mechanical analyses have been performed for the considered example. For the silt, the clayey silty sand, and the sand, the hydraulic transient analyses have been first solved then the evolution with time of the lateral earth pressure has been obtained. Figure 3.6a and Figure 3.6b report the evolution with the time and depth of the matric suction and the shear stress parameter that is strictly correlated to the evolution of the volumetric water content (equation 3.39). The matric suction tends to reduce with time, and the volumetric water content tends to increase. Figure 3.6c shows the evolution of the lateral earth pressure for the three investigated soils according to equation (3.39).

Regarding the silt, the transient flow is a slow process, and the matric suction needs considerably long time to evolve; for the infiltration rate ($i_1 = k_s = 1.0 \times 10^{-7}$ m/s), the analyses have been performed up to 1000 h of seepage simulation. After 500 h of transient infiltration, pore water pressure reduced almost to 0, and the volumetric water content reached almost the saturated one (effective stress parameter equal to 1).

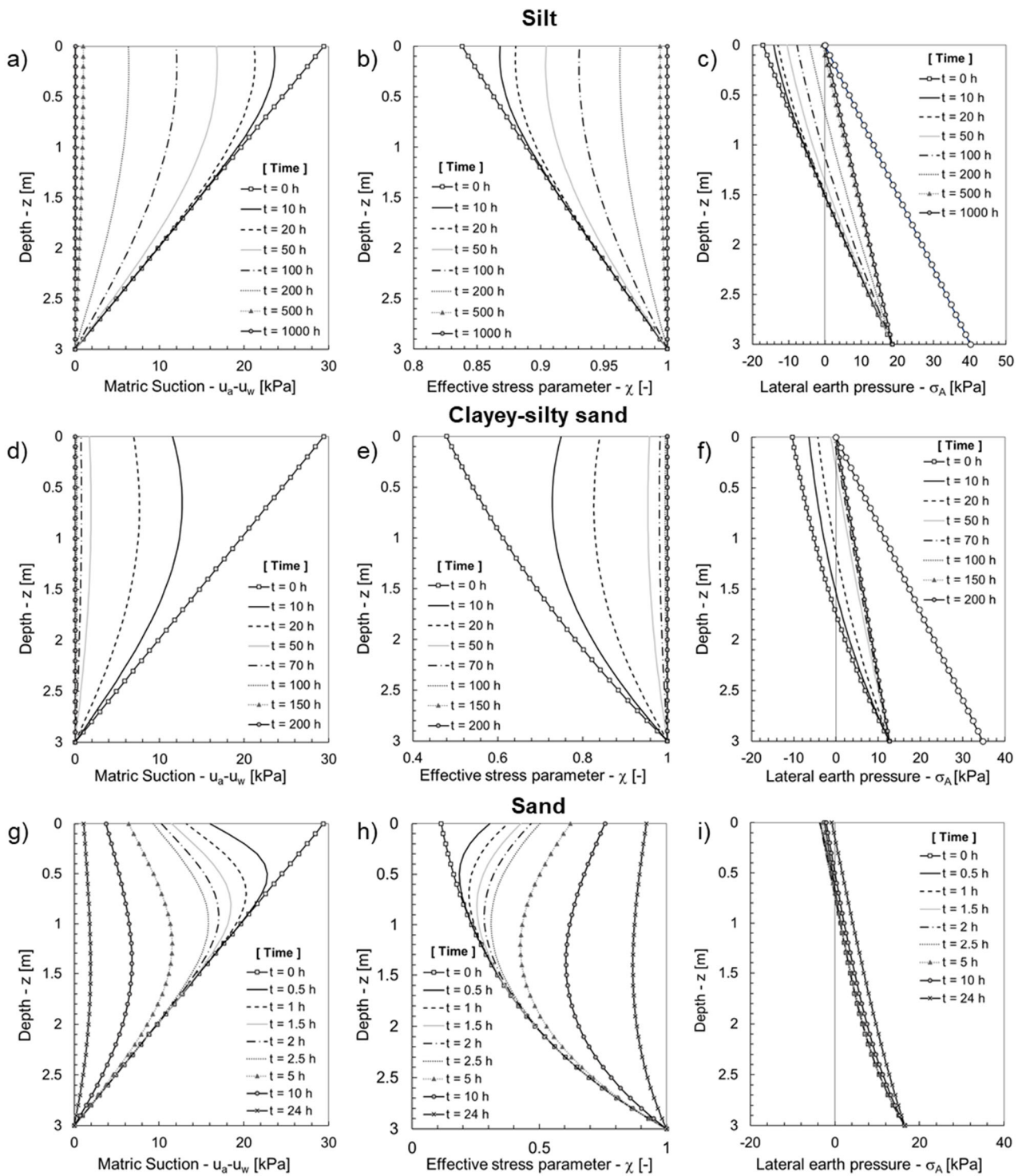


Figure 3.6 Evolution of the matric suction, effective stress parameter, and lateral earth pressure profiles with the time.

The lateral earth pressure distribution tends to the steady-state solution (chapter 2) by increasing with the time. At the initial condition (i.e., linear distribution of pore water pressure above the groundwater table), prior the simulation of the rainfall event ($t=0$), the horizontal stress at the active state is negative up to a depth of 1.5 m, while, between 1.5 and 3

m is positive. With the evolution of the transient flow, the portion of the soil body affected by tension lateral stress ($\sigma_{h,A} < 0$) reduces with time increasing the overall thrust of the soil. At the reached steady-state condition, the horizontal stress distribution is totally positive.

Moreover, the center of gravity of the horizontal pressure distribution moves with time upwards. Therefore, the overall overturning moment acting on a retaining structure will increase not only a cause of the increase of the magnitude of the thrust but also of its eccentricity. At the initial steady-state condition, the magnitude of the horizontal thrust is 14.4 kN with an eccentricity (respect to the bottom the retaining structure) of around 0.5m at the final steady-state ($t=1000$ h) 29.7 kN and 1.0 m respectively.

Regarding the clayey silty sand, characterized by a lower air entry value and a higher saturated hydraulic conductivity with respect to the silt, the transient seepage has been modeled by imposing an infiltration rate $i_1 = k_s = 4.8 \times 10^{-6}$ m/s. After 10 h of transient seepage, the reduction in the matric suction, and the increase in the volumetric water content over the space are higher respect to that of the silt. After 100 h the matric suction is almost disappeared, and the steady-state condition can be considered to be reached (Figure 3.6d). The lateral earth pressure and the initial eccentricity respect to the bottom of the retaining structure change from 7.5 kN and 0.4 m to 16,5 kN and 1 m (Figure 3.6f).

Figure 3.6g,h, and i shows the evolution with time of the matric suction, effective stress parameter, and the lateral earth pressure at active state for the sand under a constant infiltration rate ($i_1 = k_s = 1.0 \times 10^{-4}$ m/s). The time needed to reach the steady-state condition is significantly lower if compared to that of silt and the clayey silty sand. After 24h of transient infiltration, the matric suction is almost 0 in the whole soil body. However, analyzing the evolution with time of the lateral earth pressure at active state, an increase of the lateral thrust is present, but the change in the magnitude is significantly lower with respect to silt and the clayey silty sand. At initial condition, the thrust has a value of 22 kN and after 24 h of transient seepage 25 kN. In the upper part of the soil body, considering that the values of the volumetric water content are low at the initial condition, the transient seepage has an opposite effect. At the early stages of the simulation, the infiltration causes an increase of the volumetric water content that associated with a non-zero value of the pore water pressure. The wetting front is an unsaturated wetting front that is propagating with the time

downwards. This increase in the matric suction, combined with a low vertical net stress, allows for a temporary decrease of the lateral earth pressure at active state at the upper part of the retained soil. With time evolution, this temporary effect tends to dissolve, and the horizontal stress increase with the increase of the volumetric water content. The eccentricity at the initial condition is higher with respect to that of the other soils, but it does not change significantly respect to the silt and the clayey-silty sand: from 0.8 m to 1 m.

The time needed for the total disappearing of the matric suction will depend on the retention properties of the retained soils and their infiltration capacity with respect to the rainfall event. In the previous case, the considered infinite rainfall event was different among the three considered soils. By considering the case of the sand, for example, the infiltration rate imposed equal to the rainfall intensity was equal to $i_1 = 1.0 \times 10^{-4}$ m/s that corresponds to 8640 mm/day. The latter corresponds to an unrealistic rainfall intensity but it provides an idea on the potential for the consideration of matric suction in the computation of the lateral earth thrust. For this reason, the analyses reported above are now performed by assuming as infiltration rate a constant value coming from a statistical analysis of real rainfall data. The analyses are performed by considering 5 days of rain.

The cumulated precipitations over five days are available for the meteorological station of Sierre (CH). The inferred data (Figure 3.7a), span from 1966 to 2015 and are processed by adopting the generalized extreme value distribution (Figure 3.7b).

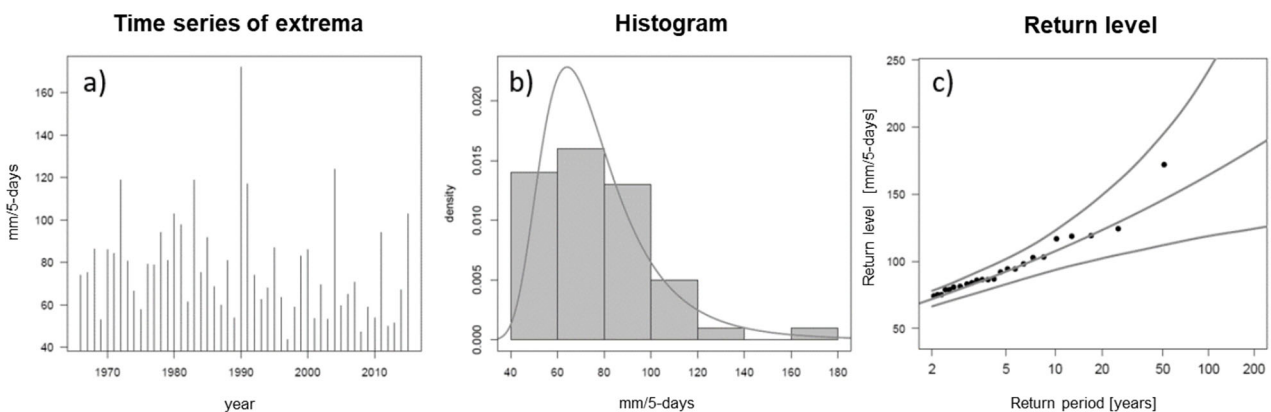


Figure 3.7 a) Extreme value analysis for five-days data; b) histogram of extrema, fitting with the GEV density distribution; c) evolution of the return level with the return period, the upper and lower lines represent the 95% confidence intervals (MeteoSwiss, 2016).

The intensities values for the corresponding period of return and the 95% confidence interval are reported in Figure 3.7c. Assuming a return period of 100 years, the design rainfall intensity is resulted in being 164.3 mm/5-days or 1.36 mm/h. Figure 3.8 shows the results of the analyses.

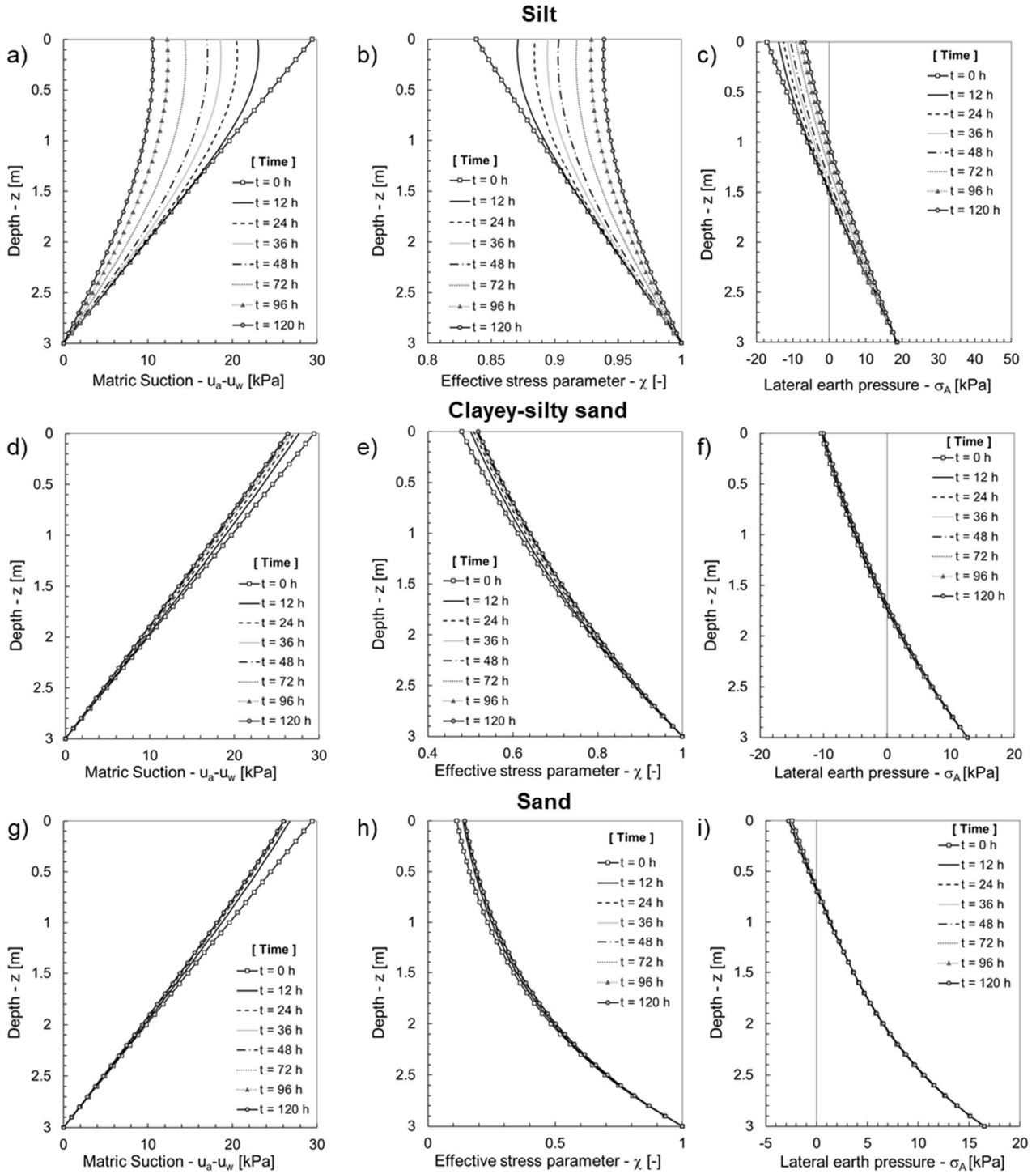


Figure 3.8 Evolution of the matric suction, effective stress parameter, and lateral earth pressure profiles during the 5 days of rain. Infiltration rate equal to 1.36 mm/h for all the considered soils.

With respect to the previous scenario, all the considered soils did not reach full saturation. The matric suction profiles and the lateral earth pressure distribution are influenced by the simulated rainfall event, especially for the silt. While, for the clayey-silty sand and the sand, a little variation of the lateral earth pressure distribution and matric suction profiles are found.

3.5 Conclusions

Rainfall events can induce significant changes in the resulting thrust on the geostructures. A rational design approach would suggest to identify and quantify the effects induced by the infiltrations during rainfall events. In this chapter, an analytical closed-form formulation has been presented in the framework of uncoupled hydro-mechanical analyses. The approach described in the previous sections is characterized by a series of hypotheses that should be considered when interpreting the results. Regarding the soil-structure interaction, a Rankine theory has been chosen, and consequently, all the hypotheses of this method are implicitly assumed. Regarding the hydraulic behaviour, the hysteresis of the water retention curve was not considered; the latter is assumed to be constant in time. A one-dimensional transient model for the hydraulic analyses was employed considering the simplified geometry of the problem. A two-dimensional or a three-dimensional model would require a numerical approach with a loss of the analytical closed-form formulation. Anyway, under the given hypotheses, the employed methodology allows describing the soil-structure interaction during the rainfall events considering hydro-mechanical behaviour of unsaturated soils with an analytical model. The procedure has been implemented for a simple geometry by considering as retained soil three different geomaterials were suitably chosen to highlight the role played by the hydro-mechanical properties of soils and the effects that they have on the computation of the lateral earth pressure.

The main outcome of this chapter can be summarized as follows:

- the simulation of the rainfall events and the consequential seepage has a significant effect on the magnitude of the lateral earth pressure that has been quantified at different time steps. This led to an increase of the actions on the retaining structure causing a reduction of the factor of safety;

- the change in the magnitude of the lateral earth pressure is not the only effect that will induce an increase of the actions on the retaining structure. Also, the point of force application changes with time at its variation depends significantly on the hydro-mechanical properties of the involved geomaterial;
- the transient response of the system is significantly different among the three investigated soils. The time needed to reach the steady-state condition is 500 h, 100 h, and 24 h for the silt, the clayey silty sand, and the sand respectively, when the infiltration rate is imposed equal to saturated hydraulic conductivity of the considered soil.
- A statistical analysis of the available rainfall event data is needed to calibrate the infiltration models;
- the use of the unsaturated soils mechanics requires a good hydro-mechanical characterization of the involved soils considering the sensitivity of the analyses on soil's properties;
- the transient analyses suggest moving towards a more rational design approach by considering the opportunity to perform the seepage analyses respect to consider the retained soil totally saturated. Infiltration models are available in the literature and can be employed as boundary conditions for either analytical or numerical models. Starting from statistical analyses of the rainfall events, it could be possible to estimate the amount of infiltrated water and subsequently perform the transient analyses to evaluate the effect on suction changes and consequently, on the lateral earth pressure distribution.

The analytical models presented in chapter 2 and chapter 3 have been extrapolated by extending the classical theory of soil mechanics by embedding the unsaturated soil mechanics principle. At the knowledge of the author, in the literature, a validation of the models or comparison with experimental or in situ tests capable of showing the distance between the forecasted thrust and the real one is still missing. This represents a scientific challenge that is faced in the next chapters.

Chapter 4

Experimental investigation on the hydro-mechanical properties of a sandy and a silty soil: implications on the lateral earth pressure

4. Experimental investigation on the hydro-mechanical properties of a sandy and a silty soil: implications on the lateral earth pressure

4.1 Foreword

Retaining structures interact with soils that are affected by environmental actions. Drying and wetting periods can affect the interactional behaviour by increasing or reducing the actions on the retaining structures. Both steady-state and transient analytical analyses presented in the previous chapters have shown the possibility to use the mechanics of unsaturated soils for the modeling of the lateral earth pressure during rainfall events. Doubtless, when performing one-dimensional weakly coupled analytical analyses, it is required to face up with several hypotheses that allow for a convenient resolution of the mathematical formulation. Among these assumptions, the hypothesis of the non-hysteretic behaviour of the soil stood out. Moreover, to the author knowledge, a comparison between the analytical closed-form formulation and experimental or in-situ tests is missing in the literature. In this regard, a physical model has been designed on purpose, and it will be presented in a dedicated portion of the thesis (chapter 5). This chapter concerns two main aspects: i) the hydraulic and the mechanical characterization of the involved soils in the thesis; ii) the implication on the lateral earth pressure of the employed models for the water retention behaviour of the retained soils.

Various experimental techniques can be found in the literature regarding how to determine the water retention properties of the treated soil (e.g. oedometer, filter paper method, tensiometer method, negative column water technique). The choice of the most suitable experimental technique for the characterization of the water retention behaviour depends mainly on the investigated soil properties or, specifically, on their expected suction values at the desaturation point (air entry value AEV) and/or at the residual point (suction value when the degree of saturation is equal to the residual degree of saturation). The water retention properties of two soils have been tested in the laboratory: a coarse-grained soil (Itterbeck sand) and a fine-grained soil (Sion silt). The water retention properties of the sand have

been studied because it is the geomaterial employed for the physical model. The water retention curve of the silt has been obtained for two main reasons: i) testing a set of high capacity tensiometers (HCT) built on purpose for the physical model; ii) showing the implication on the shear strength (and, as a consequence, on the lateral earth pressure at active state) of the assumed model for the retention properties of the retained soils.

Regarding the Ittembeck sand, in addition to the water retention curve, the physical and mechanical properties have been investigated in the laboratory. The grains size distribution, the minimum and maximum void ratio and the specific density have been determined. Moreover, to investigate soil properties at laboratory 1g scale with respect to in-situ conditions, the shear strength parameters have been obtained by performing direct shear tests at low and high vertical stress.

Regarding the Sion silt, more attention is focused on: i) the characterization of the water retention behaviour; ii) how to achieve it in a reasonable time; iii) its dependence on the deformations observed during the imposed suction path. In this regard, a set of high capacity tensiometers have been built thanks to the collaboration of the University of Strathclyde in the framework of secondments of the TERRE project. The laboratory facility, originally designed by Prof. Alessandro Tarantino, has been manufactured, set up, and calibrated at Laboratory for Soil Mechanics at Swiss Federal Institute of Technology in Lausanne. After presenting the manufacturing steps of the equipment, the experimental investigation on silt's retention property is described. The combined use of HCT and a dew-point hygrometer (WP4C) have allowed achieving the experimental results related to the water retention behaviour for both drying and wetting path.

An appropriate modeling of the soil water retention behaviour resulted in being crucial for the computation of lateral earth thrust.

4.2 Itterbeck sand

4.2.1 Physical properties

The Itterbeck sand (Figure 4.1) is characterized by a content of SiO_2 higher than 97% (Terzis, 2017). The sand has been selected as tested geomaterial for the physical modeling for two main reasons: i) the mechanical behaviour of sand is well known in geomechanics and

this helps in the calibration of the physical model in dry conditions; ii) the expected water retention properties were consistent with the desired water content distribution in the physical model (see section 5.1).

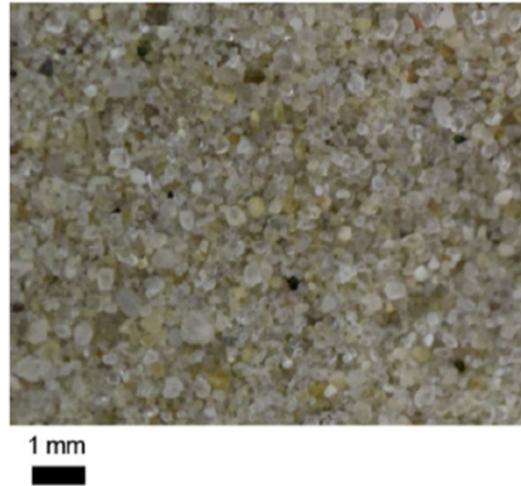


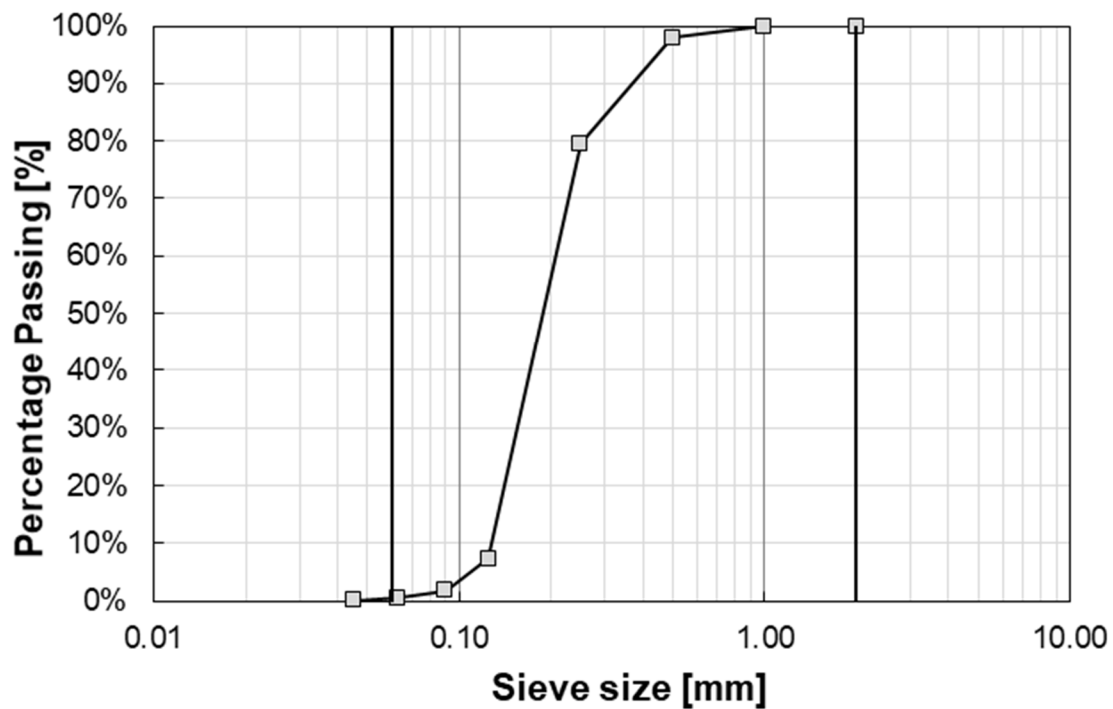
Figure 4.1 *Itterbek sand under a microscope (Terzis, 2017).*

The physical properties of the sand in terms of particle size distribution, minimum and maximum void ratio, and specific density were determined. The grain size distribution has been obtained according to ASTM D422-63 and is shown in Figure 4.2. The results indicate that the soil includes less than 2% of fines. The dimensions of the grains corresponding to 10%, 30%, and 60% of the passing percentage (D_{10} , D_{30} , D_{60}) are 0.128 mm, 0.155 mm and 0.207 mm, respectively. These data allow for the calculation of the uniformity coefficient (C_u) and the coefficient of curvature (C_c). According to the obtained values, the sand can be labeled as SP according to the Unified Soil Classification System (USCS).

The minimum (e_{min}) and the maximum (e_{max}) void ratio have been achieved according to ASTM D4253-16 and ASTM D4254-16, respectively, and are equal to 0.55 and 0.88. The specific density of the soil was achieved by the water pycnometer test, according to ASTM D854-02. Figure 4.3 shows the evolution of the sand bulk density within the whole range of the void ratio (e_{min} - e_{max}) at different degrees of saturation. The evolution of the bulk density with the degree of saturation represents an important point that has to be highlighted because it plays a role in the evolution of the total vertical stress during rainfall events. Table 4.1 summarized the achieved physical properties of the sand.

Table 4.1. *Ittembeck sand's physical properties.*

D_{10} [mm]	D_{30} [mm]	D_{60} [mm]	C_u [-]	C_c [-]	e_{min} [-]	e_{max} [-]	ρ_s [g/cm ³]
0.128	0.155	0.207	1.62	0.91	0.55	0.88	2.65

**Figure 4.2** *Grain size distribution.*

4.2.2 Direct shear tests from very low to high vertical stress

To characterize the mechanical properties, direct shear tests were performed. It is accepted that the Mohr-Coulomb's failure peak envelope is not linear, but it curves at low vertical stress. According to Valore et al. 2017, the curvature of the failure envelope in the very low effective stress range is the most important single cause of the scale effects that afflict 1g tests on reduced-scale models; it cannot be neglected in the interpretation of the results of single-gravity physical tests.

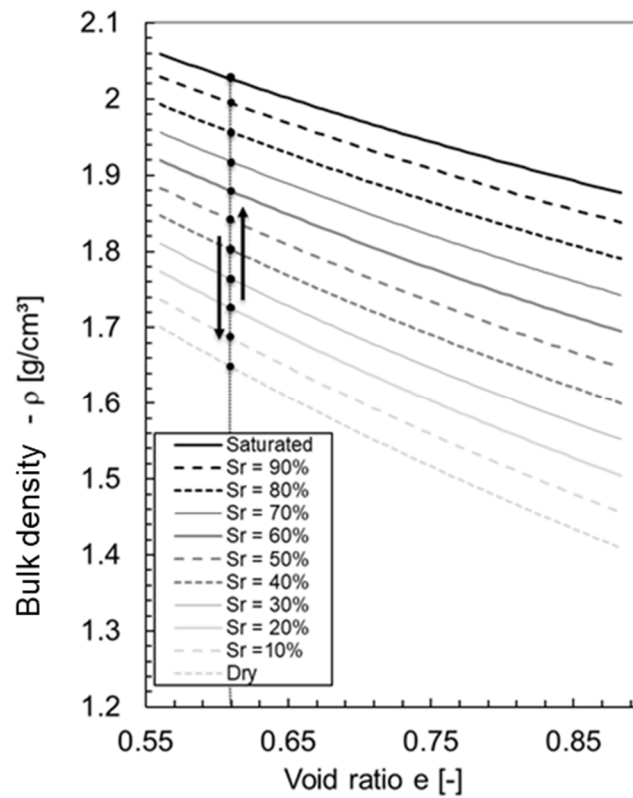


Figure 4.3 Evolution of soil bulk density with the void ratio at different degree of saturation.

The shear strength parameters of the sand were determined by performing direct shear tests from very low to relatively high vertical stress focusing on both the peak and the constant volume (CV) envelope (i.e., critical state). The tests were performed in dry conditions. The investigated range of vertical stress are: i) 0 to 10 kPa; ii) 10 to 50 kPa; iii) 50 to 250 kPa and iv) 250 to 500 kPa. The imposed vertical stresses were calculated by considering the expected level of vertical stress along with the depth of the physical model. Performing the tests at very low vertical effective stress (0-10 kPa) by using a conventional direct shear apparatus is inadvisable due to the resolution of the conventional types of equipment. For this reason, conventional direct shear device was modified to investigate the peak failure envelope at the level of the vertical effective stress expected in the physical model. The tests conducted at higher vertical effective stress were performed with a conventional direct shear apparatus. The low-stress device makes use of the same lower and upper halves of a conventional direct shear box. Its bottom part was kept fixed while the top part was allowed to slide. The interface between the upper and the lower part of the box was modified by attaching on both the surfaces a thin layer of Teflon® to reduce the friction. The application

of the vertical and horizontal stress was controlled by filling-up two small containers with sand. The first one was placed on top of the sample (i.e. producing the confinement or vertical force), while the second one was connected to the upper part of the direct shear box through a rope and pulley system (i.e. shearing or horizontal force), as shown in Figure 4.4. A micrometer was placed at the back of the direct shear box to measure the horizontal displacements.

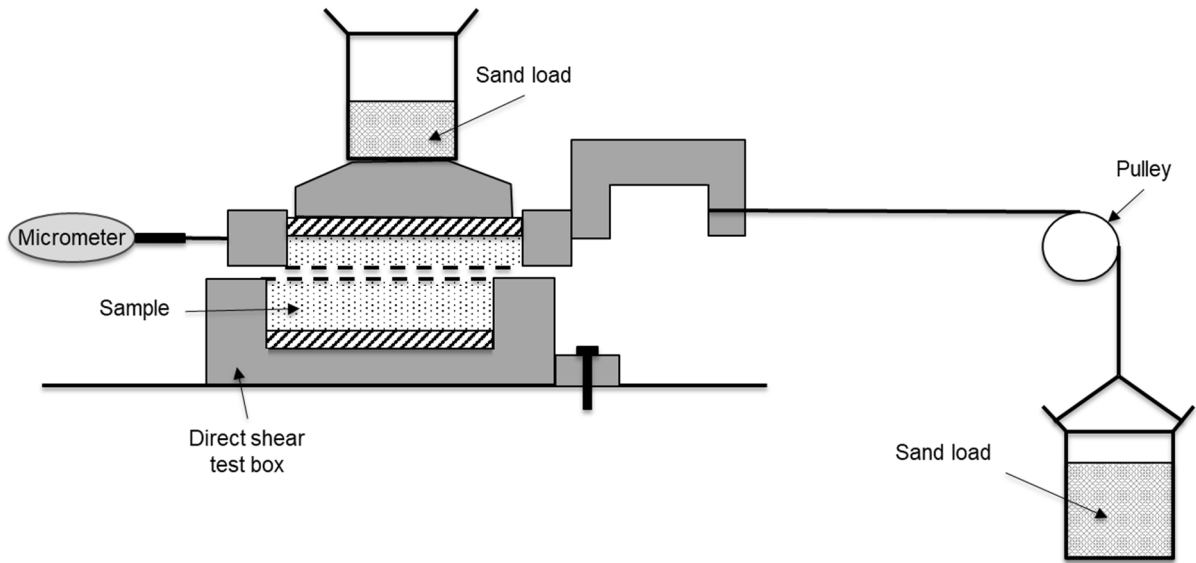


Figure 4.4 Schematic representation of the employed direct shear test device for low vertical stress.

In this configuration, the tests can be performed in control of force and as a consequence only the peak shear strength can be measured.

The values of the imposed load have been corrected by considering the weight of the sand-container and the cap of the shear box ($W = 211.52$ g). A null test (empty direct shear box) was preliminarily performed in order to measure the friction of the whole system correcting the achieved results. The null test consists in the increasing of the horizontal force until the upper part of the empty device moved. The null test has been performed 5 times obtaining a value of 0.4 N as a triggering horizontal force with a standard deviation of 0.05 N. The samples were prepared by pouring the sand in the direct shear test box, at the target void ratio ($e_0 = 0.62$). The latter corresponds to the expected average density in the physical model (dry pluviation technique). Figure 4.5 reports the results of the performed tests in the ranges 0-10 kPa and 10-50 kPa, while Figure 4.6 in the ranges 50-250 kPa and 100-500 kPa.

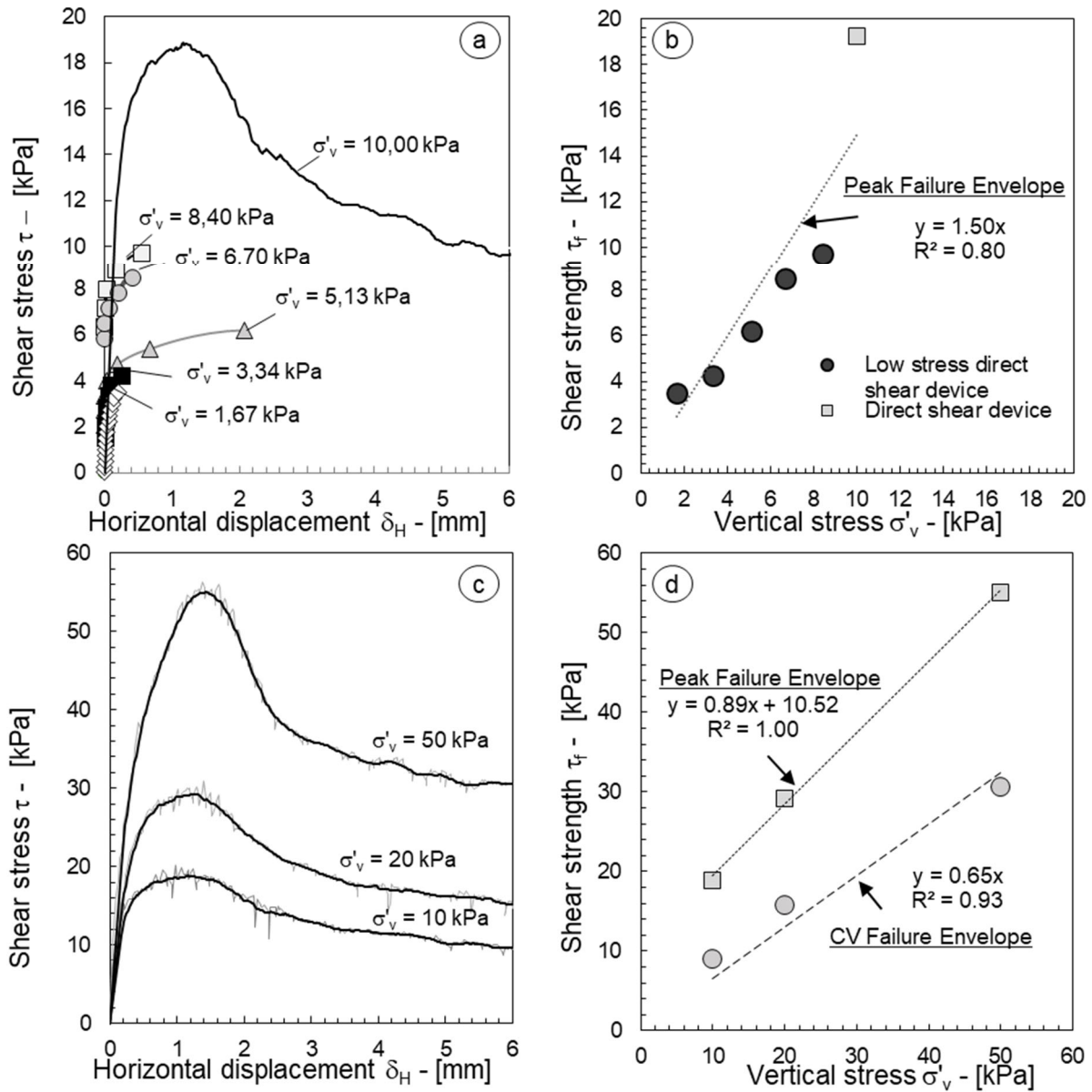


Figure 4.5 a) Results of the direct shear tests performed in the range of vertical stress expected in the physical model; b) Peak failure envelope at low effective stress; c) Results of the direct shear tests performed in the range 10-50 kPa; d) Failure envelopes in the range 10-50 kPa.

The envelope of the all performed tests and the evolution of the peak and the constant volume shear strength angle within the chosen ranges of vertical effective stress are reported in Figure 4.7. The tests performed under control of force (0-10 kPa) allow computing the peak shear strength angle ϕ'_p that resulted in being 56° . It was impossible to characterize the post-peak behaviour in that range of effective vertical stress. However, the shear strength angle at constant volume (ϕ'_{cv}) was determined in the higher ranges of vertical effective stress, and it resulted in being equal to 32° . These results are in good agreement with data reported by Valore et al. 2017 for a similar material tested in similar conditions.

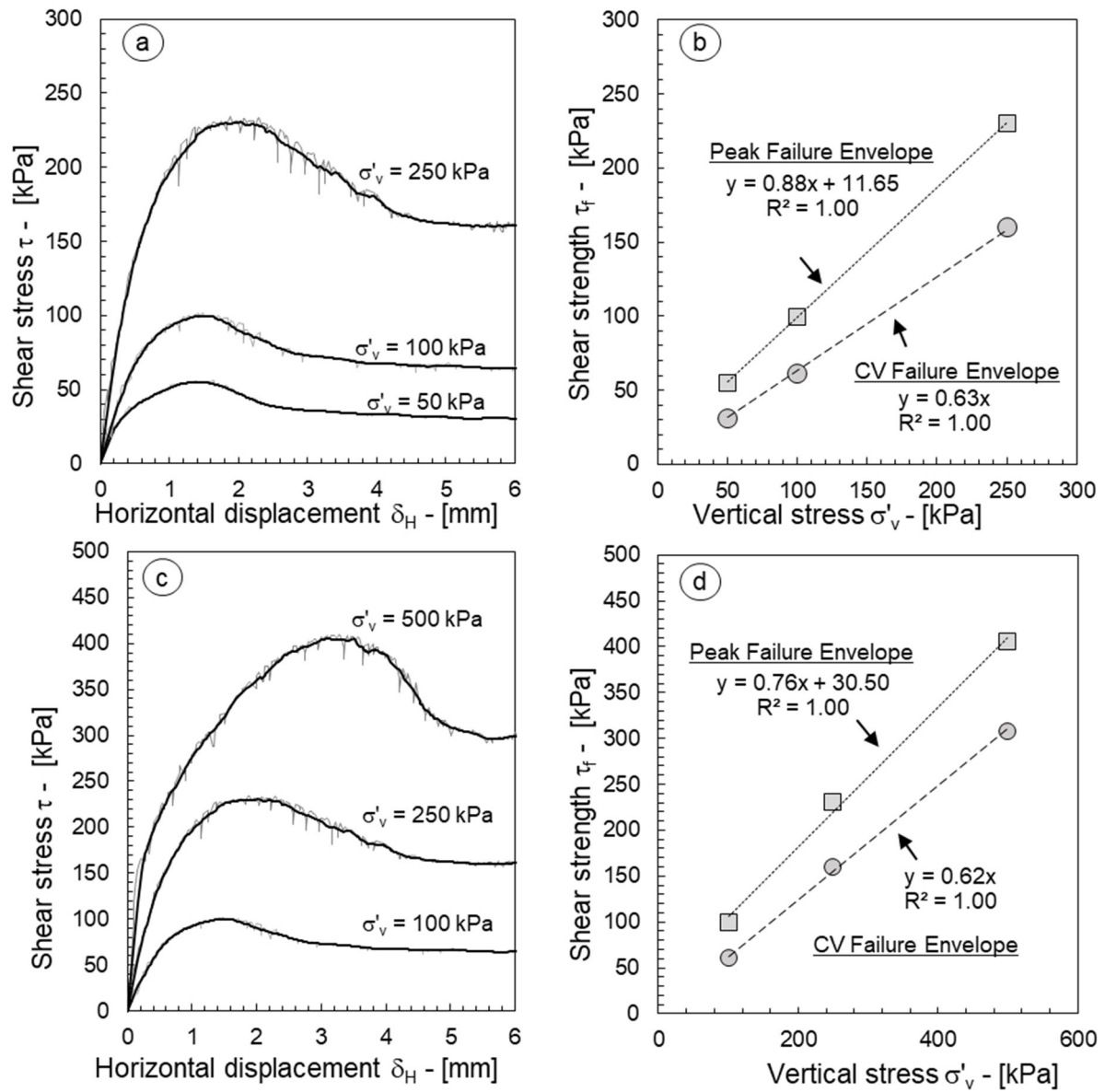


Figure 4.6 a) Results of the direct shear tests performed in the range 50-250 kPa; b) Peak failure envelope in the range 50-250 kPa; c) Results of the direct shear tests performed in the range 100-250 kPa; d) Failure envelopes in the range 100-500 kPa.

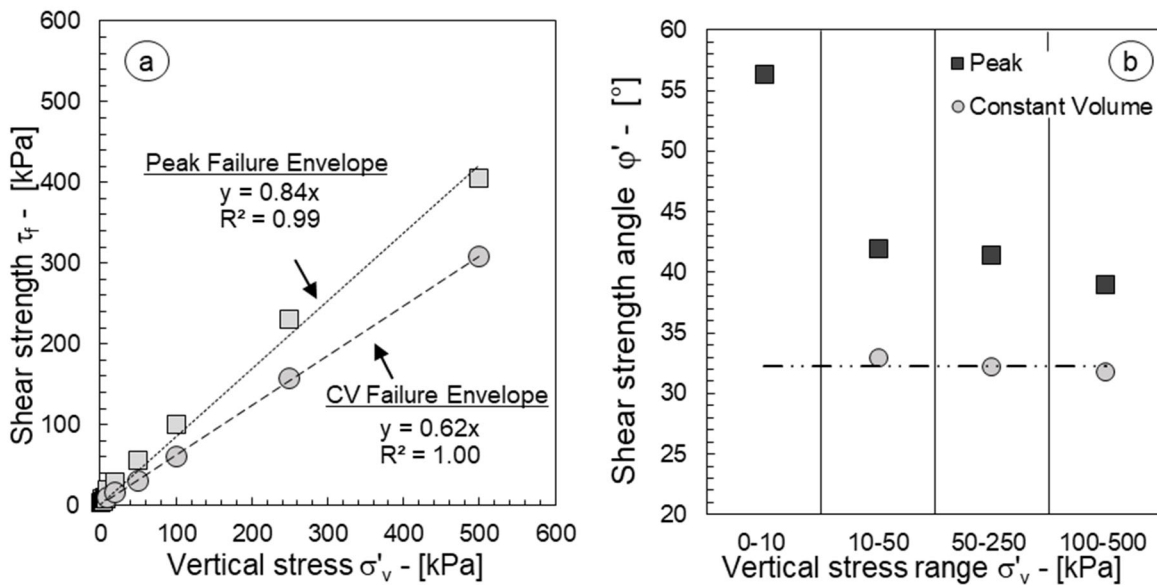


Figure 4.7 a) Peak and constant volume failure envelope of the all performed tests; b) evolution of the peak and the CV shear strength angle within selected ranges of vertical effective stress.

4.2.3 Water retention behaviour

To characterize the water retention behaviour of a geomaterial, the constitutive relation between suction and the degree of saturation (or volumetric water content) has to be established. Reliable measures of the imposed suction can be recorded with various devices depending on some specifics of the investigated soils. When working with sandy soils, very small suction changes induce significant changes in terms of water content. The hanging water column method (Haines, 1930) represents a convenient method to characterize the water retention behaviour of the geomaterial. The first step of this method consists in the establishment of the hydraulic continuity between the sample/s and a burette through a hydraulic connection. The burette is placed at its initial position in the way that the water level coincides with the height of the samples. By lowering the position of the burette, a hydraulic gradient will be generated, and the water will drain from the sample/s to the burette. The procedure relies on the application of suction by keeping the air pressure in the soil equal to the atmospheric pressure. Possible layouts allowing for the application of the method can be found in Haines, 1930 and Sharma and Mohamed, 2003.

In this case, the specimens were placed into a conveniently modified pressure plate apparatus. Figure 4.8 shows a schematic representation of the employed device. The samples

were placed on a ceramic disk preventively saturated (AEV equal to 0.5 MPa). The pressure inside the cell was kept equal to the atmospheric one, while the water outlet tube of the pressure plate ceramic was connected to a burette through a flexible tube. The burette was linked to a spillway that allows imposing a constant suction, and to collect the water flowed out from the soil samples. The soil samples were prepared in cylindrical rings (14 mm height and 36 mm diameter). At their bottom, a filter paper was glued. The sand was compacted in the ring up to achieve the target void ratio ($e_0 = 0.62$). All the specimens were saturated by capillary rise by leaving the sample partially submerged in water in a closed environment for two days. Afterward, the samples were placed into the pressure plate on the ceramic disk previously saturated, establishing the fluid continuity with the water in the rest of the system (i.e., the flexible tube and the burette).

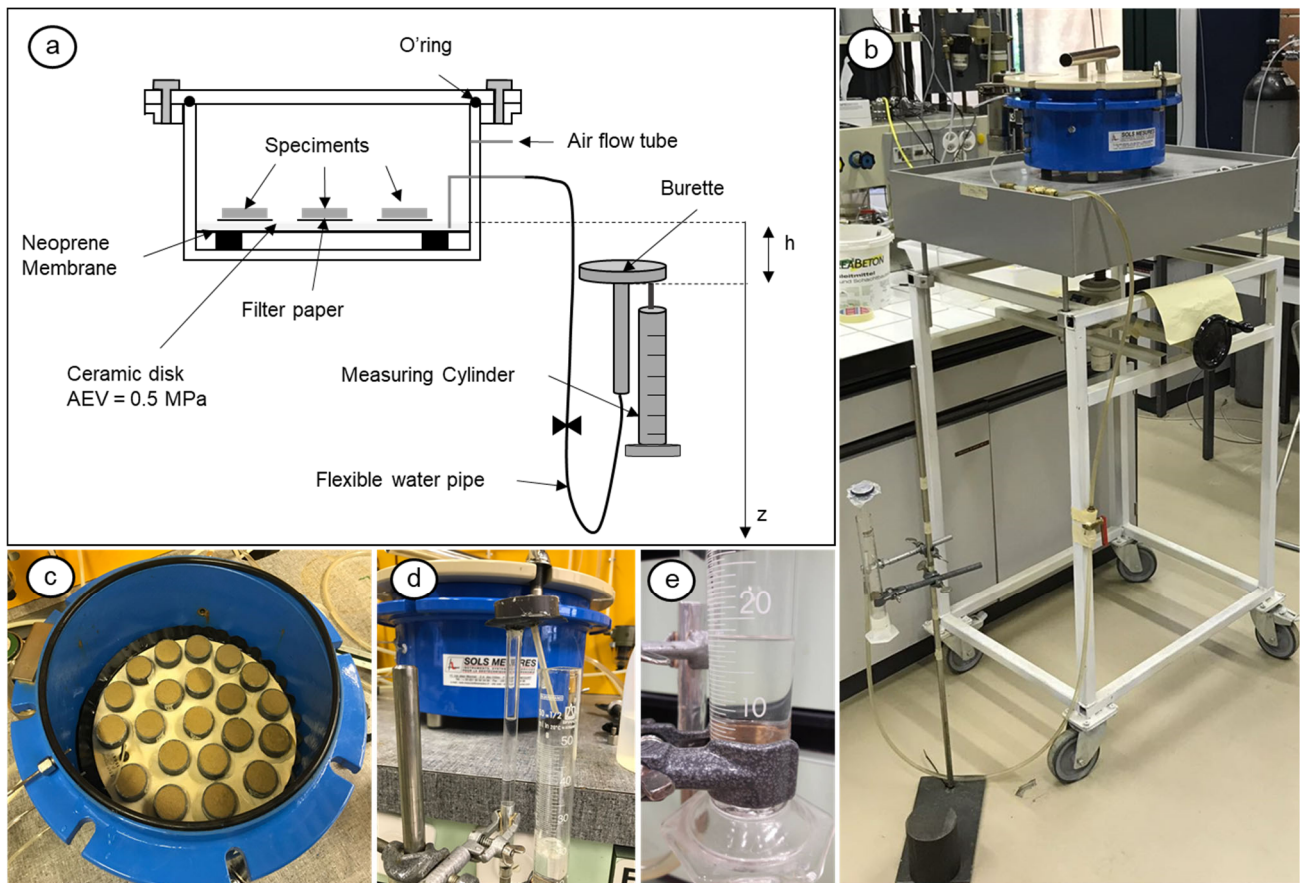


Figure 4.8 a) Schematic representation of the performed test; b) overall picture of the employed device; c) specimens on the ceramic disk; d) and e) zoom on the burette and the measuring cylinder.

Both the drying and the wetting path were investigated. The whole set of experiments was performed in 4 months.

Nine different suction heads were applied by lowering the burette: 5 cm, 10 cm, 20 cm, 30 cm, 40 cm, 50 cm, 60 cm, 70 cm, and 100 cm with respect to the reference level corresponding with the ceramic disk. For each step, equalization was considered to be reached when the water stopped to flow into the measuring cylinder. Afterward, three samples were removed from the pressure plate apparatus, divided into two parts and placed in the oven to measure the water content. In this way, it was possible to get six values of degree of saturation, the highest and the lowest values were excluded, and the average value of the others was taken as a data point of the main drying water retention curve. To compute the degree of saturation, the assumption of negligible volume change in the specimen during the test has to be taken.

Regarding the wetting, the samples were prepared, saturated, and then placed into the pressure plate. In this case, the burette was lowered from the position zero to 100 cm directly, and after the equalization, it was raised-up 80 cm, 60 cm, 40 cm, 20 cm, and 10 cm. For each step, water was added to the burette until the water level did not change in the burette. To avoid evaporation from the top of the burette, a plastic tube had been linked to the airflow tube of the pressure plate to the top of the burette.

Then, two samples were removed from the pressure plate apparatus, divided into two parts and placed in the oven to measure the water content. Four values of water content, and therefore, degree of saturation, were obtained; the average value was taken as a data point of the wetting path. The residual degree of saturation has been achieved by exposing the specimens to the environmental condition of the laboratory for two weeks allowing the drying of the material by evaporation. During this period, the temperature (on average $T = 21.5^{\circ}\text{C} \pm 2.5^{\circ}\text{C}$) and the relative humidity ($\text{RH} = 66\% \pm 5\%$) of the laboratory were recorded in order to achieve an indicative value of the suction at which the samples were exposed. This was possible by using Kelvin's equation (4.1). Knowing the molecular mass of the water ($\omega_v = 18.016 \text{ kg/kmol}$), the universal gas constant ($R = 8.314 \text{ J}\cdot\text{mol}^{-1}\cdot\text{K}^{-1}$) and specific volume of water at 21.5°C ($v_{w0} = 1.00212 \cdot 10^{-3} \text{ kg/m}^3$).

$$\psi_t = - \frac{RT}{\omega_v v_{w0}} \ln (\text{RH}) \quad (4.1)$$

Equalization time was longer in wetting than in drying because of time due to the manual water supplement that has to flow in the specimens: when the burette was raised up, after a certain amount of time, the water level decreased, reaching a new equilibrium lower respect to the required one. At that stage, more water had to be added until equalization was achieved.

The results of the tests are reported in Figure 4.9.

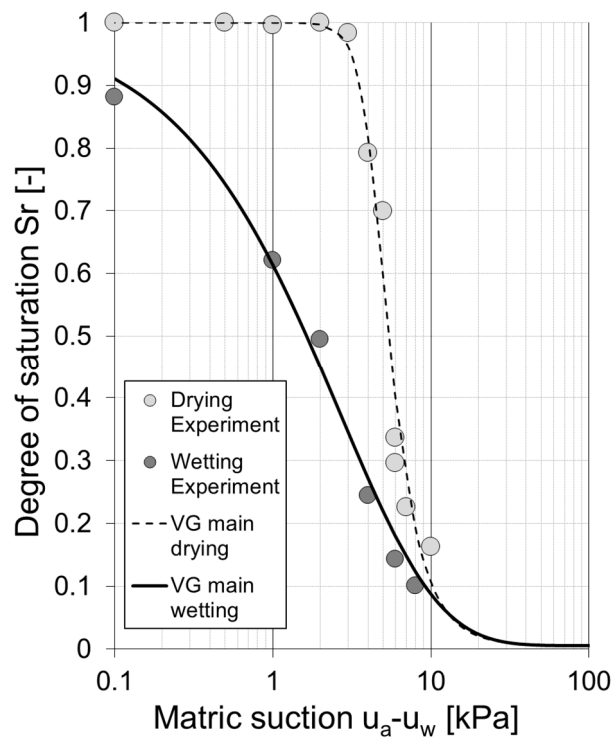


Figure 4.9 Water retention curve: experimental and modelling results.

The air entry values can be estimated to be between 2 and 3 kPa. The residual degree of saturation ($S_{r,res}$), as expected for a sandy soil, is resulted in approaching the zero. The behaviour is strongly hysteretic, the slope of the drying path is significantly high if compared with that of the wetting path. Moreover, the latter does not reach the full saturation condition. This peculiarity has already been studied in the literature and it is due to the air that remains stuck in the pores of the soils during the wetting (e.g. Milatz et al. 2018). The obtained experimental data were fitted with van Genuchten model (equation 2.5) for both wetting and drying paths by using a statistical method (least-squares method).

Table 4.2. Calibration parameters of van Genuchten model.

Path	$S_{r,res}$	α	n	m
[-]	[-]	[1/kPa]	[-]	[-]
Drying	0.005	0.23	6.23	0.44
Wetting	0.005	0.004	0.72	27.77

4.3 The employed High Capacity Tensiometers

The control and the measurement of suction represent two fundamental aspects of experimental unsaturated soil mechanics. Several techniques can be used to control or measure suction, and the choice of the most suitable device depends on the purpose of the experimental campaign. The goal of the test will consequently affect the choice of the suction range of investigation, the duration of the tests, and the type of suction that has to be monitored (e.g., total suction or matric suction). Romero (2001) classified the suction control method in: i) vapor transfer (control of relative humidity or total suction with volatile or not volatile solutes; ii) predominant liquid phase transfer (control of matric suction with osmotic technique or axis translation technique). In addition, Murray and Sivakumar (2010) have classified the suction measurement instruments as reported in Table 4.3 .

For this research activity, it was necessary to rely on an instrument capable of covering the widest range of measurable matric suction and, meanwhile, to have a handy device, fast in reaching the equilibration and characterized by a short reacting time for continuous suction measurement. All these features can be recognized for the tensiometers. Tensiometers have been deeply used in soil science, but usually tensiometers can reach suction values of 100 kPa.

During the last decades, several research efforts have been developed in building tensiometers capable of overcoming this limitation. Ridley and Burland (1993) first developed High Capacity Tensiometers (HCT) capable of measuring matric suction values up to 1500 kPa. Afterward, several instruments have been designed, manufactured and successfully used

for laboratory (Guan and Fredlund, 1997, Take and Bolton, 2003, Sjoblom 2000, Tarantino and Mongiovi, 2003, Toker, 2002, Laurenço et al., 2006, Mendes, 2018). Mendes (2018) presented a new model of Ultra High Capacity Tensiometers (UHCT) capable of reaching suction values of about 7000 kPa. The UHCTs are in the development phase.

Table 4.3. Suction measurement instruments Murray and Sivakumar (2010) modified.

Instrument	Suction component measured	Typical measurement range (kPa)	Equalibration time
Pressure plate	Matric	0 - 1500	Hours/day
Tensiometers and suction probes	Matric	0 - 7000	Minutes
Thermal conductivity sensors	Matric	1 - 1500	Hours/days
Electrical conductivity sensors	Matric	50 - 1500	Hours/weeks
Filter paper contact	Matric	0 - >10000	2-57 days
Thermocouple pycrometers	Total	100 - 8000	Minutes/hours
Transistor psychrometers	Total	100 - 70000	About 1 hour
Chilled mirror psychrometer	Total	1 - 60000	Minutes
Filter paper non contact	Total	1000 - >10000	2-14 days

In this research activity, thanks to the secondment period finalized to the transfer of knowledge in the framework of the European project TERRE, a set of HCTs have been manufactured under the supervision of Professor Alessandro Tarantino. In particular, the tensiometers that have been manufactured are the Trento (TN) HCT. Their schematic representation is reported in Figure 4.10. The tensiometers are characterized by their body and their cap in stainless still AISI 316. It has a cylindrical shape. At the bottom of the device, a porous ceramic with AEV equal to 1.5 MPa is placed. In order to have a symmetric response in terms of mechanical behaviour, the diaphragm is placed in the middle of the sensor at 0.1 mm away from the porous ceramic. The diaphragm is machined to 0.4 mm thickness from

a solid stainless steel solid cylinder, where a strain gauge is glued. The gap between the ceramic filter and the diaphragm forms the water reservoir.

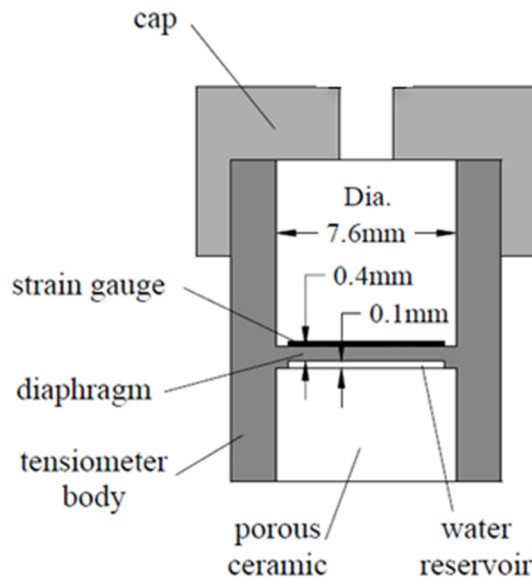


Figure 4.10 Schematic layout of the Trento tensiometer (modified after Tarantino and Mongiovi, 2002).

Tensiometric technique relies on a working principle that corresponds to the measurement of a pressure differential across a high air entry porous ceramic. This peculiarity is shared with the well-known axis translation technique (Marinho et al., 2008). The tensiometer must be saturated, or, in other words, the reservoir and the porous of the ceramic must be filled with deaerated water. Once the instrument is saturated, it can be placed in contact with the soil. If the soil is in unsaturated conditions, a hydraulic gradient will generate between the soil and the reservoir of the tensiometer; as a consequence, water will be removed from the reservoir inducing a deflection of the diaphragm. The strain gauge placed on the diaphragm will measure the deformation of the stainless-steel diaphragm. The acquisition data system will record the variation of voltage output from the strain gauge configured in Wheatstone bridge circuit.

4.3.1 Manufacturing

First, the bodies of the tensiometers were manufactured; then the diaphragm was subjected to an intensive polishing process (Figure 4.11a and Figure 4.11b). Meanwhile, the saturation chamber was assembled too. The latter is the device that hosts the tensiometers that must be kept saturated during their non-operativity. The saturation chamber (Figure 4.11c)

is also the place where the tensiometers are calibrated. It is characterized by six interconnected tensiometers' cylindrical containers, two in-out flow valves, a manual hydraulic piston and a manometer. All the pieces are connected at the base through a hydraulic joint. Its two sides have been tightened with special O-rings. The saturation chamber was assembled while it was submerged in deaerated water afterward, and pressure-tightness was checked by imposing a pressure of 40 bar with the manual piston. The chamber needed some additional reloading and flashing prior to keep the applied pressure.

The bodies of the tensiometers were placed in a high-temperature oven to be subjected to a stress-relieving process. The latter is a heat treatment process in which a metal is subjected to a constant temperature (below its critical temperature) followed by controlled cooling. The advantages of stress-relief include: i) the relieving of internal stresses, ii) the returning of the material to a strength level approximately equivalent to where it was prior to forming; iii) the increase of the mechanical strength of the material. The bodies of the tensiometers were heated up to 350°C in 30 minutes; then, this temperature was kept constant for 3 hours. Subsequently, the instrumentation remained in the oven to cool down to the environmental temperature (1 day). The pieces have changed their color after the process (Figure 4.11f).

The tensiometer body were placed in the tensiometer holders of the saturation chamber, and a pressure of 40 bar was applied directly to the diaphragms. This pressure was applied initially with cycle of 1 day, then it was kept constant for seven days. This procedure helps to yield the diaphragm and ensure that the diaphragm then defects in the elastic range. Meanwhile, the porous ceramic was reduced in size up to achieve a diameter 0.1 mm smaller than the inner diameter of the tensiometer body and few millimeters longer than the tensiometer's length (Figure 4.11d,e). At this stage, the ceramic was glued to the tensiometer's body by using an epoxy glue then the residual part of the ceramic was smoothed.

A circular pattern strain gauge was glued on the upper face of the diaphragm, and electrical connections have been welded to create a Wheatstone bridge. The cables passing through the cap were protected by special sealing making the circuit water-proof. The electrical connections of the cables were designed in a way that extension cables can be added for em-

ploying in physical modeling or in-situ tests. The cables were connected to a data acquisition system characterized by one portable chassis hosting one module of four LAN outputs. In this way, it is possible to record simultaneously the output voltage from four tensiometers. Figure 4.11g shows the tensiometer at its final configuration.

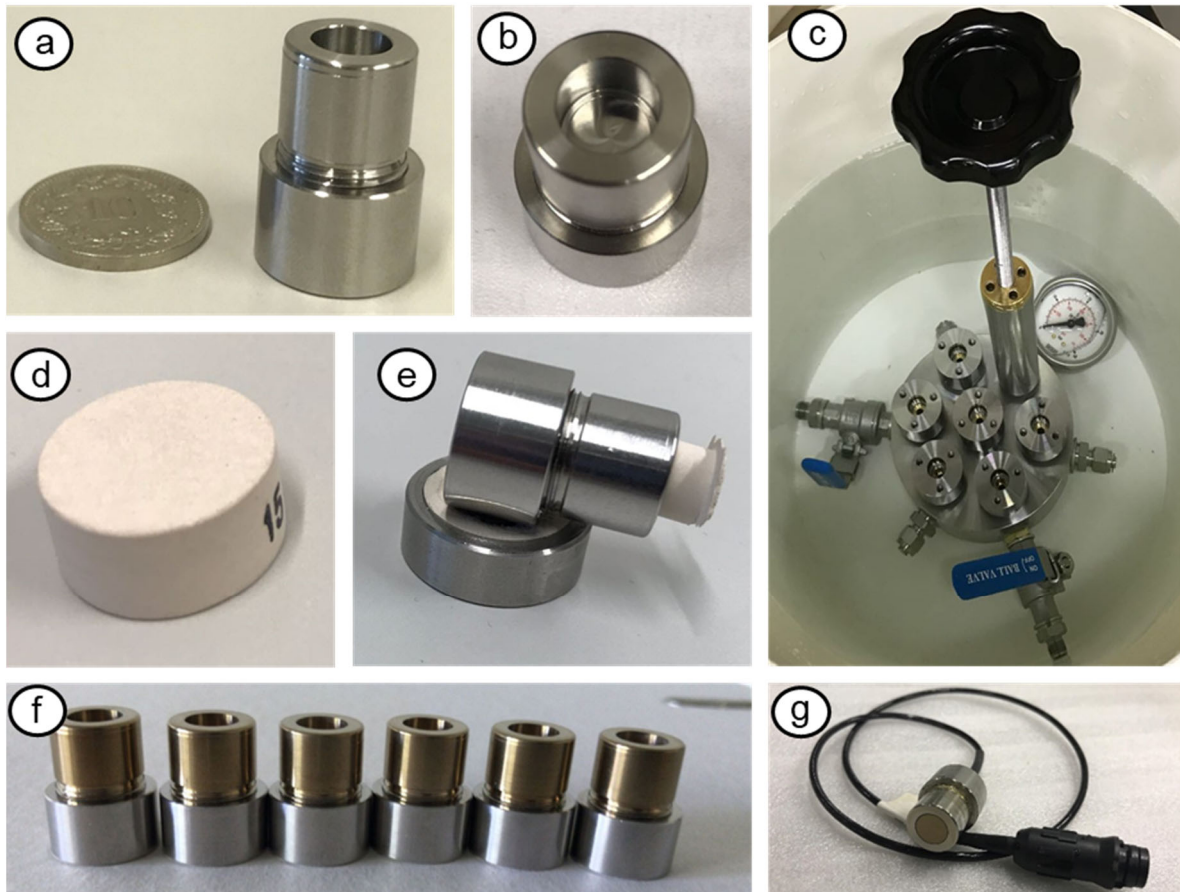


Figure 4.11. a) Tensiometer's body ; b) detail of the diaphragm; c) saturation chamber; d) porous ceramic AEV = 1.5 MPa; e) Size-reduction of the porous ceramic; f) Tensiometers' body after stress relieving heat treatment; g) Manufactured tensiometer.

4.3.2 Saturation and cavitation of the tensiometers

Although the design of HCT is an important consideration, design alone cannot ensure the measurement of tensile water pressures. Indeed, it can be argued that one of the most important factors determining the success or failure of tensiometer measurements relates to the saturation of the device (Marinho et al., 2008). The first saturation of the porous ceramic is considered to be a critical step in the experimental procedure (Ridley and Burland, 1999). In this regard, a special piece has been manufactured. It is a cylindrical piece characterized

by three interconnected in/outflows: in two of them, a valve was plugged in (valve A and B); while at the third, at the top of the saturation chamber, one of the tensiometer's containers was connected (Figure 4.12). Valve A was connected to a vacuum pump and valve B to a pressure/volume controller (P/V controller). Initially, the dry tensiometer was placed in its container, valve B was closed, and attention was paid in removing the air from the pipe between the controller and the valve. Valve A was open, and the vacuum was applied. Figure 4.13 shows the evolution of the voltage (at the first saturation, the tensiometer is not calibrated yet) with the time during the first saturation procedure and following cycles of loading and unloading. At its initial configuration (dry porous ceramic) the tensiometer was recording a voltage of $-1.075 \mu\text{V}$.

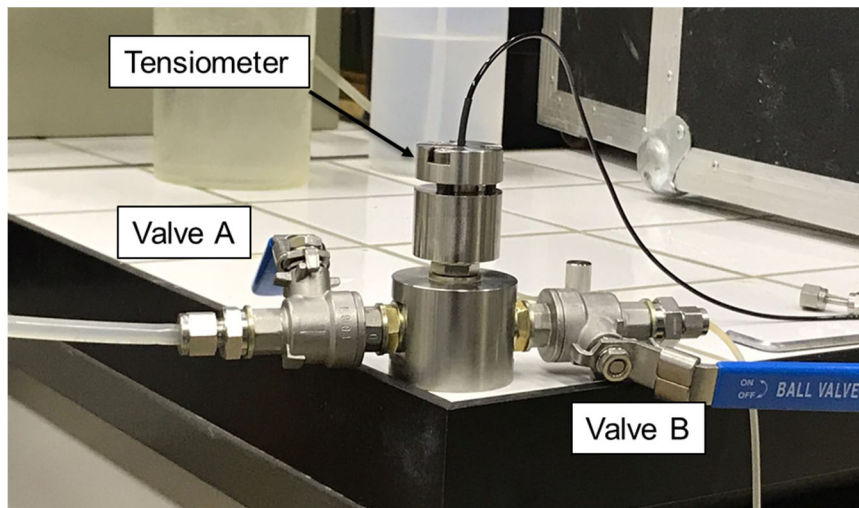


Figure 4.12. The device employed for the first saturation of the tensiometers.

When the vacuum was created (-100 kPa), the voltage increased rapidly to $-1.055 \mu\text{V}$, and it was constant along the whole period of functioning of the vacuum pump. After 15 minutes the valve A was closed, the vacuum pump switched off; meanwhile, the pressure in the pipe was increased to the maximum possible by the P/V controller (2000 kPa), then valve B was open. Water started to flow before into the device; then, it rose through the porous ceramic filling the reservoir of the tensiometer. The voltage started to reduce, taking almost 5 minutes to generate the breakthrough at which the voltage reduced to $-1.425 \mu\text{V}$. The pressure was maintained constant for almost 20 minutes, and the voltage remained constant as well. This was considered as an indication of the good stability of the instrument. After 40 minutes from the beginning of the test, the applied pressure was cyclically reduced to 0 and increased to 2000 kPa . The reaction of the tensiometers was immediate, and the reached

voltage values at the minimum and the maximum applied pressure were equal during the cycling showing evidence of elastic behaviour of the diaphragm.

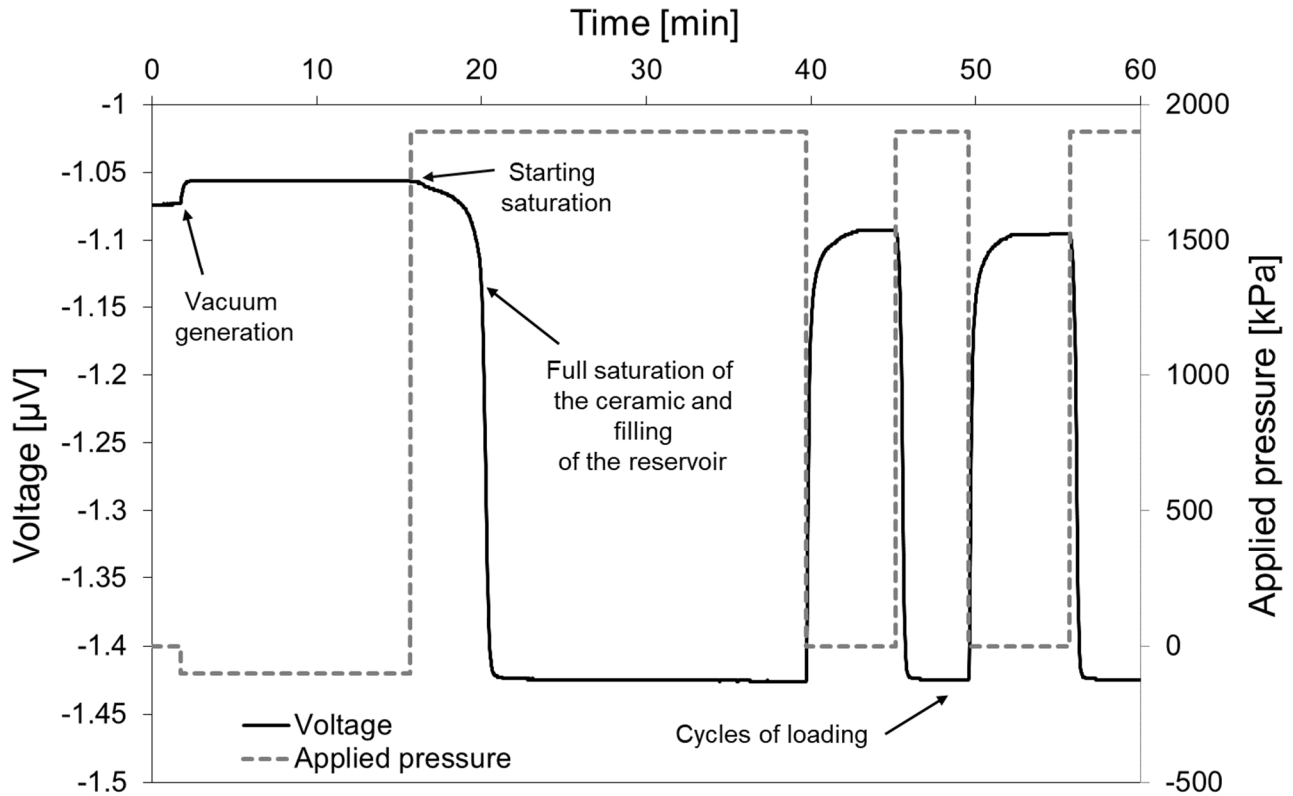


Figure 4.13. Voltage evolution recorded by the data acquisition system during the first saturation of a tensiometer.

Once the tensiometers were saturated, cavitation of the sensor was induced in order to check the maximum values of negative pore water pressure that can be recorded. Tarantino (2004) explained the assumed mechanism controlling the cavitation: “*cavitation originates from undissolved gas nuclei existing in the interstices in the container's wall rather than from free cavities in the liquid (Harvey et al., 1944). A free spherical gas nucleus is usually unstable and tends to either expand indefinitely or go into a solution (Mongiovi and Tarantino 2002). On the contrary, a gas nucleus in a cavity in the container wall may remain undissolved even under a high-water pressure. In fact, the air-water interface, concave on the water side, can sustain the high-water pressure, thus preventing air dissolution. When pressure is decreased to negative values, these nuclei can expand and eventually trigger cavitation. This process is controlled by gas diffusion across the gas-liquid boundaries and creeping of the gas-liquid-solid junction determined by the advancing and receding of contact angles*”. To induce the cavitation, the tensiometer was exposed to atmospheric conditions letting dry the porous

ceramic (figure 4.14). At $t = 0$ the tensiometer was in free water recording 0 kPa; after around 30 seconds, the tensiometer was put in contact with the atmosphere, and the negative pore-water pressure drops down to -1100 kPa after almost 1 minute. The pressure raised up to -100 kPa as expected.

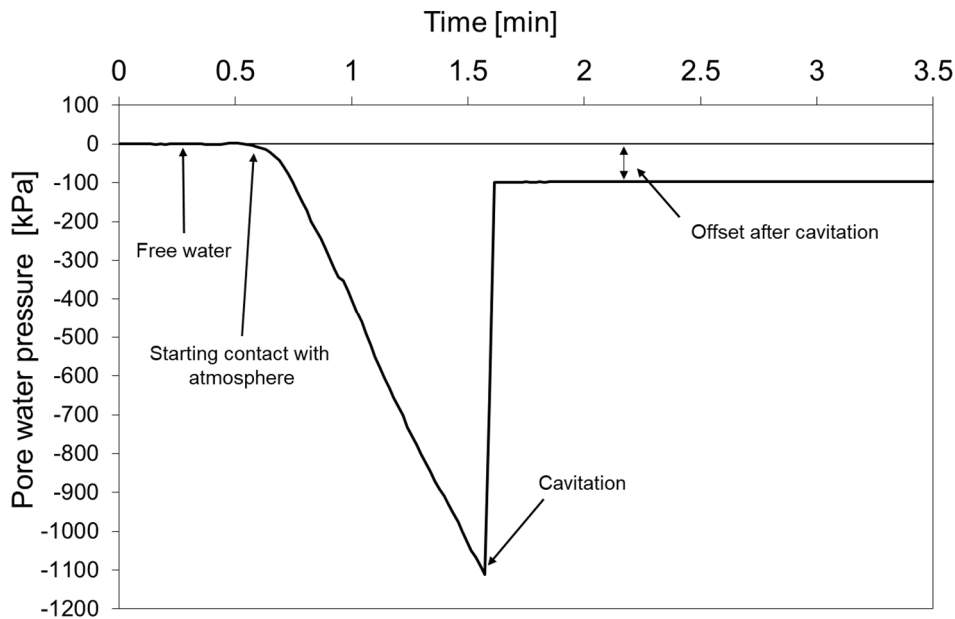


Figure 4.14. Voltage evolution recorded by the data acquisition system during cavitation.

The check of the cavitation, as the first saturation of the tensiometers, was satisfactory, and the behaviour of the devices agreed with that of other HCTs described in the literature (e.g. Lourenço et al. 2008.).

4.3.3 Calibration and preconditioning prior suction measurements

The calibration of the tensiometers has been done in the saturation chamber. It consists in applying a positive water pressure to the tensiometer that will induce a deformation of the diaphragm; the acquisition data system will record a variation of voltage that can be related to the applied pressure identifying the calibration curve. The instruments have been calibrated in the range 0 – 2000 kPa (Figure 4.15a and b) and 0 – 100 kPa (Figure 4.15c and d). The applied pressure has been progressively increased and decreased in order to investigate possible hysteretic behaviour. The calibration curves are linear and consequently are identified by a linear equation, which intercept is called “offset” and the angular coefficient “sensitivity.” In the range 0 – 2000 kPa, the check of the calibration shows errors of 5 kPa

and 9 kPa respectively at the beginning and the end of the calibrated range. The curve reported in Figure 4.15b has a typical shape well known in experimental geomechanics when calibrating devices characterized by a linear calibration curve.

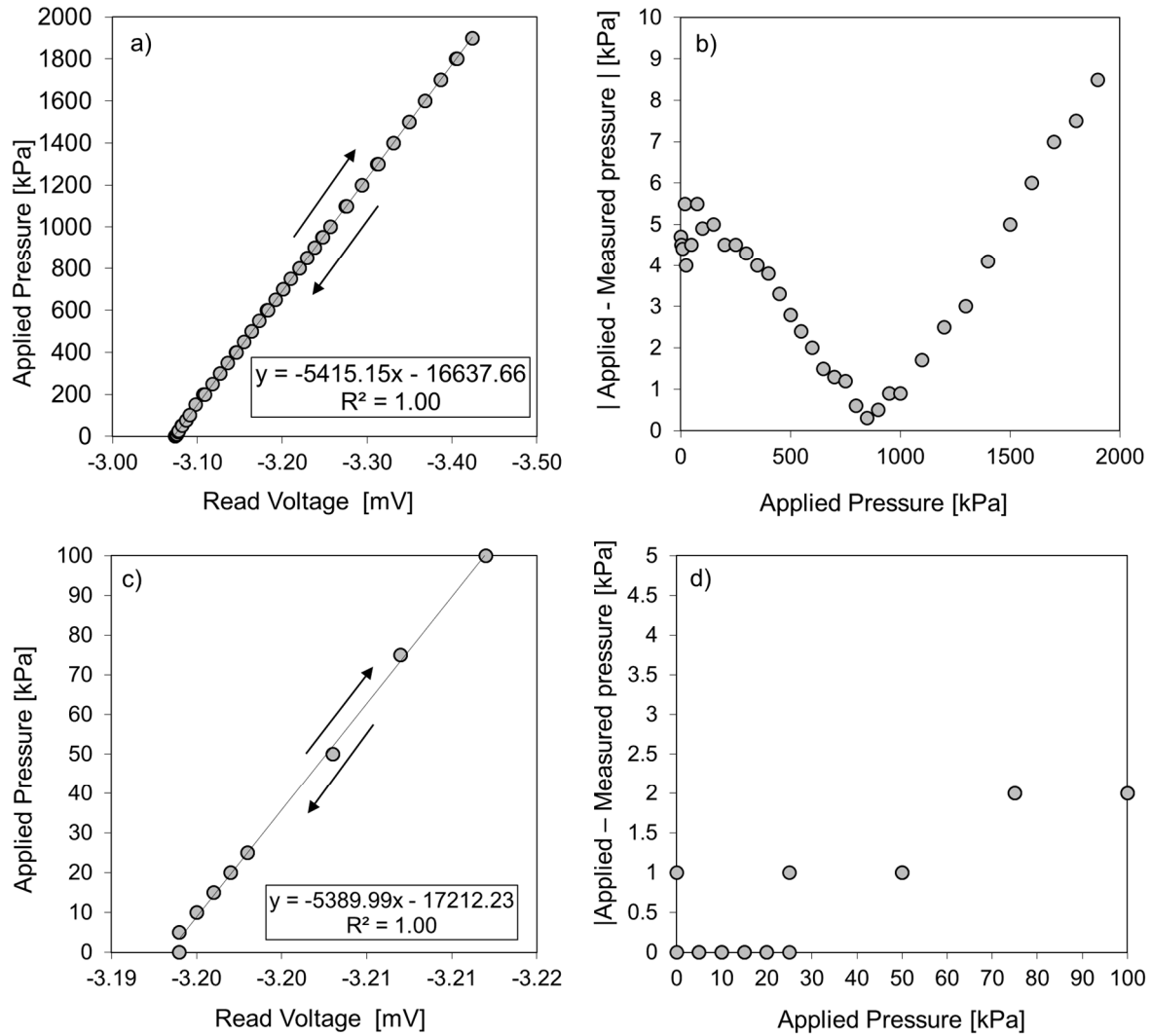


Figure 4.15. a) Calibration curve in the range 0 – 2000 kPa; b) check of the calibration in range 0 – 2000 kPa; c) calibration curve in the range 0 – 100 kPa; d) check of the calibration in range 0 – 100 kPa.

If low values of suction are expected, by calibrating the tensiometers in the range 0 – 100 kPa, the error reduces significantly.

Prior to start with the measurements, a special procedure should be followed: the preconditioning. Marinho et al., (2008) considers that the preconditioning of the water contained within the porous filter and the reservoir before employing the tensiometers plays a crucial role in the acquisition of reliable suction measurements. The preconditioning technique used for these tensiometer has been chosen thanks to the “transfer of knowledge” program

in the framework of the European project TERRE between the University of Strathclyde and the Swiss Federal Institute of Technology in Lausanne. Before starting with suction measurements, two steps of preconditioning are employed: first “unloading by steps” afterward “drying cycles.” Let’s assume that initially, the calibrated tensiometers are in the “at rest” condition (i.e., the tensiometers must be kept saturated during their inoperative period in the saturation chamber under the pressure of 4 MPa), first the pressure is reduced by steps, and pressure measurements are recorded to check the calibration. Each step consists of a reduction of 1 MPa. Afterward, the HCT is removed from its support and is put in contact with the atmosphere letting it dry. At this stage, attention must be paid in avoiding cavitation of the instrument. The procedure is repeated until the recorded value of pressure is constant. The latter can be assumed as the initial offset of negative pore water pressure measurements and has to be compared with the final offset achieved after the measurements and the induced cavitation for data interpretation. Table 4.4 summarizes the procedure during both the phases of the preconditioning.

Table 4.4. *Unloading by steps (on the left) drying cycles (on the right) example for a HCT.*

Applied Pressure [MPa]	Measured Pressure [kPa]	Time [min]	Condition of the HCT	Measured Pressure [kPa]	Time [min]
40	4007.25	0	Free water	3.65	32.25
30	3005.78	7.00	Free water	2.52	34.85
20	1999.32	13.44	Free water	-0.54	36.41
10	10001.52	18.71	Free water	-0.51	38.58
0	3.25	25.32	Free water	-0.52	40.12

At this stage, it is possible to argue that the manufacturing of HCTs was successful and they have to be tested in contact with soils. In the next section, the water retention behaviour of a silty soil is characterized. The test has a dual objective: control the behaviour of the manufactured HCT in contact with soil and characterize the water retention behaviour of a fine material simulating drying and wetting paths.

4.4 Sion Silt

The material tested in the laboratory is the Sion Silt characterized by 72% of silt, 20% of sand and 8% of clay, and it can be classified as a clayey sandy silt (CL/ML) in the Unified Soil Classification System (USCS).

The soil has been compacted in a conventional Proctor apparatus to produce several specimens characterized by the same void ratio. An initial sample was created with initial water content (w_0) of 21.1% and an initial void ratio (e_0) equal to 0.63 (average of the specimens). Afterward, the specimens were extruded from the sample and placed in 60 mm diameter (D) and 15 mm height (h) rings. The bottom of the rings was closed with a filter paper, and the top of the specimens was carefully smoothed. The specimens were covered with a plastic cover to prevent evaporation from the top, and they were placed in a box partially filled with water to saturate them via capillary rise. The experimental setup (Figure 4.16) is characterized by: an electronic balance (resolution of 0.01g), a series of HCTs, an HCTs' saturation chamber connected to a pressure-volume controller, a data acquisition system for the HCTs, a digital camera fixed on a still frame placed above the electronic scale. On the scale, a circular plastic container was glued to host one of the specimens to record the change in water mass during both drying and wetting paths.

A second similar container was employed to host a second specimen, to record the evolution of matric suction. In this regard, a hole at the bottom of the second container was created in order to allow the hydraulic contact between the ceramic of the HCT and the specimen. The surface contact between the HCT and the container was sealed with a mastic paste during the experiments in order to prevent water leaks or preferential evaporation channels. As introduced earlier in the text, HCTs should be capable of measuring matric suction theoretically up to the ceramic air entry value (1500 kPa), even if cavitation after the test has happened for a suction value higher than 2000 kPa. Moreover, to explore the water retention behaviour of the tested soil at higher suction values, a third specimen has been initially subjected to the same paths as the other two, and after, dew-point hygrometer (WP4C) was used to record higher suction values (total suction in this case). Two tests have been performed simulating both drying and wetting paths. The drying path was simulated, leaving the three specimens in contact with the laboratory atmosphere. This method, also

known as “continuous drying,” has been investigated by Gallipoli et al., 2007 and Lourenço et al., 2011. An overestimation of suction values is possible especially if the tensiometer is placed at the evaporation surface. This is because while the evaporation happens, the whole specimen has not time to get the equilibrium. For this reason, it has been decided to place the tensiometer at the bottom of the specimen.

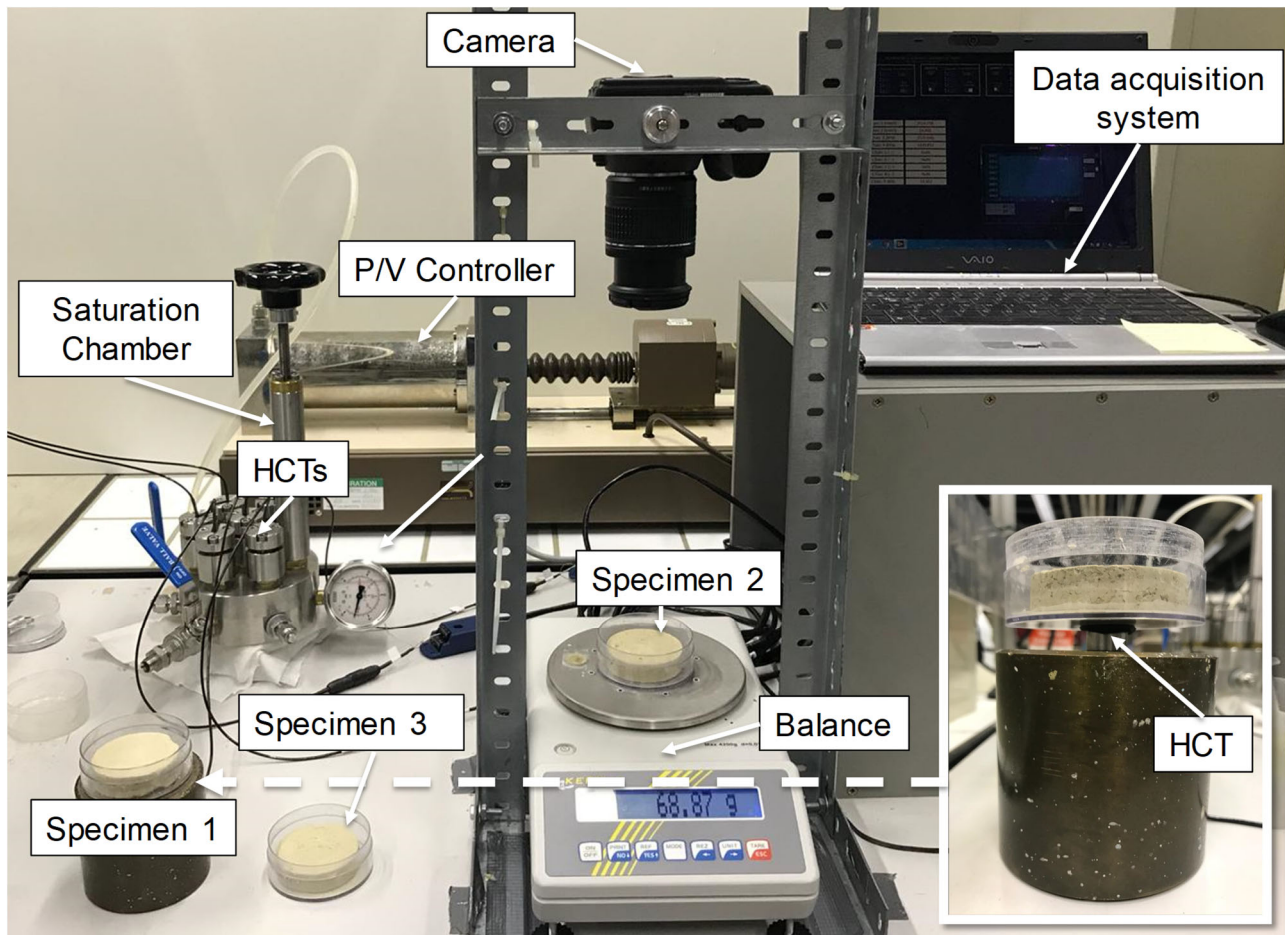


Figure 4.16. View of the experiment setup.

A different method, known as “drying by step,” can be applied, preventing continuous evaporation and allowing the specimen to get the equilibrium (Lourenço et al., 2011). As it will be discussed after in the thesis, the soil water retention model needed for the modeling of the seepage is related to the wetting path; for this reason, it has been decided to adopt a continuous drying method and wetting by step method for the present experiment.

A first test (test 1) has been performed by drying two specimens up to almost 1000 kPa. The matric suction was recorded in one specimen, while the changes in water content were measured in the other. At different time steps, pictures were taken in order to monitor

changes in volume. Figure 4.17 shows the evolution of the matric suction with time during the drying path. Shrinkage of the specimen could be observed with the naked eye. At 1000 kPa, the wetting path was started, and the whole amount of the evaporated water was added in ten steps in both the specimens with a syringe. As mentioned before, during each step, evaporation was prevented, covering the specimens allowing for equalization. Figure 4.18 shows the evolution of the matric suction during the wetting path.

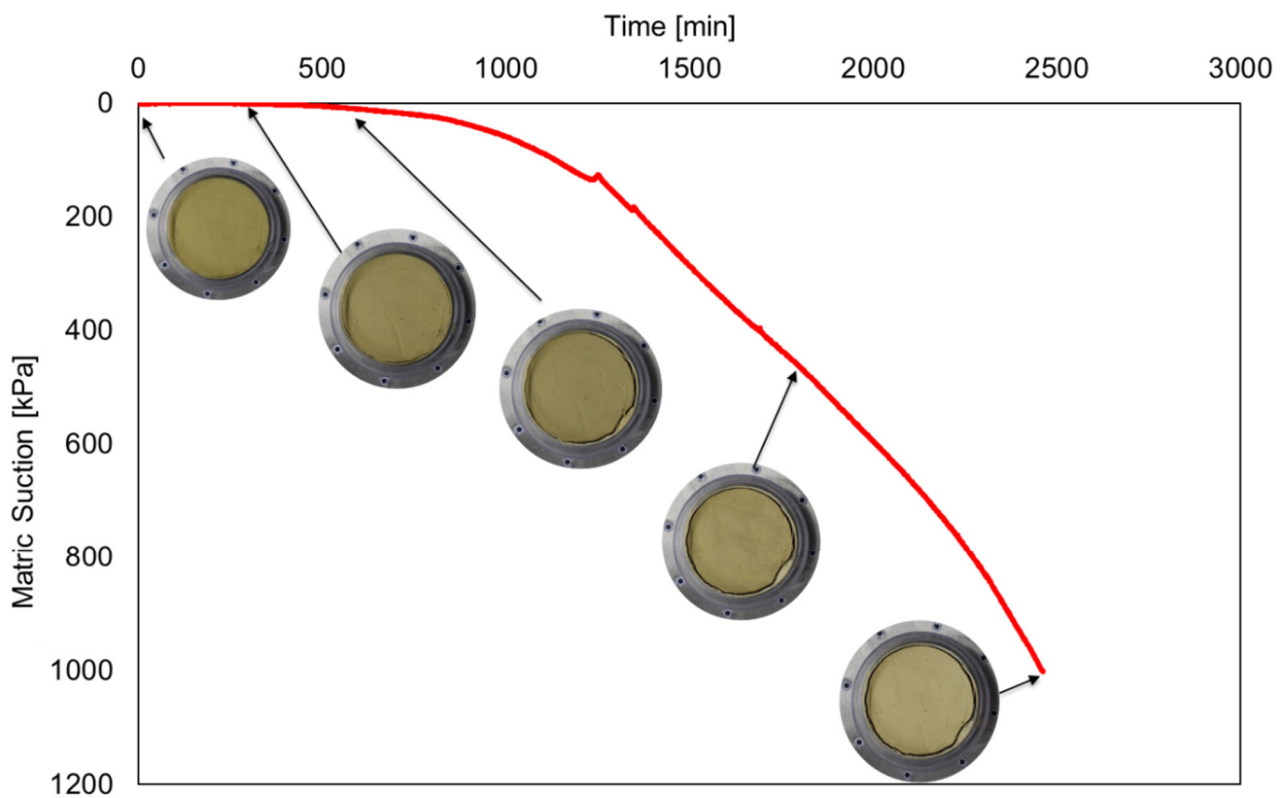


Figure 4.17. Matric suction evolution with time, drying test 1.

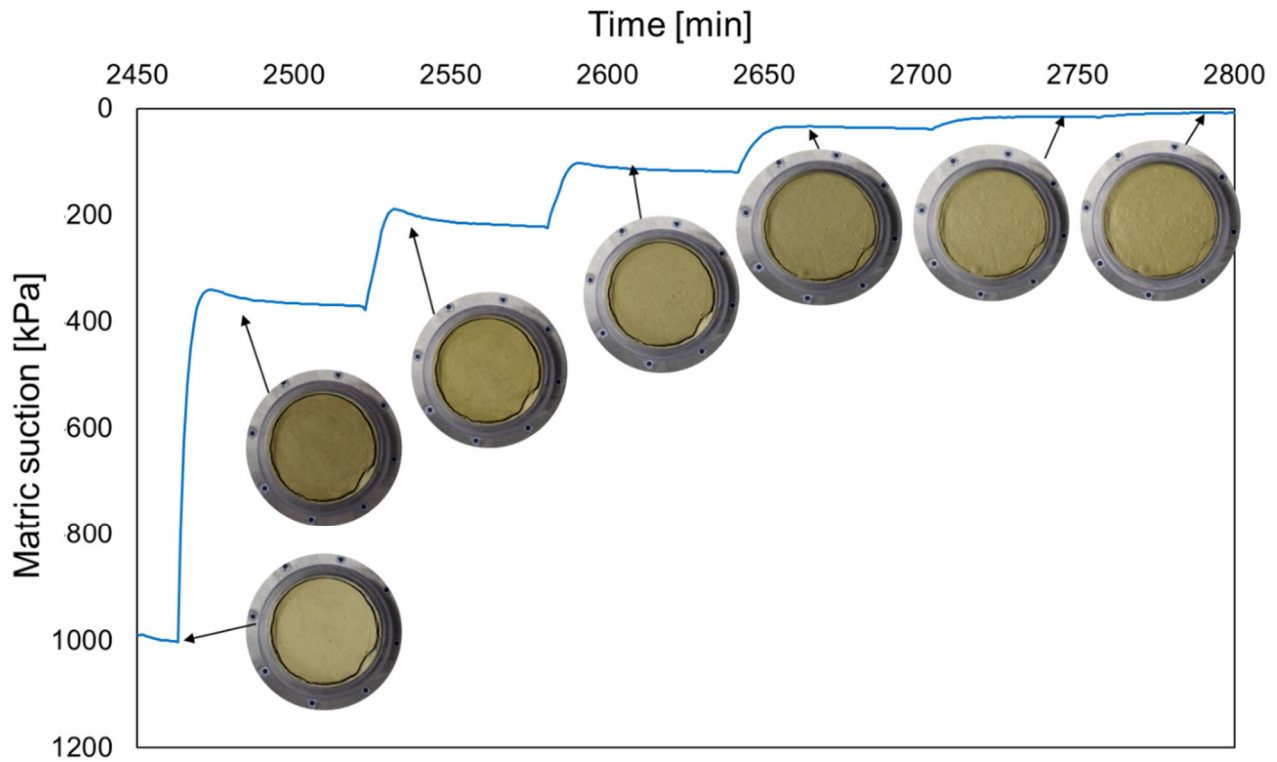


Figure 4.18. Matric suction evolution with time, wetting test 1.

The test was repeated (test 2) involving three specimens. Matric suction was recorded up to the cavitation of the tensiometer, while the specimens have been exposed to the laboratory atmosphere for a few days in order to get them close to the residual water content. A part of the third specimen was prepared to be placed in the WP4C. A similar approach can be found in (Ferrari et al., 2014). The wetting path was started again, but values of matric suction could be recorded only once they were inside the operative range of the HCTs. During the wetting path, volume changes could be easily noticed too. In this regard, deformation records are needed to follow the evolution of the degree of saturation. The pictures from the top were analyzed via a photogrammetric technique, and the changes in the average diameter were measured. The resolution of this method has been estimated to be around 0.1 mm. Figure 4.19 shows some examples of the shrinkage and swelling of a specimen observed during the experiments. The assumption of isotropic behaviour is made in order to get the changes in volume. It is assumed that, for each step, the radial deformation is equal to the vertical. At the end of the tests, the specimens have been totally dried in the oven, and, considering that the shrinkage limit was already achieved during the performing of the

test, the diameter measured with the photogrammetric technique was double-checked with a caliber.

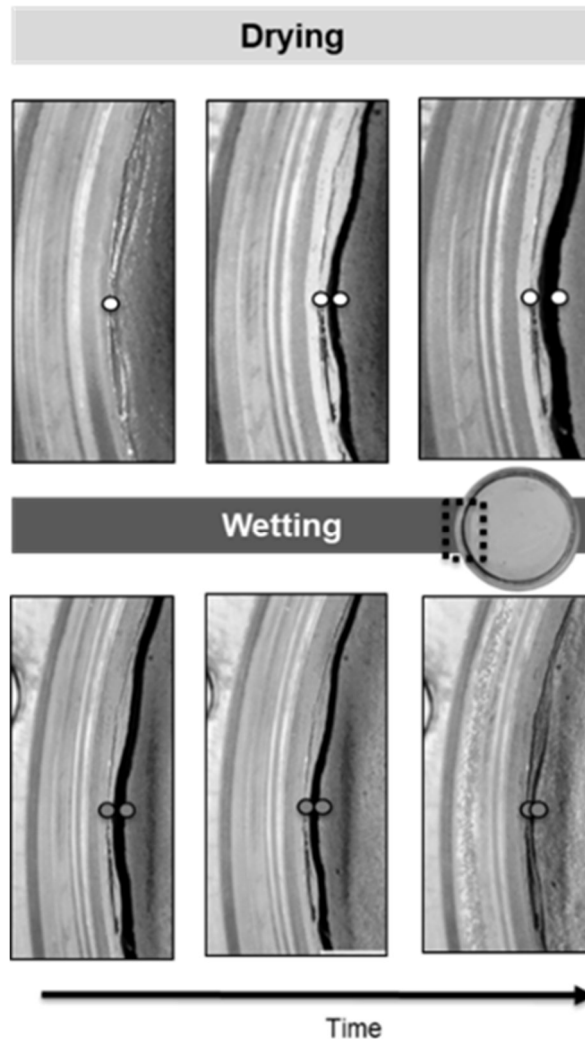


Figure 4.19. Shrinkage and swelling during drying and wetting paths, zoom on the specimen border.

In Figure 4.20a, the results of the tests are reported in terms of the degree of saturation and suction. They are plotted in terms of suction since data referring to HCTs corresponds to matric suction, while WP4C data correspond to total suction. Figure 4.20b) shows the shrinkage and the swelling curve for Test 1. It is possible to observe that the majority of the deformation happens before the air entry value, and the shrinkage limit is achieved after a few hundreds of kPa. For this reason, high suction values measured with the WP4C have been associated with the degree of saturation considering the volume of the specimens at the shrinkage limit. Moreover, the swelling curve has shown that the initial void ratio is not totally recovered during the wetting. The overlap with the two techniques suggests that

osmotic suction is marginal. The experimental results have been fitted via a Van Genuchten's model for both the main drying and the main wetting curves. The parameters of the fitting models for wetting and drying paths are summarized in Table 4.5

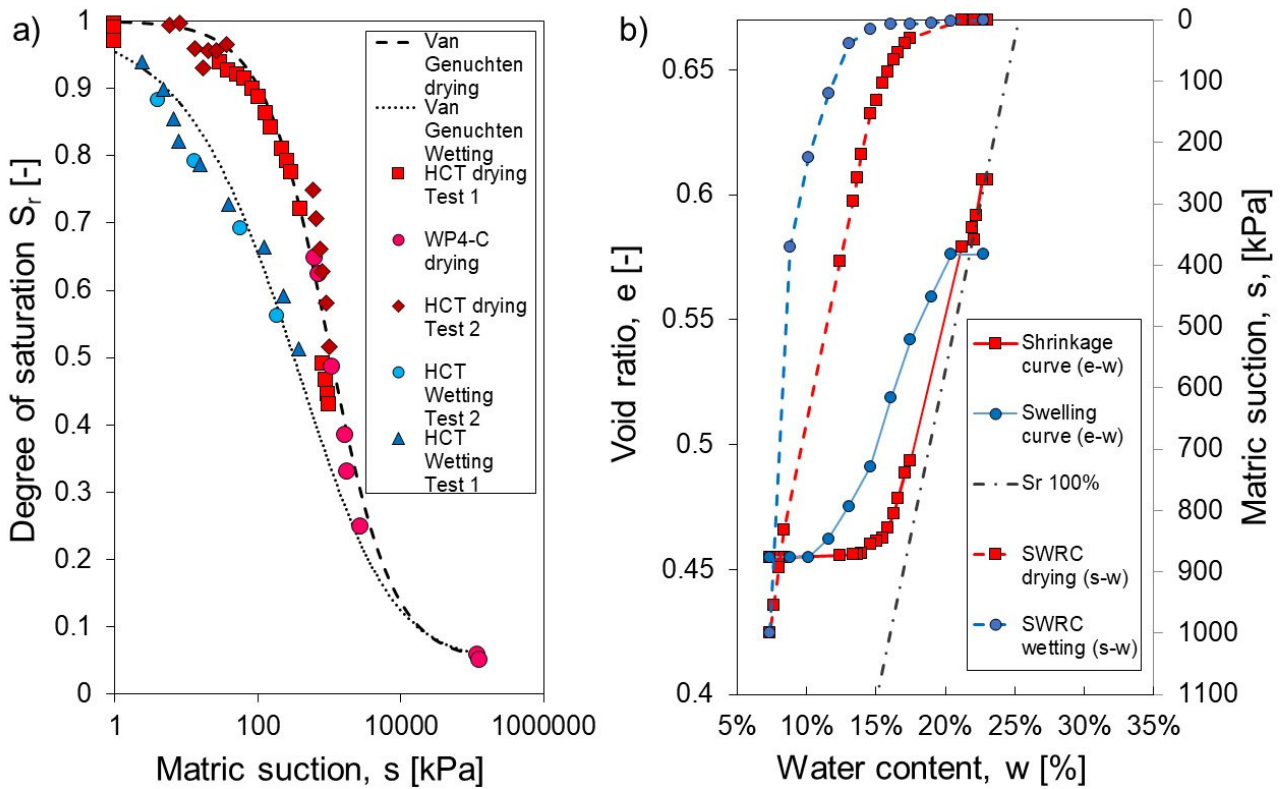


Figure 4.20. a) Water retention curves; b) evolution between void ratio and matric suction with water content

Table 4.5. Calibration parameters of Van Gehuchten's model.

Path	$S_{r,res}$	α	n	m
[-]	[-]	[1/kPa]	[-]	[-]
Drying	0.05	0.001	0.96	1.93
Wetting	0.05	$6.7 \cdot 10^{-4}$	0.50	1.98

4.5 Conclusions: implication of the assumed water retention model on the lateral earth pressure

According to Chapters 2 and 3, where analytical analyses were performed (both steady-state and transient conditions), the lateral earth actions of unsaturated soils are significantly influenced by environmental actions. The changing of matric suction in space and time results in changes in effective stress consequently. For this reason, the choice of a correct constitutive relation between the degree of saturation and suction represents a key step when hydro-mechanical analyses are performed. Assuming a single water retention curve, as required by the analytical analyses, can induce a non-correct computation of suction evolution and so of the effective stress. For example, the experimental analyses reported in this chapter have highlighted that both the analyzed soils (i.e., sand and silt) have specific peculiarities that characterize their water retention behavior that should be considered. In particular, a common feature is the hysteretic behavior of both the geomaterials that plays a crucial role in the implementation of the hydro-mechanical analyses for the computation of lateral earth actions. To emphasize the effects of the choice of the water retention model, a comparison between the available shear strength computed with the main drying curve and the main wetting curve follows for each investigated soil. In this regard, Figure 4.21 shows the evolution of the failure shear strength of the investigated soil with the suction. Three reasonable net stress values were chosen compatibly with the dimensions of a common retaining wall. It is immediately noticeable that the failure shear strength adopting the main drying Van Genuchten curve is always higher than that obtained with the main wetting curve. Consequently, lateral earth actions will result in higher values if the main wetting curve is chosen.

On the other hand, the wetting curve generates lower degrees of saturations than the drying curve (at the same suction), in turn generating lower hydraulic conductivity and, hence, lower infiltration rate. The wetting curve is therefore not conservative with respect to the estimation of the loss of suction due to rainfall.

For a scanning wetting path, the analysis will be placed in the middle of these two scenarios. This will be from one side closer to reality, but, on the other hand, the analyses cannot be

performed through an analytical closed-form formulation and should be performed numerically.

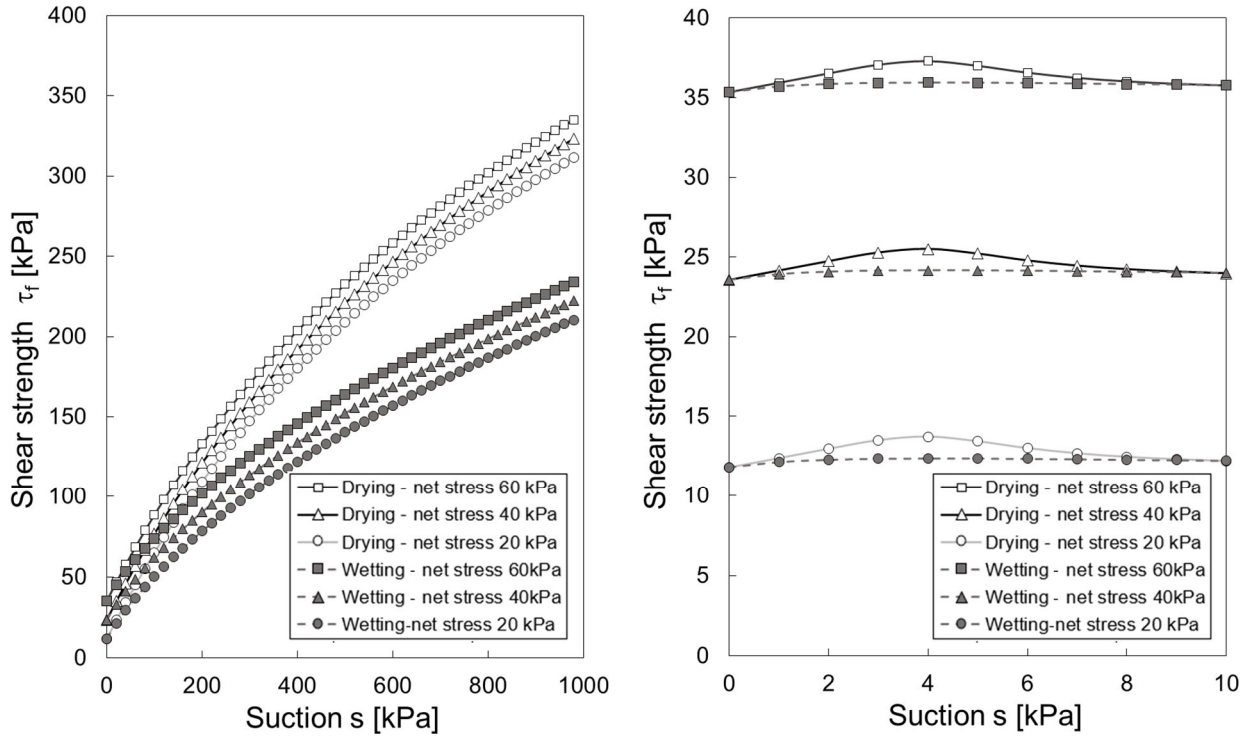


Figure 4.21. Evolution of shear strength with suction at different normal stress: comparison between the adopted water retention curve (main drying or main wetting curve) for the silt (left) and the sand (right).

Summarizing, the choice of the water retention model plays a crucial role in the hydro-mechanical modeling of the interaction between unsaturated retained soils and retaining structure. If cycles of drying and wetting periods are modeled, it is suggested to take into account the hysteretic behaviour of the retained soils that will lead to a more realistic hydro-mechanical behaviour of the retained soil. On the other hand, this will induce a loss of closed-form formulation with an increase in the computational cost and in the soil parameters to be characterized. The effect of the hysteretic behaviour of the soils under drying and wetting path on the lateral earth thrust are highlighted in the next chapter, that deals with the interpretation of the experimental results of the physical modeling.

Chapter 5

Physical modelling of retaining structures interacting with unsaturated soils

5. Physical modelling of retaining structures interacting with unsaturated soils

5.1 Foreword

Physical modeling has been extensively used to investigate the soil-structure interaction at 1g-scale (Terzaghi, 1920, Tsagareli, 1965, Rowe and Peaker, 1965, Bransby, and Milligan, 1975, Fang and Ishibashi, 1986, Fang et al., 1994, Symons and Clayton, 1992, Take and Valsangkar, 2001, Fang, et al., 2002, Khosravi et al., 2013, Yang and Tang 2017) and in the centrifuge environment (Bolton and Powrie, 1987, Bolton and Powrie, 1988, Richards and Powrie, 1998). Despite extensive studies conducted on saturated and dry soils, there remains a need to investigate how retaining walls interact with unsaturated soils. Moreover, the safety margin of many existing retaining walls can be determined more accurately by considering the presence of negative pore water pressure (Vo et al. 2016). Many attempts to include unsaturated soil principles in the computation of the lateral earth thrust can be found in the literature (see chapter 2: Pufahl et al., 1983, Lu and Likos, 2004, Vahedifard et al., 2015, Tavakkoli and Vanapalli, 2011, Fredlund and Rahardjo, 1993, Vanapalli and Oh, 2012, Stanier and Tarantino, 2013). These contributions have mainly extended to partially saturated soils the conventional analytical methods usually employed for dry or saturated geomaterials. Limited experimental studies on the interaction between unsaturated soils and retaining structures are available. For example, Vo et al., (2013) presented a rotating rigid retaining wall interacting with unsaturated soils focusing on the passive state. In this chapter, a new physical model capable of investigating the interaction between retaining walls and unsaturated soil is presented. The physical model is capable of reproducing several soil conditions: starting from the at-rest state, both the active and the passive states can be reached by imposing horizontal displacements. The horizontal component of the lateral earth thrust can be controlled or measured. Moreover, by continuously measuring the matric suction and by controlling the groundwater table, the experimental set-up is capable of catching the effects of the partially saturated conditions on the lateral thrust. The tests can be carried out with a variety of different soils. In this chapter, first, the experimental apparatus is presented, then experimental results are provided. In particular, the main aim of the reported performed tests is to study the effects of the partially saturated condition

on the failure mechanisms at the active state and the influence of matric suction changes on the at rest lateral earth thrust. The experimental results are interpreted by making a comparison with the analytical models available in literature in an attempt to validate these theoretical approaches or understand the grade of accuracy to be expected.

5.2 The physical model

The physical model was designed and built at the Laboratory for Soil Mechanics of the Swiss Federal Institute of Technology in Lausanne. It is characterized by a reinforced steel container 1.30 m high, 1 m large, and 1 m wide. The container is divided into two parts: the first one is capable of containing 0.4 m³ of soil, while the complementary part is devoted to host the model of the retaining structure and the instrumentation for controlling the soil-structure interaction. The dimensions of the model were chosen according to the expected magnitude of the lateral earth thrust measurable with the available instrumentation and the minimum width required to achieve the plane strain conditions (Bransby and Smith, 1975 suggested to adopt a ratio between the depth and the height equal to 2 in order to reduce the influence of the lateral friction between the retained soil and the walls of the box). The chosen height of the retained soil is 80 cm, while the retaining structure was placed on a plane above the bottom of the box at 30 cm of height. This allows controlling the groundwater table level below the retaining wall model and, as a consequence, to impose the hydraulic boundary condition. Two of the container walls are made of aluminum and are reinforced with steel frames to prevent lateral deformations.

The physical model is equipped with: i) a water-filled hydraulic cylinder connected to a pressure-volume controller to measure the horizontal lateral earth thrust (displacement control); ii) an LVDT to measure the displacements of the wall when the lateral earth thrust is imposed or to provide a redundant measurement of the horizontal displacement when the displacement is imposed via the hydraulic cylinder; iii) low friction linear guideways that allow only the horizontal displacement; iv) tensiometers to measure the soil matric suction; v) a 3 cm thick glass wall to observe the failure surface via particle image velocimetry (PIV) technique; vi) an external reservoir to control the hydraulic boundary condition; vii) a rainfall simulator. Figure 5.1 shows: the 3D schematic conception of the physical model (Figure 5.1.a), a picture of the overall experimental set-up (Figure 5.1.b), the water-

filled hydraulic cylinder (Figure 5.1.c), the linear guideways (Figure 5.1.d) and one of the tensiometer supports.

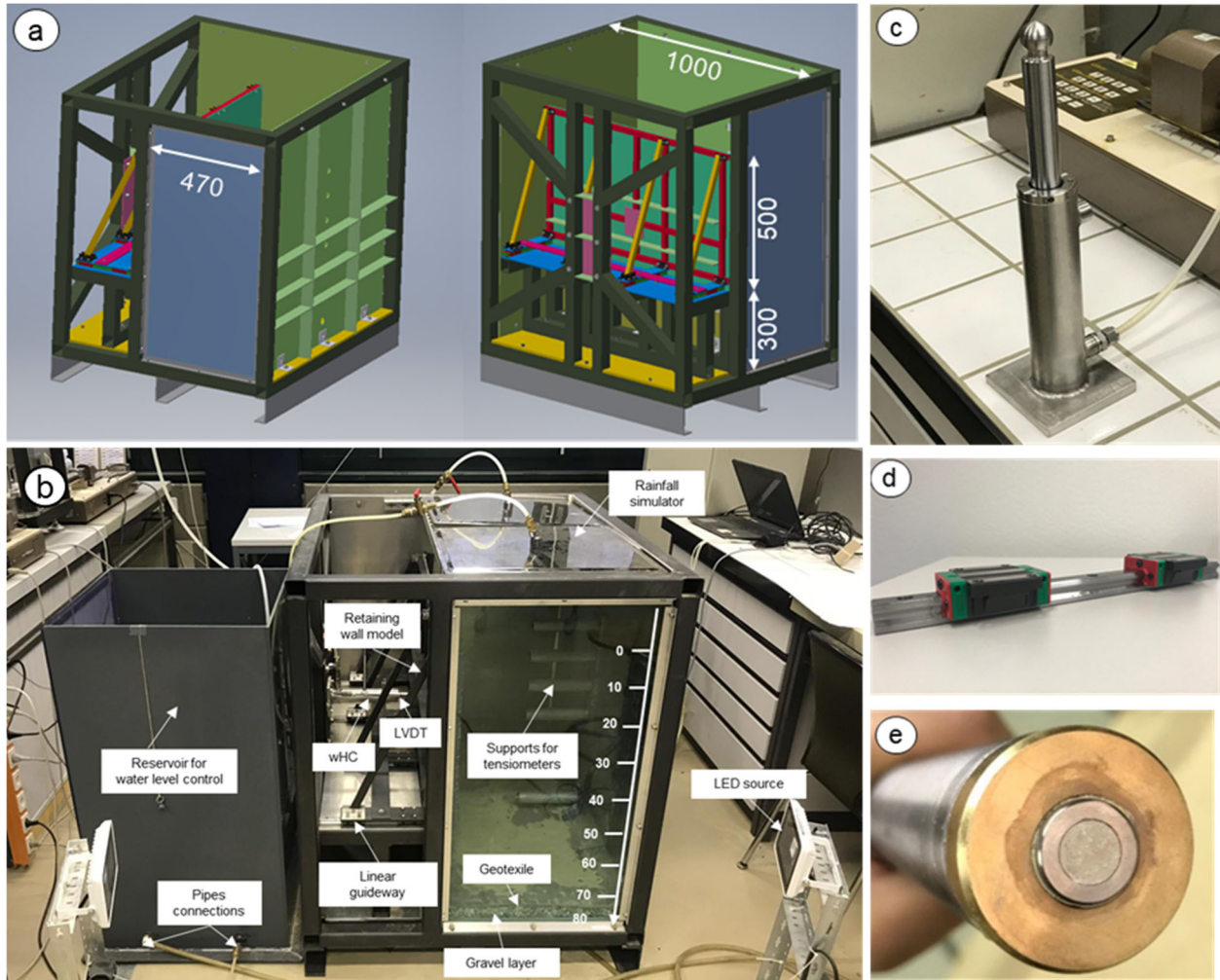


Figure 5.1. a) 3D schematic conception of the physical model; b) hydraulic water filled cylinder detail; c) overview of the experimental set-up; d) detail of a linear guideway; e) detail of a tensiometer's support.

5.3 Design, building, and calibration of the experimental devices

5.3.1 The water-filled hydraulic cylinder

The idea was to use a device capable of controlling either the force or the displacement of the soil-structure system. The choice has fallen on a double effect water-filled hydraulic cylinder that was connected with a pressure-volume controller. By controlling either the pressure or the volume in the hydraulic cylinder, it was possible to satisfy the design needs.

The diameter of the device was designed by considering the expected lateral earth thrust with respect to the condition of the retained soil dry (active state) or saturated (at rest condition). By knowing the acting forces on the retaining structure, the presumed pressure in the hydraulic cylinder is computed by varying the diameter. The operative range of the pressure/volume controller is 2000 kPa, and, to err on the side of caution, the selected maximum working pressure was 1500 kPa. Consequently, the diameter was identified: 40 mm (Figure 5.2.a).

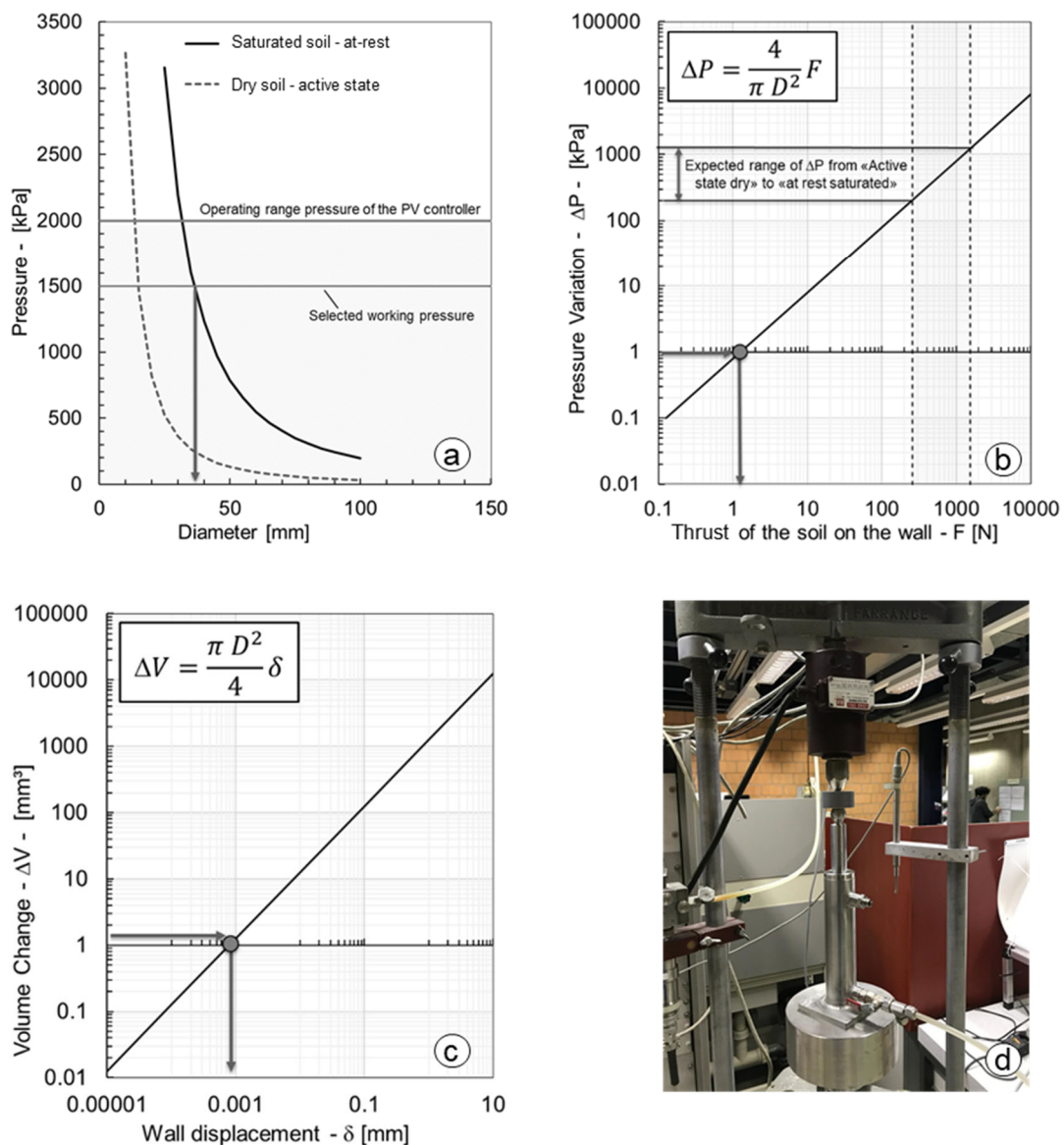


Figure 5.2. Design graphs for the choice of the hydraulic cylinder's diameter.

Moreover, the resolution of the instrument was firstly estimated. It is obvious that the resolution of the hydraulic cylinder, depended on the resolution of the pressure-volume controller (1 kPa in terms of pressure and 1mm^3 in terms of volume). Therefore, the aim of these analyses was to identify the correspondence between the resolution in terms of force and displacement with that already known in terms of pressure and volume. By neglecting the internal friction (unknown beforehand), the two resolutions were estimated by a simple geometrical relation regarding the circular section of the designed device. A variation of the volume in the controller of 1 mm^3 corresponds to a theoretical displacement of 0.001 mm, while a pressure variation of 1 kPa imposed by the controller corresponds to a hypothetical force variation of 1 N (Figure 5.2.b and Figure 5.2.c).

The chosen material was stainless steel. Moreover, in the front of the hydraulic cylinder, a sphere was welded to avoid any possible bending of the piston inside the instrumentation. The first saturation of the device was performed. Firstly, a vacuum pump was connected with the hydraulic cylinder to remove the air, afterward, the hydraulic cylinder was saturated with deaerated water and connected to the pressure-volume controller.

The whole system was calibrated in a frame equipped with a load cell to identify the relation between the applied load and the pressure in the controller (Figure 5.2.d). The calibration data are reported in Figure 5.3. It was performed in the two following scenarios: i) loading and unloading by keeping the volume in the hydraulic cylinder constant (to simulate the at-rest condition); ii) loading and unloading by allowing the volume variation in the hydraulic cylinder (to reproduce the transition between the at-rest condition and the active state).

Figure 5.3a and b show the calibration curve for the case i) while Figure 5.3c and d are related to the case ii). The relation between the applied force and the recorded pressure is linear for the loading and the unloading scenario for both the scenarios with an R^2 close to 1. On the other hand, the behavior of the system is not symmetric, considering the loading and unloading phases. For this reason, two calibration curves were considered.

The stainless-steel water-filled hydraulic cylinder was placed at 1/3 of the wall model height, on the back of the retaining structure.

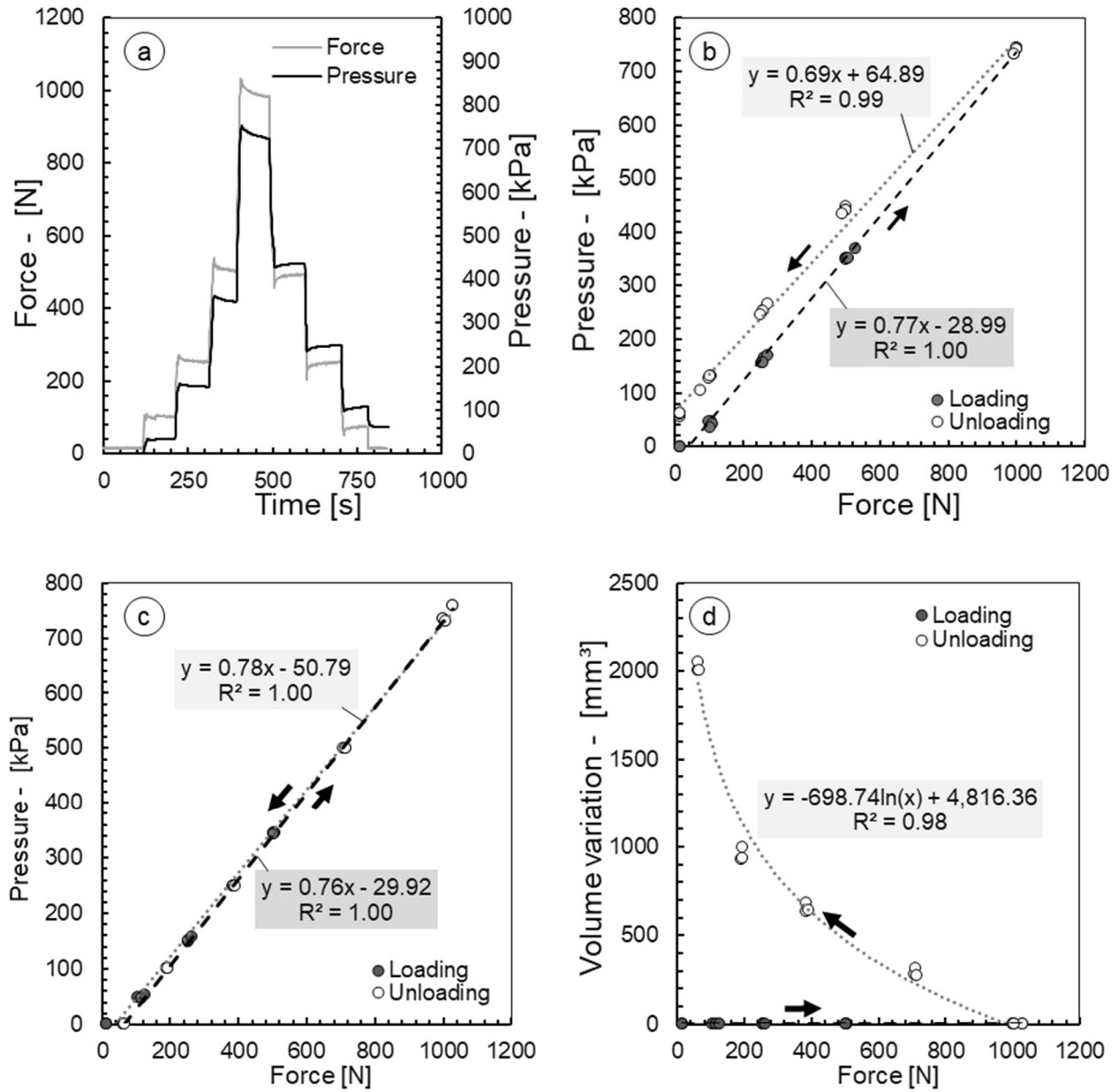


Figure 5.3. a) Evolution of the measured force and the measured pressure applied to the water-filled hydraulic cylinder during the calibration phase (scenario 1); b) calibration curve during loading and unloading steps at constant volume (scenario 1); c) calibration curve during loading at constant volume and unloading with variation of volume (scenario 2); d) variation of volume during loading and unloading (scenario 2).

5.3.2 Linear guideways

An LVDT is placed at the same level as the hydraulic cylinder, and four linear guideways are placed at the bottom of the retaining structure in order to allow uniquely for a horizontal displacement of the system. The linear guideways are characterized by two features: high

positioning accuracy and constant load capacity in both vertical direction and horizontal direction. When a load is moved by a linear recirculating ball guide, the generated friction is of the rolling type, and the difference between the static and dynamic friction coefficient is minimal. As a result, no slide bearing occurs during the displacement of the load. Each guideway accounts for two sliding blocks where the retaining structure is fixed. In this way, any possible bending moment induced by the eccentricity of the lateral earth thrust of the retained soil can be transferred at the linear guideways that, thanks to their low friction system, allow for the simple horizontal displacement of the soil-structure system. According to this configuration, the horizontal component of the lateral earth thrust can be measured.



Figure 5.4. Details of the designed linear guides and assembling in the physical model.

5.3.3 The High Capacity Tensiometers

At the back of the container, five tunnels were installed to allow the installation of the supports for the tensiometers. The tunnels have a diameter of 3 cm, and they are 25 cm long. Their length has been chosen with the intent to place the tensiometers as close as possible to the failure surface (active state) without compromising its development. Moreover, this solution allows having fast maintenance in case of cavitation of the tensiometers. The

Trento High Capacity Tensiometers (HCTs) were employed (see section 4.3). The tensiometers were saturated according to the procedure proposed by (Tarantino and Mongiovì, 2003), and they were calibrated in the range 0-100 kPa according to the expected range of matric suction in the retained soil. They were calibrated in the positive range of pressure following the procedure proposed by (Tarantino and Mongiovì, 2003). Also, in this case, the calibration curve is linear for both loading and unloading with an R^2 very close to 1.

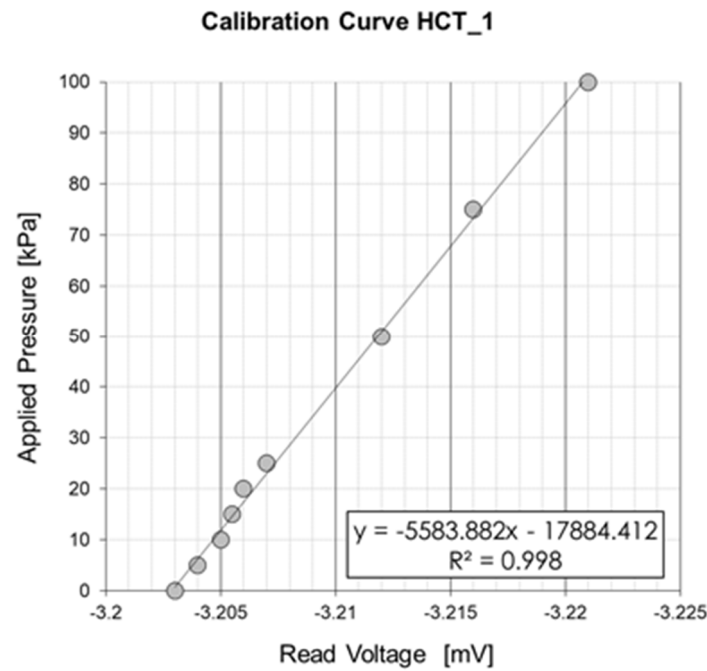


Figure 5.5 Calibration curve tensiometer 1.

5.3.4 The instrumentations for the PIV

The glass wall allowed for the observation of the failure surface through the PIV. The Open-PIV code (Taylor et al., 2010) was used for the analysis of the pictures. On the side of the box (in front of the glass wall), a NIKON D3300 camera was placed to record the evolution of the failure surface. To ensure the acquisition of suitable images for the PIV, two LED lights were placed on the two sides of the camera. However, during the preliminary test for the calibration of the PIV tools, the soil particles were tiny, and the texture structure was not clear. Additional tracer particles were added, and they were placed at the interface with the glass wall. The benefits due to the adoption of the additional tracers placed in layers were

clearly noticeable, and the results of the PIV analyses were significantly improved: performing the test without the additional tracers did not allow for the observation of the failure surface. A mesh influence analysis has been performed to choose the size of the interrogation window and the spacing. The tested meshes were: 128x128, 64x64, 32x32, 16x16, and 8x8 pixels for both spacing and interrogation window size. The results of the mesh-influence test are reported in Table 5.1. The use of the 8x8 mesh grid did not provide results due to convergence problems, while the 16x16 grid provided good results in terms of identification of the failure surface, but the algorithm was solved only partially. The resolution of the output images increased with the decrease of both mesh sizing and spacing, and the failure surface was better recognizable. There was not significant difference among the all tested mesh grids in terms of maximum recorded velocity, and as a consequence, the 32x32 mesh was selected as an optimal compromise.

Table 5.1. Results of the sensitivity mesh analysis.

Interrogation window size [-]	Spacing [kN/m ³]	Result of the analysis [kN/m ³]	Max instantaneous displacement [mm]	Quality of result pictures
128 x 128	128 x 128	Solved	0.57	Poor
64 x 64	64 x 64	Solved	0.53	Acceptable
32 x 32	32 x 32	Solved	0.56	Good
16 x 16	16 x 16	Partially solved	0.50	Very Good
8 X 8	8 X 8	No solution	-	-

5.3.5 The instruments for controlling groundwater level and to simulate rainfall events

The hydraulic boundary condition was imposed by controlling the GWT level below the model of the retaining structure. The container was connected with an external reservoir where the water level can be controlled with a millimeter resolution. At the bottom of the container, a gravel layer (3 cm) was placed to allow the simultaneous application of the hydraulic boundary condition for all the width and the length of the soil mass. The gravel

and the retained soil are separated by a geotextile sheet to avoid the penetration of the tested soil in the more permeable layer but allowing the water to pass through it.

A rainfall simulator (two shower heads) is installed at the top of the box container. It is characterized by 648 nozzles that are spread on a panel of 0.5 m by 1 m covering the whole soil surface. The rainfall simulator is connected to the laboratory's water network, and the flow is controlled by a digital flowmeter.

The designed system has been calibrated to have a constant rainfall intensity. Each shower head was placed on the top of the reservoir. The flow in the system was progressively increased up to get the desired infiltration rate. The latter was measured by observing with the time the increase of the water level in the reservoir. The electronic flowmeter was used to control the application of a constant flow during both the calibration and the performance of the tests. Figure 5.6 shows the calibration of the two devices.

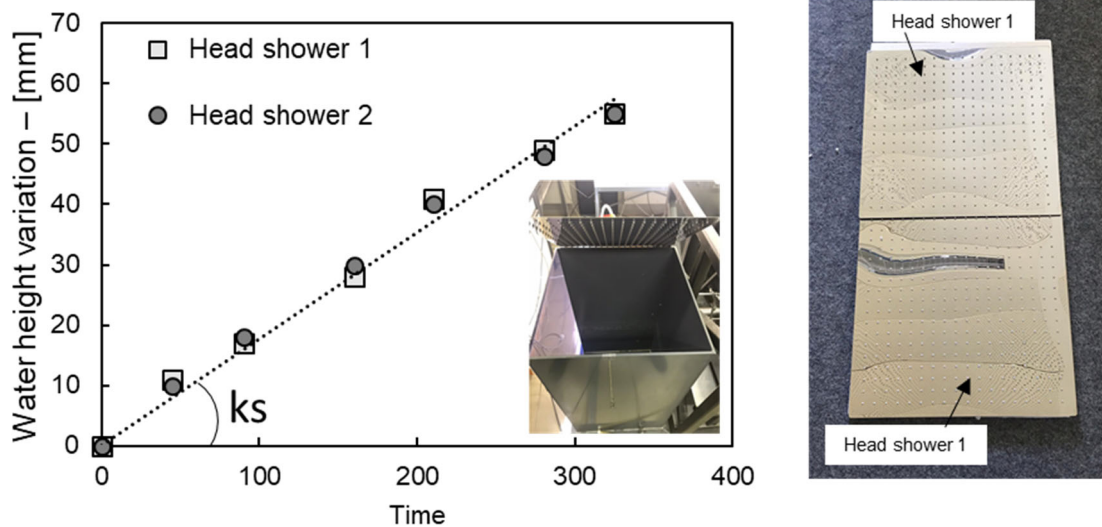


Figure 5.6 Calibration curve of the rainfall simulator.

5.4 Experimental phases and tested soil

Two test typologies were performed. The first deals with the investigation of the lateral earth thrust of unsaturated soils at the failure conditions (active state), while the second typology intends to investigate the effects of matric suction variation on the lateral earth thrust in the at-rest conditions.

The failure condition was induced by imposing a horizontal displacement on the retaining structures. This type of test was performed firstly in dry conditions (Test 1.1) then the partial saturation conditions were simulated by controlling the water level below the retaining structure and wetting the retained soil by the capillary rise (Test 1.2). During the transition phase between the at rest and the active state, the horizontal component of the lateral earth thrust was measured. The second test typologies consist of the measurement of the horizontal component of the lateral earth thrust in the at-rest condition by simulating matric suction changes induced by the rising of the water level (wetting from the bottom, Test 2.1), drop-down of the water level (Test 2.2) and simulation of rainfall events by performing infiltrations from the top (Test 2.3). Figure 5.7 shows the schematic representation of the performed tests.

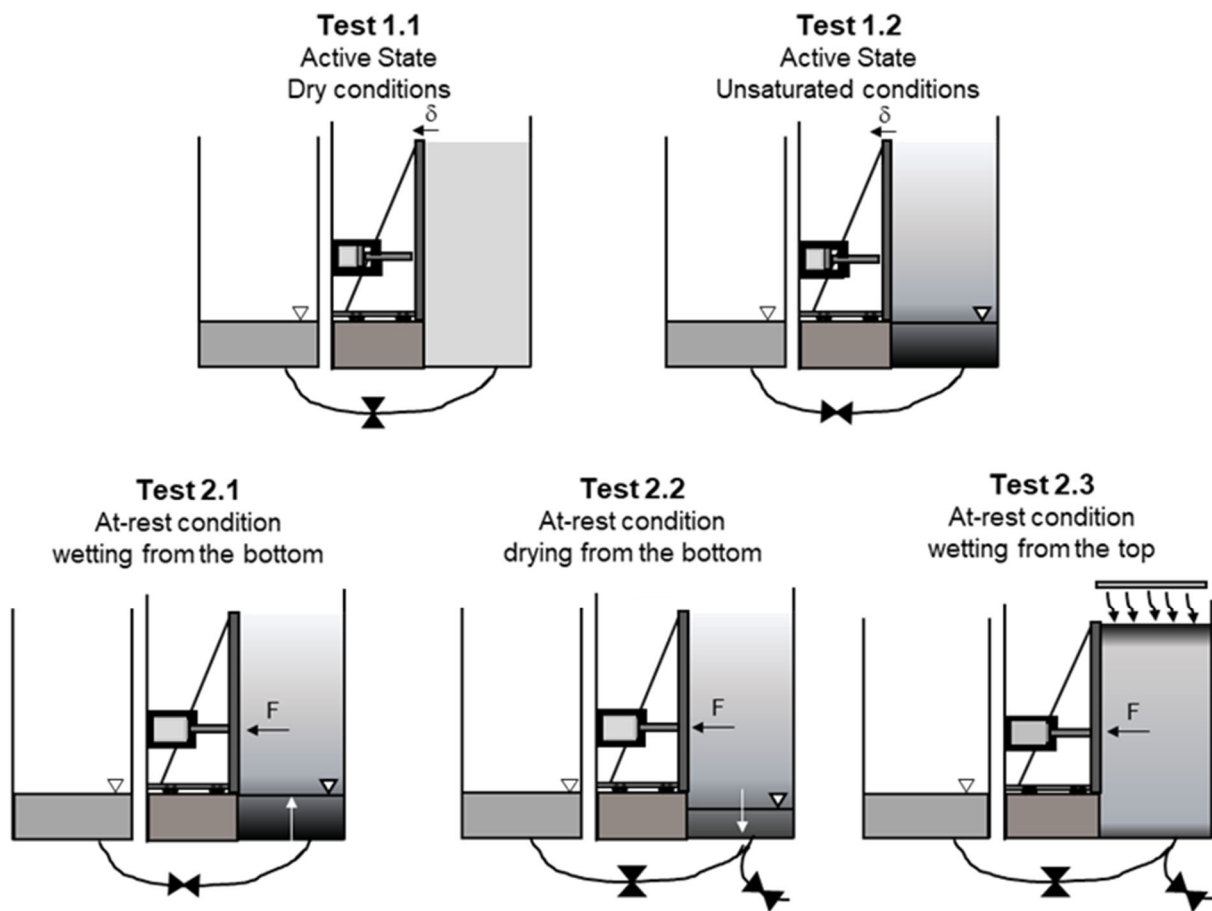


Figure 5.7 Schematic representation of the performed tests.

For all of them, the container was filled following the dry pluviation technique. The average initial void ratio (e_0) is resulted to be 0.6. The height of the retained soil was divided into layers of 10 cm, and the drop height was kept constant.

Regarding Test 1.1, first, at the bottom of the box, a gravel layer and the geotextile were placed, then the soil was drop-in keeping constant the falling height (50 cm). The retaining structure model's height was divided into five parts (10 cm each), and the box was filled by steps. During the backfilling phase, the volume in the controller was kept constant, and the increase in the pressure was recorded. Due to the deformation of the whole system, the LVDT recorded a minimal horizontal displacement that was corrected by controlling the pressure in the hydraulic cylinder, thus allowing the soil-structure system to return to its initial position. This procedure is followed to keep the K_0 conditions. Once the box was filled up to the required height, a displacement was applied to achieve the failure. The displacement was applied by controlling the volume in the hydraulic cylinder and recording the decrease in pressure.

Regarding Test 1.2, the filling procedure was precisely equal to that of Test 1.1. Before applying the displacement, the container was hydraulically connected with the external reservoir, and the GWT was set at the base of the retaining structure (30 cm). After waiting for the capillary rise, the displacement was imposed to observe the failure of the partially saturated soil. During the test, the matric suction was measured by using the HCTs. The transition phase between the at-rest state and the failure was recorded with a camera. The acquired pictures were processed (PIV analysis) with the objective of observing the differences in the failure mechanism between the two tests.

Test 2.1, 2.2 and 2.3 were conducted in series: first water was injected from the bottom imposing the water level at the base of the retaining wall model ($z = 50$ cm); after the propagation of the unsaturated front (Test 2.1) upwards in the retained soil, a drying path was simulated by decreasing the water level to 80 cm (Test 2.2). Once steady-state conditions were achieved, a rainfall event with an intensity equal to the saturated hydraulic conductivity of the soil ($k_s = 1 \times 10^{-4}$ m/s) was simulated (Test 2.3).

The tested material is the fine sand (Ittemberk sand) which hydro-mechanical properties have been investigated in section 4.2. The achieved peak (φ'_p) and the constant volume

(ϕ'_{CV}) shear strength angle are resulted to be 56° and 32° , respectively. As reported in the dedicated chapter, with respect to the water retention behaviour, both the drying and the wetting path were studied. Moreover, Figure 5.8 shows the analysis of the experimental results that were initially fitted with Van Genuchten's model, identifying the shape of the main soil water retention curves. This model does not allow considering either capillary hysteresis or the volume dependence on suction. Considering that the performed tests simulated the alternation of drying and wetting paths, it has been decided to adopt the water retention model proposed by Nuth and Laloui (2008). In particular, in this work, dealing with coarse granular material, only the capillary hysteresis is considered, while it has been assumed that there is no volume variation on suction changes. The fitting parameters for the adopted model are reported in Table 5.2.

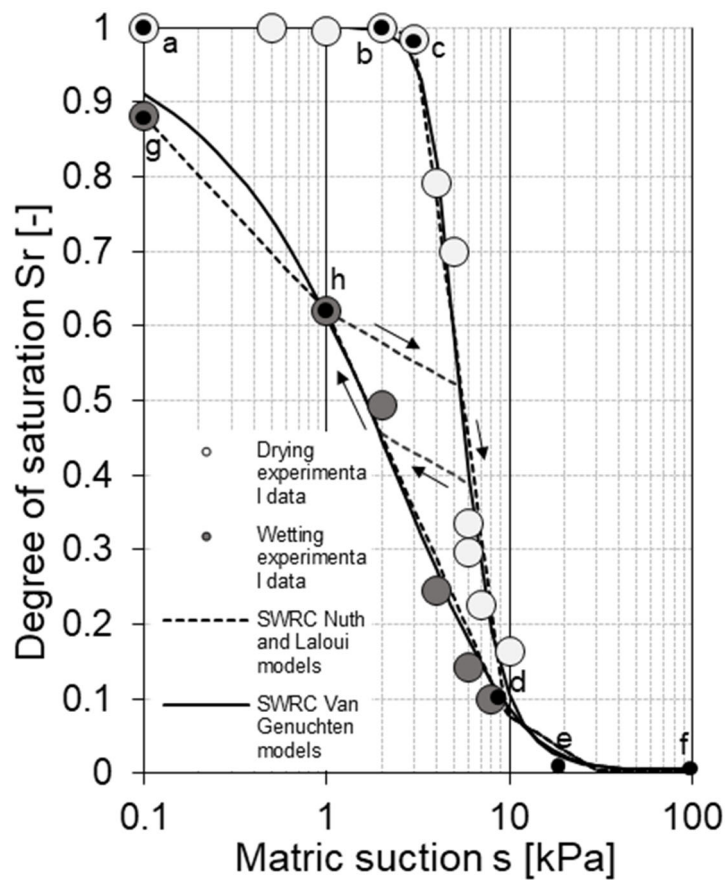


Figure 5.8. Water retention behaviour. Experimental data and employed fitting models.

Table 5.2. Parameters of the adopted fitting curves modelling the water retention behaviour.

Main drying		Main wetting	
Path	m_{α} [1/kPa]	Path	m_{α} [1/kPa]
a-b	0	g-h	-0.260
b-c	-0.057	h-d	-0.545
c-d	-1.865	d-e	-0.273
d-e	-0.273	e-f	0
e-f	0		

Scanning	
Path	m_{α} [1/kPa]
-	-0.142

5.5 Results and analysis

In this section, the results of the performed tests are reported. First, the effects of the partial saturation on the failure mechanism at the active state are shown (Test 1.1a, 1.1b, and 1.2) then the influence of matric suction changes on the lateral earth thrust in the at-rest condition is presented (Tests 2.1, 2.2, and 2.3). The two topics are treated in separate subsections. The comparison between analytical models and the experimental results is reported for both the investigated cases.

5.5.1 Effects of partial saturation on the failure mechanism at the active state

During the backfilling phase of the tests, the horizontal force and the horizontal displacement were measured. Small deformations of the retaining wall model were observed. This implied a lower measured horizontal force. To prevent the loss of the at-rest condition (null

horizontal displacement), the force was corrected by pushing back the wall model at its initial position. Figure 5.9.a shows the evolution of both the horizontal displacement and the lateral earth thrust during the backfilling phase for Test 1.a. Similar trends were found for all the performed tests. The observed values of the horizontal displacement remain lower than the displacement estimated at the active state. By performing PIV analysis, the displacement at which the failure occurred was identified (horizontal displacement at which the failure surface was observed). Making an analogy with the direct shear tests reported in the subsection 4.2.2, it can be noticed that, for the observed amount of displacements (Figure 5.9.a), the soil did not reach the peak shear resistance yet (Figure 4.5a). Moving from the at-rest state to the failure, the peak shear strength has to be mobilized. This would imply consequences in terms of scale effects and should be considered if these results would be projected on a prototype scale.

Figure 5.9.b shows the comparison between the experimental values of the horizontal force in the at-rest conditions and the theoretical model computed according to the following relation:

$$P_0 = \int_0^H K_0 \sigma'_v dz = \int_0^H K_0 \rho_d g z dz \quad (5.1)$$

Where σ'_v is the vertical stress computed as the product between the dry density (ρ_d), the depth (z), and the gravity acceleration (g). The coefficient of earth pressure at rest has been computed, according to Jaky (1944):

$$K_0 = 1 - \sin \varphi' \quad (5.2)$$

Where φ' is the shear strength angle imposed equal to the constant volume shear strength angle (Mesri and Hayat, 1993). This theoretical expression fits well with the experimental results. The final obtained value of the horizontal force represents the initial condition for the performed tests.

The active state was obtained by imposing a horizontal displacement rate of 0.01 mm/sec. Figure 5.10 reports the obtained experimental results in terms of force-displacement relation ($F-\delta$).

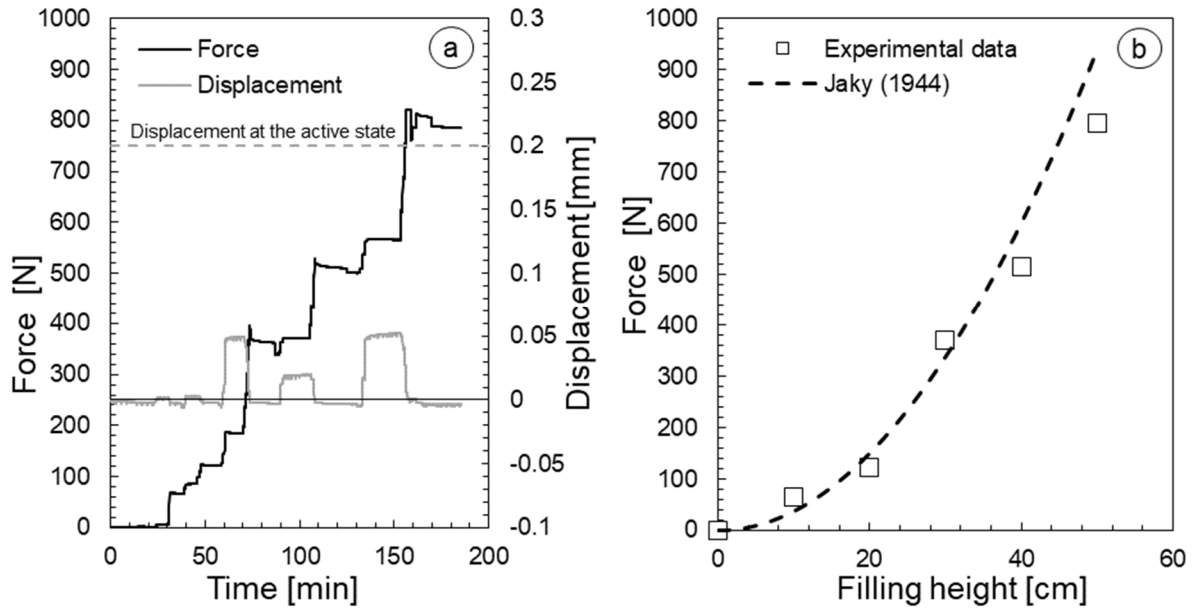


Figure 5.9. a) Evolution of the measured horizontal displacement during the backfilling phase (Test 1.1a); b) comparison between experimental data and Jacky's theoretical model (Test 1.1a).

Test 1 was performed twice (Test 1.1 a and 1.1b) to verify its repeatability. The tests have shown a similar evolution: starting from the initial “at rest” condition, the measured horizontal force immediately reduced with the applied horizontal displacement. Afterward, with the increase of the displacement, the measured force tends to stabilize (presumed active state), a residual condition was obtained, and the force continued to decrease with the increase of the applied displacement.

Regarding Test 1.1a and Test 1.1b, as introduced above, the formation of the failure surface (PIV analysis) was observed after 20-30 seconds since the beginning of the test. At that time, the LVDT was measuring between 0.1 - 0.2 mm of horizontal displacement. These values correspond in the $F-\delta$ curve to the phase where the force was almost constant (Figure 5.10b). The combined interpretation of the PIV analysis (horizontal displacement at which the failure surface was observed) and the two results allows deducing that, in correspondence of that time (20-30 seconds after the beginning of the test), at that specific displacement values (0.1-0.2 mm), the active state was reached.

In Test 1.2, the imposition of the groundwater table at the base of the wall resulted in a capillary rise.

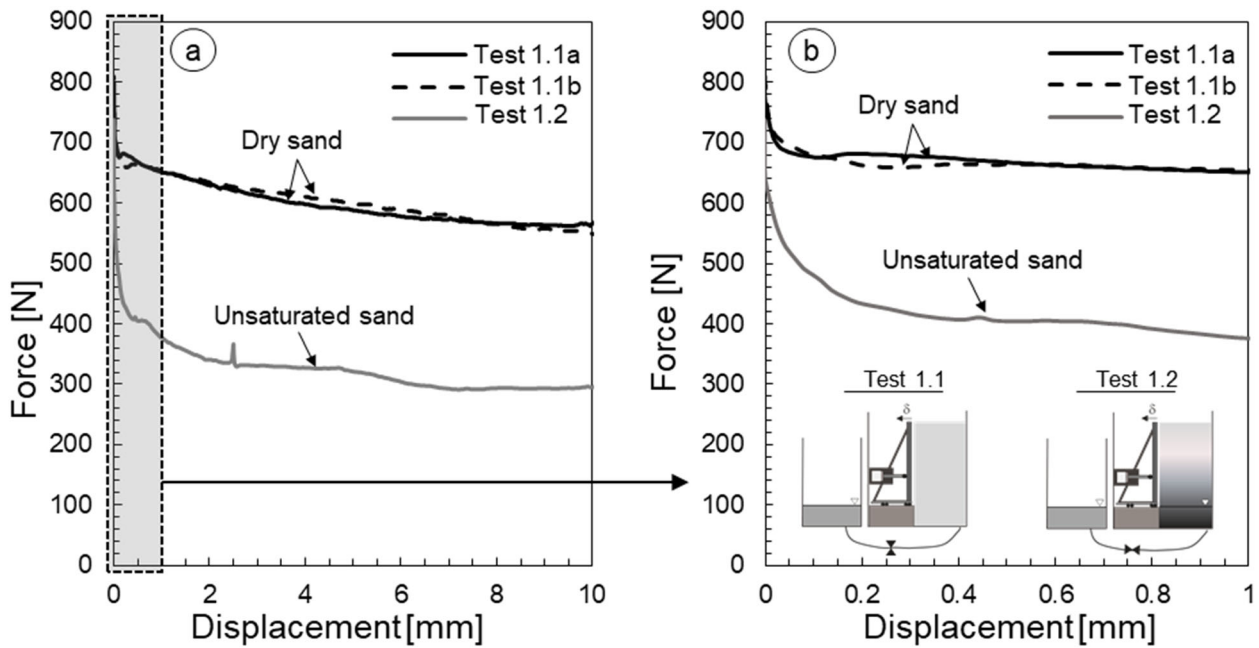


Figure 5.10 a) Results of Test 1 and Test 2 in terms of force evolution with the horizontal displacement; b) zoom on the first millimeter of the tests.

The length of the partially saturated portion of the soil was 22.5 cm, on average, in agreement with the water retention behaviour obtained with the performed tests (subsection 4.2.3).

At this stage, two tensiometers were placed 10 cm and 20 cm above the imposed water table ($z = 40$ cm and 30 cm, respectively) in the unsaturated portion of the soil. Figure 5.11 shows the evolution of the pore water pressure recorded by the tensiometers. The tensiometers were initially submerged in free water for about 15 minutes to check their initial offset; the measured water pressures were correctly equal to zero. During the installation phase, a significant variation of the water pressure was observed (positive values). After a few minutes, the recorded values of suctions equalized and remained stable. The displacement rate was imposed at 83 minutes, and the force was recorded. No change in pore-water pressure was observed. At the end of the test, the tensiometers were removed and placed in free water. During this phase, first, the values of the recorded water pressure reduced as expected (variation of water pressure opposite to that observed during tensiometers' installation), then it raised tending to 0 kPa. The average suction values measured during the test were 3.2 kPa and 2.5 kPa at $z = 30$ cm and $z = 40$ cm, respectively. The standard deviation was 0.3 kPa for both measurements. The measured values of matric suction are consistent

with the expected values by observing the capillary rise and the water retention curve (Figure 4.9).

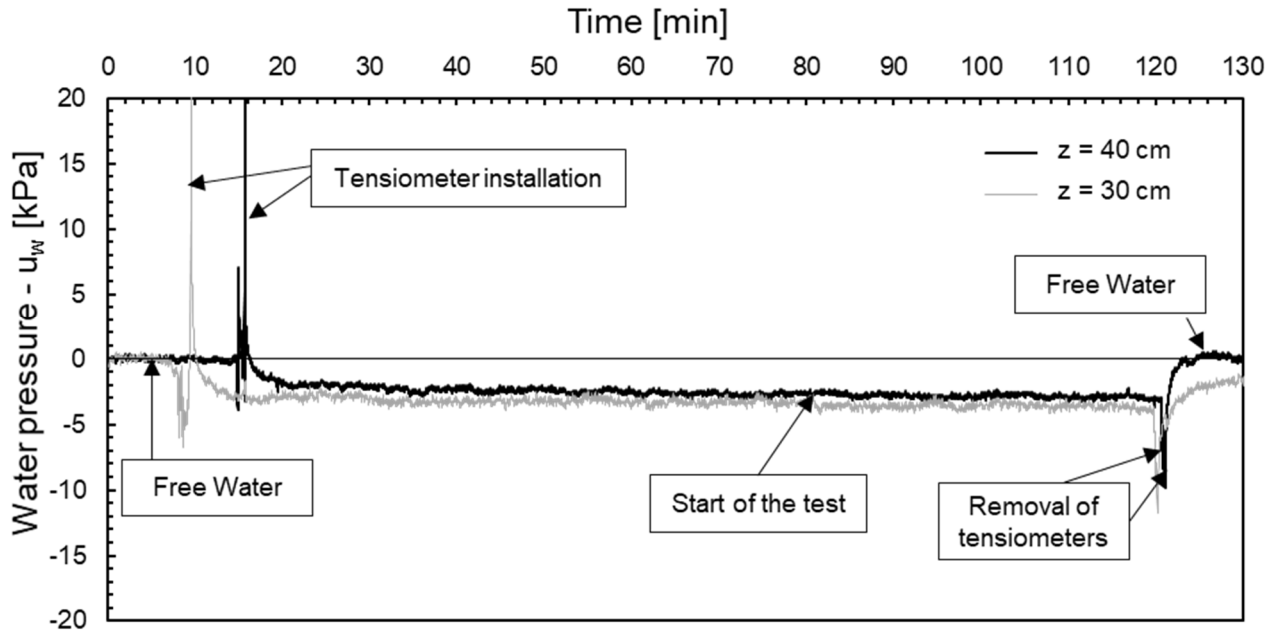


Figure 5.11 Measured pore water pressure with the tensiometers.

After reaching the steady-state condition, the displacement rate was imposed, and the force was recorded. Regarding the F - δ relation, the active state was achieved at higher displacements (0.3 – 0.4 mm), and the value of the force is resulted to be lower if compared with that of Test 1.1a or 1.1b.

The main goal of performing PIV analysis was to observe the shape of the failure surface of the two performed tests highlighting the differences. Figure 5.12 and Figure 5.13 show the displacements of the mobilized soil mass with the time in terms of absolute displacement ($d = \sqrt{u^2 + v^2}$, where u and v are horizontal and vertical displacement respectively). The frames were extrapolated every 30 seconds and were processed for the computation of the displacement field. The results are reported at 0 s, 120 s, 240 s, 360 s, 480 s, 600 s, and 930 s that correspond to the instantaneous absolute displacement with reference to the previous frame. This allows following the evolution of the shape of the failure surface with the time. Eventually, to have a quantitative assessment of the displacement field, the cumulative of the displacement is reported.

The results of the PIV analyses allow identifying the differences between the two failure surfaces. The amount of soil affected by the failure is lower in Test 1.2 with respect to Test1.1a or b.

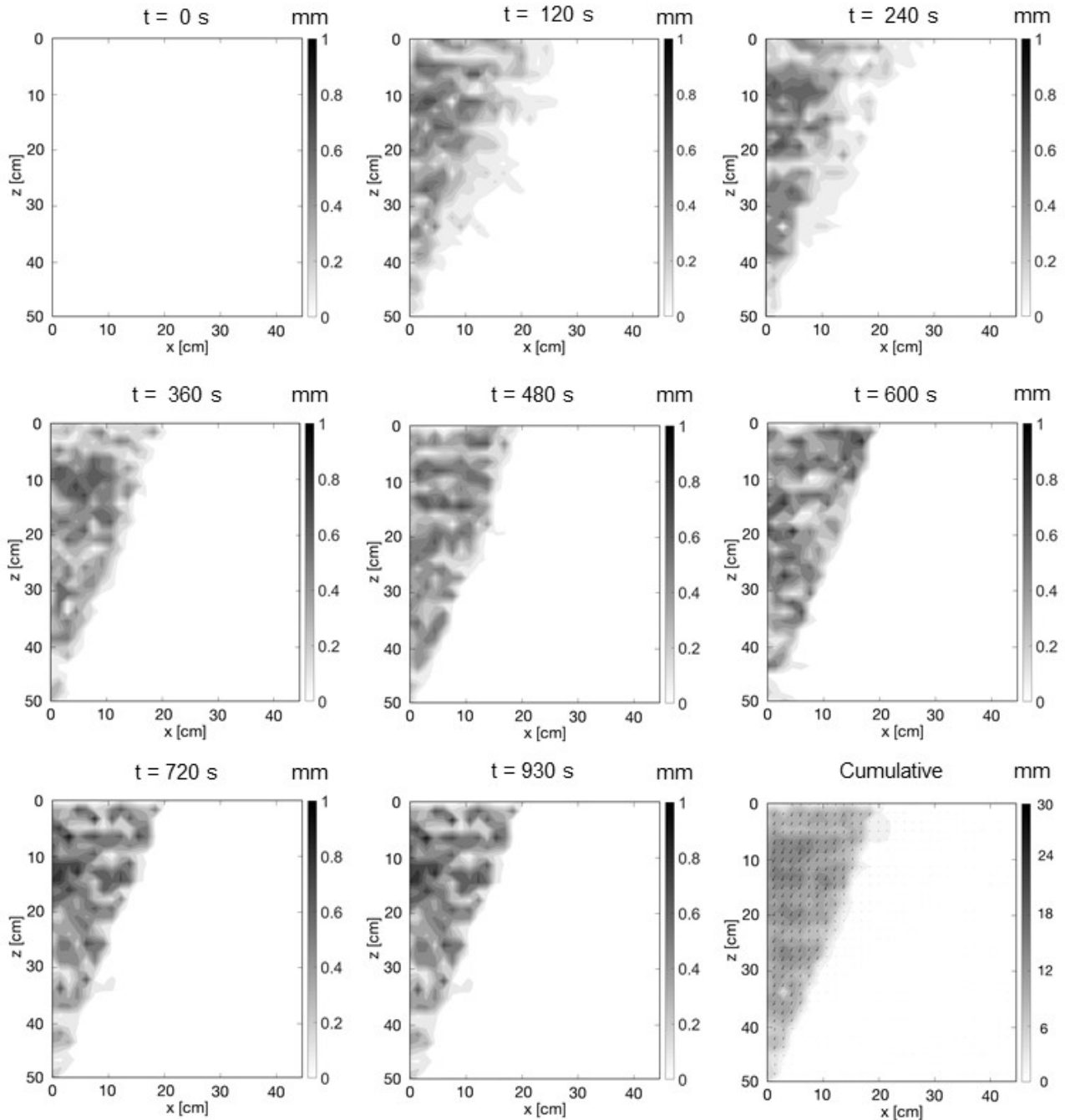


Figure 5.12. Results of the PIV analysis Test 1.1a.

The failure surface of the soil in unsaturated conditions can be approximated as piecewise function composed of two straight lines characterized by different slopes (Figure 5.14): for Test 1.2, in the portion of soil affected by capillary rise, the slope of the failure surface (80°)

is higher with respect to that in dry conditions (67°) while, in the upper part, a similar slope to Test1 was observed (66°).

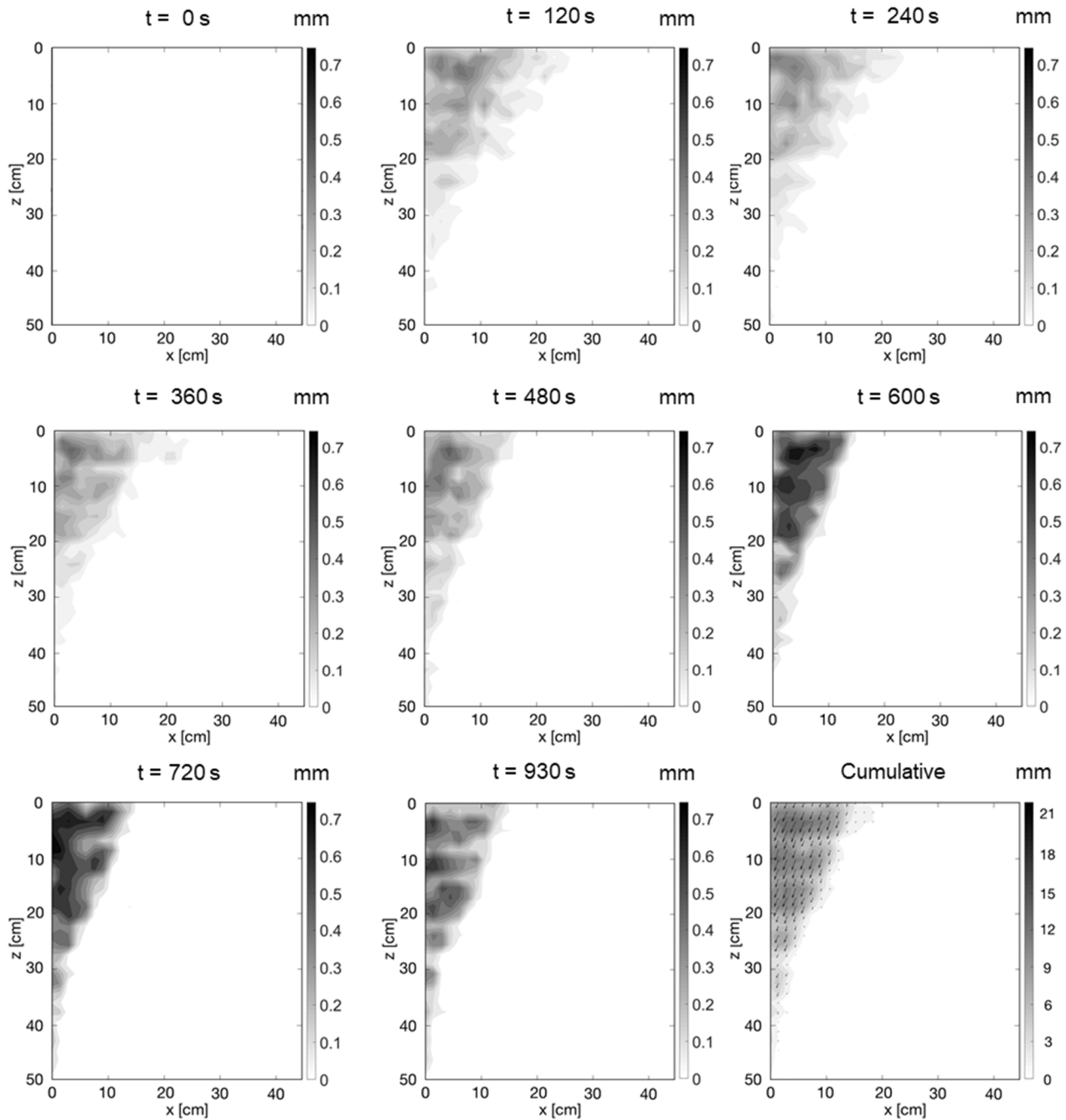


Figure 5.13. Results of the PIV analysis Test 1.2.

On the other hand, it has to be highlighted that the side effects play a role in the identification of the failure surface. For this reason, the failure surfaces were also observed from the top. A curvature of the failure surface was found close to the walls of the container for both

the tests. Figure 5.14a shows a view of the failure surface of Test1 from the top. The distance of the failure surface from the wall-model was measured at the top of the soil body at the maximum distance from the two side walls.

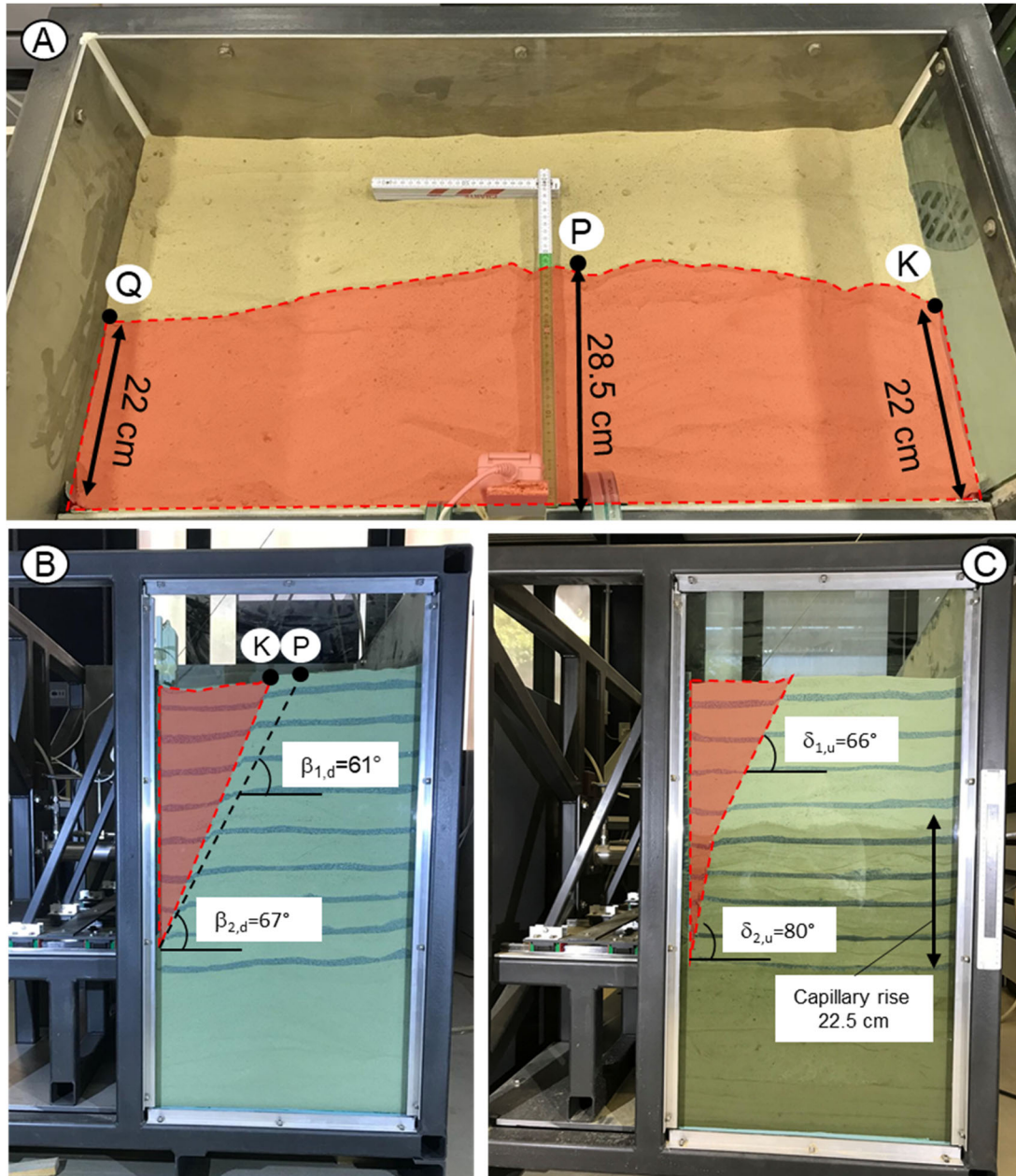


Figure 5.14 a) Failure surface view from the top (Test 1.1a); b) Failure surface lateral view (Test 1.1a); c) Failure surface lateral view (Test 1.2).

In this position, the fact that the observed failure surface in dry condition has a slope (θ) of almost 61° is a confirmation of the measured shear strength angle at constant volume: by inverting the following relation according to Rankine (1857)'s theory the chosen shear strength angle is found again:

$$\theta = \left(\frac{\pi}{4} + \frac{\varphi'_{CV}}{2} \right) \simeq 61^\circ \Rightarrow \varphi'_{CV} \simeq 32^\circ \quad (5.3)$$

5.5.1.1 Comparison between the experimental results and the analytical model (active state)

The achieved experimental results are interpreted and analysed in the attempts to make a comparison with the analytical formulation at the active state. The theoretical formulation reported in chapter 1 is here recalled. The lateral net horizontal stress at the active state is computed as follows

$$\sigma_A - u_a = (\sigma_v - u_a)K_A - 2\sqrt{K_A}c' - S_r(u_a - u_w)(1 - K_A) \quad (5.4)$$

By integrating over the depth equation (5.4) it is possible to obtain the horizontal component of the lateral earth thrust that is compared with the experimental results:

$$P_A = \int_0^H (\sigma_A - u_a) dz \quad (5.5)$$

Suction measurements were employed to compute the degree of saturation distribution by exploiting the water retention curve (Figure 5.8). At the interface between the unsaturated and the dry portion of the retained soil, the matric suction value is guessed by adopting a linear model within the available suction measurements. By assuming no volume variation with suction changes, the unit weight (for the computation of the vertical net stress) has been computed according to the following relation:

$$\gamma = \gamma_d + \gamma_w S_r \frac{e_0}{1 + e_0} \quad (5.6)$$

As can be observed from Figure 5.15, at a given matric suction profile, two degrees of saturation profiles can be identified, and as a consequence, the lateral earth pressure distribution will be affected too.

This represents a crucial point in the computation of the lateral earth thrust of unsaturated soil that is revealed to be dependent on the choice of the water retention behaviour model. If the main wetting curve is selected for the computation of the involved stress, the resulting

horizontal stress at the active state will result to be higher with respect to the selection of the main drying curve.

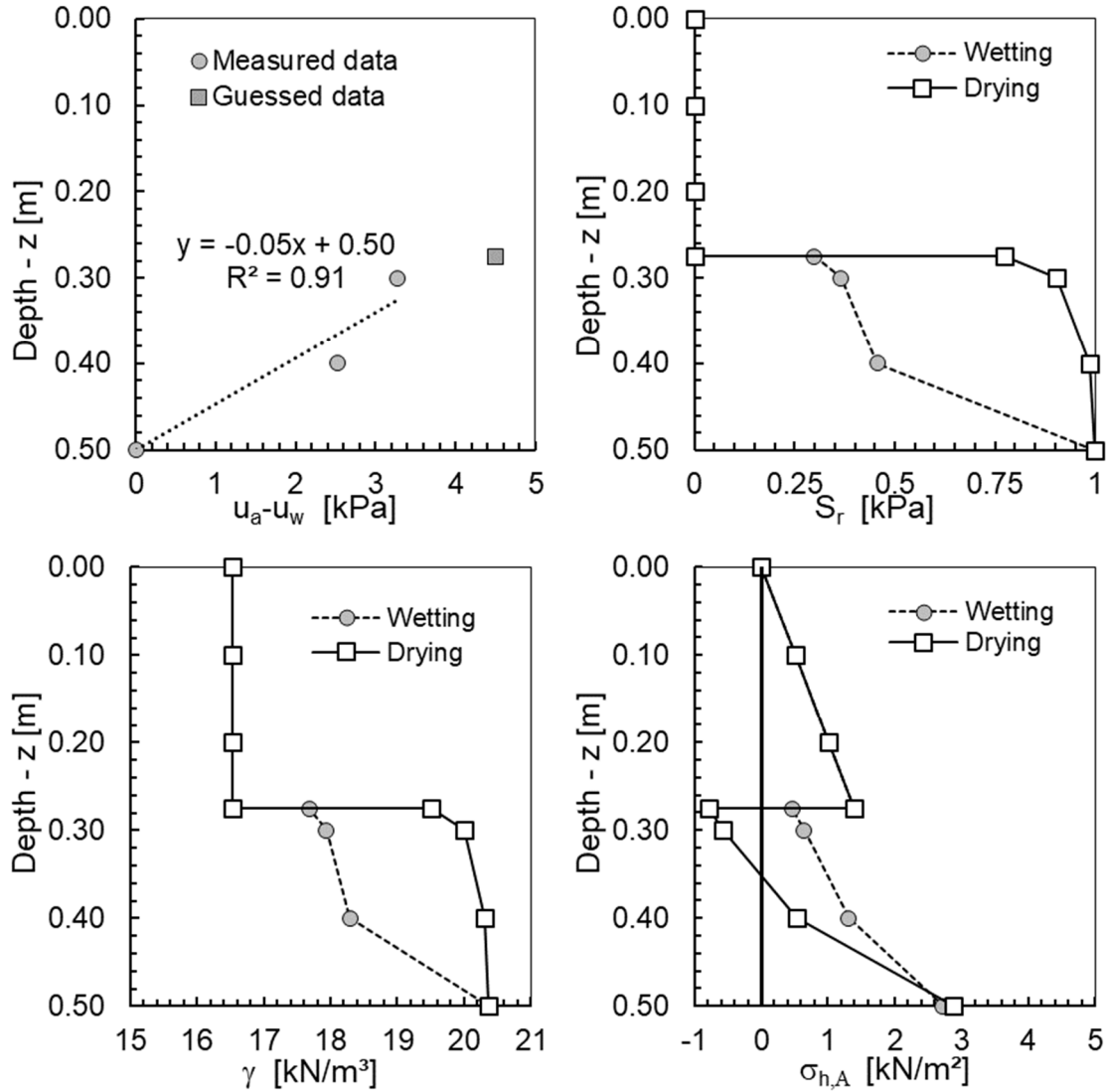


Figure 5.15 a) Matric suction profile in the unsaturated portion of the retained soil; b) Degree of saturation profile; c) unit weight profile; d) lateral earth pressure distribution according to extended Rankine's theory.

According to equation 5.4, the computed horizontal component of the lateral earth thrust is 635 N in dry condition and 505 N or 368 N for the test performed in unsaturated conditions adopting the main wetting or the main drying water retention curve respectively.

Figure 5.16 shows the comparison between the experimental results and the theoretical values achieved according to the extended Rankine's theory. In dry conditions, the experimental results (Test 1.1a and Test 1.1b) and the theoretical formulation are in very good agreement while in the unsaturated scenario (Test 1.2) the experimental curve falls within

the range of values delimited by the thrust calculated with the main wetting and drying retention curve models. The importance of the choice of the water retention model is even more evident when computing the integral of the lateral earth pressure distribution. The adoption of the main drying water retention model can lead to an underestimation of the thrust of unsaturated soils, while a more conservative approach can be followed by choosing the main wetting curve of the water retention model.

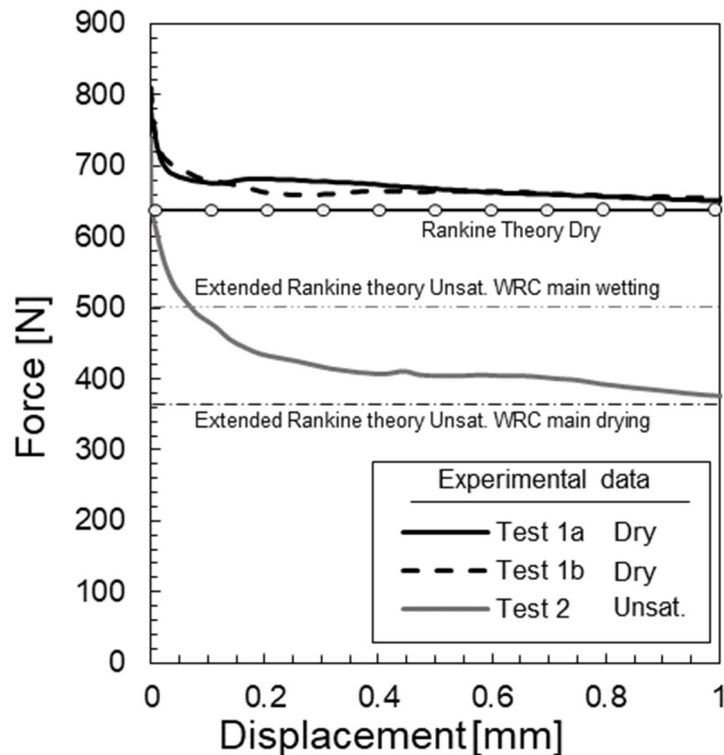


Figure 5.16 Comparison between experimental results and theoretical formulation.

5.5.2 Effect of partial saturation on the lateral earth thrust at the at-rest state

Test 2.1, Test 2.2, and Test 2.3 were conducted in series maintaining the at-rest conditions (null horizontal displacement) by preventing volume variation in the water-filled hydraulic cylinder. The results of the tests are reported in Figure 5.17. After the backfilling of the container (measured horizontal force equal to 798 N), Test 2.1 starts at $t = 124$ min. Water was injected from the bottom and, after the saturation of the gravel layer (at depth of 80 cm), water raised-up in the retained soil. Initially, a slight decrease (787 N) followed by an increase (843 N) in the measured horizontal force was observed. Once the water level reached the level of the wall base ($z = 50$ cm), it was maintained constant at that depth.

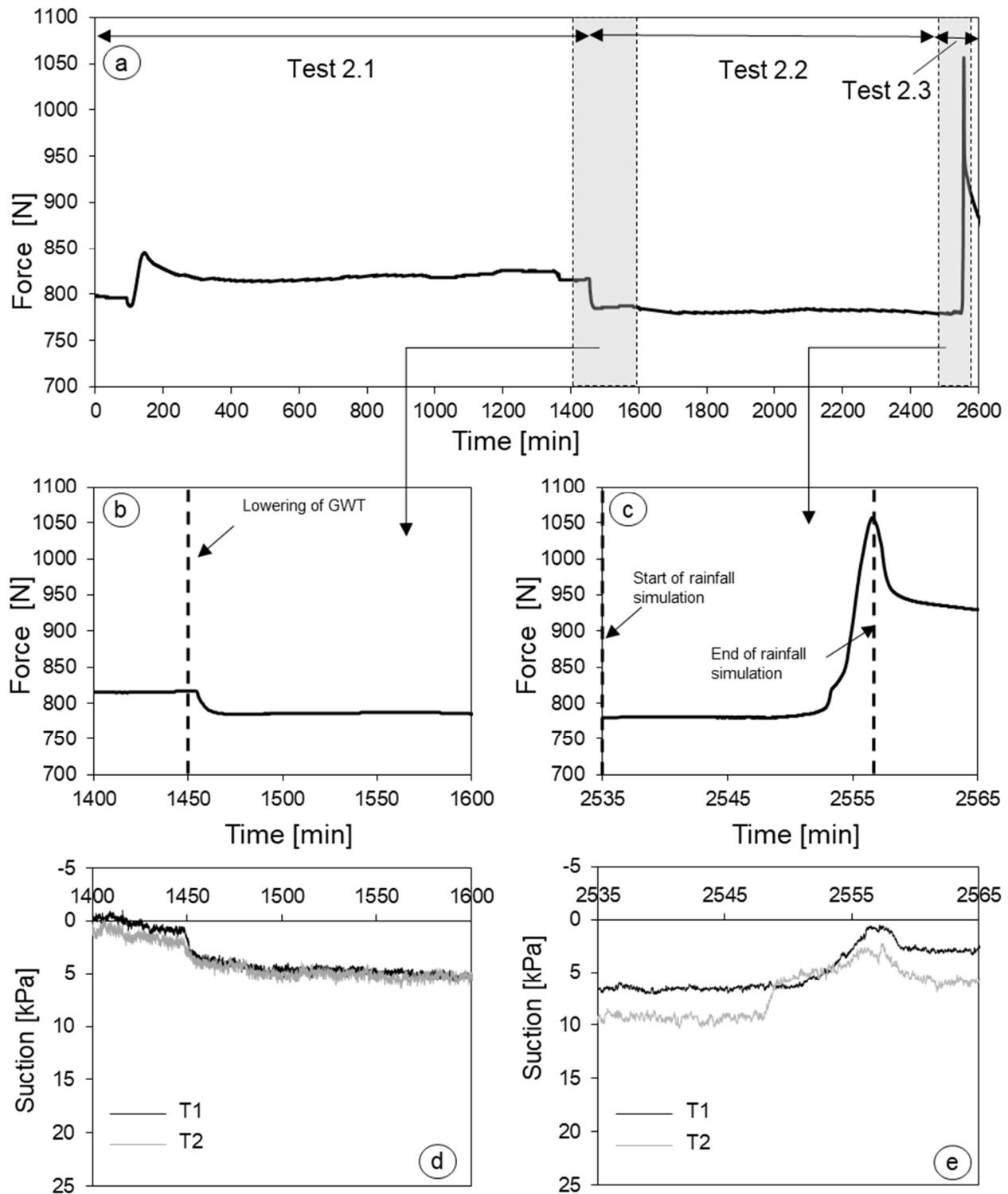


Figure 5.17. a) Measured horizontal component of the lateral earth thrust; b) measured horizontal component of the lateral earth thrust, zoomed-in at the time of the GWT lowering c) measured horizontal component of the lateral earth thrust, zoomed-in at the time of the rainfall event simulation; d) measured matric suction at the time of the GWT lowering; e) measured matric suction at the time of the rainfall event simulation.

At this stage, an unsaturated front started to propagate in the retained soils; menisci were generated within the soil body as well as the matric suction. Once the steady-state was

reached, two tensiometers (T1 and T2) were installed within the unsaturated portion of the retained soils at the depth $z = 40$ cm (T1) and $z = 30$ cm (T2). After 50 minutes ($t = 1450$ min), the matric suction values were considered equalized, and Test 2.2 was initialized: the water level was reduced, opening the drain in the gravel layer at the bottom of the box. The matric suction values recorded by the tensiometers increased while the total horizontal component of the lateral earth thrust measured by the water-filled hydraulic cylinder reduced (784 N). Comparing Figure 5.17b and Figure 5.17d, the shape of the two curves is similar. This result is a good achievement because it shows a clear measured relation between changes in matric suction and lateral earth thrust. The imposed boundary condition was kept until $t = 2535$ min. At that time, the matric suction values were 6 kPa and 9 kPa, respectively.

It has to be noticed that, as expected, the matric suction values measured by T2 are higher with respect to that of T1, and both of them are higher with respect to a hypothetical hydrostatic distribution of the pore water pressure. This is highly likely due to evaporation and the condition of equilibrium obtained, especially by T2 that is placed closer to the dry portion of the retained soil.

At $t = 2535$ min, Test 2.3 was started, the rainfall simulator was activated, and a wetting front started to propagate from the top to the bottom. Initially, when the wetting front was propagating in the portion of soil that was not affected by the capillary rise (Test 2.1 and Test 2.2), no change in the horizontal component of the lateral earth thrust was observed. When the wetting front reached the position of T2, the latter recorded a reduction of the matric suction (6 kPa). With the time and the propagation of the wetting front, T1 reacted as well. With the proceeding of the rainfall simulation, the matric suction values continue to decrease, reaching a minimum of almost 0 kPa for T1 and 2 kPa for T2. Meanwhile, the horizontal component of the lateral earth thrust increased, reaching a maximum value of 1055 N. At $t = 2557$ min, the rainfall simulation has been stopped, water continued to flow-down, matric suction increased again, and the horizontal component of the earth thrust reduced.

5.5.2.1 Comparison between the experimental results and the analytical model (at-rest state)

The results reported above are now interpreted in the framework of the analytical analysis. With respect to the at-rest condition, the earth pressure coefficient at rest (K_0): is defined as the ratio between the horizontal (σ'_h) and the vertical effective stress (σ'_v):

$$K_0 = \frac{\sigma'_h}{\sigma'_v} \quad (5.7)$$

According to the choice of effective stress definition, the earth pressure coefficient at rest can be modified by considering the partial saturation (Oh et al. 2013). By adopting the generalized effective stress definition, it is possible to obtain:

$$K_0 = \frac{(\sigma_h - u_a) + S_r (u_a - u_w)}{(\sigma_v - u_a) + S_r (u_a - u_w)} \quad (5.8)$$

By extrapolating the ratio between the total horizontal stress and the total vertical stress, it is possible to identify the lateral earth pressure coefficient for unsaturated soils in terms of net stress:

$$K_0^* = \frac{(\sigma_h - u_a)}{(\sigma_v - u_a)} = K_0 - \frac{(1 - K_0) + S_r (u_a - u_w)}{(\sigma_v - u_a)} \quad (5.9)$$

Both the coefficient of lateral earth pressure in terms of net stress (K_0^*), and the total vertical stress (σ_v) have been computed for all the steps of the performed tests. The height of the wall-model (H) has been discretized in 5 parts, every 10 cm to compute the lateral earth pressure profile. Pore air pressure (u_a) is assumed to be equal to the atmospheric pressure while pore water pressure distribution is deducted from the imposed hydraulic boundary conditions and the values measured by the tensiometers. Regarding the simulation of the rainfall event, the top of the retained soil is assumed saturated with a water pressure of 0 kPa. The linear distribution of water pressure is assumed within the depths at which water pressure values are known (imposed hydraulic boundary conditions or measured by tensiometers). Thanks to the model adopted for the interpretation of the water retention behaviour (Figure 5.8), the degree of saturation profiles are obtained. The followed paths (both drying and wetting scenarios) are reported in Figure 5.18.

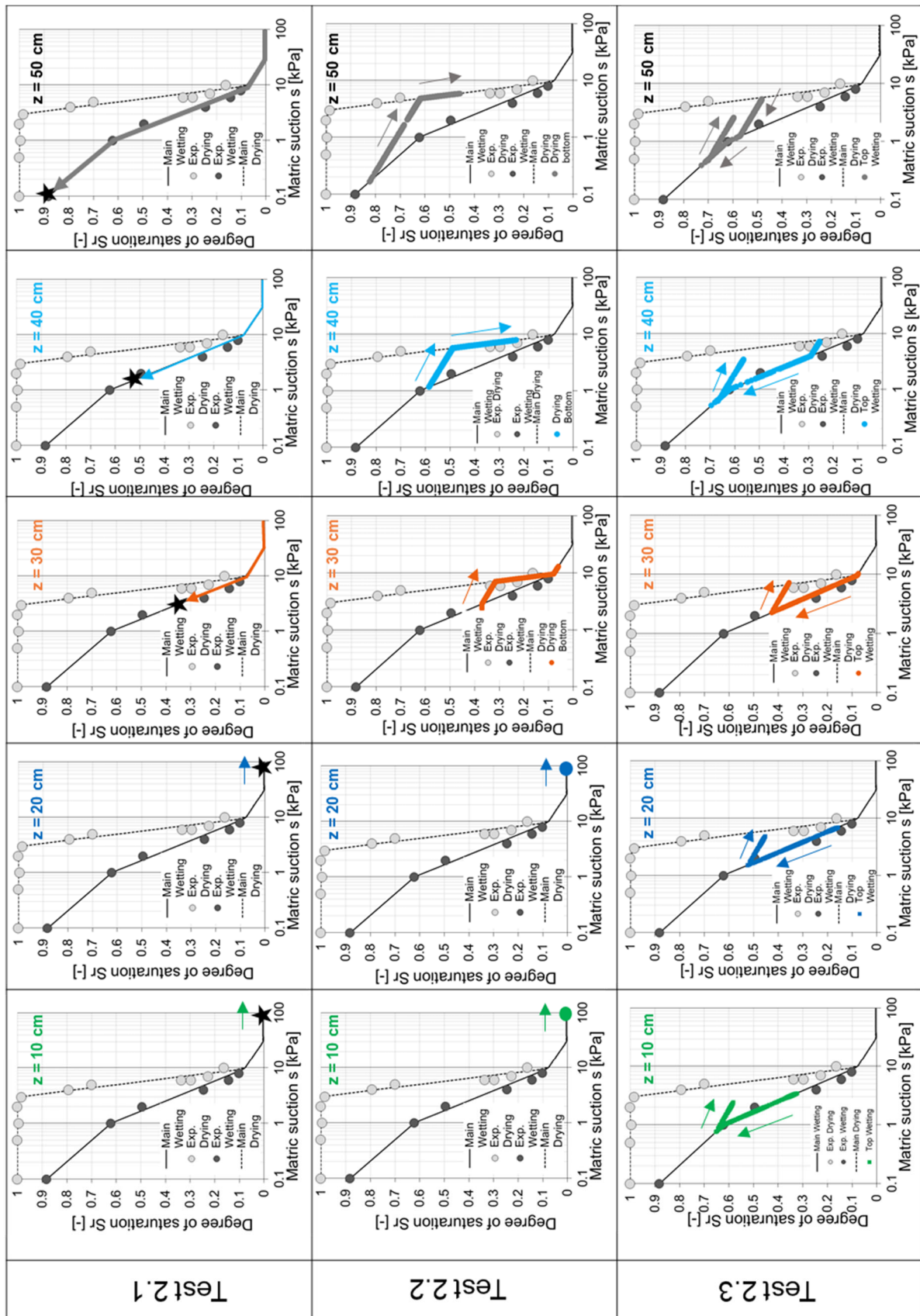


Figure 5.18. Representation of the drying and wetting paths on the SWRC at 10 cm, 20 cm, 30 cm, 40 cm and 50 cm of depth.

The adopted hysteretic model allowed to compute the degree of saturation by knowing the suction values by moving from the drying to the wetting path and the other way around.

By adopting equation 5.6 the soil unit weight has been computed for the identification of the vertical net stress. The evolution with the time of the pore water pressure (u_w), the degree of saturation (S_r), the total vertical stress (σ_v) and the coefficient of earth pressure at rest (K_0^*) are reported in Figure 5.19 at the depths of the discretized domain. The evolution of the pore water pressure in Test 2.1 represents the equalization of the values recorded by the tensiometers and can be considered the initial condition for the following tests. And, the star symbols represent the initial point for Test 2.2 at which the suction values equalized.

In Test 2.2 (drying from the bottom) with the decrease of the porewater pressure (u_w) (increase of matric suction) and the related decrease in the degree of saturation (S_r), the decreasing of the lateral earth pressure coefficient defined in terms of net stress can be noticed. While, in Test 2.3, first, due to the wetting, K_0^* tends to increase then when the seepages stopped, a reduction is observed.

During the drying from the bottom (Test 2.2), an initial reduction of K_0^* is found in the unsaturated portion of the retained soil ($z = 30$ cm, 40 cm, and 50 cm), followed by an increase that is resulted to be higher at lower depths. This is due to the path followed in the water retention curve and the level of vertical stress. Figure 5.20 also shows the evolution of K_0^* with the time during the simulation of the rainfall event at the depths of the discretized domain.

In the end, the horizontal component of the lateral earth thrust in the at-rest condition is measured during suction variation induced by seepages or variation of the imposed hydraulic boundary conditions. The results of the tests are compared with the integral of the theoretical expression of the earth pressure distribution in the at-rest condition:

$$P_0 = \int_0^H K_0^* (\sigma_v - u_a) dz \quad (5.10)$$

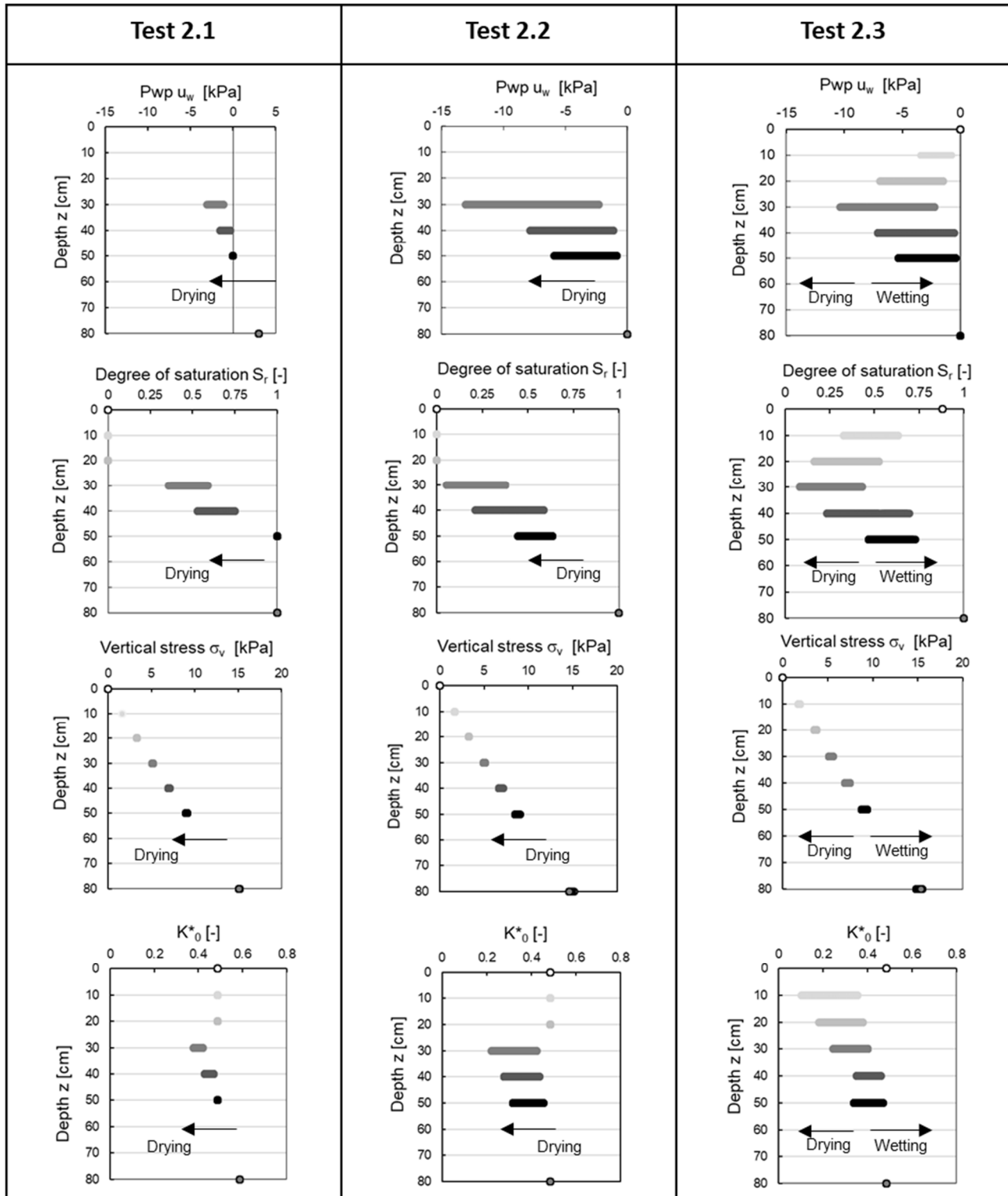


Figure 5.19. Evolution with the depth of the pore water pressure, the degree of saturation, the total vertical stress, and the lateral earth pressure coefficients computed for the Test 2.1 2.2 and 2.3 according to the analytical model.

This is consistent with the measured horizontal component of the lateral earth thrust (P_0). The evolution of K_0^* with the time within the three tests is reported in Figure 5.20. According to equation 5.10, once K_0^* and σ_v profiles are known within the retained soils, it is possible to compute horizontal component of the lateral earth thrust.

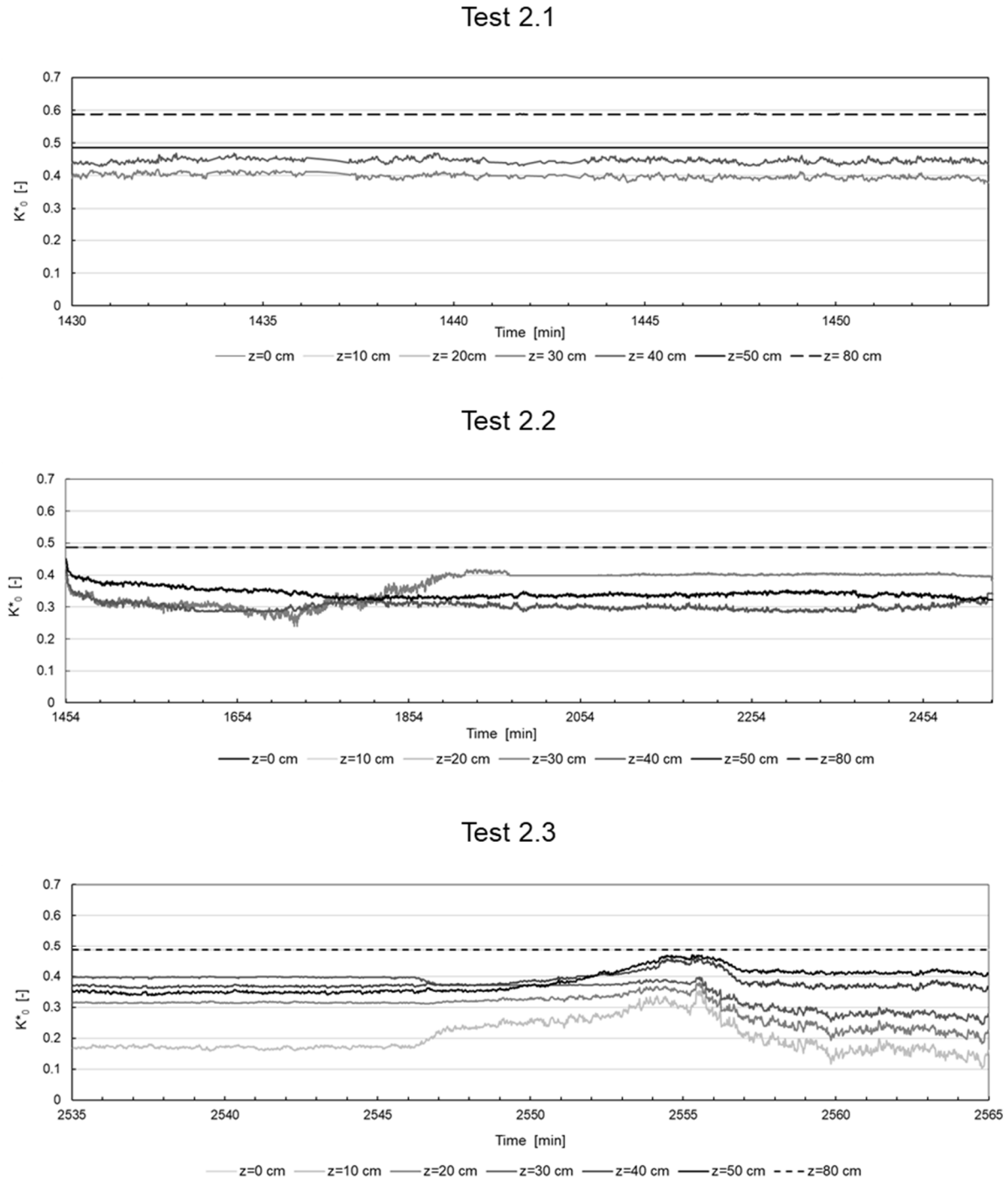


Figure 5.20. Evolution with the time of the lateral earth pressure coefficient computed at different depths.

The comparison between the values of the horizontal thrust computed with the analytical expression (equation 5.10) and the measured one is shown in Figure 5.21.

Globally the analytical model, which exploits matric suction measurements, is in agreement with the experimental data for the three tests. On the other hand, some discrepancies can be identified. The increase of the matric suction observed at the beginning of Test 2.1 and at the end of Test 2.3 allows computing the decrease of the horizontal thrust that is higher with respect to measured values. The noise of the curves is due to that of suction measurements. Indeed, a small variation of matric suction can induce a considerable change in the degree of saturation. On the other hand, the peak value of the horizontal force is caught by the adopted model with a difference of 52 N.

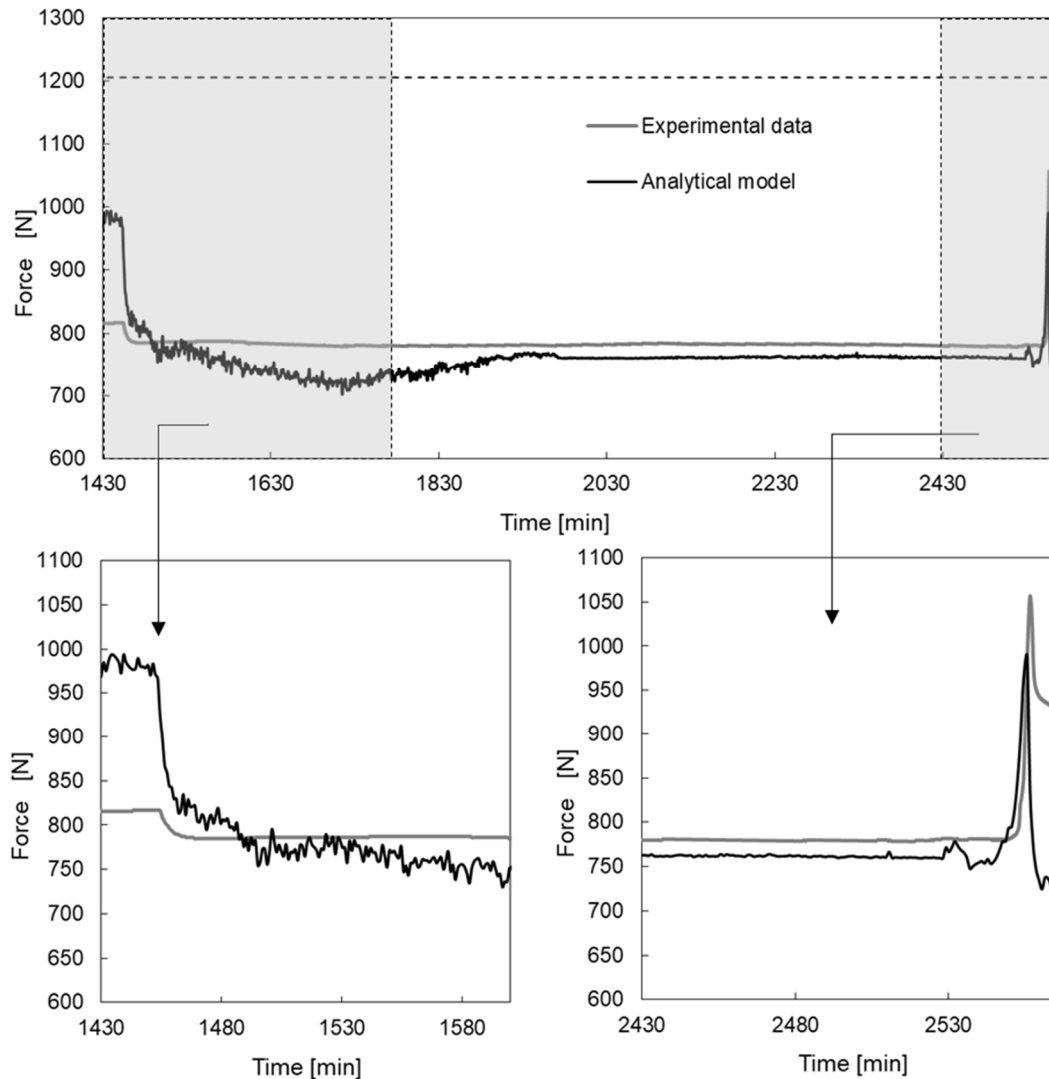


Figure 5.21. The horizontal component of the lateral earth thrust, a comparison between the analytical model and the experimental values.

5.6 Conclusions

In this chapter, a 1-g physical model for the interaction between unsaturated soils and retaining structures has been presented. In the first part of the chapter, the model has been detailed describing its peculiarities. The design of the apparatus, the chosen size of the box-container, the materials, and the employed measurement systems have been detailed. In the second part of the chapter, first performed tests are described then the experimental results have been reported.

The performed tests have shown that the physical model is capable of measuring the lateral earth thrust in both dry and unsaturated conditions. The comparison between Test 1.1a, Test 1.1b, and Test 1.2 has revealed that the lateral earth thrust at active state is lower if the soil is partially saturated. Moreover, the performed PIV analysis has shown that the partially saturated retained soil is characterized by a different failure mechanism with respect to the case of dry soil. The slope of the failure surface is resulted to be higher in the portion of soils affected by capillary rise.

In the at-rest condition (Test 2.1, Test 2.2, and Test 2.3), the variation of the horizontal component of the lateral earth thrust with matric suction changes has been experimentally obtained. Both the increase and the reduction of matric suction have been found to be related to an increase or decrease of the horizontal component of the lateral earth thrust, respectively.

Moreover, the chapter presents a comparison between analytical and experimental analyses. The physical modeling has been used to investigate first the failure mechanisms at the active state then the influence of matric suction changes on the horizontal component of the lateral earth thrust in the at-rest condition. The analytical formulations are resulted to be in generally good agreement with the experimental results even if a greater discrepancy between the theoretical model and experimental results has been found for the at rest scenario.

At the active state, the choice of the retention model (main drying or main wetting curve) is resulted to be a key point in the computation of the lateral earth thrust of unsaturated re-

tained soils. Adopting the main wetting curve in the analytical analyses is more precautionary respect to employ the main drying curve. The experimental data are resulted to be within the range of values identified by adopting the theoretical extension of Rankine's theory.

In view of a possible adoption of the unsaturated soil mechanics for geotechnical analyses of retaining structures, the analytical models are suggested to be employed as pre-estimation of the lateral earth thrust acting on permanent or temporary retaining structures.

Chapter 6

Long-term performance and life cycle assessment of energy piles in three different climatic conditions

6. Long-term performance and life cycle assessment of energy piles in three different climatic conditions

The content of this chapter has been published in:

Journal Paper: *Sutman, M., Speranza, G., Ferrari, A., Larrey-Lassalle, P. and Laloui, L., 2020. Long-term performance and life cycle assessment of energy piles in three different climatic conditions. Renewable Energy, 146, pp.1177-1191.*

Contribution of the Candidate: literature review, analysis of input data, implementation of the life cycle assessment model, analysis and interpretation of the life cycle assessment analysis, paper writing.

6.1 Foreword

The research activities reported in this chapter were carried out in the framework of the T.E.R.R.E. European Project. The Candidate was involved in this inter-sectoral and intra-European project via a “joint-enrolment” between the Laboratory of Soil Mechanics of the Swiss Federal Institute of Lausanne (EPFL) and the industrial partner Nobatek/Inef4. In this context, the Candidate has worked on the investigation of the environmental performance of thermal activated pile foundations (equipped with a ground source heat pump) making a comparison with a traditional piles foundation (equipped with a conventional heating and cooling system).

6.2 Introduction

Global energy requirements are expected to expand by 30% by 2040 as a result of global economy growth with an annual rate of 3.4%, a projected population increase of 1.6 billion, and inevitably increasing urbanization (International Energy Agency, I. E. A., 2017). Space heating and cooling is the world’s largest energy sector, for instance, it accounts for 50% of the final energy consumption of Europe (European Commission, 2016). It was also responsible for 28% of global energy-related CO₂ emissions in 2017 (International Energy Agency, I. E. A., 2019a). Fossil-fuel-based and conventional electric equipment still dominate the global building market, which accounts for more than 80% of the heating equipment (International Energy Agency, I. E. A., 2019b). Moreover, owing to global warming, economic

growth, and urbanisation, the use of energy for space cooling has more than tripled between 1990 and 2016 (International Energy Agency, I. E. A., 2018). In this context, the development and diffusion of reliable, economically viable, and environment-friendly technologies for meeting a significant portion of the energy requirements of the building sector is an important challenge.

The energy pile concept is a technology that enables the use of renewable energy sources for efficient space heating and cooling. In this system, the piles that are already required for structural support are equipped with geothermal loops for performing heat exchange operations to exploit the near-surface geothermal energy. The idea behind the energy geostructures comes from the fact that the temperature of the ground remains the same throughout the year after a certain depth (8-10 meters). Therefore, with the integration of the geothermal loops and the heat carrier fluid circulating within them, the heat is extracted from the ground to heat the buildings during winter. Similarly, during summer, the extra heat is injected into the ground to cool them. In this system, ground source heat pumps (GSHP) are often required which work intermittently in order to adapt the temperature of the circulating fluid to meet the energy demands from the building side.

Given the great potential of energy piles for reducing the dependency on fossil fuels, various in situ tests were performed on this subject (Laloui et al., 2006, Bourne et al., 2009, You et al., 2016, Mimouni and Laloui., 2015, Faizal et al., 2016, Rotta Loria and Laloui, 2016, Sutman et al., 2019). Moreover, several models or tools with varying complexity were developed for the analysis and design of energy piles (Knellwolf et al., 2011, Bourne-Webb et al., 2014, Salciarini et al., 2014, Rotta Loria et al., 2016, Makasis et al., 2018, Sutman et al., 2018). Although the previous research has answered the majority of the fundamental questions on the mechanisms governing the thermo-mechanical behaviour of energy piles, in these studies the temperature changes have been imposed to the test piles instead of being natural consequences of an actual operation. In a few studies, the long-term behaviour of energy piles employed in real operations have been monitored (Brandl, 2006, Loveridge et al., 2016, McCartney et al., 2017). Nevertheless, no experimental data has yet been published in order to perform a systematic comparison of the long-term performance of energy piles under different climatic conditions, i.e., energy piles being subjected to various heating and cooling demands. In addition, although the role of geotechnical engineering in sustainable

development is being increasingly recognized (Basu et al., 2014), there still exist uncertainties related to the actual environmental impact of these so-called green geostructures on their life cycle (LC), which is influenced by the material production, transportation, execution, use, and end of life (EOL) and greatly depends on the demand/supply relationship between the upper structure and energy piles.

Considering the above-mentioned challenges, a 3D finite element model for a group of energy piles was developed which is capable of taking into consideration the real operating philosophy of a GSHP, i.e., intermittent operation. Moreover, the actual space heating and cooling demands of a reference office building from three cities in Europe (Seville, Spain; Rome, Italy; and Berlin, Germany) were employed in the model to represent three diverse climatic conditions (warm, mild, and cold, respectively). In this paper, the numerical model is first described in detail. The heating and cooling demands versus supply data, temperature of the heat carrier fluid as well as of the piles and the soil are then reported for the purpose of comparison. Next, a life cycle assessment (LCA) model is implemented to estimate the environmental impacts of the energy piles employed in the different cities. Finally, a comparison with a conventional heating and cooling system is presented in terms of human health, ecosystem quality, climate change, and resource depletion.

6.3 Material and methods

One of the main goals of this study is the assessment of the long-term performance of energy piles in different climatic conditions (i.e., different heating and cooling demands). To obtain a thorough comparison in this respect, the space heating and cooling demands for a reference building type at different climatic conditions should be employed as the input in numerical simulations. The ENTRANZE Project (ENTRANZE, 2019, Zangheri et al., 2014) presents the necessary data for this purpose, where the heating and cooling energy demands for four different reference building types (single family house, apartment block, office building, and school) are systematically determined using the whole building energy simulation program, EnergyPlus. Among the reference buildings employed in the ENTRANZE Project, the reference office building was selected for the analysis presented in this paper. The reference building is a medium-size, five-story building with 3-m high floors. The net

heated area of the building is 2400 m². Each floor of the building is of the same size of 30 m × 16 m, in length and width, respectively.

Within the ENTRANZE Project, 10 key cities, in other words ten climatic conditions, in Europe are reported to be selected for building energy simulations while considering the winter severity index (WSI), summer severity index (SSI), and climatic cooling potential (CCP) as indicators. From among the 10 cities, three were selected for the present study: Seville, Rome, and Berlin. These cities, in particular, were selected to represent three different climatic conditions and diverse space heating and cooling demands (Figure 6.1). Seville, with a high SSI and low WSI, represents the case of a heat pump operation more on the cooling side. In contrast, Berlin represents a case with high heating and significantly low cooling demands. Furthermore, the heating-cooling demands in Rome lie between those of the two former cities with almost balanced space heating and cooling requirements.

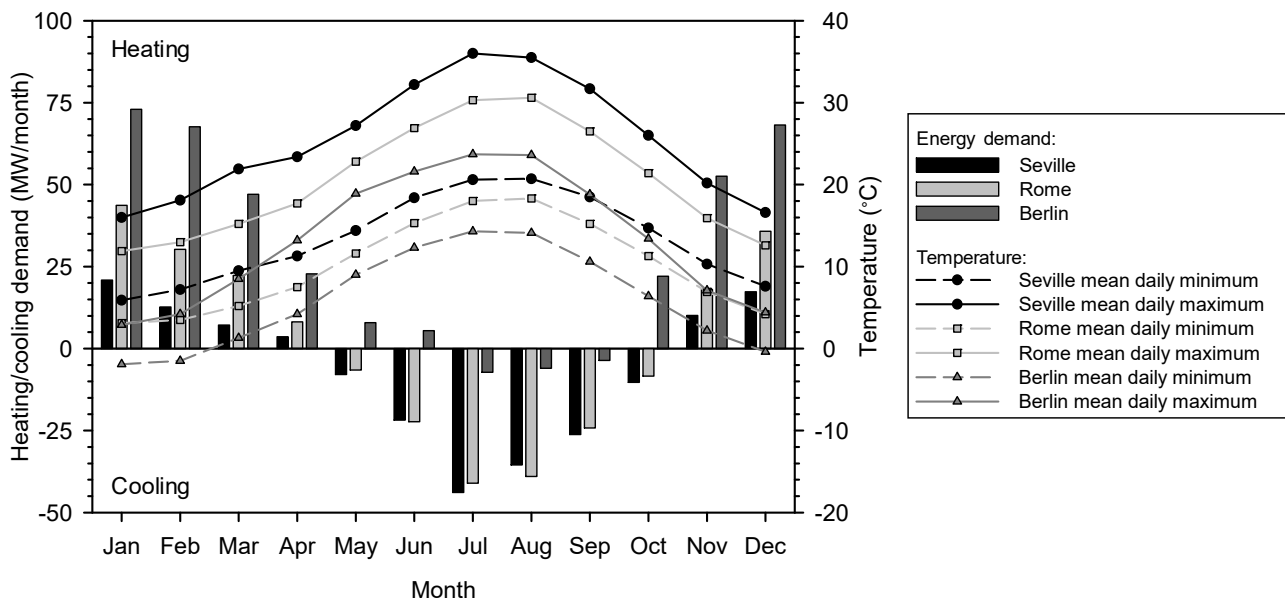


Figure 6.1. Heating/cooling demand histogram; minimum and maximum mean daily temperatures at Seville, Rome, and Berlin.

6.3.1 3D Finite Element Modelling of an Energy Pile Group

A 3D time-dependent finite element model (Figure 6.2.a) was built using the COMSOL Multiphysics Software (COMSOL, 2018) to investigate the long-term performance of energy piles,

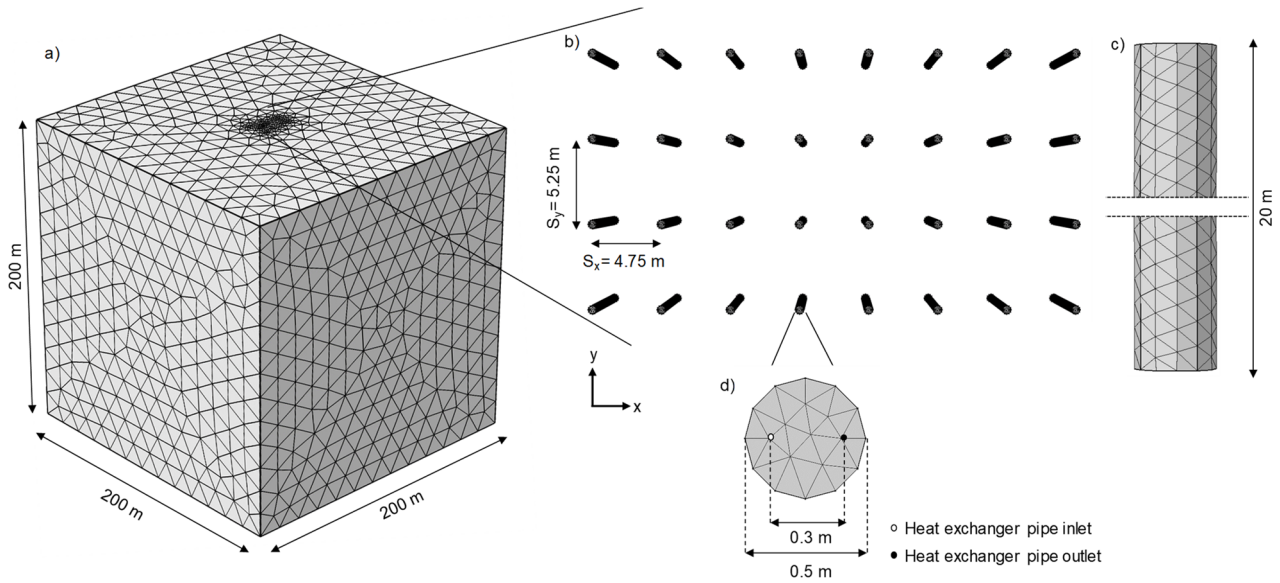


Figure 6.2. a) Finite element mesh; b) Energy pile foundation layout; c) Energy pile geometry and pipe positions.

thus allowing the intermittent operation of the heat pump. In other words, in the presented model, the heat pump operates until the daily heating/cooling demand of the building is met, following which the operation is automatically terminated until the next day. The intermittent operation of the heat pump allows the temperatures of the pile and soil to recover to some extent during the stoppage times, which is also the case for the actual geothermal operations of energy piles. The heating-cooling demands presented in the previous section were employed in the model for this purpose. Although the employed mathematical formulation has proved to be adequate in modelling heat transfer in pipes and porous media regarding energy piles (Rotta Loria and Laloui, 2016), the enhancement of the model with GSHP remains to be corroborated with the experimental data becoming available.

With reference to the foundation of the reference building, 32 piles that were 0.5 m in diameter and 20 m in length were employed. The piles had a 4.75-m and 5.25-m centre-to-centre spacing in the x- and y-directions, corresponding to pile spacing ratios of 9.5 and 10.5, respectively (Fig. 2.b). Each pile was equipped with a single U-loop pipe, with a central distance of 0.3 m between the entering and exiting pipes.

Regarding the discretization of the model, mesh independence analyses were performed and element quality was controlled systematically in order to avoid erroneous interpretation of the model results. The model comprises of extremely fine and extra fine meshes of 902,104 elements in total to characterize the soil (590,509 elements) and pile (311,595 elements) domains. Tetrahedral, triangular, linear and vertex elements were employed to describe the finite element model. Regarding the pipes, Pipe Flow Module of COMSOL Multiphysics Software was employed, which idealizes the 3D flow within pipes to edge elements. The mesh for the pipes were defined by 8,075 edge elements.

6.3.1.1 Mathematical formulation

In the presented model, the heat transfer in the porous media module was employed for the pile and soil domains. The soil domain was assumed to be isotropic and fully saturated with water. For both the soil and pile domains, equivalent thermal properties characterising the fluid and solid phases were assigned, and pure thermal conductivity was anticipated, which is governed by the following equation:

$$\rho c \frac{\partial T}{\partial t} - \text{div}(\lambda \mathbf{grad} T) = 0 \quad (6.1)$$

where ρ is the density, c and λ are the specific heat capacity and thermal conductivity, respectively, including both fluid and solid components, T is the temperature, and div and \mathbf{grad} are the divergence and gradient operators, respectively. With respect to the heat transfer in the pipes within the energy piles, the following equation was employed while considering an incompressible fluid in the pipes:

$$\rho_f A_p c_f \frac{\partial T_f}{\partial t} + \rho_f A_p c_f \mathbf{u}_{f,i} \cdot \mathbf{grad} T_f = \text{div}(A_p \lambda_f \mathbf{grad} T_f) + \frac{1}{2} f_D \frac{\rho_f A_p}{d_h} |\mathbf{u}|^3 + q'_w \quad (6.2)$$

where ρ_f , c_f , and λ_f are the density, specific heat capacity, and thermal conductivity of the fluid, respectively; A_p and d_h are the cross-sectional area and hydraulic diameter of the pipe, respectively; T_f is the temperature of the fluid; $\mathbf{u}_{f,i}$ is the velocity vector; and f_D is the Darcy friction factor. q'_w represents the heat transfer through the unit length of the pipe wall and is governed by the following equation:

$$q'_w = 2h_{eff}\pi r_{in}(T_{out} - T_f) \quad (6.3)$$

where r_{in} and T_{out} are the inner diameter and outer temperature of the pipe, respectively, and h_{eff} is the effective heat transfer coefficient of the pipe, which is governed by the following equation:

$$h_{eff} = \frac{2\pi}{\frac{1}{r_{in}h_{int}} + \frac{\ln(r_{out}/r_{in})}{\lambda_p}} \quad (6.4)$$

where r_{out} and λ_p are the outer diameter and thermal conductivity of the pipe, respectively, and h_{int} is the convective heat transfer coefficient inside the pipe, which is obtained using the following equation:

$$h_{int} = Nu \frac{\lambda_f}{d_h} \quad (6.5)$$

The Nusselt number (Nu) is the ratio of the convective to conductive heat transfer across a boundary and is given by the below equation:

$$Nu_{turb} = \frac{(f_D/8)(Re - 1000)Pr}{1 + 12.7\sqrt{f_D/8}(Pr^{\frac{2}{3}} - 1)} \quad (6.6)$$

The Reynolds number (Re) is the ratio of the inertial forces to viscous forces (Equation 6.7), and the Prandtl number (Pr) is the ratio of the momentum diffusivity to thermal diffusivity (Equation 6.8).

$$Re = \frac{\rho_f u d_h}{\mu_f} \quad (6.7)$$

$$Pr = \frac{\mu_f c_f}{\lambda_f} \quad (6.8)$$

Finally, the Darcy friction angle can be obtained using a simplified Haaland Equation (Haaland, 1983) for a low relative roughness, Colebrook Equation [Colebrook, 1939], as shown below:

$$\sqrt{\frac{1}{f_D}} = -1.8 \log_{10} \left(\frac{6.9}{Re} \right) \quad (6.9)$$

6.3.1.2 Boundary and Initial Conditions

The Neumann boundary condition with no heat flux is assigned to the ground surface since in most energy pile applications, thermal insulation is ensured between the slab and the upper environment. On the other hand, prescribed temperature (Dirichlet) boundary condition is specified for the vertical sides and the bottom boundary. The size of the soil domain is taken large enough at distances where the heat exchange operations have no effect, in order to avoid any boundary effects. The average annual ground temperatures for three cities, which is determined by relating the air temperature to the ground temperature (Kusuda and Achenbach, 1965), are assigned to the vertical sides and bottom boundaries, as well as to all the materials used in the model as the initial condition.

6.3.1.3 Material properties

In the presented model, the climatic conditions of the three cities were used to define the average ground temperature and also the heating and cooling demands from the building side. However, the soil conditions and material properties were the same for the three cities for the purpose of systematically comparing the long-term response of energy piles to three different energy demands. The soil domain in the model is assumed to be isotropic, fully saturated, medium dense sand. The pile domain is assumed to be reinforced concrete. The material properties for both the soil and pile domains are presented in Table 6.1. Table 6.2 presents the properties assigned to the pipes for which 1-inch, cross-linked polyethylene (PEX) pipe type was assumed. Regarding the water circulating within the pipes, temperature-dependent properties were assigned for the density, thermal conductivity and specific heat capacity determined by (Ionescu and Neagu, 2017).

6.3.1.4 Idealized Heat Pump

A 30-kW water-to-water heat pump is used in the analysis conducted for the three reference cities. To simulate the intermittent operation of the heat pump, indicator states are included in the model, which monitor whether the daily heating/cooling demand is fulfilled for each time step. Once the demand is fulfilled, the heat pump operation stops until the

next day, but the water still continues to flow within the pipes, thus allowing thermal recovery.

Table 6.1 Material properties for the soil and pile domains

Parameter	Sand	Concrete
Density [kg/m ³]	1990	2300
Poisson's Ratio []	0.3	0.2
Thermal Conductivity [W/(m·K)]	2.5	1.8
Specific Heat Capacity [J/(kg·K)]	1175	880

Table 6.2 Properties assigned for the pipe

Property	Value
Inner Diameter [m]	0.0262
Pipe Wall Thickness [m]	0.0029
Thermal Conductivity [W/(m·K)]	0.41
Nominal Velocity of Flow [m/s]	3.7

In addition to the GSHP system, an auxiliary system (conventional boiler or chiller) is also taken into consideration, if the GSHP system is not competent in delivering the entire heating/cooling demand. The amount of energy supplied by the auxiliary system is particularly important in this study as it is essential to employ it in the LCA analysis.

The energy balance governing the building heating/cooling operation is shown below:

$$Q_{sec} = Q_{prim} + W_{hp} + Q_{aux} \quad (6.10)$$

where Q_{prim} is the energy supplied by the energy piles, W_{hp} is the energy input for the operation of the heat pump, and Q_{aux} is the energy to be supplied by an auxiliary system. The heating and cooling demands of the office building, which vary depending on the reference city and time, are introduced in the model (Figure 6.1) to represent the secondary circuit (Q_{sec}).

The inlet ($T_{in,prim}$) and outlet ($T_{out,prim}$) temperatures of the water circulating within the piles are not constant but vary depending on the heating/cooling demand of the secondary circuit, coefficient of performance (COP) of the heat pump, as well as the heat transfer within the pipes and porous media.

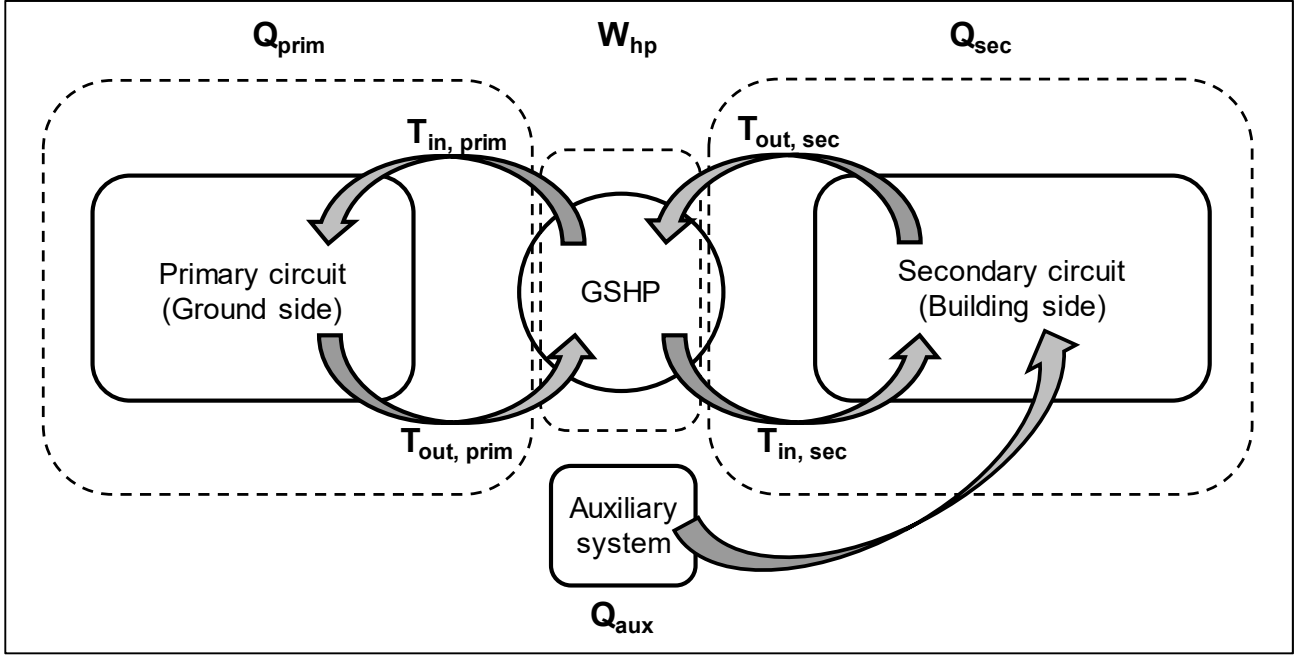


Figure 6.3. Scheme of a GSHP system.

The maximum COP of a heat pump is characterised by the source ($T_{out,prim}$) and delivery ($T_{in,sec}$) temperatures (Sarbu and Sebachievici, 2014) in Kelvin (Figure 6.3) while considering the reverse Carnot cycle for the heating (equation 6.11) and cooling modes (equation 6.12).

$$COP_{C,h} = \frac{T_{in,sec}}{T_{in,sec} - T_{out,prim}} \quad (6.11)$$

$$COP_{C,c} = \frac{T_{in,sec}}{T_{out,prim} - T_{in,sec}} \quad (6.12)$$

However, the Carnot COP represents the ideal reversible case, which cannot be achieved using a heat pump in practice. Therefore, the Carnot COP is multiplied by an efficiency factor to obtain the actual COP of the heat pump.

$$COP_{hp} = COP_C \eta_{hp} \quad (6.13)$$

where η_{hp} represents the efficiency factor and varies between 0.3 and 0.5 for small electric heat pumps and between 0.5 and 0.7 for efficient electric heat pumps (Kärkkäinen, 2012). Considering typical delivery temperatures for heating (45–90 °C for radiators) and cooling (5–15 °C for chilled water) operations, the possible COP values for a GSHP are presented in Figure 6.4, wherein the delivery temperatures for heating and cooling are fixed at 65 °C and 5 °C, respectively.

As expected, the efficiency of the heat pump increases as the temperature difference between the source and delivery temperature decreases and as the efficiency factor increases. For the present study, a designated efficiency factor of 0.5 is used for the heat pumps in the three reference cities. An algorithm has been employed in the model, which determines the COP depending on the source temperature (equations. 11 and 12); this allows the COP to vary with time for the reference cities.

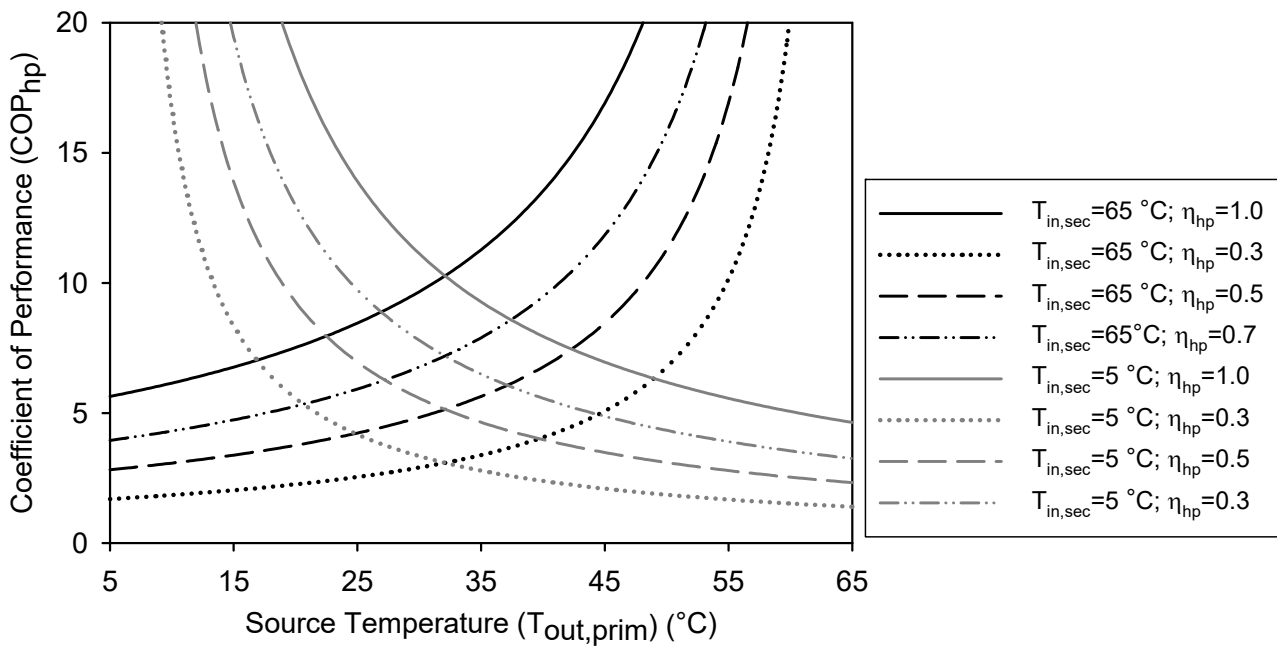


Figure 6.4. COP of GSHP with respect to the source temperature.

In the presented model, the primary circuit of the system is completely modelled in the performed numerical analyses while the contributions provided by the GSHP, secondary circuit, and auxiliary system are idealised as described above. The idealised modelling of the GSHP and secondary circuit allows to achieve the fraction of the heating/cooling demand to be supplied by the energy piles (Q_{prim}), while the portion of the energy that cannot be supplied by the GSHP system is assumed to be covered by the auxiliary system.

6.3.2 Life Cycle Assessment

The environmental performance of energy piles should be compared with that of a conventional heating and cooling system to demonstrate its benefits from an environmental point of view. In this study, the LCA methodology is adopted to evaluate the potential environmental impacts while taking into consideration the material extraction, transportation, execution, use, and disposal. The analyses are performed by implementing the LCA model in the software SimaPro 8.0.3. (PRe Consultants, 2014)

The international standards ISO 14040, 2006 and ISO14044 describe the LCA methodology and the related analysis phases such as goal and scope definition, life cycle inventory (LCI), life cycle impact assessment (LCIA), and interpretation, which are followed in this study. The goal and scope definition step includes the definition of the functional unit (measure of the function of the system), the reference flow (quantitative reference unit required to satisfy the functional unit), and the boundaries of the system. In this work, the functional unit has been defined as follows: “To fulfil the heating and cooling demands of an office building for one year”. The considered design time spans of the building and the electric heating/cooling system were assumed to be 50 years and 20 years, respectively, and were accorded to the functional unit. The reference flow and system boundary are illustrated in Figure 6.5. Two scenarios were selected in the present work to satisfy the annual heating and cooling demand for the three reference cities. In the first case, the function of the deep foundation was only to transfer the mechanical loads to the subsoil while a gas boiler and air conditioner were selected to meet the heating and cooling demands. In contrast, in the second case, the coupling between a group of energy piles and a GSHP was considered.

The flows between the investigated system and the environment, in terms of input and output products, resources, wastes, and emissions, were identified during the LCI. The input data of the LCI are reported in Tables 3 and 4 for the conventional system and energy piles, respectively. The amount of materials was obtained following the geotechnical design of the group of piles (EN 1997).

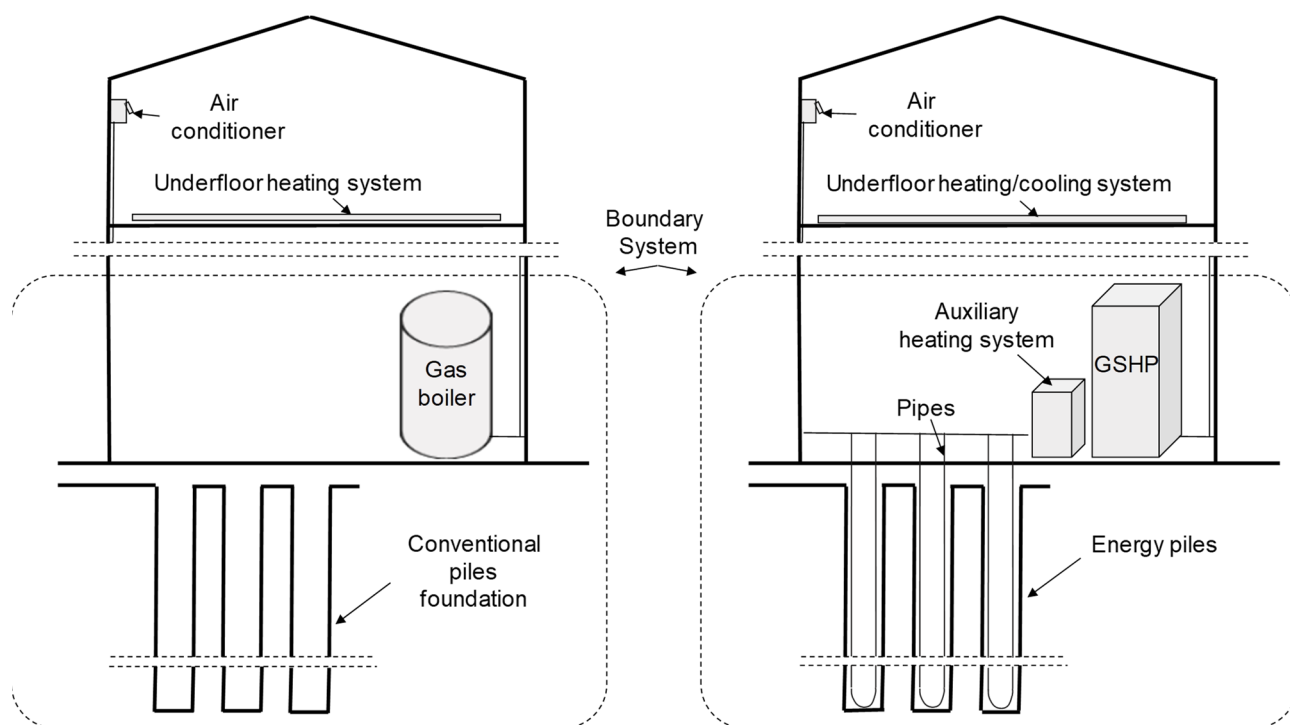


Figure 6.5. a) Office building with pile foundation furnished by a conventional heating and cooling system; b) Office building equipped with energy piles.

The transportation distance was hypothesised as 50 km while the drilling time was obtained in consultation with a specialised company. With respect to the use phase, the amount of energy required in terms of natural gas or electricity was obtained while considering the available heating and cooling demands and the results of the finite element analysis simulation reported in Subsection 6.3.1.

The latter allowed for the estimation of the geothermal energy that can be exploited by the thermal activation of the piles for the considered scenarios. According to the different heating and cooling demands and in situ temperature of the ground, the GSHP system behaves differently for each considered city, and therefore, the corresponding impact on the environment differs. With respect to the electricity supply, national flows were selected with respect to the three reference cities. The disposal scenario takes into consideration the recycling of all the involved materials, while assuming the recycling rates of the construction and demolition waste for the corresponding countries (Monier et al., 2013). The last column of Table 6.3 and Table 6.4 reports the selected environmental flow from the LCI database ecoinvent (Wernet et al., 2016).

During the LCIA phase, the inventoried flows contributing to a given environmental impact category were achieved, the results of which are presented in terms of two main types of indicators selected at two different levels of the impact pathway: midpoint (Appendix B) and end points (Section 6.3).

Table 6.3 LCI of the conventional systems for the three reference cities (SV: Seville; RM: Rome; BE: Berlin).

Life Cycle Step	Input	Amount SV/RM/BE	Unit	Flow from ecoinvent Database
Material Production	Concrete	6,51	m ³	Concrete, normal {CH}
	Rebars	40,00	t	Reinforcing steel {GLO}
	Boiler	0,05/0,10/0,20	-	Oil boiler, 10 kW {CH}
Transportation	Concrete	795,00	tkm	Transport, freight, lorry 16–32 metric ton, EURO5 {GLO}
	Rebars	2,00	tkm	
	Machines	95,30	tkm	
	Transport of Pipes	0,19	tkm	
	Transport (EOL)	797,19	tkm	
Execution	Excavation	34,00	m ³	Excavation, hydraulic digger {GLO}
	Drilling	1,00	hr	Machine operation, diesel, >=74.57 kW, high load factor {GLO}
Use	Heating	71,19/163,26/364,98	MWh	Heat, central or small-scale, natural gas {Europe without Switzerland}
	Cooling	142,44/138,93/20,88	MWh	Electricity, medium voltage {ES/IT/DE}
End of Life (EOL)	Boiler	12,20	kg	Used industrial electronic device {CH}
		0,15	kg	Inert waste, for final disposal {CH}
		3,35	kg	Waste reinforcement steel {CH} collection for final disposal
		2,65	kg	Waste reinforcement steel {CH} treatment of, recycling
		0,05	kg	Waste plastic, mixture {Europe without Switzerland}
		0,40	kg	Inert waste, for final disposal {CH}
	Reinforced concrete	15,90	kg	Waste reinforced concrete {Europe without Switzerland}
		13,70	t	Waste concrete {Europe without Switzerland}
		-2,23	t	Recycling concrete (Rock crushing {RER}) processing
		5,60	t	Waste reinforcement steel {RoW}
	Soil	4,61	kg	Drilling waste {CH} treatment of, residual material landfill

The midpoint indicators usually indicate a change in the environment caused by a human intervention, while endpoint or damage indicators assess damages to (in the majority of cases) three areas of protection, i.e., human health, ecosystem quality, and resources. The

Impact 2002+ (Jolliet et al., 2003) method was selected for performing the LCIA for all the considered cases.

Table 6.4 LCI of energy piles for the three reference cities (SV: Seville; RM: Rome; BE: Berlin).

Life Cycle Step	Input	Amount SV/RM/BE	Unit	Flow from ecoinvent Database
Material Production	Concrete	6,50	m ³	Concrete, normal {CH}
	Rebars	40,00	kg	Reinforcing steel {GLO}
	GSHP	0,01/0,02/0,04	-	Heat pump, 30 kW {RER}
	Auxiliary System	0,00/0,26/0,66	-	Auxiliary heating unit, electric, 5 kW {CH}
	Refrigerant	3,94	kg	Refrigerant R134a {RER}
	Pipes	3,80	kg	Extrusion, plastic pipes {RER}
		38,40	m	Polyethylene pipe, DN 200, SDR 41 {GLO}
Transportation	Concrete	795,00	tkm	Transport, freight, lorry 16–32 metric ton, EURO5 {GLO}
	Rebars	2,00	tkm	
	Machines	95,30	tkm	
	Transport of Pipes	0,19	tkm	
	Transport (EOL)	797,19	tkm	
Execution	Excavation	34,00	m ³	Excavation, hydraulic digger {GLO}
	Drilling	1,00	hr	Machine operation, diesel, >=74.57 kW, high load factor {GLO}
Use	Heating			
	Renewable	53,14/109,14/108,81	MWh	Energy, geothermal, converted
	Heat pump	19,26/56,08/104,39	MWh	Electricity, medium voltage {ES, IT, DE}
	Auxiliary	0,00/0,00/80,39	MWh	Electricity, medium voltage {ES, IT, DE}
	Cooling			
	Renewable	30,93/108,81/17,91	MWh	Energy, geothermal, converted
End of Life (EOL)	Heat pump	5,31/24,97/3,79	MWh	Electricity, medium voltage {ES, IT, DE}
	Auxiliary	6,48/6,45/0,00	MWh	Electricity, medium voltage {ES, IT, DE}
	GSHP	20,40	kg	Used industrial electronic device {CH}
		3,29	kg	Inert waste, for final disposal {CH}
		7,94	kg	Waste reinforcement steel {CH} collection for final disposal
		6,26	kg	Waste reinforcement steel {CH} treatment of, recycling
		0,29	kg	Waste plastic, mixture {Europe without Switzerland}
		0,15	kg	Inert waste, for final disposal {CH}
		1,00	kg	Used refrigerant R134a {GLO}
	Reinforced concrete	16,00	t	Waste reinforced concrete {Europe without Switzerland}
		13,70	t	Waste concrete {Europe without Switzerland}
		-2,23	t	Recycling concrete (Rock crushing {RER}) processing
		5,60	kg	Waste reinforcement steel {RoW}
	Pipes	32,70	kg	Waste polyethylene/polypropylene product {CH}
		0,53	kg	PE (waste treatment) {GLO} recycling of PE
	Soil	4,61	t	Drilling waste {CH} treatment of, residual material landfill

The end point results are presented in terms of climate change ($\text{kgCO}_{2,\text{eq}}$), human health (disability-adjusted life year–DALY), resource depletion (MJ), and ecosystem quality (potentially disappeared fraction of species $\text{PDF}\cdot\text{m}^2/\text{year}$).

The results of the LCA are presented for the three reference cities mentioned above in order to investigate the influence of the heating or cooling demands (direct consequences of the respective local climate) on the environmental performance of the investigated systems. Due to the difference in heating and cooling demands among the reference cities, the outputs of the FEM differ for each case which consequently affects the environmental analysis of the examined cases.

6.4 Results and Discussion

Both the 3D finite element model (Section 2.1) and the LCA analysis (Section 2.2) were employed to reveal the long-term energy performance and environmental impacts of an energy pile project in three different cities (Seville, Rome, and Berlin).

Figure 6.6 shows the influence of the intermittent operation of the GSHP on the water temperature circulating within the pipes during the transition from heating-to-cooling and cooling-to-heating operational modes. The example plot is given for Seville. The upper part of the figures shows the temperature of the water while the lower one shows the operation and stoppage periods within the same timeframe. The figure shows the decrease in the temperature of the circulating fluid with the operation of the heat pump during the heating mode, and the recovery (i.e., increase) of the temperature during the stoppage times, which is the contrary for the case of cooling. A temperature difference of 2–4 °C between the operation and stoppage times can be observed in the figure. The same simulation principle was applied for Rome and Berlin wherein the model was employed for 1 year without interruption.

In this section, the results of the analyses for the three cities under consideration are presented in terms of (i) energy demand and supply, (ii) temperature change along the energy piles and the surrounding soil, and (iii) LCIA in terms of climate change, human health, resources, and ecosystem quality.

6.4.1 Energy Demand and Supply

The comparison of the monthly heating and cooling demands from the building side and the available output from the primary circuit are presented in Figure 6.7, along with the seasonal fluctuation of the heat carrier fluid.

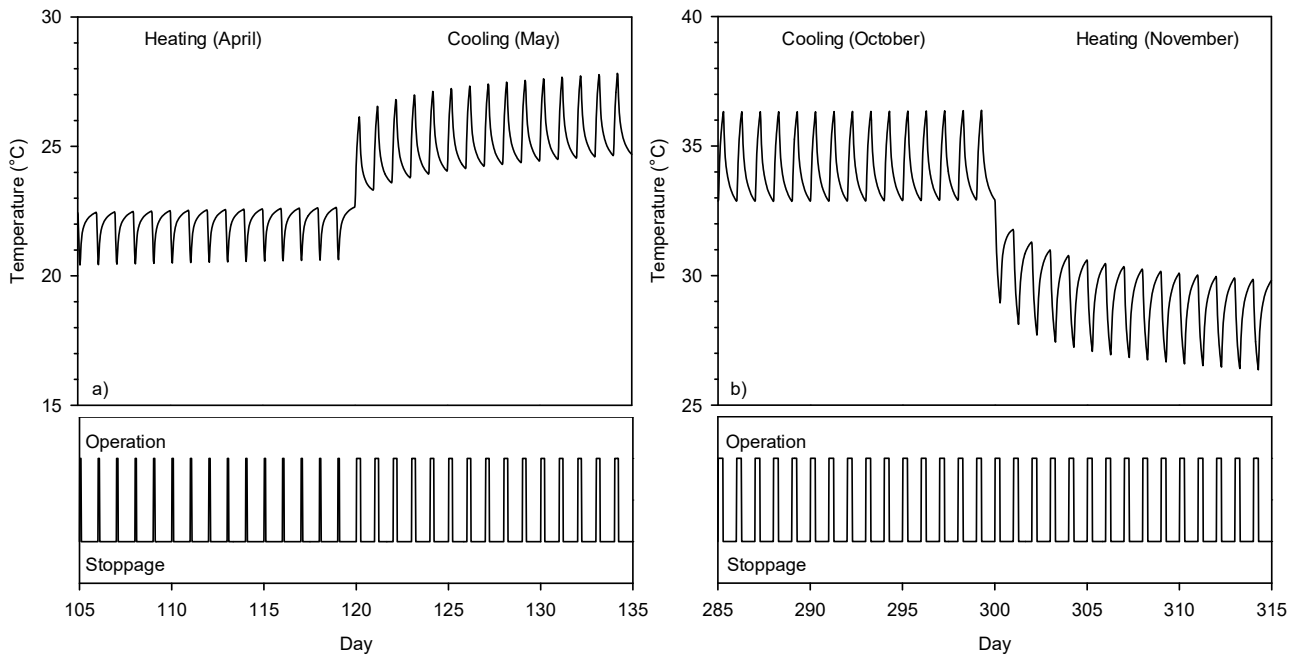


Figure 6.6 Temperature fluctuation of the water circulating in the pipes due to intermittent operation of GSHP during transition from a) Heating to cooling, b) Cooling to heating (Seville).

The demand/supply balance was checked iteratively at 30-min intervals for each day of the simulation, which resulted in a slightly higher supply as compared to the demand during some months if the demand was provided at a shorter time than 30 min. The comparison of the demand and supply shows that the majority of the heating and cooling demand in Seville was met by the GSHP, while an auxiliary cooling system was employed only for the month of July to cover the remaining 13% of the cooling demand (Figure 6.7a). Similar results were obtained for Rome (Figure 6.7b); although the heating demand was higher than that of Seville, the GSHP was capable of realising the required supply, while an auxiliary cooling system was required for the peak cooling periods (i.e., months of July for 11% and August for 6%). In the case of Berlin, the heating and cooling demands, which are characterised by dominant heating and limited cooling, were quite diverse as compared to the former two. The requirement of an auxiliary heating system for the four months of November (14%),

December (33%), January (38%), and February (32%), i.e., during winter, can be observed in Figure 6.7c, while the limited cooling demand was met entirely by the GSHP.

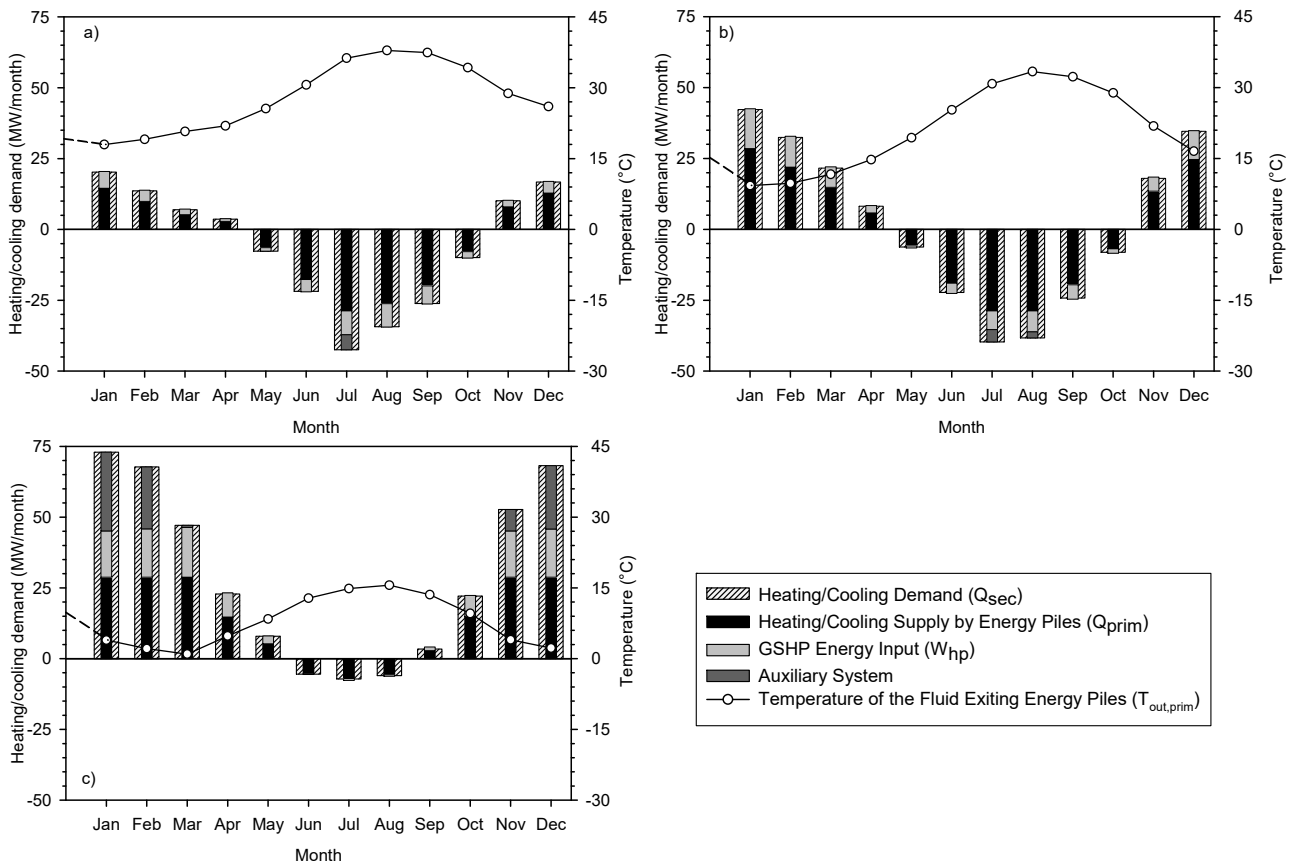


Figure 6.7. Annual distribution of energy demand and supply; temperature of the heat carrier fluid for a) Seville, b) Rome, and c) Berlin cases.

The initial temperatures of the involved elements (i.e., soil, piles, pipes, and heat carrier fluid), which were considered to be constant, were determined by relating the air temperatures to the ground temperatures, which corresponds to 19.2 °C, 15.2 °C, and 9.8 °C for Seville, Rome, and Berlin, respectively. The initial conditions also involved the temperature of the fluid exiting the energy piles ($T_{out,prim}$) as being originally equal to the average ground temperature. Following the start of the geothermal operations, $T_{out,prim}$ showed an annual fluctuation, which was associated with the corresponding heating and cooling demands from the building side. The temperature decrease during the heating operation which was followed by a recovery and a temperature increase period are in agreement with the case studies presented by Brandl, 2006.

6.4.2 Temperature Fluctuations along Energy Piles and in the Surrounding Soil

As a result of their unique roles, the energy piles are exposed to daily and seasonal temperature variations during their lifetime. Temperatures in the pile and in the surrounding soil fluctuate during the day in between operation and stoppage times resulting in short-term temperature changes. Furthermore, there is a seasonal increase in temperatures after episodes of heat injection during summer followed by seasonal temperature reductions during heat extraction in winter.

These temperature changes may cause axial displacements, additional axial stresses, and changes in the shaft resistance, with a daily and seasonal cyclic nature, along their lengths. Moreover, geothermal operations characterised by excessive heat extraction may cause temperatures along the energy piles to decrease below zero, eventually resulting in the formation of ice lenses in the adjacent soil. To prevent the freezing and thawing of the soil during successive heating and cooling operations, which are associated with heave and settlement, a minimum temperature of 2 °C on the shaft of the energy piles is recommended (Brandal, 2006). Finally, a change in the in situ temperature of the ground in the long-term due to geothermal operation of the energy piles should be prevented as it may have a significant impact on the efficiency of the GSHP system. Therefore, the appropriate prediction and monitoring of the temperature fluctuations along the energy piles and surrounding soil is of paramount importance.

To investigate this phenomenon, the temperature evolution along the centre pile and that in the surrounding soil during the geothermal operation in the three cities are presented in Figure 6.8. The maximum temperature decrease and increase due to heat extraction and injection, respectively, and the residual temperature change along the energy pile after 1 year of geothermal operation are specified in the figure. The temperature variations with respect to the in situ temperature of the piles are within the typical range (± 15 – 20 °C) for operating energy piles (GSHP Association, 2012).

The comparison of the temperature variations along the energy pile and surrounding soil (Figure 6.8.) reveals that the soil closer to the energy pile (at a 1-m distance) exhibits a rapid response to the geothermal operation with higher temperature variations, which lags behind and decreases in magnitude at a greater distance (2.4 m) from the piles. Moreover, the

soil at a 2.4-m distance, which is equidistant from the two rows of energy piles, experiences temperature variations as well, although very limited, which evidences the thermal interactions between the neighbouring piles.

Considering the ground temperature variation during the geothermal operation of the energy piles, three types of thermal responses are observed in Figure 6.8: (i) long-term temperature increase in the case of Seville due to cooling-dominant geothermal operation, (ii) thermal balance in the case of Rome, and (iii) long-term temperature decrease in the case of Berlin due to heating-dominant geothermal operation. Influences on the in situ temperature of the ground in the long-term should be avoided during geothermal operations, which significantly depends on the balance of the heating and cooling demands from the building side, as well as the ground water flow corresponding to the natural thermal recharge of the soil, which was not taken into consideration in the present study. In the case of low permeability, the balance between heat injection and extraction should be ensured for the long-term thermal equilibrium of the ground temperature. In contrast, in the case of soils characterised by high permeability, with a ground water flow greater than 0.5 m/day, the ground temperature equilibrium may be ensured by the groundwater flow, after unbalanced heating-cooling operations (Laloui and Di Donna, 2011). Therefore, a special thermal design for the specific GSHP operations is of paramount importance for taking into consideration the space heating/cooling needs and hydrogeological ground conditions, in order to ensure that despite seasonal fluctuations, the in situ ground temperature remains the same in the long-term.

6.4.3 Life Cycle Impact Assessment

The results reported in Section 6.3.1 in combination with the available data from the EN-TRANZE Project were used for the LCI of the two systems (i.e., conventional piles and energy piles) for the three reference scenarios (Section 6.2.2).

The first remarkable outcome of the LCIA is the confirmation that the heating and cooling (use phase) are the main contributors to the climate change impact with respect to the other life cycle stages (material production, transportation, execution, and end of life).

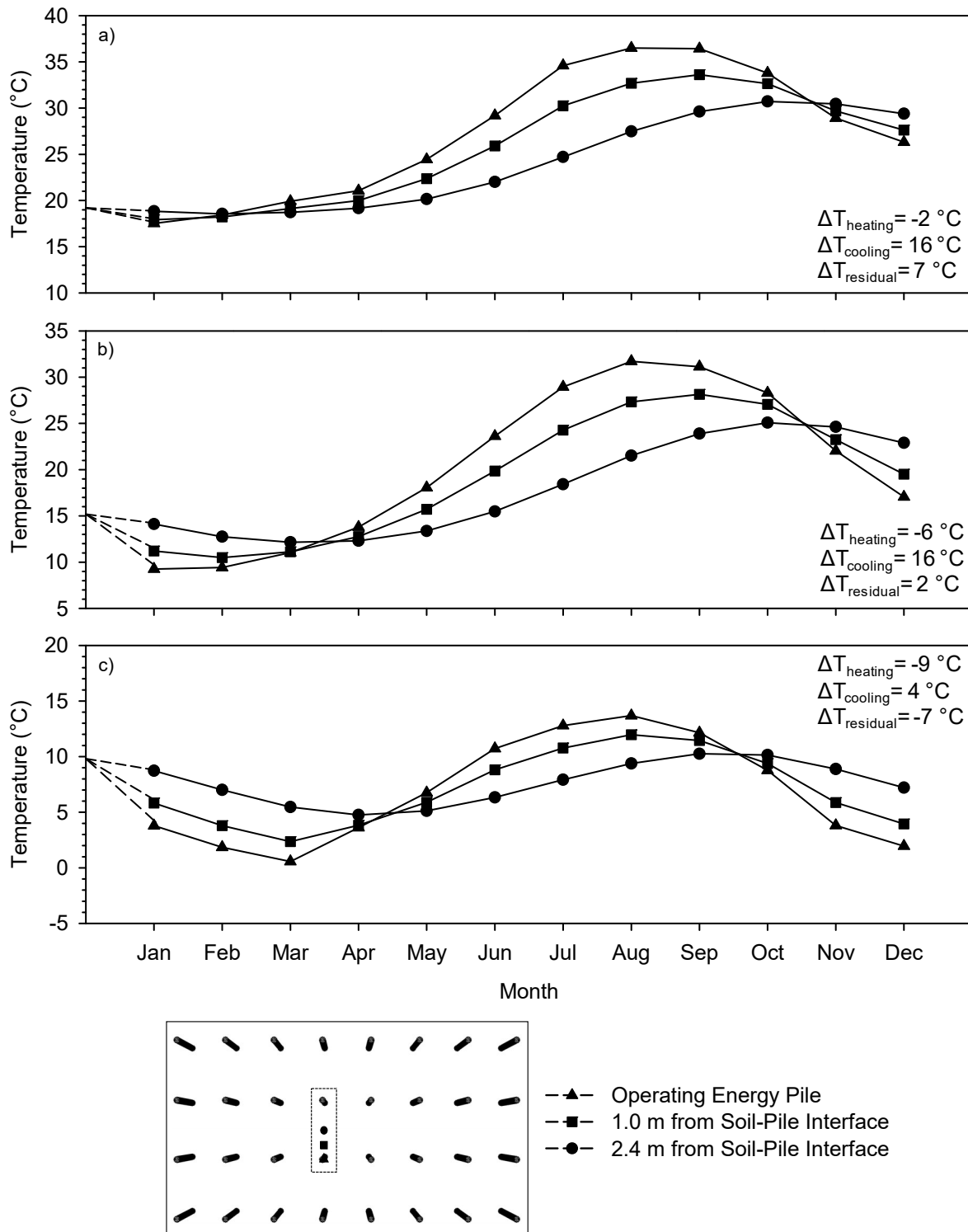


Figure 6.8 Pile and soil temperature during geothermal operations in a) Seville, b) Rome, and c) Berlin.

Considering a conventional pile foundation and a conventional heating and cooling system, Figure 6.9 shows that the use phase contributes up to 98% of the total climate change impact while the residual 2% is represented by the other steps of the geostructure LC (e.g.,

material production, transportation, execution, and end of life). These results clearly identify the LC phase wherein it is potentially possible to reduce the impact on the environment. The energy piles, exploiting the geothermal energy in principle and can aid in reducing the impacts of the use phase. Nevertheless, there are a number of key points that are required to be considered before arriving at this conclusion: additional materials (i.e., pipes, GSHP, and auxiliary system) and different energy sources are required to be introduced in the LC of the system while adopting the energy piles concept. Moreover, the environmental performance is highly dependent on the heating and cooling demands (i.e., the local climate), which consequently varies during the different periods of the year. Finally, the way the energy is produced to satisfy heating and cooling needs differs depending on the country under consideration. Therefore, despite introducing the same energy source in an LC model, it can result in different environmental impacts as the country under consideration changes. The outcomes of the LCIA are used in this study to examine these features.

Figure 6.10 shows the results of the LCIA in terms of the four “endpoint” indicators employed by the Impact2002+ method, while the “midpoint” indicators are reported in the Appendix B, in Figs. A.1, A.2, and A.3. It is directly noticeable that the environmental performance of both investigated systems strongly depends on the countries and the heating and cooling demands.

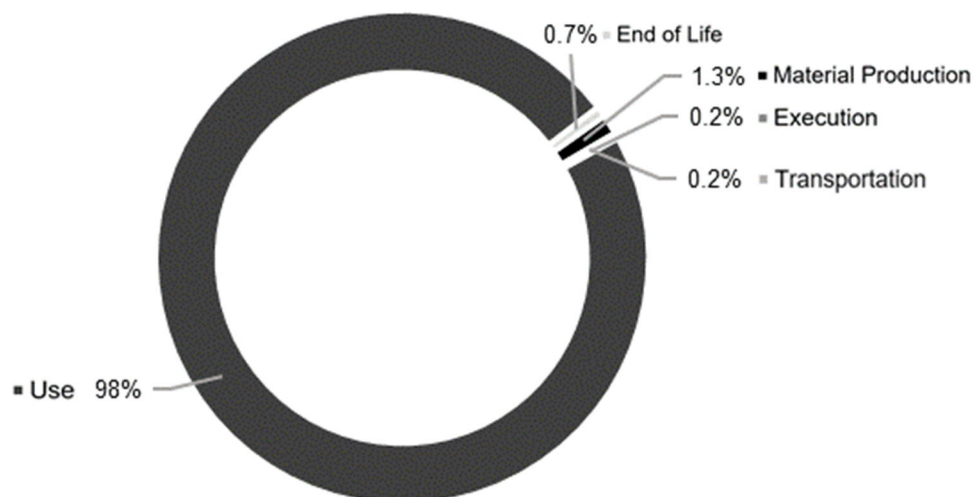


Figure 6.9. Contribution to the total environmental impact in terms of climate change from the different LC stages (average of the three reference cities).

For example, on only considering the conventional system, the indicators presented different scores for the three reference cities (e.g., for climate change: Seville 83358 kgCO_{2eq}, Rome 101457 kgCO_{2eq}, and Berlin 103700 kgCO_{2eq}). Generally, the environmental analysis rewarded the energy piles that showed a considerable reduction of impacts.

With reference to the cities of Seville and Rome, the score of all the indicators was significantly in favour of the energy piles, which showed a reduction of 65% and 55% in terms of the equivalent CO₂ emissions, 61% and 64% in terms of human health, 64% and 60% in terms of resources depletion, and 57% and 42% in terms of ecosystem quality, respectively.

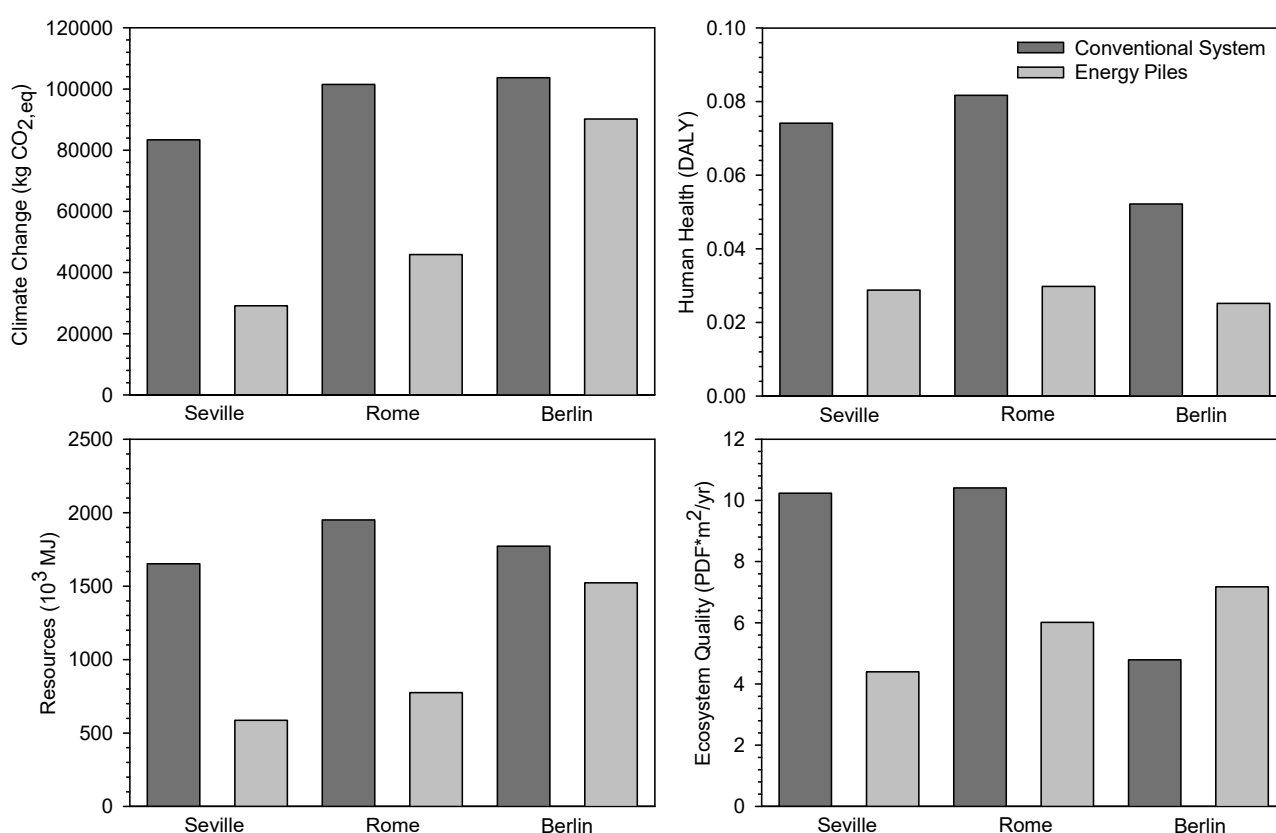


Figure 6.10. Indicators of the environmental performance of the conventional system and the energy piles for the three reference cities.

A lower reduction of the impacts was found in the case of Berlin: 13% in terms of climate change, 52% for human health, and 14% for resources depletion. The ecosystem quality was the only score in favour of the conventional system. Based on the midpoint indicators reported in the Appendix B, the ecosystem-related midpoint indicators in line with end-point results for ecosystem quality are ionising radiation, land occupation, ozone layer depletion, terrestrial ecotoxicity, and mineral extraction. These results are explained by the

high amount of auxiliary energy required to meet the heating demand in Berlin, which was not satisfied by exploiting only the geothermal source, and the consequential high electricity demand for the use of the energy pile system.

Moreover, the analysis of the midpoints reported in the Appendix B clearly illustrates why energy piles have a negative impact on the ozone layer depletion in each city. This is due to the presence of refrigerant in the infrastructure of the heat pump.

Figure 6.11 reports a detailed overview of the environmental indicators for all the considered scenarios. The results are reported for each month of the reference year. As was expected, the peak values of the indicators can be identified during winter for the case of Berlin and during summer for Seville and Rome.

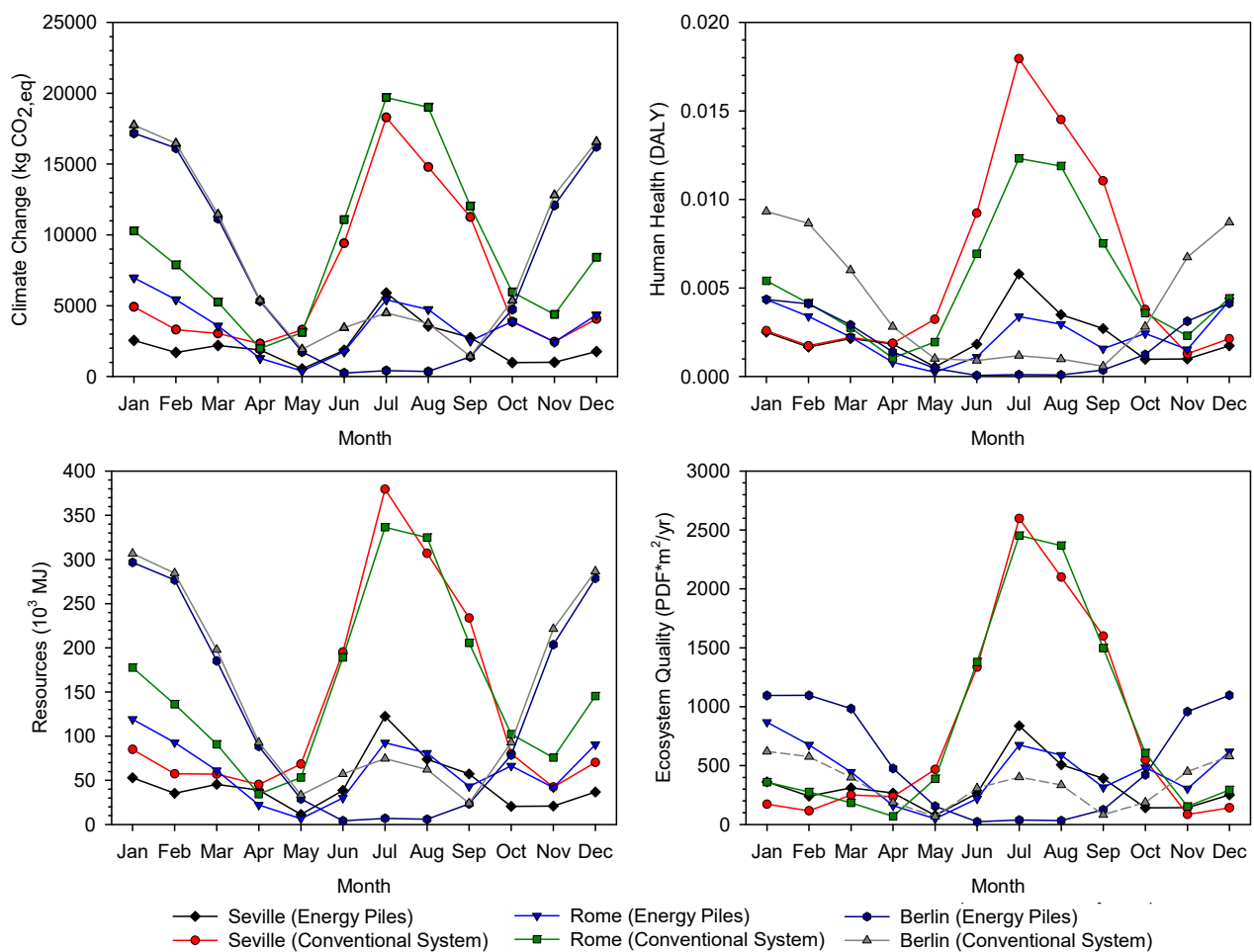


Figure 6.11 Evolution of the environmental indicators of the conventional system and the energy piles during the reference year for the three reference cities.

It is interesting to note that, on comparing the conventional system with the energy piles during the reference year, a reduction in the impacts during the heating periods was always noted, but during the cooling periods, the energy piles contributed significantly to reducing the score of the indicators. This means that the energy piles not only contributed to providing a clean energy source for the heating of the building but they were especially efficient from an environmental point of view during the cooling periods. This is a significant advantage for the energy piles over other technologies exploiting renewable energy, which mainly satisfy only the heating demand.

6.5 Conclusions

This paper presents the long-term performance of a group of energy piles in terms of meeting the heating and cooling demands of a reference office building in three different climatic conditions. For this purpose, a 3D finite element model was developed, which is capable of taking into consideration the intermittent operation of a GSHP, as well as the heating and cooling demands from the building side with a monthly varying nature. The results obtained on using the finite element model, in terms of meeting the heating and cooling demands from the building side, were employed to perform an LCA analysis.

With this study, finally a quantitative comparison of the environmental impact between a conventional heating and cooling system and energy piles has been presented in terms of climate change, resource consumption, human health, ecosystem quality. The comparison among three reference climate scenarios has provided clear evidences regarding the adoption of the energy pile system in the selected areas. With the use of energy piles, the LCA demonstrated a reduction in terms of equivalent CO₂ emissions, human health, resources depletion, and ecosystem quality for Seville and Rome, respectively, while the reduction was lower in the case of Berlin. The comparison of the conventional and GSHP systems showed that the energy piles yielded the highest reduction in indicators during the cooling periods, which is considered to be partially related to the higher coefficient of performance of the GSHP during summer months. According to this study, the energy pile technology, providing a clean energy source for both heating and cooling of the buildings, is more efficient from an environmental point of view compared to conventional systems. Moreover,

their environmental performance has revealed to be especially satisfactory during the cooling periods, which is a significant advantage with respect to other renewable energy technologies satisfying solely the heating demand.

Chapter 7

Conclusions

7. Conclusions

This Ph.D. thesis was devoted to the geomechanical performance of retaining structures in unsaturated soils and the estimation of the environmental impact of geostructures by comparing conventional and low-carbon design solutions. Emphasis was placed on the possibility of adopting an unsaturated design approach with respect to conventional design methods. The mechanics of unsaturated soils employed in geotechnical design have been seen to potentially contribute to the sustainability of the geostructure industry. On the other hand, both temporary and permanent retaining structures must be safe during their whole life span. For these reasons, in the attempt to include the potential benefits provided by partial saturation in design procedures, the performance of seepage analyses and the assessment of the loss of the matric suction is considered the critical point.

A significant gap exists between the state of knowledge of unsaturated soil mechanics in the scientific community and the conventional design procedure in engineering practice. One of the main reasons is the complexity of the available models that describe the behavior of unsaturated soils and the efforts needed to obtain soil parameters in terms of both number of soil parameters and time to acquire them. Chapter 2 and Chapter 3 have shown that basic principles of unsaturated soil mechanics can be integrated into conventional geotechnical design procedure for the computation of the lateral earth pressure of unsaturated soils under climatic loads, such as rainfall events. On the other hand, when simplified models are employed, assumptions must be made. In Chapter 4, the experimental characterization of the water retention behavior of the tested soils has shown the impact that these assumptions can lead when implementing simplified uncoupled analytical models are implemented for the computation of the lateral earth thrust of unsaturated soils. Moreover, in the attempt to provide a validation of these simplified analytical formulations, a comparison is made with experimental evidence reported in Chapter 5.

Moreover, the quantification of the environmental impacts avoided by adopting low carbon geotechnical solutions was reported not only for a retaining wall (Chapter 1), but also for a deep foundation (Chapter 7).

Details on the thesis contribution and perspective follow.

7.1 Thesis contribution

The design of a cantilever retaining structure interacting with unsaturated soils was described in chapter 2, considering the infiltration rate in steady-state conditions. Three different types of retained soils were considered. The differences in the unsaturated design approach and the conventional one were discussed, highlighting strengths and weaknesses. Soil properties, in terms of water retention features, have been found to play a crucial role in the analyses. Moreover, the choice of the boundary conditions in terms of infiltration rate affects the magnitude of the lateral earth thrust. For this reason, it should be chosen by considering the statistics of rainfall events. One of the limitations of the analytical closed-form formulation reported in Chapter 2 is that it does not consider time effects. Indeed, the analytical solutions are achieved in steady-state conditions. Chapter 3 intended to extend the uncoupled hydro-mechanical analyses by considering the transient state. The implemented procedure can be regarded as a simplified method which investigates the time needed for the total loss of the matric suction. The simulation of the rainfall events has shown a significant effect on the magnitude of the lateral earth pressure that has been quantified at different time steps. The change in the magnitude of the lateral earth pressure resulted not only in an increase of the forces acting on the retaining structure but also in the variation of its point of application over time. Its evolution depends significantly on the hydro-mechanical properties of the considered geomaterial. The transient response of the system is also significantly dependent on the retention properties of the considered soil. However, despite a number of hypotheses and assumptions are behind the simplified implemented analytical models, the transient analyses suggest that it may be beneficial to move towards a more rational design approach respect to considering the retained soil as totally saturated. Infiltration models are available in the literature and can be employed as boundary conditions for either analytical or numerical models. Starting from statistical analyses of the rainfall events, it could be possible to estimate the amount of infiltrated water and subsequently perform the transient analyses to evaluate the effect on suction changes and, consequently, on the lateral earth pressure distribution.

Furthermore, the changing of matric suction in space and time resulted in changes in effective stress. For this reason, the choice of a correct constitutive relation between the degree of saturation and suction represents a crucial step when hydro-mechanical analyses are

performed. By assuming a single water retention model, as required by the analytical analyses, one can incorrectly compute the suction evolution and consequently of the effective stress. The experimental analyses reported in Chapter 4 have highlighted that the hysteretic behavior of the geomaterials plays a crucial role in the implementation of the hydro-mechanical analyses. This was highlighted by comparing the available shear strength computed with the main drying curve and the main wetting curve of the water retention behavior. The adoption of the main wetting curve leads to a lower shear strength (higher lateral earth thrust) with respect to the adoption of the main drying curve. On the other hand, it generates lower degrees of saturations than the drying curve. Lower water content is associated with lower hydraulic conductivity and, hence, lower infiltration rate. The adoption of the wetting curve is conservative with respect to the shear strength, but it is not with respect to the estimation of the loss of suction due to rainfall.

A significant contribution of the Ph.D. thesis is represented by the comparison of the available analytical models with experimental results. In this regard, a 1-g physical model for the interaction between unsaturated soils and retaining structures has been designed and built. Details on the experimental set-up and design procedure have been reported. The apparatus has been shown to be capable of measuring the lateral soil thrust in both dry and unsaturated conditions. Two types of tests have been performed. The first was related to the effect of the partial saturation condition on the failure mechanism at the active state and the consequential magnitude of the horizontal component of the lateral earth thrust. The second was related to the effect of suction changes on the horizontal component of the lateral earth thrust in the at-rest condition.

The results of the performed tests have shown that:

- The designed experimental apparatus is capable of measuring the lateral earth thrust of soils tested in various conditions (at rest state, active state, increase and reduction of the groundwater level, simulation of rainfall events). In particular, the tests performed in dry condition have been shown to be consistent with the classical Rankine's theory.
- The condition of partial saturation of the retained soil is characterized by a different failure mechanism with respect to the case of dry soil. The slope of the failure surface

is higher in the portion of soil affected by capillary rise. This is an important outcome because it suggests that care must be taken when the lateral earth thrust is computed according to the upper bound theorem of the limit analysis by assuming the shape of the failure surface (e.g., linear failure-surface, logarithmic spiral);

- In the at-rest condition, the variation of the horizontal component of the lateral earth thrust with matric suction changes has been experimentally obtained. Both the increase and the reduction of matric suction have been found to be related to an increase or decrease of the horizontal component of the lateral earth thrust, respectively.
- By analysing the comparison between analytical and experimental analyses, the analytical formulations are found to be in generally good agreement with the experimental results even if a greater discrepancy has been found between the theoretical model and experimental results for the at rest scenario. In the active state, the choice of the retention model (main drying or main wetting curve) is found to be a key point in the computation of the lateral earth thrust of unsaturated retained soils. The experimental data are found to be within the range of values identified by adopting the theoretical extension of Rankine's theory. The definition of the coefficient of earth pressure at rest in terms of total stress depending on the degree of saturation, suction, and net vertical stress could be employed for the determination of the horizontal lithostatic earth pressure distribution in terms of total stress for dry, saturated and unsaturated soils. This would imply an adequate knowledge of the hydrological conditions of the site in question and specifically the porewater pressure profile (both positive and negative). It has to be remarked that the coefficient of earth pressure at rest (K_0), defined in terms of effective stress, is not dependent on suction, as shown experimentally by Oh et al. 2013.

In view of a possible adoption of unsaturated soils mechanics for geotechnical analyses of retaining structures, it is suggested to employ the analytical models as a pre-estimation of the lateral earth thrust acting on permanent or temporary retaining structures. The adoption of numerical models that properly considers the hydro-mechanical behaviour of unsaturated soils is strongly encouraged for a more comprehensive investigation of the soil-structure interaction in partially saturated conditions, especially if the effects of suction

changes are considered. It has to be remarked that the investigated methods are suitable for granular geomaterials. Expansive soils require more advanced investigations for a realistic estimation of the lateral earth thrust and its evolution with suction changes.

Moreover, in this thesis, a method for the evaluation of the environmental performance of geostructures has been investigated. Among the different available environmental methodologies, the LCA has been selected because it allows for the computation of the environmental impacts from the extraction of raw material to the disposal scenario. The literature review has shown that LCA models can be implemented for geostructures by following the standards that exist at the international and European level. It is difficult to generalize an LCA study for a category of geostructure because each one is different from every other one, but the LCA is a powerful tool that can help in the decision support system to identify less impactful solutions.

- An LCA model for the cantilever retaining wall, from the extraction of raw materials to the disposal scenario and the impacts of each of the life cycle stages, were identified. With respect to the other models found in the literature, the end of life scenario modeled here turned out to be a non-negligible stage in the retaining wall's life cycle, leading to significant negative environmental impacts in the disposal scenario. However, it could lead to a positive impact if appropriate recycling was considered. A clear track of the environmental indicators and impact categories chosen for the LCA was provided. Furthermore, in an attempt to optimize the design of geostructures, the results encourage the use of the unsaturated design approach in geotechnical practice, as suggested recently by Houston (2019), recognizing that a deep knowledge of the hydro-mechanical behavior of unsaturated soils is currently available.
- The same methodological approach was also used to provide a quantitative comparison of the environmental impact between a conventional heating and cooling system and energy piles. Three climatic scenarios have been considered by selecting three reference cities: Seville, Rome, and Berlin. With the use of energy piles, the LCA demonstrated that the energy pile technology, providing a clean energy source for both heating and cooling of the buildings, is more efficient from an environmental

point of view compared to conventional systems. Moreover, their environmental performance has revealed to be especially satisfactory during the cooling periods, which is a significant advantage with respect to other renewable energy technologies which uniquely satisfy the heating demand.

7.2 Prospective and future research

The adoption of the mechanics of partially saturated soils for the design of geotechnical structures certainly represents a perspective which the engineering community will face in the near future. This is due not only to continuing economic and environmental pressures but also to the need to move towards a more resilient design. Precisely, the resilience of geotechnical projects also consists of their ability to deal with the environmental burdens induced by climate change, which can only be taken into account by adopting the mechanics of unsaturated soils. Although in scientific literature, the hydro-mechanical behaviour of unsaturated soils has reached a very high level of knowledge, the use of this know-how is scarcely applied in engineering practice. Therefore, the following should be encouraged: i) further physical modelling on a laboratory scale that can investigate the interaction between partially saturated soils and geotechnical structures; ii) on-site monitoring of existing or under-construction works, especially in terms of pore water pressure evolution during the entire year, paying particular attention to the exceptional events of drying or wetting; iii) research aimed at simplifying existing methods and models that characterize the behaviour of unsaturated soils starting from the number of parameters that come into play and the time needed to obtain them. With specific reference to retaining structures, the mechanics of partially saturated soils could be used at least for the design of temporary retaining structures for which the reliability provided by suction is required for a shorter time with respect to permanent retaining structures. In addition, simplified or complex analyses based on the mechanics of partially saturated soils may be used for the analysis of existing, historical or more recent construction works in order to identify the current safety factor or its evolution with respect to possible climatic loads.

Regarding the environmental performance of geotechnical structures, LCA is undoubtedly a useful tool for the evaluation of the environmental impacts of geotechnical structures, and the available

standards are considered satisfactory for the feasibility of LCA studies of geotechnical structures. Improvements are needed in the most time-consuming phase of the methodology (LCIA). In this regard, the collection of all the data involved in the geotechnical project could be significantly reduced, developing new tools in the context of the digitalization process of the construction sector.

Chapter 8

References

8. References

- Airò Farulla C., Battiato A. and Ferrari A., 2010. The void ratio dependency of the retention behaviour for a compacted clay in Unsaturated Soils - Proceedings of the 5th International Conference on Unsaturated Soils; Barcelona; Spain; 6 - 8 September 2010, vol.1, pp. 417-422.
- Abergel, T., Dean, B., & Dulac, J., 2018. Towards a zero-emission, efficient, and resilient buildings and construction sector. Global Status Report 2017.
- Amabile, A., Balzano, B., Urciuoli, G., & Tarantino, A. (2012). Effect of partial saturation on the stability of retaining diaphragms above the water table. In *Unsaturated Soils: Research and Applications* (pp. 263-268). Springer, Berlin, Heidelberg.
- ASTM, D., 2002. 854-02. Standard test methods for specific gravity of soil solids by water pycnometer,1.
- ASTM D422-63, 2007.: Standard Test Method for Particle-Size Analysis of Soils.
- ASTM D4253-16, 2016: Standard, Test Methods for Maximum Index Density and Unit Weight of Soils Using a Vibratory Table.
- ASTM D4254-16, 2016: Standard, Test Methods for Minimum Index Density and Unit Weight of Soils and Calculation of Relative Density.
- Basu, D., Misra, A. and Puppala, A. J., 2014. Sustainability and geotechnical engineering: perspectives and review. *Canadian Geotechnical Journal*, 52(1), pp. 96-113.
- Bishop, A. W., 1959. The principle of effective stress. *Teknisk Ukeblad*, 106(39), pp. 859-863.
- Bond, A. and Harris, A., 2008. Decoding eurocode 7.CRC Press.
- Bolton, M.D. and Powrie, W., 1987. The collapse of diaphragm walls retaining clay. *Géotechnique*, 37(3), pp.335-353.
- Bolton, M.D. and Powrie, W., 1988. Behaviour of diaphragm walls in clay prior to collapse. *Géotechnique*, 38(2), pp.167-189.

- Bourne-Webb, P.J., Amatya, B., Soga, K., Amis, T., Davidson, C. and Payne, P., 2009. Energy pile test at Lambeth College, London: geotechnical and thermodynamic aspects of pile response to heat cycles. *Géotechnique*, 59(3), pp.237-248.
- Bourne-Webb, P., Pereira, J.M., Bowers, G.A., Mimouni, T., Loveridge, F.A., Burlon, S., Olgun, C.G., McCartney, J.S. and Sutman, M., 2014. Design tools for thermoactive geotechnical systems. *DFI Journal-The Journal of the Deep Foundations Institute*, 8(2), pp.121-129.
- Brandl, H., 2006. Energy foundations and other thermo-active ground structures. *Géotechnique*, 56(2), pp.81-122.
- Bransby, P.L. and Milligan, G.W.E., 1975a. Soil deformations near cantilever sheet pile walls. *Géotechnique*, 25(2), pp.175-195.
- Bransby, P.L. and Smith, I.A., 1975b. Side friction in model retaining-wall experiments. *Journal of Geotechnical and Geoenvironmental Engineering*, 101(7) pp.615-632.
- Brooks, R. H. and Corey, T., 1964. Hydraulic properties of porous media. Colorado: Colorado State University.
- Camera, C., Masetti, M. and Apuani, T., 2012. Rainfall, infiltration, and groundwater flow in a terraced slope of Valtellina (Northern Italy): field data and modelling. *Environmental Earth Sciences*, 65(4), pp.1191-1202.
- Chandrasekaran, S.S., Owaise, R.S., Ashwin, S., Jain, R.M., Prasanth, S. and Venugopalan, R.B., 2013. Investigation on infrastructural damages by rainfall-induced landslides during November 2009 in Nilgiris, India. *Natural hazards*, 65(3), pp.1535-1557.
- Chau, C., Soga, K., Nicholson, D., O'Riordan, N., and Inui, T. (2008). Embodied energy as an environmental impact indicator for basement wall construction. In *GeoCongress 2008: Geosustainability and Geohazard Mitigation* (pp. 867-874).
- Chen, J.M., Tan, Y.C. and Chen, C.H., 2003. Analytical solutions of one-dimensional infiltration before and after ponding. *Hydrological processes*, 17(4), pp.815-822.

- Colebrook C. F. (1939), Turbulent flow in pipes with particular reference to the transition region between the smooth and rough pipe laws, *Journal of the Institution of Civil engineers*. 12(8)
- Collin, J.G., 2001. Lessons learned from a segmental retaining wall failure. *Geotextiles and Geomembranes*, 19(7), pp.445-454.
- COMSOL Multiphysics® v. 5.3. www.comsol.com. COMSOL AB, Stockholm, Sweden.
- Coulomb, C.A., 1776. An attempt to apply the rules of maxima and minima to several problems of stability related to architecture. *Mémoires de l'Académie Royale des Sciences*, 7, pp.343-382.
- Damians, I. P., Bathurst, R. J., Adroguer, E. G., Josa, A., and Lloret, A. (2016). Environmental assessment of earth retaining wall structures. *Environmental Geotechnics*, 4(6), 415-431.
- Dixit, M. K., Fernández-Solis, J. L. and Culp, C. H., 2010. Identification of parameters for embodied energy measurement: a literature review. *Energy and Building*, Volume 42, p. 1238–1247.
- Dregne, H. E., 1976. *Soils of arid regions* (Vol. 6). New York: American Elsevier.
- EC-JRC, 2010. International Reference Life Cycle Data System (ILCD) Handbook–general guidance document for life cycle assessment–detailed guidance.
- DSE, 2007. *Recyclage des déchets minéraux de chantier dans le canton de Vaud*, Switzerland: Département de la sécurité et de l'environnement.
- Eichenberger, J., Ferrari, A., and Laloui, L., 2013. Early warning thresholds for partially saturated slopes in volcanic ashes. *Computers and Geotechnics*, Volume 49, pp. 79-89.
- ENTRANZE Policies to Enforce the Transition to Nearly Zero Energy Buildings in the EU-27, accessed June 2019, <https://www.entranze.eu/>.
- EN 15978, 2011. Sustainability of construction works–assessment of environmental performance of buildings–calculation method.

- EN, B., 2002. EN 1997-1: Eurocode 7: Geotechnical design - Part 1: General rules.
- Escario, V. and Saez, J., 1986. The shear strength of partly saturated soils. *Géotechnique*, 36(3), pp. 453-456.
- Eurofer, 2012. http://www.steelconstruction.info/images/6/65/Reinforcing_Steel.pdf
- European Commission. An EU Strategy on Heating and Cooling, COM (2016) 51 Final; European Commission: Brussels, Belgium, 2016.
- Faizal, M., Bouazza, A. and Singh, R.M., 2016. An experimental investigation of the influence of intermittent and continuous operating modes on the thermal behaviour of a full scale geothermal energy pile. *Geomechanics for Energy and the Environment*, 8, pp.8-29.
- Ferrari, A., Eichenberger, J. and Laloui, L., 2013. Hydromechanical behaviour of a volcanic ash. *Géotechnique*, 63(16), pp. 1433-1446.
- Fang, Y.S. and Ishibashi, I., 1986. Static earth pressures with various wall movements. *Journal of Geotechnical Engineering*, 112(3), pp.317-333.
- Fang, Y.S., Chen, T.J. and Wu, B.F., 1994. Passive earth pressures with various wall movements. *Journal of Geotechnical Engineering*, 120(8), pp.1307-1323.
- Ferrari, A., Favero, V., Marschall, P. and Laloui, L., 2014. Experimental analysis of the water retention behaviour of shales. *International Journal of Rock Mechanics and Mining Sciences*, 72, pp.61-70.
- Fredlund, D. G., Morgenstern, N. R. and Widger, R. A., 1978. The shear strength of unsaturated soils. *Canadian geotechnical journal*, 15(3), pp. 313-321.
- Fredlund, D. G. and Rahardjo, H., 1993. Soil mechanics for unsaturated soils. John Wiley and Sons.
- Gallipoli, D., Toll, D., Evans, F. and Medero, G., 2007. Determination of the soil water retention curve with tensiometers. In *Experimental unsaturated soil mechanics* (pp. 95-102). Springer, Berlin, Heidelberg.

- Gan, J. K., Fredlund, D. G. and Rahardjo, H., 1988. Determination of the shear strength parameters of an unsaturated soil using the direct shear test. *Canadian Geotechnical Journal*, 25(3), pp. 500-510.
- Gardner, W. R., 1958. Some steady-state solutions of the unsaturated moisture flow equation with application to evaporation from a water table. *Soil science*, 85(4), pp. 228-232.
- Geiser, F., 1999. Comportement Mécanique d'un Limon non saturé. Lausanne: Ph.D. Thesis N°1942, École Polytechnique Fédérale de Lausanne, EPFL.
- Geiser, F., Laloui, L. and Vulliet, L., 2000. On the volume measurement in unsaturated triaxial test. Singapore, AA Balkema, pp. 669-674.
- Giri, R. K. and Reddy, K. R., 2015. Sustainability assessment of two alternate earth-retaining structures. In *IFCEE 2015* (pp. 2836-2845). San Antonio, Texas, U.S.A, American Society of Civil Engineers, Reston, VA, USA, Geotechnical Special Publication no.256, pp. 2836-2845.
- Green, H., and GA Ampt 1911. Studies on soil physics. Part I. The flow of air and water through soils. *J. Agric. Sci*, 4, pp.1-24.
- GSHP Association, Thermal pile design, installation and materials standards. Ground Source Heat Pump Association, National Energy Centre, Davy Avenue, Knowlhill, Milton Keynes, MK5 8NG, (2012)
- Gu, X. W., Zhang, W. M. and Xu, G. M., 2010. Earth pressure at rest of expansive soil against retaining wall. *Physical Modelling in Geotechnics*.
- Guan, Y., and Fredlund, D. G., 1997. Use of the tensile strength of water for the direct measurement of high soil suction. *Canadian Geotechnical Journal*, 34(4), 604-614.
- Haaland, S.E., 1983. Simple and explicit formulas for the friction factor in turbulent pipe flow. *Journal of Fluids Engineering*, 105(1), pp.89-90. Han, Z. and Vanapalli, S. K., 2016. Stiffness and shear strength of unsaturated soils in relation to soil-water characteristic curve. 66(8), pp. 627-647.

- Haines, W.B., 1930. Studies in the physical properties of soil. V. The hysteresis effect in capillary properties, and the modes of moisture distribution associated therewith. *The Journal of Agricultural Science*, 20(1), pp.97-116.
- Ho, D. Y. and Fredlund, D. G., 1982. Increase in strength due to suction for two Hong Kong soils. Hawaii, In *Proceedings of the ASCE specialty conference on engineering and construction in tropical and residual soils*, pp. 263-296.
- Horton, R.E., 1933. The role of infiltration in the hydrologic cycle. *Eos, Transactions American Geophysical Union*, 14(1), pp.446-460.
- Houston, S.L., 2019. It is Time to Use Unsaturated Soil Mechanics in Routine Geotechnical Engineering Practice. *Journal of Geotechnical and Geoenvironmental Engineering*, 145(5), p.02519001.
- International Energy Agency, I. E. A. (2017), *World Energy Outlook 2017*, OECD Publishing, Paris/IEA, Paris, <https://doi.org/10.1787/weo-2017-en>.
- International Energy Agency, I. E. A. (2018), *The Future of Cooling*, OECD Publishing, Paris/IEA, Paris.
- International Energy Agency, I. E. A. (2019a) <https://www.iea.org/tcep/buildings/> (last updated 25 January 2019).
- International Energy Agency, I. E. A. (2019b) <https://www.iea.org/tcep/buildings/heating/> (last updated 13 March 2019).
- Ionescu, V. and Neagu, A.A., 2017. Finite Element Method Analysis of a MEMS-Based Heat Exchanger with Different Channel Geometries. *Energy Procedia*, 112, pp.158-165.
- Inui, T.; Chau, C.; Soga, K.; Nicolson, D.; O’Riordan, N., 2011. Embodied energy and gas emissions of retaining wall structures. *Journal of Geotechnical and Geoenvironmental Engineering*, 137(10), pp. 958-967.
- ISO14040, 2006. *Environmental management - life cycle assessment - principle and framework*.

- ISO, 2006. ISO 14044: Environmental management - Life Cycle Assessment - Requirements and guidelines.
- Jolliet, O.; Margni, M.; Charles, R.; Humbert, S.; Payet, J.; Rebitzer, G.; Rosenbaum, R. et al., 2003. IMPACT 2002+: a new life cycle impact assessment methodology. *The international journal of life cycle assessment*, 8(6), p. 324.
- Kärkkäinen, S. and Oy, E., 2012. Heat pumps for cooling and heating. International Energy Agency Demand-Side Management Programme Task VXII, IEADSM report.
- Kendall, A., Raymond, A. J., Tipton, J. and DeJong, J. T., 2017. Review of life-cycle-based environmental assessments of geotechnical systems. *Proceedings of the Institution of Civil Engineers-Engineering Sustainability*, Thomas Telford, pp. 1-11.
- Khosravi, M.H., Pipatpongsa, T. and Takemura, J., 2013. Experimental analysis of earth pressure against rigid retaining walls under translation mode. *Géotechnique*, 63(12), pp.1020-1028.
- Knellwolf, C., Peron, H. and Laloui, L., 2011. Geotechnical analysis of heat exchanger piles. *Journal of Geotechnical and Geoenvironmental Engineering*, 137(10), pp.890-902.
- Kusuda, T. and Achenbach, P.R., 1965. Earth temperature and thermal diffusivity at selected stations in the United States (No. NBS-8972). National Bureau of Standards Gaithersburg MD.
- Laloui, L., Nuth, M. and Vulliet, L., 2006. Experimental and numerical investigations of the behaviour of a heat exchanger pile. *International Journal for Numerical and Analytical Methods in Geomechanics*, 30(8), pp.763-781. Laloui, L., 2010. *Mechanics of Unsaturated Geomaterials*. John Wiley and Sons.
- Laloui, L. and Di Donna, A., 2011. Understanding the behaviour of energy geo-structures. *Proceedings of the Institution of Civil Engineers*, 164(4), p.184.
- Laloui, L., Ferrari, A., Li, C. and Eichenberger, J., 2015. Hydro-mechanical analysis of volcanic ash slopes during rainfall. *Géotechnique*, 66(3), pp. 220-231.

- Lee, M. and Basu, D., 2015. Sustainability assessment of mechanically stabilized earth walls. From Fundamentals to Applications in Geotechnics: Proceedings of the 15th Pan-American Conference on Soil Mechanics and Geotechnical Engineering, pp. 830-837.
- Liang, W. B., Zhao, J. H., Li, Y., Zhang, C. G., & Wang, S. (2012). Unified solution of Coulomb's active earth pressure for unsaturated soils without crack. In *Applied Mechanics and Materials* (Vol. 170, pp. 755-761). Trans Tech Publications Ltd.
- Lourenço, S. D. N., Gallipoli, D., Toll, D. G., Augarde, C. E., Evans, F. D., & Medero, G. M. (2008). Calibrations of a high-suction tensiometer. *Géotechnique*, 58(8), 659-668.
- Lourenço, S. D. N., Gallipoli, D., Toll, D. G., and Evans, F. D. (2006). Development of a commercial tensiometer for triaxial testing of unsaturated soils. In *Unsaturated Soils 2006* (pp. 1875-1886).
- Lourenço, S.D.N., Gallipoli, D., Toll, D.G., Augarde, C.E. and Evans, F.D., 2011. A new procedure for the determination of soil-water retention curves by continuous drying using high-suction tensiometers. *Canadian geotechnical journal*, 48(2), pp.327-335.
- Loveridge, F.A., Powrie, W., Amis, T., Wischy, M. and Kiauk, J., 2016, August. Long term monitoring of CFA energy pile schemes in the UK. In *Energy Geotechnics* (pp. 585-592). CRC Press.
- Lu, N. and Likos, W. J., 2004. *Unsaturated Soil Mechanics*. New York: Wiley, p. 321.
- Mendes, J., Gallipoli, D., Tarantino, A., and Toll, D. (2019). On the development of an ultra-high-capacity tensiometer capable of measuring water tensions to 7 MPa. *Géotechnique*, 69(6), 560-564.
- Milatz, M., Törzs, T., Nikooee, E., Hassanizadeh, S. M., & Grabe, J., 2018. Theoretical and experimental investigations on the role of transient effects in the water retention behaviour of unsaturated granular soils. *Geomechanics for Energy and the Environment*, 15, 54-64.
- Mimouni, T. and Laloui, L., 2015. Behaviour of a group of energy piles. *Canadian Geotechnical Journal*, 52(12), pp.1913-1929.

- Makasis, N., Narsilio, G.A. and Bidarmaghz, A., 2018. A machine learning approach to energy pile design. *Computers and Geotechnics*, 97, pp.189-203.
- Marinho, F. A. M., Take, W. A., and Tarantino, A. (2008). Measurement of matric suction using tensiometric and axis translation techniques. In *Laboratory and field testing of unsaturated soils* (pp. 3-19). Springer, Dordrecht.
- McCartney, J.S. and Murphy, K.D., 2017. Investigation of potential dragdown/uplift effects on energy piles. *Geomechanics for Energy and the Environment*, 10, pp.21-28.
- McNary, J. V., 1925. Earth pressure against abutment walls measured with soil pressure cells. *Public Roads*.
- Mesri, G. and Hayat, T.M., 1993. The coefficient of earth pressure at rest. *Canadian Geotechnical Journal*, 30(4), pp.647-666.
- Monier, V., Hestin, M., Trarieux, M., Mimid, S., Domrose, L., Van Acoleyen, M., Hjerp, P. and Mudgal, S., 2011. Service contract on management of construction and demolition waste. Report EU Commission.
- Murray, E.J. and Sivakumar, V., 2010. *Unsaturated Soils: A fundamental interpretation of soil behaviour*. John Wiley and Sons.
- Ng, C.W.W., Zhan, L.T., Bao, C.G., Fredlund, D.G. and Gong, B.W., 2003. Performance of an unsaturated expansive soil slope subjected to artificial rainfall infiltration. *Géotechnique*, 53(2), pp.143-157.
- Péron, H., 2008. Desiccation cracking of soils. Lausanne: Ph.D. Thesis N°4025, École Polytechnique Fédérale de Lausanne, EPFL.
- Philip, J.R., 1969. Theory of infiltration. In *Advances in hydroscience* (Vol. 5, pp. 215-296). Elsevier.
- PRe Consultants. SimaPro (8.0.3.), LCA Software. Amersfoort, the Netherlands (accessed May 2019). <https://simapro.com/> (2014).

- Pufahl, D. E., Fredlund, D. G. and Rahardjo, H., 1983. Lateral earth pressures in expansive clay soils. *Canadian Geotechnical Journal*, 20(2), pp. 228-241.
- Rafalko, S. D., Sankey, J. E. and Freitag, N., 2010. Sustainability measures for MSE walls and baseline environmental impact evaluations. *Earth Retention Conference 3*, pp. 486-493.
- Rankine, W.J.M., 1857. II. On the stability of loose earth. *Philosophical transactions of the Royal Society of London*, (147), pp.9-27.
- Richards, D.J. and Powrie, W., 1998. Centrifuge model tests on doubly propped embedded retaining walls in overconsolidated kaolin clay. *Géotechnique*, 48(6), pp.833-846.
- Ridley, A. M., and Burland, J. B., 1993. A new instrument for the measurement of soil moisture suction. *Géotechnique*, 43(2), 321-324. Romero, E., 2001. Controlled-suction techniques. *Proc. 4th Symposium Brasileiro de Solos Não Saturados*, Porto Alegre, Brasil.
- Rosone, M., Farulla, C. A., and Ferrari, A., 2016. Shear strength of a compacted scaly clay in variable saturation conditions. *Acta Geotechnica*, 11(1), 37-50.
- Rosone, M., Ziccarelli, M., Ferrari, A. and Farulla, C.A., 2018. On the reactivation of a large landslide induced by rainfall in highly fissured clays. *Engineering Geology*, 235, pp.20-38.
- Rotta Loria, A.F. and Laloui, L., 2016. Thermally induced group effects among energy piles. *Géotechnique*, 67(5), pp.374-393.
- Rotta Loria, A.F. and Laloui, L., 2016. The interaction factor method for energy pile groups. *Computers and Geotechnics*, 80, pp.121-137.
- Rowe, P.W. and Peaker, K., 1965. Passive earth pressure measurements. *Géotechnique*, 15(1), pp.57-78.
- Salager, S., 2007. Etude de la rétention d'eau et de la consolidation des sols dans un cadre thermo-hydro-mécanique. MontPellier.
- Salager, S., Nuth, M., Ferrari, A. and Laloui, L., 2013. Investigation into water retention behaviour of deformable soils. *Canadian Geotechnical Journal*, 50(2), pp. 200-208.

- Salciarini, D., Ronchi, F., Cattoni, E. and Tamagnini, C., 2013. Thermomechanical effects induced by energy piles operation in a small piled raft. *International journal of Geomechanics*, 15(2), p.04014042.
- Sarbu, I. and Sebarchievici, C., 2014. General review of ground-source heat pump systems for heating and cooling of buildings. *Energy and buildings*, 70, pp.441-454.
- Scotto di Santolo, A., Evangelista, L. and Evangelista, A., 2017. Gravity retaining walls in unsaturated pyroclastic materials: observations and numerical modelling. *Rivista Italiana di Geotecnica*, Volume 1, pp. 26-42.
- Sharma, R.S. and Mohamed, M.H.A., 2003. Patterns and mechanisms of migration of light non-aqueous phase liquid in an unsaturated sand. *Géotechnique*, 53(2), pp.225-239.
- Siemens, G. A., 2017. Thirty-ninth Canadian Geotechnical Colloquium: Unsaturated Soil Mechanics: Bridging the Gap Between Research and Practice. *Canadian Geotechnical Journal*.
- Soga, K., Chau, C., Nicholson, D. and Pantelidou, H., 2011. Embodied energy: Soil retaining geosystems. *KSCE Journal of Civil Engineering*, 15(4), pp. 739-749.
- Sjoblom, K. J. , 2000. The mechanisms involved during the desaturation process of a porous matrix (Doctoral dissertation, Massachusetts Institute of Technology).
- Srivastava, R. and Yeh, T.C.J., 1991. Analytical solutions for one-dimensional, transient infiltration toward the water table in homogeneous and layered soils. *Water Resources Research*, 27(5), pp.753-762.
- Stanier, S. A. and Tarantino, A., 2013. An approach for predicting the stability of vertical cuts in cohesionless soils above the water table. *Engineering Geology*, Volume 158, pp. 98-108.
- Sutman, M., Olgun, C.G. and Laloui, L., 2018. Cyclic Load–Transfer Approach for the Analysis of Energy Piles. *Journal of Geotechnical and Geoenvironmental Engineering*, 145(1), p.04018101.

- Sutman, M., Brettmann, T. and Olgun, C.G., 2019. Full-scale in-situ tests on energy piles: Head and base-restraining effects on the structural behaviour of three energy piles. *Geomechanics for Energy and the Environment*, 18, pp.56-68.
- Symons, I.F. and Clayton, C.R.I., 1992. Earth pressures on backfilled retaining walls. *Ground Engineering*, 25(3), pp.26-34.
- Take, W. A., and Bolton, M. D. (2003). Tensiometer saturation and the reliable measurement of soil suction. *Géotechnique*, 53(2), 159-172.
- Take, W.A. and Valsangkar, A.J., 2001. Earth pressures on unyielding retaining walls of narrow backfill width. *Canadian Geotechnical Journal*, 38(6), pp.1220-1230.
- Tarantino, A., and Di Donna, A. (2019). Mechanics of unsaturated soils: simple approaches for routine engineering practice. *Italian Geotechnical Journal*.
- Tarantino, A., and El Mountassir, G. (2013). Making unsaturated soil mechanics accessible for engineers: Preliminary hydraulic-mechanical characterisation & stability assessment. *Engineering geology*, 165, 89-104.
- Tarantino, A. and Mongiovì, L., 2003. Calibration of tensiometer for direct measurement of matric suction. *Géotechnique*, 53(1), pp.137-141.
- Tavakkoli, N. and Vanapalli, S. K., 2011. Rational approach for the design of retaining structures using the mechanics of unsaturated soils. *Pan-Am CGS Geotechnical Conference*, Canadian Geotechnical Society.
- Taylor, Z.J., Gurka, R., Kopp, G.A. and Liberzon, A., 2010. Long-duration time-resolved PIV to study unsteady aerodynamics. *IEEE Transactions on Instrumentation and Measurement*, 59(12), pp.3262-3269.
- Terzaghi, K., Peck, R. B. and Mesri, G., 1996. In: *Soil Mechanics in Engineering Practice*. John Wiley and Sons, p. 332.
- Terzis, D., 2017. Kinetics, Mechanics and Micro-structure of Bio-cemented Soils (Thesis N°8147). EPFL.

- Toker, N. K. (2002). Improvements and reliability of MIT tensiometers and studies on soil moisture characteristic curves (Doctoral dissertation, Massachusetts Institute of Technology).
- Tsagareli, Z.V., 1965. Experimental investigation of the pressure of a loose medium on retaining walls with a vertical back face and horizontal backfill surface. *Soil Mechanics and Foundation Engineering*, 2(4), pp.197-200.
- Vahedifard, F., Leshchinsky, B. A., Mortezaei, K. and Lu, N., 2015. Active earth pressures for unsaturated retaining structures. *Journal of Geotechnical and Geoenvironmental Engineering*, 141(11).
- Vahedifard, F. et al., 2016. Role of suction stress on service state behavior of geosynthetic-reinforced soil structures. *Transportation Geotechnics*, Volume 8, pp. 45-56.
- Vahedifard, F., Tehrani, F. S., Galavi, V. and Ragno, E., 2017. Resilience of MSE Walls with Marginal Backfill under a Changing Climate: Quantitative Assessment for Extreme Precipitation Events. *Journal of Geotechnical and Geoenvironmental Engineering*, 143(9).
- Valore, C., Zicarelli, M. and Muscolino, S.R., 2017. The bearing capacity of footings on sand with a weak layer. *Geotechnical Research*, 4(1), pp.12-29.
- Van Genuchten, M., 1980. A closed-form equation for predicting the hydraulic conductivity of unsaturated soils. *Soil science society of America journal*, 44(5), pp. 892-898.
- Vanapalli, S. K., 2009. Shear strength of unsaturated soils and its applications in geotechnical engineering practice. New Castle, Australia, *Unsaturated Soils – Buzzzi, Fityus and Sheng*.
- Vanapalli, S. K., Fredlund, D. G. and Pufahl, D. E., 1996. Model for the prediction of shear strength with respect to soil suction. *Canadian Geotechnical Journal*, 33(3), pp. 379-392.
- Vanapalli, S. K. and Oh, W. T., 2012. Stability analysis of unsupported vertical trenches in unsaturated soils. *GeoCongress 2012, State of the art and practice in geotechnical engineering*, pp. 2502-2511.

- Vo, T. and Russel, A. R., 2016. Interaction between Retaining Walls and Unsaturated Soils in Experiments and Using Slip Line Theory. *Journal of Engineering Mechanics*, 143(4).
- Warrick, A.W., Lomen, D.O. and Yates, S.R., 1985. A Generalized Solution to Infiltration 1. *Soil Science Society of America Journal*, 49(1), pp.34-38.
- Wernet, G., Bauer, C., Steubing, B., Reinhard, J., Moreno-Ruiz, E. and Weidema, B., 2016. The ecoinvent database version 3 (part I): overview and methodology. *The International Journal of Life Cycle Assessment*, 21(9), pp.1218-1230.
- Wroth, C. P. and Houlsby, G. T., 1985. Soil mechanics-property characterization and analysis procedures.
- Xu, Q. and Zhang, L., 2010. The mechanism of a railway landslide caused by rainfall. *Landslides*, 7(2), pp.149-156.
- Yoo, C., 2013. Effect of rainfall on performance of geosynthetic reinforced soil wall using stress-pore pressure coupled analysis. In *Geo-Congress 2013: Stability and Performance of Slopes and Embankments III* (pp. 566-573).
- You, S., Cheng, X., Guo, H. and Yao, Z., 2016. Experimental study on structural response of CFG energy piles. *Applied Thermal Engineering*, 96, pp.640-651.
- Yuan, F. and Lu, Z., 2005. Analytical solutions for vertical flow in unsaturated, rooted soils with variable surface fluxes. *Vadose Zone Journal*, 4(4), pp.1210-1218.
- Zangheri, P., Armani, R., Pietrobon, M., Pagliano, L., Boneta, M.F. and Müller, A., 2014. Heating and cooling energy demand and loads for building types in different countries of the EU. *Polytechnic University of Turin, end-use Efficiency Research Group*, 3.
- Zhang, C., Zhao, J. H., Zhang, Q. H., and Xu, F. (2010). Unified solutions for unsaturated soil shear strength and active earth pressure. In *Experimental and Applied Modeling of Unsaturated Soils* (pp. 218-224).

Appendix

Appendix A - Details of the box design

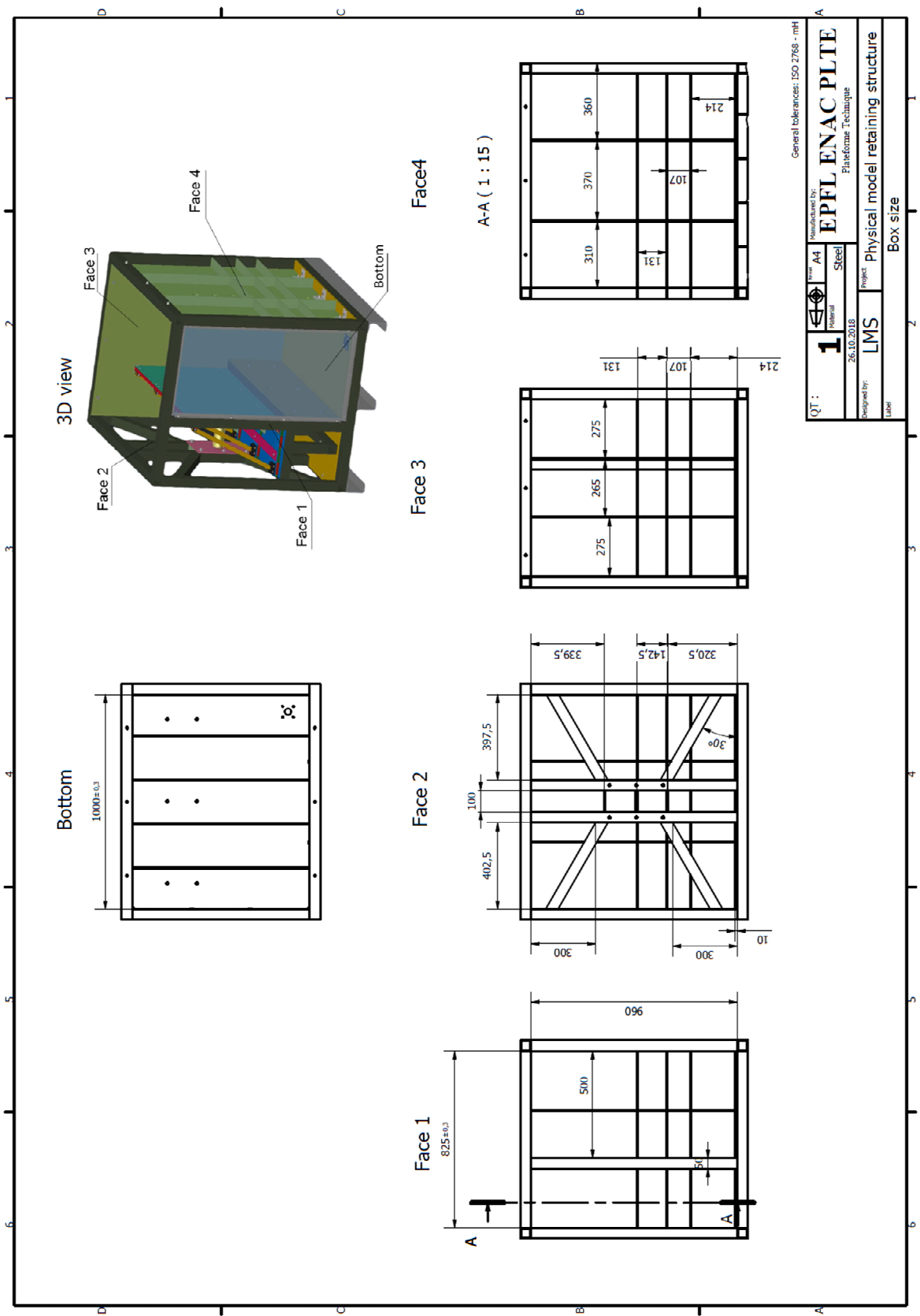


Figure A.1. Details of box the design.

Appendix B – Midpoint indicators' scores

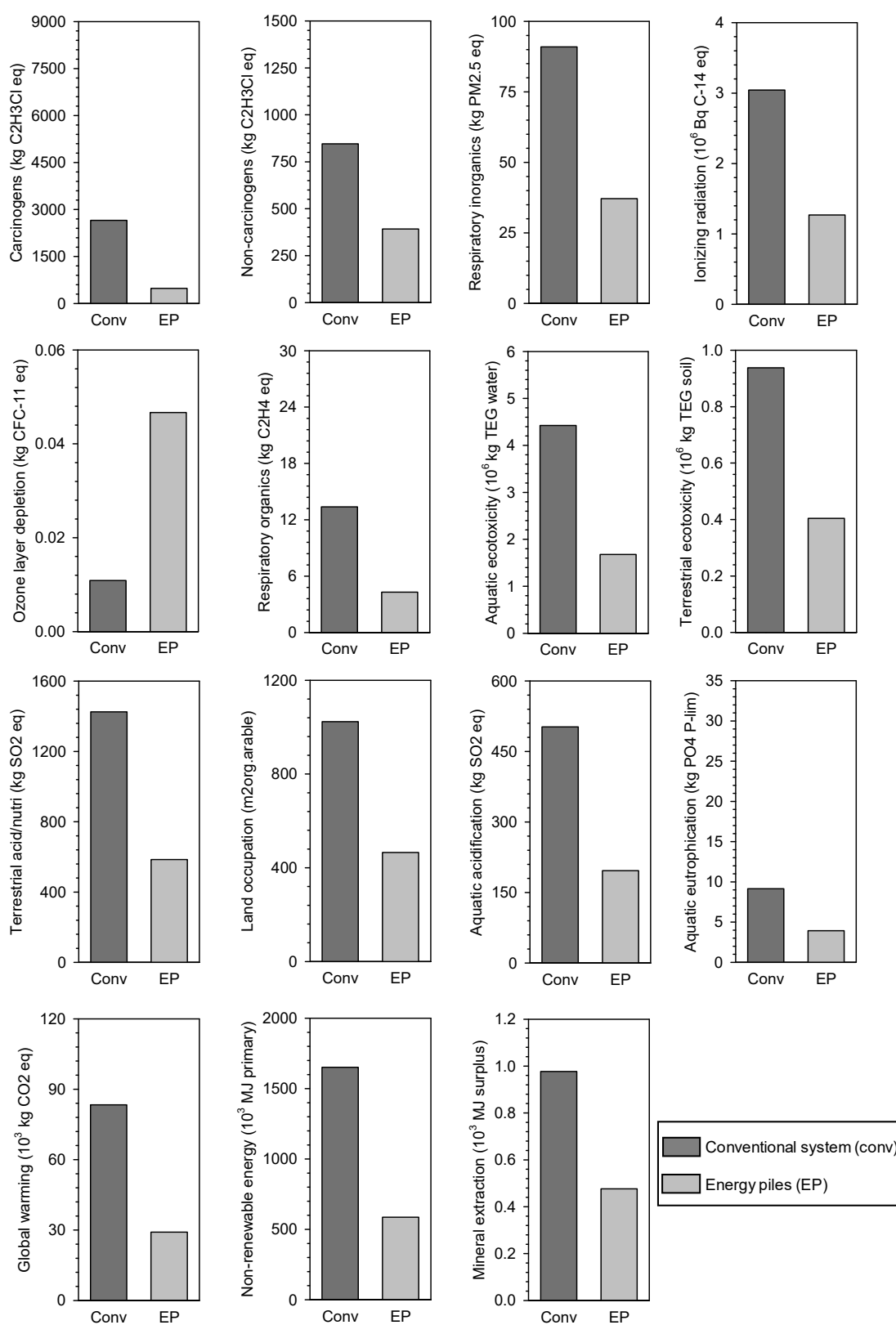


Figure A.2. Midpoint indicators of the conventional system and the energy piles for Seville

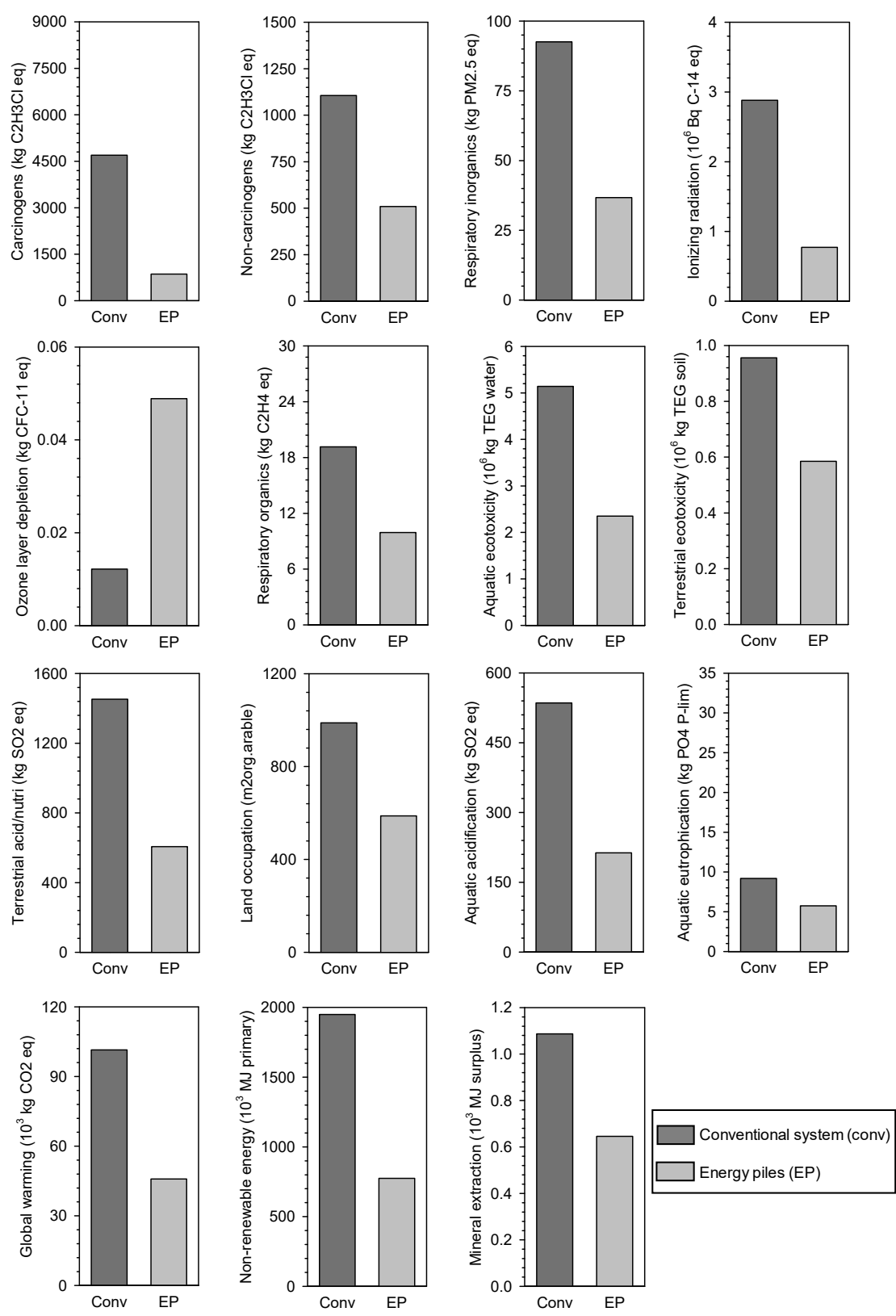


Figure A.3. Midpoint indicators of the conventional system and the energy piles for Rome

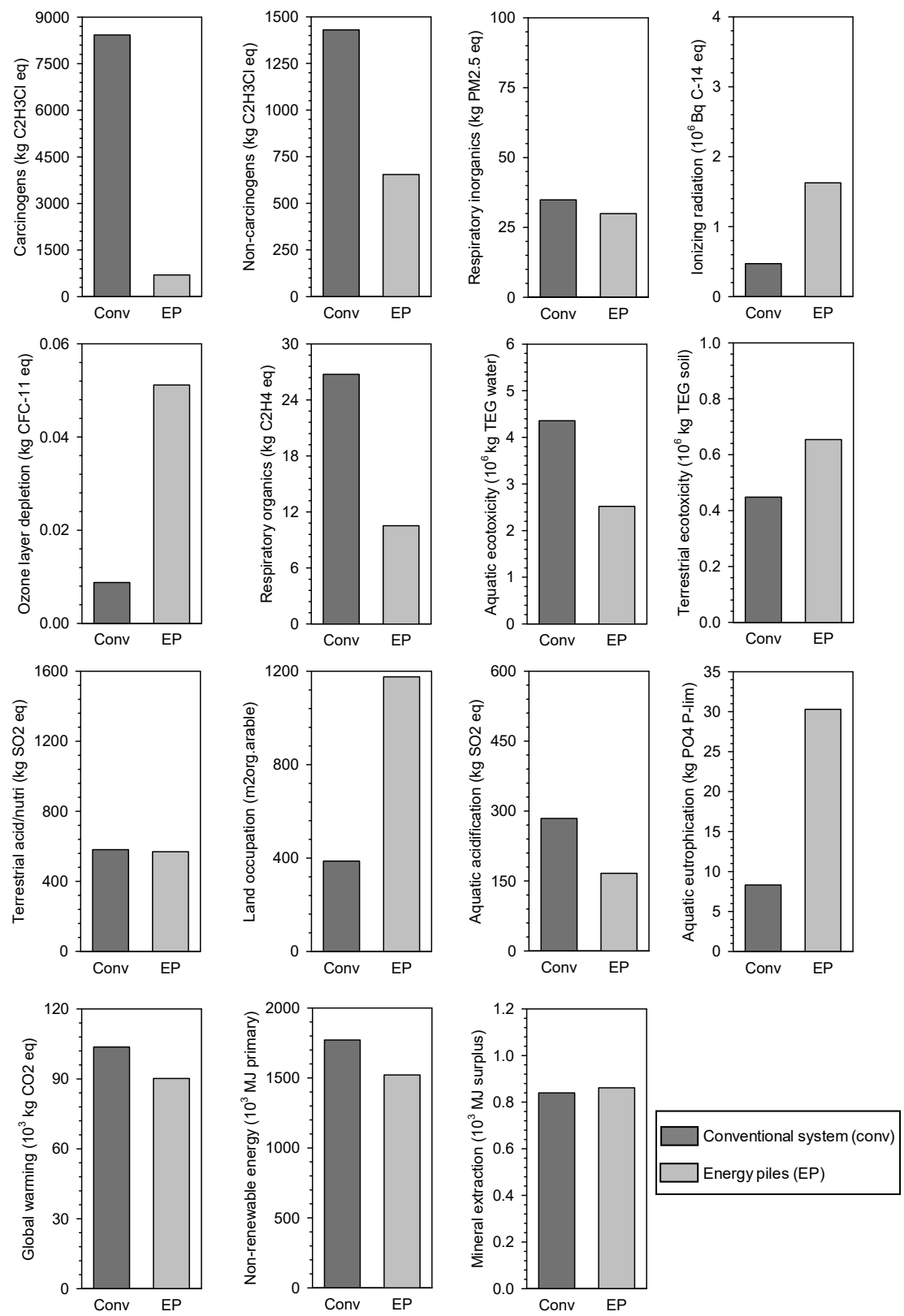


Figure A.4. Midpoint indicators of the conventional system and the energy piles for Berlin

Curriculum Vitae



GIANLUCA SPERANZA

Civil Engineer

Research Engineer with a background in civil engineering skilled in building and geotechnical construction. Interested in: complex infrastructures project, renewable energies, sustainable infrastructures, design of environmentally-conscious and cost effective solutions, slope stability, mitigation and risk assessment of landslides.

CONTACT



gianluca.speranza7@gmail.com



CH: +41779693907
IT: +393248728996



Avenue de Tivoli 2^E
1007 Lausanne - CH

SKILLS

Hard

- Construction Design
- FEM modelling
- Laboratory and field tests
- Life cycle assessment

Soft

- Critical thinking
- Team working
- Ease of learning
- Proactivity

SOFTWARES

Office	Advanced
Geostudio	Good
Zsoil	Good
SAP2000	Good
SCIA	Basic
Revit	Basic
Autocad	Advanced
Comsol	Basic

LANGUAGES

Italian	Mother tongue
French	B2
English	C1



International (CH) Driving License A1 , B

HOBBIES

Cooking, Motors, Travelling

Personal Information

- **Country:** Italy
- **Date of born:** 24/06/1990
- **Place of born:** Vallo della Lucania (SA) - Italy
- **Swiss residency permit:** B

Education

11/2016-06/2020	Ph.D.- EPFL Geomechanics, Supervisor Prof. L. Laloui.	
10/2012-07/2015	Master in Civil Engineering University of Salerno (IT)	
09/2009-09/2012	Bachelor in Civil Engineering University of Salerno (IT)	
09/2004-07/2009	High School – Scientific Studies Liceo Scientifico L. da Vinci Vallo della Lucania	

Professional Experience

05/2017 – 10/2019	Research Engineer Nobatek/Inef4 - Bordeaux France. Marie Curie ESR – Joint recruitment with EPFL	
10/2015 - 11/2016	Civil Engineer GR design and consulting - Italy	
02/2015 - 06/2015	Stage Géotechnical Engineer Deltares – The Netherlands - Erasmus	

For more information refer to the LinkedIn profile scanning the QR code or clicking on this [LINK](#).



Scientific publications



Journal papers:

- Effects of partial saturation on the lateral earth thrust: a comparison between analytical and experimental analyses. Gianluca Speranza, Alessio Ferrari, Lyesse Laloui (In preparation).
- Physical modelling for the lateral thrust of unsaturated soils. Gianluca Speranza, Alessio Ferrari, Lyesse Laloui (In preparation).
- Life cycle environmental assessment of retaining walls in unsaturated soils. Gianluca Speranza, Alessio Ferrari, Pyrene Larrey Lassalle (Submitted).
- Long-term performance and life cycle assessment of energy piles in three different climatic conditions. Melis Sutman, Gianluca Speranza, Alessio Ferrari, Pyrène Larrey-Lassalle, Lyesse Laloui, 2020. Renewable Energy, (<https://doi.org/10.1016/j.renene.2019.07.035>).
- Peduto Dario, Maximilian Huber, Gianluca Speranza, Joris van Ruijven, and Leonardo Cascini. "DInSAR data assimilation for settlement prediction: case study of a railway embankment in the Netherlands." Canadian Geotechnical Journal 54, no. 4 (2016): 502-517 - (<https://doi.org/10.1139/cgj-2016-0425>).

Conference papers:

- A physical model for the interaction between unsaturated soils and retaining structures. Gianluca Speranza, Alessio Ferrari, Lyesse Laloui (Accepted - Lisbon - Portugal 19th -21th October 2020).
- An experimental investigation on the water retention behaviour of a silty soil for the computation of the lateral earth thrust on a retaining wall. Gianluca Speranza, Alessio Ferrari, Maxime Pousse, Lyesse Laloui (Glasgow 26th-28th June-2019,<http://doi.org/10.5281/zenodo.2792408>).

Teaching activities



- Assistant for the master course Slope Stability at EPFL 2016-2017, 2017-2018, 2018-2019.
- Assistant for the master course Geomechanics at EPFL 2017-2018, 2018-2019.
- Supervisor of the Master student Andrea Caldirola (Erasmus student from Politecnico di Torino). Internship and master thesis work at EPFL February-October 2018.

Others activities



- Member of the organizing committee for the Winter School on Geomechanics for Energy and the Environment 2020.
- Member of the organizing committee for the Winter School on Geomechanics for Energy and the Environment 2018.
- Member of the organizing committee for the Symposium on Energy Geotechnics Lausanne 25th-28th September 2018.
- Reviewer for the Journal Geomechanics for Energy and the Environment (Elsevier reviewer recognition April 2018).
- Member of the reviewer committee for the Proceedings Book Energy Geotechnics, Ferrari, A., & Laloui, L. (2018).
- Co-organizer of the Doctoral School on Unsaturated Soil Mechanics 2017 at EPFL.